Novel efficient wing buoyant aircraft design for enhanced aerodynamic performance

Mohammad N Hasan

Reg. no:150257963

Supervisors

Dr Jose L. Curiel-Sosa

Dr Andrzej F Nowakowski

This thesis submitted to the University of Sheffield in partial fulfilment of the requirements for the degree of Doctor of Philosophy

April 2021

Abstract

The current research aims to design a novel concept for an efficient wing buoyancy assisted aircraft *(EWBA)* by investigating the optimum aerodynamic efficiency of next-generation aircraft features; this *EWBA* is entirely different from a current traditional airship and aircraft. Typically, the *EWBA'*s applications are limited to cargo, logistics support, and surveillance, depending on market demands. In the relevant literature, very little attention has been paid to optimising the design features by computational design point methods case of an airship. Firstly, the new concept for the *EWBA* mathematical model involved the design of separate aerostatic and aerodynamic models. The computation method was developed to determine the maximum take-off weight *(MTOW)* from a set of parameters – namely payload, crew, and fuel fraction. Values for additional features such as power loading, wing loading, and optimal wing area were also obtained via *MATLAB* to satisfy the full mission profile concerning weight balance; all these constraints are determined through design point. After then, the *3D* model of 6:1 prolate spheroid, tail hull, straight wing hull, and efficient wing buoyant airship *(EWBA)* was designed in Solidworks after several iterations. Then, the computational fluid dynamics *(CFD)* method was verified using 6:1 prolate spheroid experimental data. The pressure-base ANSYS Fluent (Ansys 16.1) solver was successfully employed for investigating the aerodynamic performance of efficient wing buoyant airship *(EWBA),* planner wing, and tail hull airship and compared its aerodynamic parameters; namely the lift coefficient, drag coefficient, and lift to drag ratio by using the Reynolds-averaged Navier-Stokes *(RANS)* governing equation $(k-\varepsilon)$ and the *RSM* model. The numerical results were reasonably agreed with experimental results of 6:1 prolate, specifically lift coefficient, drag coefficient, and pressure coefficient. The aerodynamic efficiency of numerical data for the *EWBA* model was significantly improved compared to the straight wing airship and other wingless models (tail hull and prolate airship). The ratio of aerostatic lift to aerodynamic lift *(ASL-to-ADL)* was adequately balanced for the proposed *EWBA* model with advanced wing elements. This represents a significant improvement to the current airship. The new *EWBA* offers a greater payload capacity and higher velocity than a conventional airship. Furthermore, fuel costs are reduced significantly by 49%, leading to a positive environmental impact.

Acknowledgements

I would like to thank foremost my supervisor, Dr Jose L. Curiel-Sosa, for his enduring guidance, encouragement, and support, throughout this project. I am very honoured to be able to work with him. He has been played an inspiring role model for over three years of my research, and I am looking forward to learning more from him for much longer. I also would like to sincerely thank Dr Andrzej F. Nowakowski, I also highly appreciate his guidance and comments during the early stage of my PhD research, which will be greatly helped to achieve my goals. Finally, no words can completely describe how grateful I am to my family, especially my mother, my brother Mr Humayun Akbar and my wife, who immensely support in throughout my life.

Table of Contents

List of Figures

List of Tables

Nomenclature

b	Wingspan, m
AR	Aspect ratio
BLC	Boundary layer control
BR_{To}	Buoyancy ratio at take-off
CAM	Computational Aerodynamic Model
CFD	Computational fluid dynamic
C_d	2D drag coefficient
C_D	Drag coefficient
C_{Do}	Zero-lift drag coefficient
C_{Di}	Induced drag coefficient
C_{DV}	Volumetric Drag
C_{D0f}	Fuselage drag at 0^0
C_L	Lift coefficient
C_l	2D lift coefficient
C_{li}	Ideal lift coefficient
$C_{L\,max}$	Maximum lift coefficient
C_m	2D pitching moment coefficient
Cp	Pressure coefficient
CO_2	Carbon dioxide
C_r	Wing root chord, m
C_t	Wingtip chord, m
C_{DV}	Volumetric drag coefficient
CG	Centre of gravity
CAD	Computational aerodynamic model
CA	Conventional Airship
CS	Certification Specification
$COSPAR$	Committee on Space Research
D	3D drag force, N
D_i	Diameter of a propeller, m
$DCAM$	Design computational aerodynamic model
DES	Detach eddy Simulation

Nomenclature

DNA	Direct numerical Simulation
ISA	International Standard Atmosphere
FVM	Finite Volume method
J	Advanced ratio, $= U_\infty / n_s D_{in}$
L	3D lift force,
LLT	Lifting line theory
LTA	Lighter than Air
L/D or C_L/C_D	Lift to drag ratio
L_{buoy}	Buoyancy lift, N
$LRFD$	Standard load and resistance factor
BR	Buoyancy ratio
E	Aerodynamic efficiency
FF_H	Form factor
C_f	Skin friction drag
f_m	The function of Mach number
f_{LD}	The function of fuselage distance
g	Gravitational force
$\frac{h}{b}$	Height over span ratio
K	Kinetic energy, N
K_c	Correction factor
$\frac{l}{d}$	Hull thickness ratio
$MAAT$	Multibody advance airship for transport
N	Propeller rotational speed, rev/s
NLF	Natural laminar flow
N_L	Number of lobs
$NOAA$	National Oceanic and Atmospheric administration
P	Propeller power
Q	Propeller torque, Nm
R	Gas constant
RSM	Reynolds stress Model

Re	Reynolds Numbers
$\bar{C}$ (MAC)	Mean aerodynamic chord number
$S\ or S_{aero}$	Wing Area, m^2
$S_{wet\ f}$	Fuse large wetted area, m^2
S_{up}	Upper wing area, m^2
S_{low}	Lower wing area, m^2
SSL	Standard Sea Level
t	Wing thickness, m
$\frac{t}{c}$	Aerofoil thickness ratio
T	Temperature, 0_C
Tr	Trust, N
T_i	Turbulence intensity level
Tu	Turbulence
U	Free steam velocity
U_∞	Incoming free stream velocity, m/s
U_t	Tangential velocity, m/s
PAX	Passenger
V	Velocity, m/s
V_{0l}	Volume, m^3
VS	Vertical stabilizer
V_R	Resultant velocity, m/s
$(V)^{\frac{2}{3}}$	Hull volume two-third
V_{T0}	Take off velocity, m/s
VLM	Vortex lattice methods
X_{cg}	Distance between wing leading edge and the centre of gravity, m
X_{ac}	Distance between wing leading edge and the aerodynamic centre, m

HBA	Hybrid buoyant aircraft
HAA	High Altitude Airship
q_1	Static pressure at station 1
q_1	Static pressure at station 2
$EWBA$	Efficient wing buoyant aircraft
$RANS$	Reynold averaged Navier- Stokes
W_{To}	Take-off weight, kg
W_E	Empty weight, kg
W_P	Payload, kg
W_F	Fuel weight, kg
W_{FIX}	Fix weight, kg
W_{VAR}	Variable weight, kg
W_C	Crew weight, kg
W_{MTOW}	Maximum take-off weight, kg
ΔW	Heaviness
W_R	Ratio (upper and lower wing area)
$\emptyset$	Climbing angle, °
e	Oswald efficiency factor
ε	Turbulent dissipation rate
μ	Viscosity
ρ	Density
ρ_a	Air density
ρ_g	Gas density
α *(AOA)*	Angle of attack, °
α_{eff}	Effective angle of attack, °
α_i	Induced angle of attack, °
ω	Propeller rotational speed, rad/s
ω_1	Boundary layer in station 1
ω_2	Boundary layer in station 2
$\Delta\omega$	Boundary layer development

Chapter 1. Introduction

1.1 Historical background of an airship and hybrid air transport

The technology for lighter-than-air (LTA) flight has been in existence for more than 300 hundred years. The first *LTA* machines were constructed by the Montgolfier brothers, who chose to use smouldering solid fuel to heat the air in the balloon and by Jacques Charles, who was the first to use hydrogen instead of hot air. The first manned flights were carried out in late 1783. Jacques-Étienne Montgolfier was the first person to take to the air in October 1783. In December 1783, Jacques Charles ascended to a height of about 550m in a manned hydrogen-filled balloon [1]. Hydrogen generated buoyancy due to the differences in density between the air and the lifting gas, enabling manned flight for more extended periods. As a result, many designers, inventors, and engineers were called to design new hydrogen-filled balloons.

In 1852, the French engineer Henri Gifford invented the first powered airship; this was equipped with steering control and a propulsion system. In the late 1800s, his first successful flight covered 27km; this was undoubtedly a landmark for the steam power that made the first practical test flight possible. In 1852, Ferdinand von Zeppelin, the German general and aircraft manufacturer, constructed an airship that showed a significant improvement in aerodynamic performance [1, 2]. In July 1900, Zeppelin launched an airship that was 419 ft long and powered by a 16-horsepower motor. In 1903, the Wright brothers manned their first flight. It was not until the 1900s, during the golden age of airships, that many designers began to build and test airships for famous investors. After building approximately 20 balloons and airships, Alberto Santos-Dumont changed course; as winged aircraft were much faster than airships, he began to manufacture those instead. During World War I, Germany built many airships for the purpose of bombing operations.

In the 1920s, the first commercial airship was designed; this would become very popular in the 1930s. Illustration 1.1 shows examples of early airship and balloon designs: (a) the Zeppelin, (b) Henri Giffard blimp balloon (1852)[1]. Airships were moderately successful across Europe due to their efficiency, safety, and flexibility in design. They were successfully operated through the first half of the twentieth century; even so, some investors began to

develop winged airships at around the same time [3, 4]. The highly-publicised *Hindenburg* disaster in 1937 helped to seal the fate of large airships; see Illustration 1.2a for a picture of

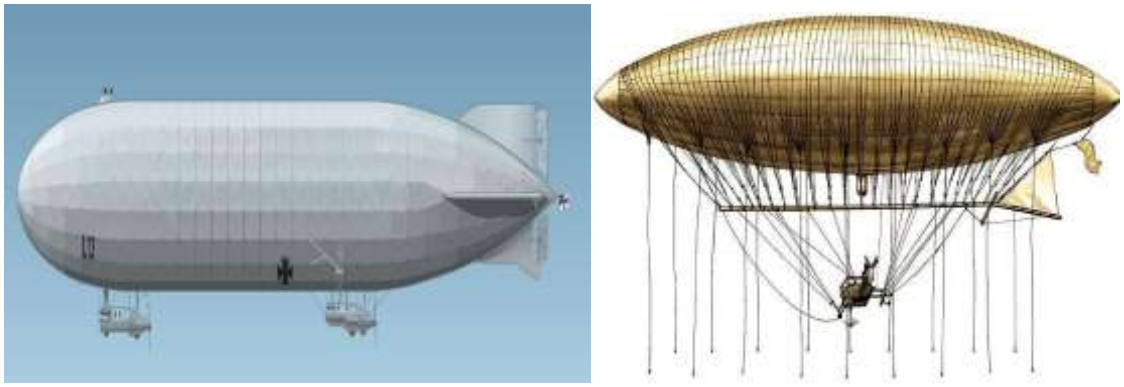

(a) (b)

Illustration 1.1 (a) Zeppelin, (b) Henri Giffard blimp balloon (1852)[1]

the accident. In comparison, hybrid buoyant air transport maintained an excellent safety record and was in operation up to the 1940s. By late 1940, the *USA* had built more than 150 non-rigid airships that were used successfully for military purposes, such as convoy escorts and submarine scouting during World War II [1, 5]. However, the large size of airships meant that they were difficult to manoeuvre, especially during ground handling [1]. The Graf Zeppelin (Illustration 1.2b) was decommissioned around the same time.

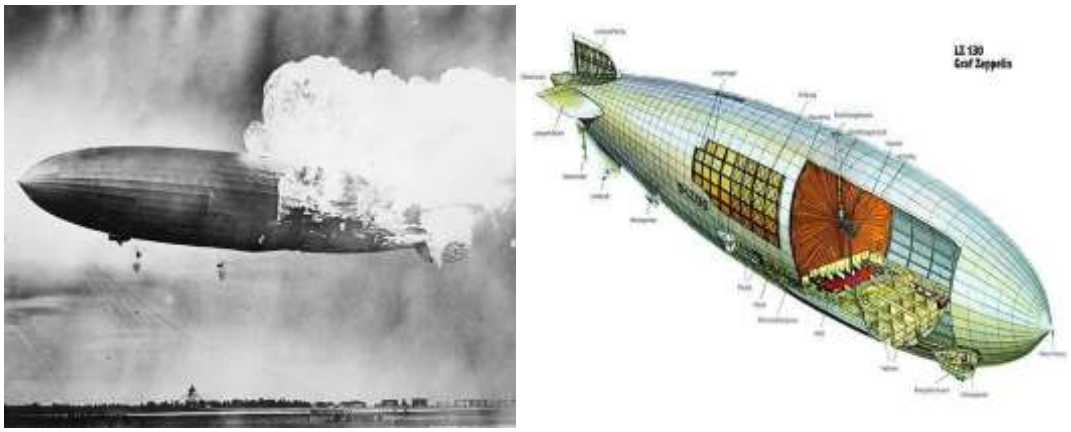

(a) (b)

Illustration 1.2 (a) Hindenburg accident, (b) Zeppelin II [4].

There has been renewed interest in airships in the last few decades due to their potential applications in a variety of areas, especially in the defence and civilian sectors. On the back of the moderate success of airships in Europe during the early twentieth century [1, 4], airship

technology was sufficiently well-established to be advanced by aerospace industries. The USA manufactured four giant rigid airships called the *Shenandoah*, *Los Angeles*, *Macon*, and *Akron* [1]. Later, *NASA* became interested in modernising airship technology. This interest soon motivated the development of airships with wings [3, 4]. Instead of advancing airship technology, researchers moved into designing hybrid buoyant air transport.

In 2010, the Hybrid Air Vehicles Ltd and Northrop Grumman began collaboration on a large longitudinal study for an Airlander-10 hybrid airship. This airship was originally developed for the US Army and was named the HAV304 [6]. Despite having spent $300 million, the project was subsequently abandoned by the US Army due to a combination of technical and performance challenges, as well as budget constraints [7]. In February 2014, the HAV304 was repurchased by Hybrid Air Vehicles at a nominal price. The company received £2.5 million ($4.16 million) in funding from the UK government to relaunch the HAV304 for civilian purposes as the Airlander 10. The Airlander 10 is one of the largest airships in the world, having a length of 91 metres, a width of 34 metres, and a height of 26 metres, with an envelope volume of 1.34 million cubic metres and a buoyancy ratio of 60:40 [8]. In August 2016, the prototype made a successful maiden test flight but unfortunately subsequently deflated when a mooring broke loose (Illustration 1.3a). Later that month, during its second flight test, the Airlander 10 suffered damage to its flight deck following a crash landing (Illustration 1.3b). Eventually, in October 2018, Hybrid Air Vehicles was awarded production approval by the Civil Aviation Authority and the European Union Aviation Safety Agency. This was considered a remarkable achievement for the Airlander 10, according to Executive Director Nick Allman [9, 10].

(a) 

(b) 

Illustration 1.3 (a) First flight test and subsequent deflation [9], (b) crash landing during the second flight test [7, 9, 10]

As observed in a recent study by Anwar et al.[4], the design concept of hybrid buoyancy aircraft (HBA), whether using fixed or rotary wings, combines *LTA* technology and heavier-than-air (HTA) technology to create *HBA* that are low-emission contenders in the air transportation sector. This is particularly important since these aircraft can be designed to fit somewhere between high- and low-speed vehicles to become next-generation aircraft.

1.2 Current uses of the airship and hybrid airship

Historically in the aerospace industries, traditional and well-known aircraft are in the category of *HTA* transport, whether an airship is in the *LTA* vehicle category. There is a further type of aircraft known as a hybrid aircraft, which behaves in a similar way to traditional aircraft due to its being heavier than air. This attribute allows its use in important sectors. Modern airships have recently been proposed for a broad range of applications.

1.2.1 Airship uses in satellites

An airship is a much less sophisticated and less costly option for satellites. Because airships can be run at low, medium and high altitudes, they require fewer sensitive antennas and also need less powerful optical lenses for image resolution. An airship can fly continuously in a predictable Earth orbit, which makes it easy to track [11]. A further benefit to consider is that satellites are inhibited by no-fly-zone restrictions [12].

1.2.2 Airlifter

Airships are suitable for heavy-lift cargo transport [13], a planetary investigation [14, 15], intelligence gathering, surveillance, and reconnaissance. Further, airships could be

industrialised and provide cargo ambulance services for urban areas. An *HBA* would probably afford the best design for a heavy lifter. These machines are able to provide a better lift function for their aerodynamic characteristics and particular gas volume. An *HBA* has good handling quality when near the ground due to it being heavier than air – this is particularly advantageous during loading and unloading on the ground [13].

In scientific, military, and commercial fields, there has been significantly increased interest in *HBA* recently, including in civilian tourism and advertising [5], surveillance [3, 16], environmental monitoring [14, 17, 18], telecommunication, stratospheric relays [19-21], and planetary investigation [14, 15]. Moreover, *HBA* transports are useful in oil, gas, pipeline, and agricultural operations [22].

1.3 Aerostatic modelling

Static lift is dependent on the principles of buoyancy. Buoyancy is dependent on the displacement of air caused by the volume of an immersed object; in this case, the object is the airship. According to Archimedes' principle, the force of buoyancy is equal to the weight of the fluid displaced, which can be expressed by the equation $B = V.\rho_a$ [3, 4, 23]. Here, B is the upward acting buoyancy force on the aircraft. V is the volume of the aircraft and ρ_a is the mean density (air density) around the aircraft. Consequently, buoyant aircraft design requires specific fluid properties, which in this case is an energetic atmosphere. This means that the aerostatic lift needs to be considered in the design of *HBA*, which depends on air properties that rely on an unstable atmosphere [22, 24].

In the Atmosphere, the force of buoyancy acts on all bodies. However, this force is negligible when compared with the weight of those bodies. At sea level, the buoyancy of a human being is approximately 0.12% of their body's weight. If the weight of a body is less than the displacement of air, there would be a net upward lift, which can be computed by the following equation:[3, 24], $L_{net} = B - W$, where, L_{net} is the net lift, W is the weight of the body and B is the buoyancy force.

If we consider the volume, V, of the aircraft, the weight equation is expressed by $W = V.\rho_g + w_0$, where w_0 is the structural weight of the envelope and ρ_g is the gas density. Now, combining the equations above, we arrive at a new expression for the buoyancy force: $L_{buoy} = V(\rho_a - \rho_g)g - w_0$, where w_0 is very small compared with V. Since the w_0 term is so small; it was not considered earlier; however, the term needs to remain for analytical purposes. This

term, which is subtracted from the $V_{ol}(\rho_a - \rho_g)g$, may be rearranged to define the gross lift of a gas cell [1, 4]. Consequently, the buoyancy lift force L_{buoy} may be expressed as:

$$L_{buoy} = V_{ol}(\rho_a - \rho_g)g \quad 1.1$$

and the lift coefficient of buoyancy may be expressed as:[24]

$$C_{L\,buoy} = \frac{L_{buoy}}{\rho_a g V^{\frac{2}{3}}} \quad 1.2$$

Where, ρ_a is the air density and ρ_g is the gas density. The gas difference $(\rho_a - \rho_g)$ is the net lift of the gas cell volume per unit. At sea level, the international standard Atmosphere (ISA) has 96% purity, which implies that the lifting capacity of helium gas is equal to 1.05 kg/m^3, compared with the lifting capacity of the aircraft's density which is 0.1785 kg/m^3. In contrast, the gas volume is dependent on the altitude and temperature of the lifting capacity of gas according to the gas laws. Therefore, the gas density can be calculated by the Clausius-Clapeyron equation for ideal gas:[3] $\rho = \frac{P}{RT}$, where the terms ρ, P, T, and R are equivalent to density, absolute pressure, temperature, and the gas constant, respectively. Traditionally, airships maintain internal pressure by using air-inflated bladders inside the envelope; these are called ballonets [3, 4, 14].

However, prior research by Agte et al.[25] argues that controlling the density of helium is an elusive technological goal. Since the notion of *HBA* technology is not completely new, the technology is being studied by the large aircraft companies Lockheed Martin and Boeing in ongoing projects such as Skycat, Aeroscraft, Airlander, and the P-791. Thus, these approaches would be applied to *HBA* as well. A further consideration in design is that the aerodynamic shape of the airship needs to determine the percentage (%) of fullness with respect to the additional required volume on the hull. The hull is adjustable to suit various manoeuvres. A ballonet can be of assistance in these circumstances to maintain the aerodynamic shape of the airship by controlling air [23, 26]. In contrast, hybrid rigid aircraft do not have this problem because aerodynamically, they are sufficiently heavy to maintain the shape of the outer fuselage during manoeuvres.

Historically, there has been a great deal of confusion in the literature regarding the numerical and experimental data of *EWBA*. Even so, there is considerable literature (albeit related to conventional aircraft) that offers an alternative perspective to *EWBA* data equivalent

to the approach for conventional aircraft. A further benefit of *EWBA* is that they use less fuel than traditional aircraft during take-off because becoming airborne relies on aerostatic lifts.

As a result, hybrid buoyant air transport offers benefits in relation to environmental issues [5, 27]. Moreover, *EWBA* uses the same landing and take-off approaches as conventional aircraft. The theory holds that by using static or buoyancy lift in *EWBA* design, emission gases could be further reduced by between 45% and 65% [27, 28]. Therefore, these newly designed forms of transport can indeed claim to be green, clean, economical, and environmentally friendly aircraft.

1.3.1 Selection of lifting gas

Helium, hydrogen, and heated air are the most common lifting gases. Mostly, lifting gases assist in the displacement of ambient air and thus achieve positive buoyancy.

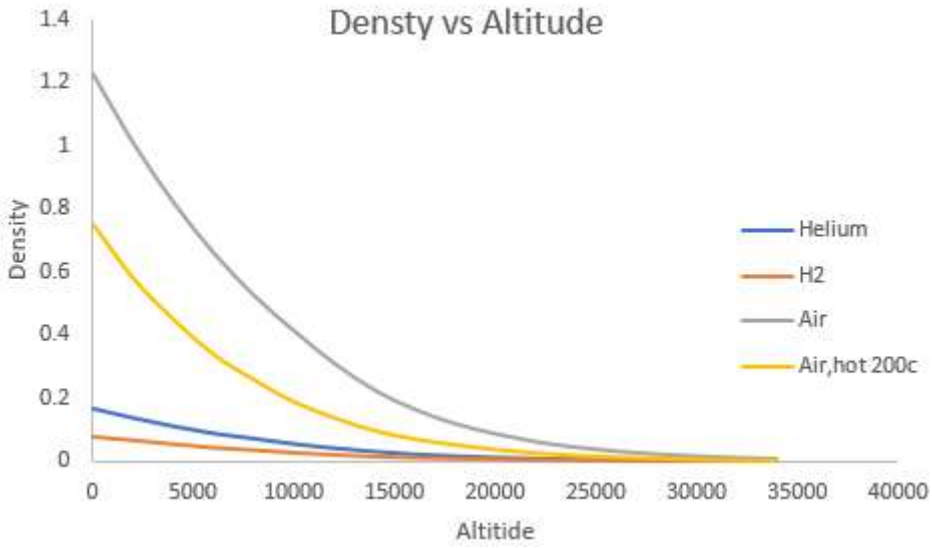

Figure 1.4 Comparisons of lifting gases

LTA flight is only possible because of buoyancy [19]. Indeed, for an aircraft to glide through the air, the weight of the air displaced has to be more than the weight of the aircraft. An aircraft will be more likely to float while there are lighter-than-air gases inside the hull. Figure 1.4 plots the densities of the most common lifting gases at different altitudes. It can be seen that hydrogen (H_2) has the lowest density of these lifting gases but that helium (He) comes a close second. Hot air, however, is only a little less dense than air at standard ambient temperatures. Although the first manned flight was achieved using hot air as a lifting gas, nowadays, hot air is only used for leisure purposes due to its comparatively low buoyancy.

Hydrogen has the lowest density of any lifting gas. Still, it tends to have a violent chemical reaction with oxygen in the presence of a flame or spark, resulting in catastrophic air disasters. For this reason, helium is chosen as the lifting gas for *EWBA*. For safety reasons, hydrogen will never be considered as a viable lifting gas where human life is at risk [29].

Thus, helium has become the lifting gas of choice for *LTA* vehicles. Unfortunately, the cost of helium is forecast to rise significantly in the future due to an increase in global demand and reduced supply, but for now, helium is widely available [29, 30].

1.3.2 Pressure control and buoyancy lift control system

Figure 1.5 depicts the traditional pressure control system used in some modern airships [3]. The diagram shows how airflow is directed into the propeller slipstream by blowers, further pushing the airflow towards the ballonets via control valves and channels. Figure 1.5 also shows the ballonet's front and rear side valves by controlling the central buoyancy position. Various alternative systems have been applied to airships to control buoyancy, for example:

- rainwater storage;
- restoration of hydrocarbons via the exhaust system;
- external vertical force;
- vector thrust;
- constant weight [3, 23].

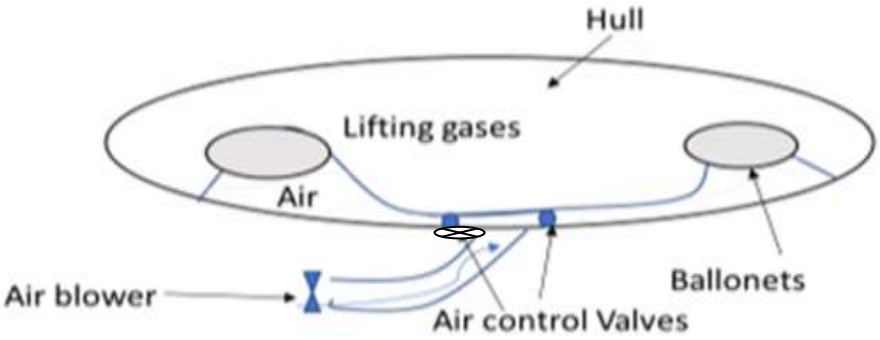

Figure 1.5 Airship pressure control system.

1.4 Aerodynamic model and fusion

In terms of the aerodynamic response of *EWBA*, initially the greatest focus during the design process, as well as literature reviews of the sizing of aircraft wings and the volume of the hull. The goal of this chapter is also to studies, the specific attention of the wing area, the aerofoil, and optimal aerodynamic performance at cruise conditions.

An aerofoil generates aerodynamic lift in accordance with airspeed, air density, and the angle of attack (AOA) [31, 32]. This principle is performed as the same as conventional aircraft for *EWBA*. Moreover, the lift is developed when the *AOA* is increased; it is always perpendicular to the resulting upcoming airflow. Indeed, various articles have been published concerning the aerodynamic performance over the last few decades; most are precisely associated with lift coefficient and a drag coefficient of traditional aircraft and airships, which has presented the lift generated by the wing as being that of traditional aircraft [4, 27, 33, 34]. This lift can be calculated by the following fundamental equation:

$$C_L = \frac{L}{\frac{1}{2}\rho_a v^2 S_w} \tag{1.3}$$

But, an airship creates most of the lift with its lifting gases. There is no drag due to lift because of the buoyancy.

However, if an airship flies at any *AOA*, it generates aerodynamic lift and as well as drag due to lift. An airship is typically flown at a very low *AOA*; thus, it produces more significant skin friction drag than a conventional aircraft and zero lift pressure (form drag); it varies with fineness ratios *(FRs)* of the airship's hull. In this research, the hull volume keeps consistent for all models to different effects of *FRs*. Figure 1.6 presents a schematic diagram of an aerodynamic *EWBA*. In fact, the design approaches were started from an aerostatic model, weight variable parameters; this scheme ran via computer-aided design tools and continued until reaching the design as aerodynamic prospects.

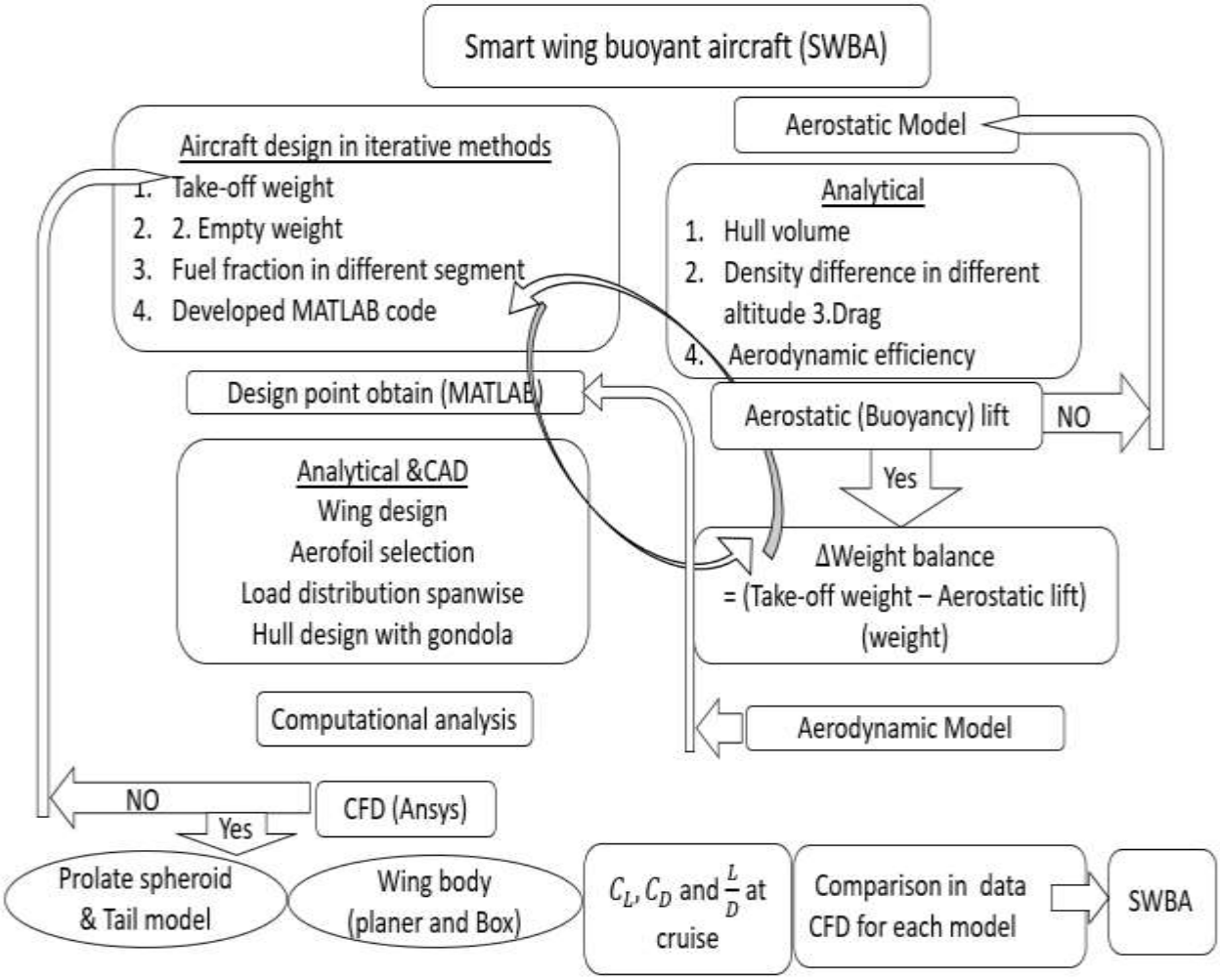

Figure 1.6: Workflow of aerodynamic *EWBA* is a schematic diagram

In an attempt to address this interesting, novel concept in *EWBA* design, the aerodynamic parameter is obtained but remains challenging due to the wing hull with lifting gases, mainly aerodynamic efficiency $\left(\frac{L}{D}\right)$. Consequently, *EWBA* design mostly concerns combination equation $C_{Lwing} + C_{Lbuoyant}$ and the balance of the buoyancy ratio. These issues will be discussed in Chapter 2.

1.4.1 Motivation to develop the advanced *EWBA*

This research pursues the innovation of an *EWBA*, which uses both *HTA* and *LTA* technology. According to Boyd [35], Hybrid aircraft can be carried considerably more payload than a conventional airship. The sensitivity of climate effects is much less than *LTA* transports;

the aerodynamic lift and buoyancy lift performance with a combination of hybrid air vehicles yields unanticipated merits than current airship and aircraft. Boyd also said, 60% of the economical cost can be reduced over traditional air vehicles [35].

First, the primary motivation for pursuing this project is the paucity of research, examination, and implementation of *EWBA* in recent decades – yet this is a form of air transport that could greatly reduce the effects of current air transport systems on climate change and its ecological impact. Environmental legislative bodies, economic legislative bodies, the aircraft manufacturing industry, and air transportation companies all have the objective of reducing air pollution. Current evidence shows that around 2.2 billion commuters contribute approximately 2% CO_2 per annum [24]. With the growth rate of traffic, this is expected to increase to 3% by 2050. The Advisory Council for Aeronautics Research in Europe, together with the aircraft industry has established coordinated action. This entails new goals for future aircraft and funding that vigorously supports research programmes involving the development of green air transport. The latest research is optimistic: the anticipated timeframe for technological development of green air transport is 20 to 40 years.

1.4.2 Further motivation of highly efficient aircraft

This section addresses the additional motivations with regard to *EWBA* research and fusions of design with dynamic and static performance in different conditions.

Aerostatic lift and atmospheric behaviour

Haque et al.[4] states that an airship is controlled by internal pressure using bladders (ballonets), as explained in the previous section, whereas *HBA* can maintain pressure through compression and expansion by means of a compressor. A number of studies in the literature have addressed the maintenance of the aerodynamic shape of an airship consistently in varying conditions. However, this is not an issue for *EWBA* as structurally; they are sufficiently solid to maintain their shape. It would be of special interest to this research to discover whether there is a sufficient theoretical and mathematical explanation to describe the aerostatic lift that determines when *EWBA* can take off and how *EWBA* will behave in the Atmosphere at different altitudes.

Initially, research into aerostatic lift was investigated by examining the behaviour of 1 kilogram of helium gas (see Table 1.1 and in **Appendix A.1**). This investigation revealed that the density of helium does not change at the same rate as its volume and that the upward thrust

and the net lift were constant. Indeed, the volume of helium has been seen to increase by a factor of 10.073, which factor has fluctuated with the volume of the hull. In fact, the flexibility of volume when designing the hull is another crucial motivation and driving force behind *EWBA*.

Aerodynamic performance

An issue of key interest in *EWBA* is their aerodynamic behaviour and performance parameters. Basically, the most variable source of aerodynamic lift comes from an efficient aircraft wing. This design does not rely exclusively on lifting gases (gases that are lighter than air), and it includes a propulsion system, control system, and buoyancy system. Most of the recent publications regarding airship technologies discuss *LTA* vehicles, even though the manoeuvrability of these aircraft is very poor, especially at low speeds. Regarding *EWBA*, with their combination of airship technologies and conventional aircraft concepts, researchers and designers need to pay greater attention to aerodynamic activities. The drag coefficient, lift coefficient, and *L/D* relies not only on the wing surface area, as in a traditional aircraft, but are also significantly reliant on the lifting surface of the *EWBA* hull, bearing in mind the existing aircraft relationship between the *L/D*, the wetted area, and the aspect ratio.

Thus, analytically, the *EWBA* is capable of tolerating extended flight during buoyancy lift with excellent stability and control by means of its wings. *EWBA* could be enabled to satisfy the gap between low-speed airships and traditional aircraft.

Combination of highly efficient advanced EWBA

As in the previous section, a design that marries the aerodynamics of the airship, the aircraft, and the *HBV* is a worthy contribution to the field [4, 36]. However, as yet, there has been no investigation into the aerodynamic performance of *EWBA* with advanced wings. Figure 1.7 illustrates the combination of *EWBA* lift with aerostatic, aerodynamic, and engine power.

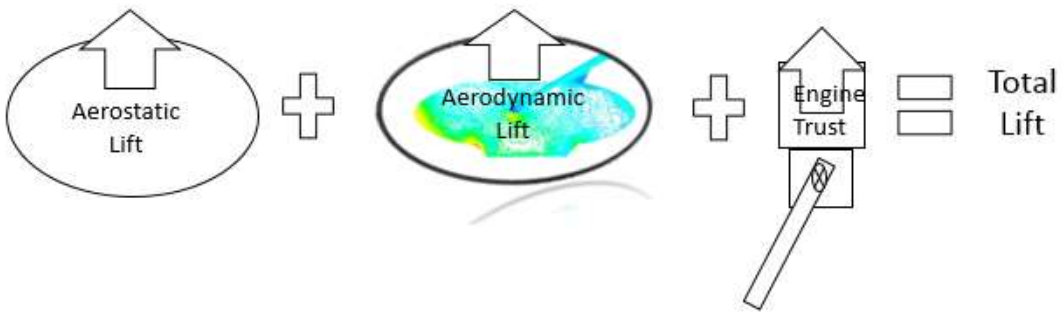

Figure 1.7 Combination lift of *EWBA*

The computational matching plot design method would be beneficial to establish the most appropriate sizing of the wing for *EWBA*. This has not yet been used in relation to the airship or hybrid airship. Furthermore, there are currently very few wind tunnel testing data available for hybrid airship vehicles [4, 27]. However, conventional aircraft data are available as an alternative for the comparison of *EWBA*. This situation provides motivation for this study of *EWBA*. Also, it should be noted that *EWBA* offers some advantages in ground handling during manoeuvring. So far, very little attention has been paid to the role of *EWBA* design, specifically the conceptual design of this kind of alternative transport. Indeed, the current literature has not dealt in depth with *EWBA* aerodynamic characteristics and aerostatic lift, nor has it made an analysis of the lifting body with a helium gas cell.

Thus, the present research intends to analyse *EWBA* design and aerodynamic performance with a ratio of buoyancy of 50.64:50.34 (aerodynamic: static) by using the computational method. It is believed that the current research will offer new perspectives from which to approach the field of research and aircraft design regarding *HTA* and *LTA* technologies and the potential of *EWBA*.

1.5 Research aim and objectives

This research aims to generate a new concept for a next-generation efficient wing buoyant aircraft $(EWBA)$ to advance traditional concepts in terms of the characteristics provided below. The *EWBA* will have a rigid, structured hull, so at sea level, the total weight on take-off is greater than the buoyancy lift; this means that the *EWBA* will behave as an *HTA* conventional aircraft. In this case, the aim is to show that an empty winged rigid airship has sufficient weight to help it remain on the ground.

The research conducted will generate a computational design for a novel *EWBA* and perform aerodynamic analysis on parameters such as lift, drag, lift coefficient, drag coefficient, lift to drag ratio, and their relationship with aerostatic force and aerodynamic force. A computational evaluation of the novel concept will be accomplished, and we expect to determine whether possibilities exist for further improvements.

Indeed, the aircraft design research area is immense, which is why this research has been narrowed to the following specific areas:

1. A review of airship research literature encompassing the aerodynamics, aerostatics, and the various computational methods for obtaining experimental data.
2. The step-by-step design of a computational *EWBA* model using an iterative approach to compute the take-off weight, empty weight, and fuel fraction for different segments via *MATLAB.*
3. In the initial design, a *MATLAB* code was conducted to find an ideal design point to consideration of wing configuration, optimise a suitable estimation of power loading, and wing loading and wing area that can be satisfied the full mission profile with the design process. This has been developed for optimum aerodynamic efficiency using advanced wings and fusion parameters.
4. Development of four separate computer-aided design models: Prolate spheroid model, tail model airship, planner wing airship, and box wing hull model by user-friend Solidworks software. Moreover, there will be an investigation into the minimisation of the hull volume's wetted area to reduce drag (skin friction). The introduction of an efficient wing design to produce an extra amount of lift; provides sustainable aerodynamic performance through the lift to drag ratio, stability, and control during the manoeuvring required on a buoyant flight.
5. An investigation into the enhancement of aerodynamic performance in terms of the lift coefficient, drag coefficient, and the aerodynamic efficiency of advanced *EWBA* by analytically and computationally. The application of computational fluid dynamics (CFD) involved in two different turbulent *RANS* equations, for example (RSM), $(k-\varepsilon)$. The numerical and analytical results will be evaluated after several iterations with 6:1 prolate spheroid experimental wind tunnel testing data with a planner, non-planner winged body, and a wingless tail hull for the investigation of aerodynamic efficiency.
6. A fundamental objective of this research is the evaluation of computational methods of varying complexity in relation to their aerostatic and aerodynamic model.

1.6 Outline of the thesis

This first chapter (Introduction) has outlined the historical context; current uses of airships and hybrid airships explained the motivations for this project and set out the research aims and objectives. Chapter 2 presents the literature review pertaining to the airship aerostatic model, the aerodynamic model, and relevant traditional aircraft design methods and studies existing combinations of aerostatic and dynamic models. The review covers the essential

parameters of aerodynamic such as the lift coefficient, drag coefficient, and aerodynamic efficiencies; Chapter 2 even considers drag in the individual sections, for example, hull drag, engine drag, wing drag, and so on. Chapter 2 also reviews the analytical, numerical, and experimental processes of the *EWBA*. Indeed, aside from Chapter 2, relevant literature is reviewed in other chapters where appropriate to the topic exposition. Chapter 3 presents the conceptual design and the iterative method, including mathematical descriptions. Before outlining the final model employed, the chapter reviews the literature on the methodology of systematic aircraft design. Chapter 4 sets out the design as a computational aerodynamics model ($DCAM$) and specifies the design of four *CAD* models based on requirements, sizing parameters as a prolate spheroid shape model by Solidworks. This chapter also considers the computational turbulence model and verifies the *CFD* model to investigate the aerodynamic performance of *EWBA. T*he mathematical consequences of the aerodynamic parameters and aerodynamic performance of the *EWBA* are assessed with analytical results.

Chapter 5 reports the numerical characteristics of the Computational Aerodynamics model, which enabled to solve and analyse fluid flow problems with the boundary conditions. Mostly Chapter 5 also studies, verification of the different turbulent models, y^+ values, the specific results of *CFD* is the meshing quality, mesh generation, and numerical evaluation in a different model. Finally, Chapter 6 presents the overall conclusion of this *EWBA* research and recommendations for further investigation.

Chapter 2. Literature review

This chapter will review the published research relevant to the scope of this thesis in the following three main areas:

- Airship aerostatic model, buoyancy control methodology, and implementation for *EWBA*
- Investigation of planar and non-planar wings configuration and aerodynamic parameters, primarily the lift coefficient, drag coefficient, and aerodynamic efficiency
- Analytical, numerical, and experimental methods and application of the aerostatic and aerodynamic models for *EWBA.*

2.1 Effect of the Atmosphere in the aerostatic lift

Atmospheric temperature, pressure, and density are the parameters that influence the buoyancy of aircraft throughout the flight path, and various approaches of airships altitude control are taken into account and studied. It is scrutinised in-depth and based on atmospheric conditions and associated thermodynamics by governing equations. This investigation leads to an enhanced existing buoyancy control methodology for *EWBA* (efficient wing buoyant aircraft) in depth. First of all, make sure the required buoyancy is available to sustain the *EWBA* in equilibrium at sea level. Secondly, this design confirms better control and safety for *EWBA* using helium as buoyant gas. Thus, this section will review the depth effect of buoyancy for aeroplanes and airships at different altitudes.

Atmospheric considerations for airship

Pressure, temperature, density, and velocity differences are closely related to aerodynamics in the aeronautical engineering field. Air density and ambient temperature differences are the functions of altitude. Numerous researches have been performed on airship atmospheric behaviour and modelling. Some of them are in the military Atmosphere due to obligation in amenity. Historically various models have been produced, but the current study only considers those which have a straight impact on this design will be testified for simplicity. Kreider [37] studied a high altitude balloon of an adequate model, where were concentrating on lifting performances. Harrington [38] developed an aerodynamic model of a high altitude Airship (HAA) operated by lighter-than-air helium gas during the U.S. military's airship

research. He analysed the methodological feasibility of loitering (LTA) manoeuvring an airship.

The U.S. Standard Atmosphere (STD) the model has been a substantial effort devoted since 1976 due to its simplicity [39-41]. This model is constructed on a very simplified step of mathematical equations. It is instrumental and significant when compared with actual atmospheric data. Instead, a more comprehensive model with experimental values is the *COSPAR* International Reference Atmosphere ($CIRA-86$) also realistic[42-45]. The case of *ISO* (the International Organization for Standardization) Standard typical equation can be confirmed by a hypothesis of the hydrostatic scheme and standard gas law. The scheme has been isolated into three individual zones: the troposphere, the lower stratosphere, and the upper stratosphere. Pressure (P), temperature (T), and density (ρ) can be estimated by $T = 15.04 - 6.49 \times 10^{-3}$.h; $P = 101290 \times \left(\frac{T}{288.08}\right)^{5.256}$ and $\rho = \frac{P}{RT}$; where R standard gas constant. In fact, between 11,000 to 25,000 meters are the lower stratosphere. But different models have been created to define this region, where the lower stratosphere is constant, and the pressure declines exponentially; hence it can be computed with T is equal to $329.61K$ and P equal to $22.65 \times e^{1.73-0.000157} \times h$. Also, the above 25,000 meters in altitude is called the upper stratosphere scheme that considered by an intensification of temperature and the pressure decline steadily; where T is equal to $-141.94 + 299 \times 10^{-3} \times h$; the US standard Atmosphere hold P, T, and ρ over the altitude(h).

The *CIRA-1986* Atmosphere scheme offers pragmatic models of atmospheric T and ρ, as suggested by the Committee on Space Research *(COSPAR)*[42, 43, 45]. Several different versions of *CIRA* have been published since the early sixties. A combination of a numerical study carried by satellites, radiosondes, and ground-based with a global climatology of atmospheric temperature, zonal velocity, and geometrical height[46].

A number of studies have shown that the U.S. standard atmospheric data are efficient and valuable for designing aerostatic models. In Figure 2.1, Dumas et al.[47] has been using the Standard Atmosphere scheme presents with an average value of temperature and corresponds latitude about 45° north. Dumas et al.[47] compared his model with the data specified by the *CIRA-86* model for several latitudes. The comparative function of interpolative results presented a good agreement with the *CIRA* model for different latitudes[42]. In Figure 2.2, the *STD* model showed a reasonable upper space; however, not lower ones where temperature initiating from 30° north at a constant zone. It is revealed that the *STD* model

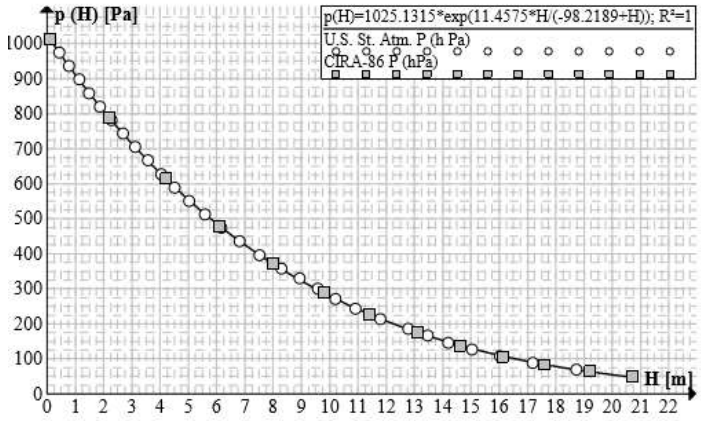

Figure 2.1: Pressure values of US STD model, CIRA-86 with Interpolating Equation[47]

assumed good agreements in the low temperatures. In Figure 2.3, Dumas et al. [47] produced

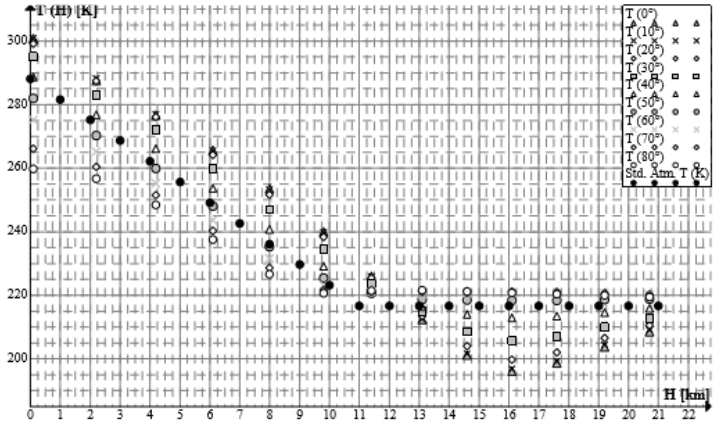

Figure 2.2: Atmospheric temperatures between CIRA-86 model and STD Atmosphere [47]

a similar comparison for density in different temperatures where *STD* data plotted alongside *CIRA* data, that was straggly each other for various latitude.

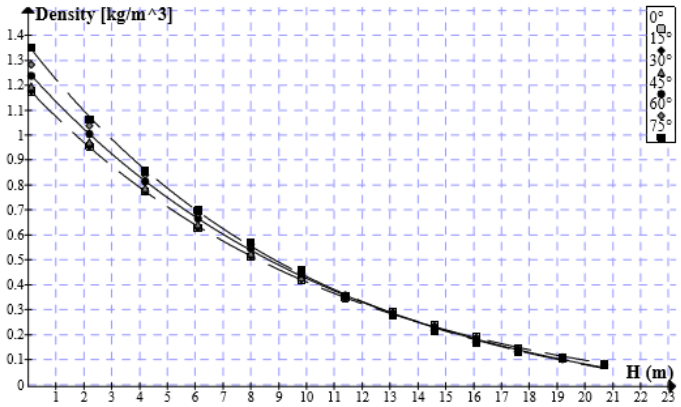

Figure 2.3: Evaluation of density at different latitude for CIRA model [47]

Kallmann et al.[48] also indicated that these functions of *P*, *T*, and ρ could be measured via the mechanisms. Alternatively, they could be coded from the U.S. Standard Atmosphere

data table, which is still a valuable and convenient data source for state-of-the-art research [49]. The account by Lopresto et al.[49] and [50] reports that NASA first published the model in 1958, then updated it in 1962, and subsequently approved a 1966 revision by the International Civil Aviation Organization ($ICAO$). After several iterations in 1976, these models were published by the National Oceanic and Atmospheric Administration ($NOAA$). Therefore, it is still the most consistent International Standard Atmosphere (ISA) data bank for aerospace and environmental researchers.

From recent publications [1, 23, 24], it is apparent that unmanned 'pressure balloons' came to be used as an envelope in high altitude researches which would be strong enough to exceed the pressure height by a substantial margin, deprived of rupture or gas discharge in high altitude. The studies found that the net lift was positive until the balloons were ascending above the pressure height; however, with a further increase in altitude, the net lift became zero (falls) at a pre-set equilibrium altitude. The effect of altitude is shown in Figure 2.4, where a fully filled gas balloon is leaving from position *'A'* at sea level, climbing to *'B'* with the constant lift to pressure height and at equilibrium temperature during this scheme. Moreover, if the balloon ascents beyond the point *'B'*, the lift will be reduced by itself at the same rate of gas as released by a control valve to prevent a build-up pressure differential through the skin. Indeed, the study also pointed out that the lift of the balloon would fall off to *'D'* if gas is released; the balloon gains a new pressure height for the gas constant. As a consequence, the balloon would descend to *'E'* at the constant lift.

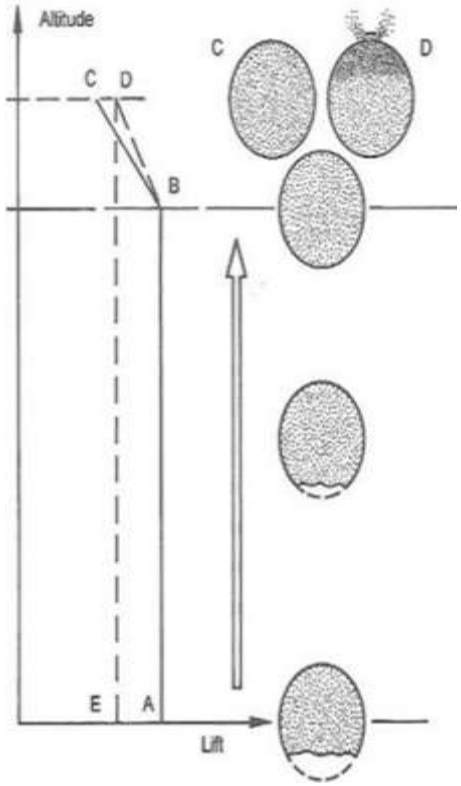

Figure 2.4: Altitude variation with lift [24]

However, if the pressure and density are reduced by the valving off, the lift would be subsequently less, the balloon is taking up to *'C'* instead of *'D'*. As a result, the original gas pressure would fall, and the lift would be increased gradually at *'B'*. So, lift return as its original value back to *'A'*. This scenario was considered as a case study by a previous researcher [24].

As other researchers have highlighted [50, 51], in the case of an airship, the atmospheric pressure height also depends on the volume of gas that is in the hull at initially. It is a function of an inflation fraction (I) ratio of a maximum volume (V_0) of hull gas and the effective volume (V_{vol}) of the gas itself. However, for I_0 a particular value might be allocated at sea level in ISA condition. Therefore, lifting gas density is equally inflated by pressure and temperature, as in the equation $\frac{I_0}{I} = \frac{\rho_a}{\rho_{a0}}$, and a mathematical value can be obtained for specific density from the hypothetical *ISA* data table **(Appendix B.1).**

Thus, atmospheric perception is essential for designing airships, especially for calculating the aerostatic lift. The principal influences emerge through air pressure and temperature changes in altitude. Also, there are some altitudes at which airship ballonets become entirely empty; this is called the pressure height altitude. It plays a crucial role in *HBA* throughout the flight mission, including at take-off, cruise, and landing, by maintaining an aerodynamic shape for the pressure envelope.

However, due to the nature of buoyancy, airships tend to be enormous. The consequences of skin friction drag, while in motion, the hydrodynamic effect can be used as merit. For example, the motion can produce a lift by shaping the aerodynamic body and providing sufficient forward velocity achieved in the air as an Aircraft.

The dynamic principle of demerit pertains to the static lift of the vehicle required for forwarding motion at finite speed to develop aerodynamic lift as Meng et al.[26]. As a result, the airship can either fly very slowly or remain airborne while forward momentum is zero. These capabilities need internal power for static lift, for example, a jet or propeller engine or ductile power. Having defined these primary sources of lifting force, one might observe that it is possible to use two kinds or even all of them together. By doing so, with the lifting surface and propulsion providing aerodynamic lift, and the hull contributing gas static lift, the hybrid aircraft is conceived.

2.2 Operational cost of the airship

In 2013[51], the price of JP-8 fuel was $3.73 per gallon, and the annual fuel cost of the U.S. Air Force was around $10 billion. The price of JP-8 had increased from $2.37 per gallon four years earlier, in 2009. According to the U.S. Air Force, the costs of aircraft transportation accounted for around 40% of the Air Force's total energy costs. These remarkable statistics on fuel costs were a key impetus for renewed interest in airship design. Indeed, the thinking behind advanced hybrid airship design draws on the traditional, established principle that lifting gas can generate a significant lift, entailing fuel cost savings and enabling economical, long-distance payload transport. Feasibly, the idea of low-cost embarkation and the need for transportation systems are logistical and general that appeared to be an accurate value for today's military and commercial users. Nevertheless, the key principle remains that airships are comparatively low-cost vehicles without potential evidence.

The cost of the hybrid airship varies with payload capacity. Naturally, a larger airship is able to carry a heavier load, as airship lifting capability is related to its volume and engine power. However, the hybrid airship also varies its lifting surface, i.e. the wing and the atmospheric effect. So, in design point optimisation, power loading and wing loading can also impact on aircraft operational costs.

In fact, there are various encouraging historical data to support the case for aerostatic vehicles. In 2009 [52, 53], a U.S. Department of Transportation report presented statistics

illustrating that the operational cost of a 500-ton hybrid airship was three to four times less than that of a Boeing 747-400 traditional aircraft.

The cost of the operational concept of the study should inform a realistic assessment. Although this might be based on existing evidence, it would require substantial extrapolation. Therefore, care should be taken in operational costs for making assessments and decisions concerning real-world air transport. Figure 2.5 presents a bar chart comparing different modes of transportation based on operation cost [54]. Figure 2.5 clearly conveys the disparities in transportation costs between the airship and traditional vehicles: airship costs are significantly less than conventional aircraft and road transport. Figure 2.6 [2] sets out the transportation cost per mile versus volume, showing that shipping cost was reduced with increases in airship volume. Metlen et al. [2] established that the volume of the airship was 200,000 m^3 and the cost per ton per mile was about $1.03, with a velocity of 136 knots. Consequently, airship transportation would be economically worthwhile in a competitive market.

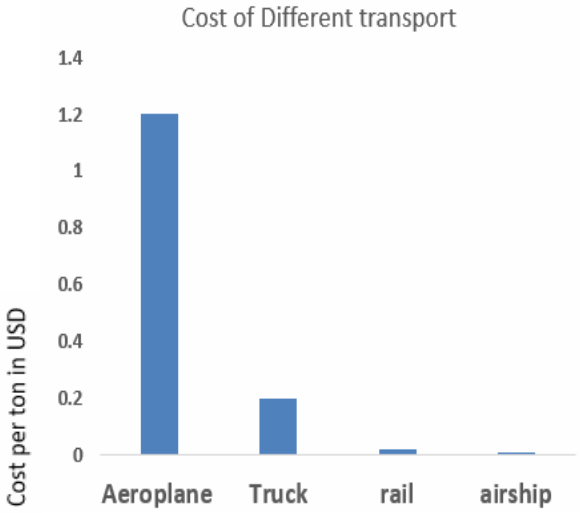

Figure 2.5: Transportation cost per ton-mile

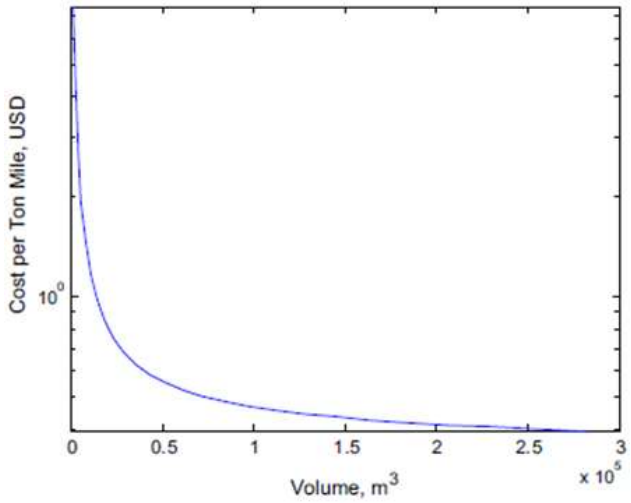

Figure 2.6: Cost per ton-mile vs volume [2]

2.3 Reynolds Number and Aerofoil characteristic behaviour

For the understanding of aerodynamic behaviour, it is vital to grasp the basic concepts of fluid dynamics, and fluid parameters include viscosity (μ), density (ρ), turbulence and laminar flow, and Reynolds number (Re). This section will review the high Re over $> 10^6$, low-speed conventional aerofoil, and scale model $Re < 10^5$ as simply an attempt to downsize to low Re, because of slow-speed flight. This section also investigates the depth of flow physic where aerodynamic efficiencies have been conducted with respect to various Re, before studying the effect of the aerofoil in terms of aircraft performance.

First of all, fluid dynamics play a significant role in the aerodynamic performance of the air vehicle, for the consideration of force, momentum, and various fluid properties: pressure, density, viscosity, and temperature [55, 56]. In chapter 4 will discuss more fluid physics: conservation laws, conservation of momentum, and conservation of energy. Consequently, caution should be exercised in the approximation of drag (D), which is one of the most unwanted parameters for an aircraft designer, but it cannot be avoided. Drag can only be reduced via efficient design. Generally, drag is a function of speed, air density, wing area, fuselage wetted area, and aircraft gematrical configuration [14, 33].

The Reynolds number is expressed as the ratio of inertial forces and viscous forces. It describes the viscous behaviour of all Newtonian fluids [33, 54, 55]. The Reynolds number is defined in equation 2.1:

$$Re = \frac{\rho UL}{\mu} \qquad 2.1$$

Where U is the freestream velocity, L is the characteristic length of the object, μ is the viscosity, and ρ is the density. It is a dimensionless aerodynamic parameter. The nature of the Reynolds number must be understood; a brief account is set out below.

In 1930, Schmitz [57] first investigated the effect of Re on an aerofoil performance. He carried out experimentation on three aerofoils, including two thin aerofoils. One of these was a flat plate; another one was a camber plate and a conventional N60 aerofoil with thickness *t/c* as 12.4% and camber 4.0%. Schmitz [57] found that the thin plate aerofoil works consistently in $Re < 10^5$. Half a century later, in 1980, Mueller [58], Seling [59], Hoerner [60, 61] found that the low Re aerodynamic was transformed, and re-igniting interest in aircraft design especially in slow-speed aircraft (airship, hybrid airship, hybrid buoyant aircraft, and *UAV*), which was the same interest with previous research experiments conducted by Schmitz: in particular, thin flat plates and camber plates are more efficient than conventional aerofoil at $Re < 10^5$. Also, he found, the lift coefficient and drag coefficient showed a small difference for camber plate aerofoil, but in the flat plate were virtually unchanged.

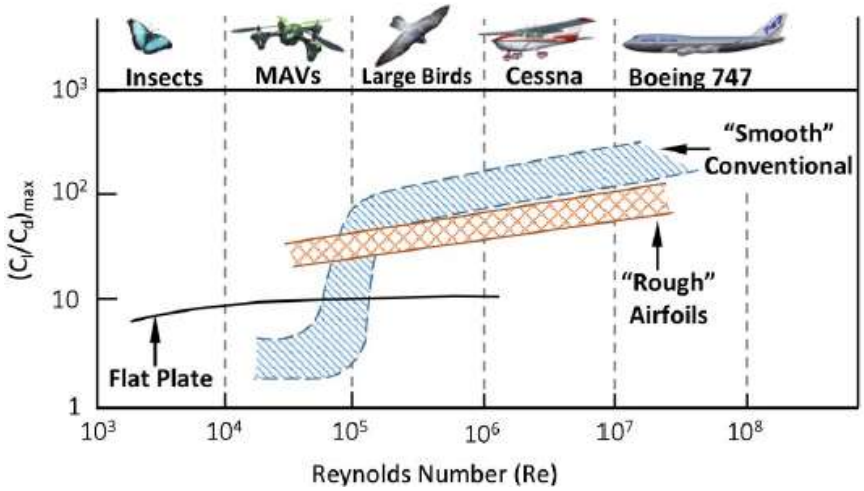

Figure 2.7: Reynolds Number *(Re)* effect in the lift to drag ratio on aerofoil [58]

A previous researcher [20] has highlighted fluid flows as the differences between low $Re < 10^5$ and high $Re > 10^6$, where he argued that aerodynamic efficiency and power requirements depend on aerofoil selection. Hence, he demonstrated a systematic understanding of aerofoil performance and aerofoil selection at $Re < 10^5$ as well as $Re > 10^6$; their sensitivities of geometrical variances would be critical for an aircraft designer. In fact, the Reynold number (Re) is also associated with the boundary layer and thickness.

In Figure 2.7 above, Hoerner [60, 61] has also shown that the maximum lift coefficient (C_{l_max}) rose 4% for camber plate whereas it rose over 180% for N60 conventional aerofoil.

Furthermore, Seling et al. [59], Mueller [58, 62, 63], and Batill [64] carried out several experiments with a series of aerofoils, where it was found that C_{Lmax} continuously increased with higher Re, and the drag coefficient (C_{d0}) decreased once $Re > 10^5$. Moreover, Seling et al. [59], also commented in pragmatic research that for 60 different types of sailplanes' aerofoils the drag polar was graphically similar and almost insensitive to Re variation above 10^5. Mueller was illustrated in Figure 2.7, an aircraft efficiency increased with increased of *Re*.

It is also necessary to discuss the difference between the laminar and turbulent fluid flow. As the aircraft moves forward, the molecules of the air and aircraft act upon each other. The laminar fluid flow moves in a layer, and the fluid particles firmly move one another in a regular fashion. It can be a uniform and rectilinear form where airflow moving consistently from the left side to the right side. The laminar flow does not always need to be formed in a straight line. Generally, an ideal flow over the aerofoil is followed by the solid body curved surface smoothly. In fact, a boundary layer is usually laminar near the leading edge [31, 65, 66]. At the same time, the turbulent flow is moving in a more disorderly, random manner. It can also be a number of disorganised streamlines and exchanging fluid from one segment to another, and fluid momentum exchange: fluid particle speed-up from slow-moving and give-up fast-moving particles, and some of them slow down themselves.

Figure 2.8 depicts streamlines over a typical aerofoil at several Re numbers for moderate *AOA* [55]. Figure 2.8 (c) shows the laminar flow over the top surface of an aerofoil exposed to a large adverse pressure gradient near the leading edge. Figure 2.8 (b) shows the shear layer separation at 50,000 < *Re* > 100,000. However, the flow till gains adequate momentum to reattach to the aerofoil surface as a turbulent boundary layer. However, for the range of Re, the reattachment point is relatively far back on the aerofoil. Figure 2.8 (a) illustrates that the laminar separation point is delayed until it is close to the aerofoil trailing edge, even at low *AOA*, due to the improvement of stability and boundary layer separation that is more resistant to flow transition [67].

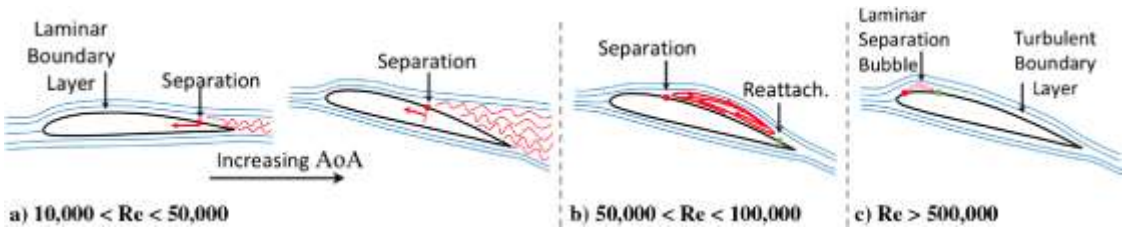

Figure 2.8: Tradition aerofoil separation in different *Re* [67]

Hence, as shown that if Reynold number ($Re < 10^5$) decreases bellow 10^5, the drag coefficient increased. Particularly flow failure to reattach due to premature flow separation. As a result, the lift coefficient is decreased. So, the lift coefficient (C_l) decreases for high *Re* beyond at the critical range and in low *Re* below the critical. On the other hand, the drag coefficient(C_d) is increased at the same time for both cases. Therefore, aerofoil selection is playing a pivotal role in aerodynamic performance for aircraft design.

2.3.1 Reynold number impact in the shape

The flow behaviour over the spheroid has become the canonical nature of the problem, even though the geometrical shape is quite simple. However, there is still a challenge in modelling the attached flow, flow separation, flow recirculation, and vortex shedding. In fact, the flow forms consistently change with the increase of *Re* upstream flow. According to Goncalves et al.[68], the flow between $Re < 10^5$ to $Re > 6\times10^6$ is trans-critical flow, and the *Re* over 200, the flow becomes 3-D, and the far-wake region is turbulent. With the Reynold number beyond 400, the turbulence flow becomes in the shear layer. As the increase of Reynold number, the turbulence flow keeps shifting upstream. The turbulence sets within a certain Reynold number. The attached boundary layer separation leads to delays that were resulting costs a sudden drop of drag coefficient as the "Drag Crisis". Moreover, the pre-critical flow about the range of $Re = 2\times10^5$ in the sub-regimes and supercritical flow at $Re = 1\times10^6$. A recovery of drag as the separation point is in beyond the $Re > 6\times10^6$. On the other hand, Wang [2, 69] reported that at high *Re* 10^7, the drag coefficient was increased by 55% relative to *Re* 10^8, and the decreases in the drag coefficient have sustained with increases of Re number beyond 10^8. Indeed, an accepted point as a flow physics, continuously deviations modelling of the flow is fairly challenging. Therefore, in all ranges of Reynold number is still elusive for a single satisfactory model despite research in many decades.

The fluid flow over the spheroid often leads to syndrome's behaviour, that is significantly influenced by an aircraft's aerodynamic performance or hybrid aircraft. Most of these issues are fluid-structure coupled problems, where computational fluid dynamic (CFD) efforts essential to be used sensibly; it is vital to attain an impartially accurate estimation of the aerodynamic lift force, drag force, and moment for aerodynamic performance. Thus, the study impacts of turbulent intensity Reynold number (Re), flow topology and transition characteristic of flow separation to offer a deft understanding of aerodynamic flow behaviour for different Reynold number.

Kuchemann and Dietrich [70] commented that flow force arises because of an object's shape and nature. An example is found in the comparison of flow around plates over a sharp front. The theory is that where the flat plate boundary layer expresses at a low Reynolds number (Re), the boundary layer is larger and extends far in front of and around the plate. It can create a large effect on the flow [71]. However, boundary layer growth over a flat plate is higher; Reynolds number is different and amenable to flow over an immersed body [32]. Besides, the form drag would be increased if the boundary layer is separated from the surface conspicuously ahead of the lifting surface. Young argued that there was no evidence for Owenard Hutton's (1929) findings regarding the wind tunnel test of separation on a body with a thickness ratio of 0.33 for an airship hull design. It is just outside the range for thickness ratio. Hoerner (1957) examined the experimental data, yield to an empirical combination formula of $\frac{C_{DV}}{C_f} = \left(\frac{l}{d}\right)^{\frac{1}{3}} + \left(\frac{l}{d}\right)^{1.2} + 24\left(\frac{l}{d}\right)^{2.7}$and comprise them with the theory that is perhaps used to assess the drag bodies. Basically, this author dealt with the drag of streamlined bodies.

However, in the case of airships, the flow over the hull is turbulent. In Hoerner's experiment, it was shown that drag is minimal if the hull thickness ratio $\left(\frac{l}{d}\right)$ is 0.217, but it was larger than Young's value (0.182). Therefore, Hoerner proposed that C_f, the parasitic drag differs with level of surface roughness and $Re > 5 \times 10^6$, where the equation is $C_f = \frac{0.043}{Re^{\frac{1}{6}}}$, combining with volumetric drag as follows:

$$(C_{DV}) = \frac{\left[0.172\left(\frac{l}{d}\right)^{\frac{1}{3}} + 0.252\left(\frac{l}{d}\right)^{1.2} + 1.032\left(\frac{l}{d}\right)^{2.7}\right]}{Re^{\frac{1}{6}}} \quad 2.2$$

Hence, a case of the aerodynamic function of the hull required high power at a low Reynold number for a conventional airship that causes excessive drag. Since the geometrical variation: camber, thickness, and aerodynamic sensitivities are significantly important to design an efficient air transport. Notably, the vehicle moves through the air while the fluid is considered stationary. The transition process from laminar to turbulent is very complex. The transition method cannot be examined analyses directly but can usually be predicted by experimental results. Moreover, the airship needs high Re and low-speed aerodynamic

characteristics of flow pattern, which is very limited in existing research. Thus, Re number plays a vital role in the determination of the aerodynamic performance of an airship.

2. 3.2 Effects of flow separation and wakes over prolate

The boundary layer separation is known as flow separation. These phenomena have occurred once a fluid flows around a curvature. Since a boundary layer flow is detached, the isolated gap transmutes into a retrain region; this gap is filled by the inverse flow as a primary vortex or secondary vortex. The resulting flow separation is also called viscous fluid[72]. The three-dimensional $(3D)$ separation of turbulent fluid flow produces thicker boundary layers

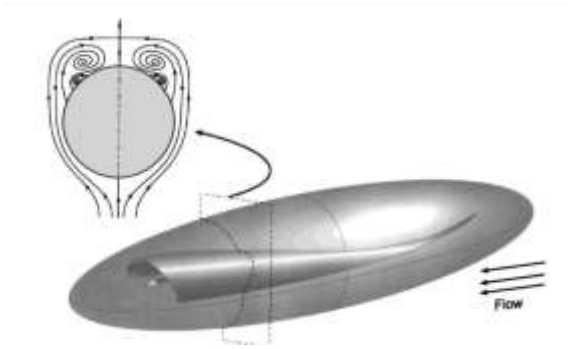

Figure 2.9: 3D flow schematic over prolate spheroid right [73]

over a solid body[73]. Figure 2.9 shown a fundamental phenomenon of the *3D* flow schematic as a visual representation of the *3D* turbulent flow. Chesnakas[74] studied flow separation in around 6:1 prolate spheroid at a different angle of attack, which is associated with the vanishing of wall shear stress. Indeed, the skin friction factor is independent of surface roughness in the laminar flow; however, in turbulent flow, it is a strong function of surface roughness due to the boundary layer [33].

The flow separation requirement is the existence of a reverse pressure gradient. The flow separation investigations occur from three aspects as a number of early scholars: visualization of flow[75], hypothetical analysis of flow-based of topology[76], and also numerical flow simulations [77-80]. According to Wang et al.[81, 82], Cary et al.[83], and Tobak et al.[76], the theorised is that, in the different AOA the flow separation scheme, the revolution of surface streamlines of an inclined body can be seen in two different natures of separation in the lee side section: free vortex forms and bubble forms. Authors also assumed, in the tail, the separation at a small *AOA* and it is moving forward as the *AOA* increases. Chesnakas and Simpson's experiments [84] and Fureby et al. [85] disclosed that in $Re < 2.08\times10^{6}$, the flow over the surface model was wrapped, and with the increase of *Re* number, turbulent separation arisen in

the tail region and slowly developed. Chesnakas's experimentations [73] revealed that in the lee side zone about the separated shear layer, asymmetrical spiral vortices were formed in a streamwise direction at high angles of attack on each side. The low-pressure vortexes are accompanied on each side and attached; it is produced an extra lift on the prolate spheroid, which has been seen in the last few decades, the experimental research along with several numerical results of the flow field.

2.4 Hull shape and aerodynamic behaviour

This section introduces the fundamental concepts underpinning the airship hull, hull design, and the aerodynamic behaviour of hull shape. This permits an elementary recap of the hypothesis; it will also help readers to gain a clear understanding of aerodynamic aspects such as hull characteristics, optimisation of airship geometry for low drag. In the state-of-arts research on *EWBA*, aerodynamic efficiency starts with the appropriate computational method for prediction.

The concept of lifting the fuselage is not new. It is derived from a few aquatic birds that generate aerodynamic lift using their bodies. It was Vogel [86] who first concluded that ducks have plenty of air in their plumage to support the lift. They can become inelegantly buoyant, perhaps requiring a negative lift. In the field of aerospace, Huyssen et al. [87] noted that many aircraft had been designed earlier by Vincent Burnelli based on the lifting-fuselage concept. Indeed, the first winged airship was designed by Santos [88], where concepts of the hybrid airship were employed. Thus, the partial aerodynamic lift was obtained through the contoured hull.

Indeed, design considerations that make a vehicle economically and ecologically viable will also strongly influence its aerodynamic efficiency. The lifting surface of wings and the hull characteristics have the potential to increase the efficiency of *HBA* by mediating certain factors such as drag and weight reduction.

Currently, few research studies have explored successful airship designs with hull bodies to reduce drag by defining shapes that result in large portions of the ship having laminar flow [89-92]. Moreover, such a vehicle has a large streamlined hull filled with a lighter gas such as helium that alliance in the relative wind direction due to skin friction [93]. Generally, the airship hull design techniques employ the same sophisticated aerofoil sections used in high-performance aircraft wing design, which is the starting point of a configuration for the airship [2, 94, 95]. According to Dodbels et al. [90], the design of an airship's hull is dominated by

consideration of aerodynamic behaviour because 90% of the lift is produced by the hull with lifting gas. The airship usually flies at a lower *AOA* at a slower speed. The fact is that an airship does not depend on the lift generated by the wings. However, an *HBA* has been created with above 51% of the aerodynamic lift contributed by its wings [4, 36]. Anwar et al.[4] observed that the hull produces a significant contribution to drag for an *HBA*. On the other hand, the maximum amount of drag is skin friction drag in an airship and *HBA*. Therefore, the Reynolds number is significant for the optimisation of an aerodynamic parameter such as zero-lift drag [4, 6, 96-99].

Carichner and Nicolai [1] stated that pressure drag and skin friction drag are varied according to the ratio of the streamlined hull length to its maximum diameter, referred to as the fineness ratio (FR) of airship hull. They also commented that this drag is proportional to *FR*. Lutz and Wagner [91], Carrion et al. [91, 100], and Tezzele et al. [101] also stated that drag reduction could potentially be accomplished by the selection of the optimal hull fineness ratio, Boundary Layer Control (BLC), and a clean profile. Thus, to reduce the hull drag, the major axis of airship hull length (ℓ) might be four to eight times bigger than its maximum diameter, applying prevailing airship design principles [1, 102]. However, the fineness ratio can be defined by $FR = \frac{\ell}{d}$ [1, 91] where 'ℓ' is the characteristic hull length and' d is the maximum diameter. A longer hull produces less pressure drag, however, the contributing factors to low-drag hull shape are skin friction, Reynolds number, pressure, pressure gradient, and volume. Hence, an optimal *FR* can be obtained where the sum of pressure drags, and skin friction drags is low. So, for an airship, the total lift-to-drag ratio $\left(\frac{L}{D}\right)$ depends on all these combinations of contributing factors [1, 94, 96, 97, 103]. In *HBA*, the lift (L) is not only reliant on hull volume; it also depends on the wing, like conventional aircraft [23, 24, 36, 95]. However, FR is the most important consideration during airship design, especially for a hull; the reason is that hull mass can be increased with the increase of surface area. As a result, overall airship empty weight would be developed. Dorrington [102] examined the flatness of the curve when $2 < FR < 8$. He found that the drag increases when FR falls below 2, due to a growth in the aft-body separation region. So, to avoid the form drag rise by a significant margin, it might be necessary to consider the finite ratio (FR) of an airship greater than 2 $(FR > 2)$. Hence, it is often worthwhile to choose a value of FR by considering the minimum volumetric drag. Table 2.1 shows wind tunnel test data, from an earlier researcher [104-107], on a $1{:}\,180$ scale model for a hull drag

Table 2.1: Drag coefficient comparison between different hull sizes and FR for airship

Model	*FR*	ℓ	*V*	*Re*	$C_{D\,VH}^{a}$	$C_{DV\,Model}$	$\frac{C_{DVmodel}}{C_{D_{VH}}^{a}}$
R26 [108]	10.5	1.22	0.0123	2.0×10^6	0.036	0.037	1.0
R36 [109]	9.37	1.4	0.0193	1.7×10^6	0.036	0.028	0.78
Puritan [110]	3.5	0.216	0.0008	0.3×10^6	0.046	0.022	0.65
Zeppelin NT [111]	2.5	0.261	0.0014	0.6×10^6	0.021	0.016	1.31
Shenandoah [112]	8.6	1.72	0.0349	2.5×10^6	0.033	0.031	0.95
R33 [113]	8.33	1.22	0.0139	2.1×10^6	0.034	0.024	0.7
Ellipsoid trip [105]	8.0	0.15	--	1.0×10^6	0.039	0.033	0.85
R101 [114]	5.57	1.24	0.0289	49×10^6	0.019	0.018	0.95
SSZ [115]	4.75	0.87	0.015	0.7×10^6	0.039	0.29	0.76
ZMC-2 Form [116]	3.0	1.76	0.301	2.1×10^6	0.034	0.026	0.74
Ellipsoid [106]	1.8	0.36	0.0237	0.6×10^6	0.064	0.065	1.0
Smooth Sphere [107]	1.0	0.175	0.0028	6.0×10^6	0.11	0.23	2.1

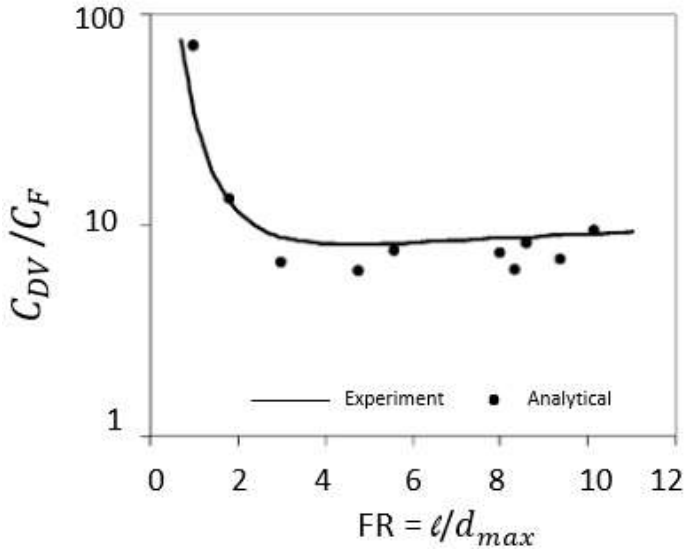

Figure 2.10: Comparisons between volumetric drag coefficient and fineness ratio (FR)[102]

coefficient, where it is shown that the drag coefficient varies with FR. In the above **Figure 2.10,** it is clear that the drag coefficient increases rapidly in FR for values below 2.0 and above 8.0. The minimum drag that occurred at *FR* is equal to 4.65, where was employed in equation 2.2 for analytical calculation.

On the other hand, Lutz and Wagner [91] showed during wind tunnel testing for an airship that the lowest total drag is found while FR was 4.62. However, they were in agreement with an earlier researcher concerning FR changes in various design factors such as hull shape and component configuration, although a lower FR would reduce the skin friction drag. The two main consequences of Dorrington's [102] wind tunnel test are firstly a small drag rise in adoption of FR lower than 4.65 (for example, he found that the drag developed by 10% when $FR = 2.8$ with a lenticular shaped hull), whereas a small drag rise is experienced even in sophisticated FR values up to 8.0, as shown in **Figure 2.10**.

A few comprehensive review articles [36, 94, 117-119] have discussed body drag coefficient variation with the 'Re' number. Goldschmied [111] also conducted wind tunnel testing on a Zeppelin NT airship at volume 8297 m^3 with FR 2.5, hull length 47.0 meters, velocity 36 m/s, Re as 10^5 at standard sea level (SSL). He found the hull drag to be 0.0162, signifying one of the most successful and revolutionary developments in the body of an airship with a Griffith aerofoil to achieve laminar using a boundary layer control (BLC) device, by making a channel in the inlet port [91]. However, if the $Re > 10^7$, laminar flow is negligible; that is how an airship hull can prevent flow separation and reduce pressure drag [91, 98, 120, 121]. This will be discussed in more detail in the following section. Goldschmied [111] would not achieve laminar flow at these higher Reynold numbers (Re).

Recently Haque et al. [28, 36] built a mathematical aerodynamic model of an airship hull. They used an Eppler 1200 aerofoil for the hull design where the laminar flow was up to 50% of the chord. The typical hull length (ℓ) was 31.5 m, width (d) was 5.93m, and the hull aspect ratio (AR) was 0.0134. Haque et al. [28, 122] obtained the lift using two different methods. First, a lifting hull was considered as the fuselage and with a false wing by *DATCOM*. Then, the airship lifting hull analyses were carried out using *ANSYS Workbench*, which was able to predict aerodynamic parameters, although the model did not include a real wing. This aerofoil shaped hull model was also validated against wind tunnel testing results [123]. On the other hand, a prolate spheroid 6:1 was investigated by Holt et al. [124] during aerodynamic characteristics of lifting body research. Wang et al. [125] also used a hull in the experimental study of ZHYUAN-1 airship with *FR* value 3.29, which is between $2<FR<8$ as an intermediate-range, where he said body shape admittedly more essential to maintain the drag coefficient at lower.

It should be noted that with traditional aircraft design, an effect of compressibility and Mach number is of concern, but this is not the case with an airship. However, *HBA* behaves more like a heavier-than-air (HTA) Vehicle. Therefore, a prolate spheroid 6:1 has been used as a hull for this design, where the volumetric drag coefficient is 0.035 as calculated by Hoerner's equation (2.2). Since it has been confirmed as a good primary approximation of efficient aerodynamic hull with Table 2.1 and **Figure 2.10,** in the case of experiment results and analytical results for a range of finite ratio (FR) between $2< FR <8$. So, these wise methods could be considered for *SWBA's* hull selection due to there are not any other design constraints.

2.5 Aerofoil and fluid flow theory

The fluid flow past aerofoils and wings has devoted the consideration of fluid mechanics over a century. Most of the previous scholars have been mathematically motivated and satisfied with these elegant techniques. The present study investigates the aerofoil profile with boundary layer in the steady flow; leading-edge separation for wing theory and application of Prandtl wing theory; the boundary layer growth approximation on the aerofoil; its effects of the circulation and pressure distribution on the steady-state flow.

As an example, Karman Trefftz [126, 127] generalised the well-known Joukowski's revolution to produce an aerofoils family having finite trailing -edge angles. The Munk's theory [128] and the Prandtl lifting line theory [129] of the thin aerofoil theories also are an example of this group; these schemes also further extended by Von Karman and his research team[67, 127, 130, 131], the lifting surface as Von Karman's treatment. In fact, the aerofoils theory, despite its considerable physical base mathematical development, namely viscous processes. The Kutta-Joukowski trailing-edge condition is the sum-up of these complicated effects approximately. According to Luckring [132], Von Karma has been described as the lift, induced drag, and viscous flow as historical development in his fluid mechanics book purely. Von Karma [127] also had a brief explanation of viscous phenomena and the effect of Reynold's number on the maximum lift coefficient of an aerofoil.

2.5.1 The aerofoil profile with boundary layer for a steady flow

Canamar et al. [133] have been suggested a fabricated camber profile to make circulation; even though they simply discarded the Kutta Joukowski condition, they found circulation equal to their estimation value, where finite velocity was ignored. Levis[134] said

Von korma was the first to successfully employ comprehensive boundary-layer and wake designs to envisage aerofoils' circulation. A very recent study by Saeed et al.[135] one of the successive approximations for wakes and boundary layer separation during design flying a wing has achieved some simplification. He assumed the boundary layer thickness is known; the boundary layer of potential flow is corrected by the displacement of the boundary layer thickness, the distributions of viscous wake along the aerofoil contour, and wake approximate position. However, it is almost impossible to calculate the boundary layer until the external flow is known and circulation. Hence, the boundary layer is a crucial feature for the determination of external flow with an adequate criterion and a refinement of the Kutta-Joukowski condition.

Figure 2.11 shows that stations 1 and 2 are the trailing edges of the upper- and lower-surface boundary layers for calculating the pressure increments at the two-point can be mathematically derived as $p_1 - \Delta p_1 = p_2 - \Delta p_2$, where the p_1 and p_2 are static pressure at station 1 and station 2, respectively with respect to velocity. On the other hand q_1 and q_2 are the viscous layer at the same station for a mathematical equation $p_1 - \frac{1}{2}pq_1^2 = p_2 - \frac{1}{2}pq_2^2$ with the following condition:

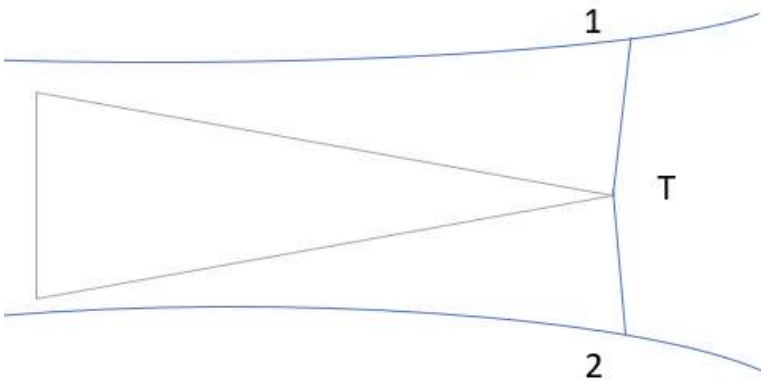

Figure 2.11: Boundary layer configuration at tailing -edge

$\left(\frac{q_1}{q_2}\right)^2 = \frac{1-\omega_1}{1-\omega_2} \approx 1 + \Delta\omega$, where ω_1 equal $\frac{\Delta p_1}{\frac{1}{2}pq_1^2}$, ω_2 equal $\frac{\Delta p_2}{\frac{1}{2}pq_2^2}$ and ω_1 - ω_2 = $\Delta\omega$ is the development of boundary layer circulation as Montgomery et al. [136]. Hence, this expression of a relationship between boundary-layer circulation and static pressure approximation methods is helpful to estimate the potential boundary layer flow; the pressure differences in the upper and lower surface.

2.5.2 Prandtl lifting line theory

The original Prandtl's lifting line theory by replacing horseshoe vortices across the three-dimensional wing attached along with the quarter chords shown in Figure 2.12:

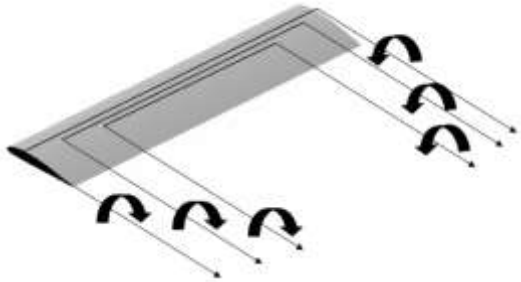

Figure 2.12: Prandtl Lifting line theory on horseshoe vortex

Each vortex is very with the magnitude, maximum value at the centre of the wing, and on the tips is virtually zero. Translated that into the lift as the following equation: $L = \rho V_{\alpha} \Gamma$, Where L is lift vector, V_{∞} is freestream velocity vector, Γ is vortex strength, an ρ is the fluid density. The assumption base lifting line theory, lift generated in each spanwise section of the wing can be associated with the lift produced by a similar *2D* aerofoil for below the stall angle, but the above stall scenario is different. Anderson [137] argues that an engineering solution may be attained if *2D* aerofoil data is known with the lifting line theory. According to Phillips[138], the numerical lifting line scheme can be converged for a wing beyond stall.

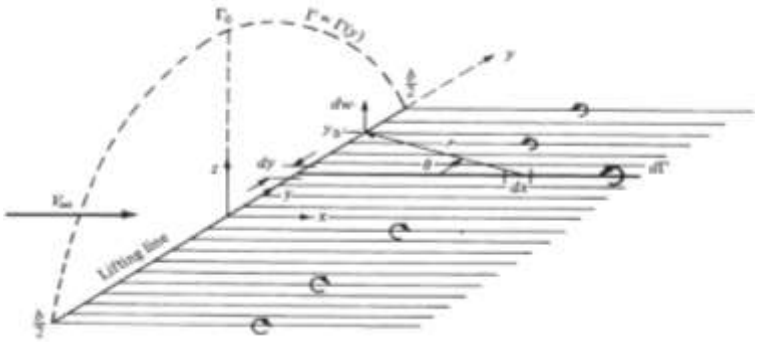

Figure 2.13: Elliptical lift distribution of a finite wing and lift zero at the wingtips[137]

In above Figure 2.13 shows more noticeably the distribution of lift on a real finite wing and trailing vortices along the wing. With the Prandtl lifting line theory, the lift and induced drag can be calculated in an inviscid and incompressible fluid when a circulation distribution is given along the span on the y-axis. However, for the case of a fixed-wing with known aerofoil data, chord, and twist distributions of each segment, the lift and drag can be computed as knowledge of the lift characteristics of an aerofoil.

On the other hand, the strong viscous effect is dominated by the stalling region of a wing, as reported by Von Karman, that follows the integral-differential equation of Prandtl lifting line theory:

$$\Gamma_{(y)} = \frac{1}{2}\,\mathrm{Uc}\,(y)\mathrm{m}(y)\left[\alpha(y) - \frac{1}{4\pi}\int_{-b/2}^{b/2}\frac{\Gamma'(n)dn}{y-n}\right] \quad 2.3$$

Where the lift curve-slope $\mathrm{m}(y)$ is negative once the solution is nonunique, $\Gamma_{(y)}$ is spanwise lift distribution, U is velocity, wing chord $\mathrm{c}(y)$, absolute angle of attack $\alpha(y)$, y = $\pm b/2$ for wingtips, when $\alpha(y)$= 0, $m< 0$, the 'b' represented the wingspan. The lift is elliptical since the twist is zero as Anderson [137]. Indeed, the wing's characteristic lifting line is confined on the *X-Y* plane if the wing lift is zero. Thus, known as a planar wing. But the cambered wing's lifting line is no longer contained to the *X-Y* plane, which is called a non-planer wing. The wing with dihedral, endplate, box wing, bi-plane, and winglets leads to the classification of the no-planer wing. This kind of wing has been studied for several schoolers such as Kroo [65], Somerville, et al.[139], Khan et al.[140], Garcia et al[141], and Gagnon et al [71] so on. They revealed that if a planar wingspan's total length is equivalent to a non-planer wing, the planer lifting line is elliptical along the wing but lower. And also, the planer wing found straight lifting lines along the wing, but the non-planer wing has a different shape of the lifting line: the box wing is formed as a butterfly shape lift distribution, due to two wingtips joint vertically each other.

2.5.3 Boundary layer flow separation

Flow separation due to viscosity is a classical concept of boundary layer separation. The progressive pressure gradient is the essential condition of flow separation. Han et al. [75] as Maskell's concept of the flow separation is unavoidable if the required condition is met, over the finite dimension separation from the solid body surface at the trailing edge and on upstream. So, it is not a steady process over the smooth surface but also severe discontinuity flow to the surface as a target.

The pressure over the upper surface created a considerable size of the separation by forming vortices and occurred an aerofoil stall as Chang[142]. In fact, the flows partially separated near the stall conditions from the aerofoil surface since aerofoil gained the maximum lift coefficient. This stall point is strictly associated with bubble separation due to flow circulation over the aerofoil surface.

Therefore, when flow travels parallelly on the upper surface and lower surface of the aerofoil, it is joined up on the trailing edge. The flow velocity over the top surface is higher

than the bottom surface of the aerofoil. Still, the upper surface pressure is lower than the bottom surface as a consequence of the Kutta condition [98, 143]. Hence, it plays a substantial role in aerodynamic performance.

Indeed, the pressure coefficient (C_p) and drag coefficient (C_d) are considerably influenced during the fluid transition from laminar to turbulent [144, 145]. During aerofoil selection, a variation of sectional wing shape, measured span-wise, should be considered. Elfes et al. [14, 146] argued as an example, in the case of low subsonic aircraft design, the *NACA* family aerofoils are the most useful. This is a unique type of aerofoil series which is contingent on the aerofoil shape of geometries.

2.5.4 Aerofoil selection criteria

The subsonic aerofoils are broadly consistent in terms of shape, although some are slightly curved. The aerodynamic characteristic, speed, and pressure along an aerofoil lifting surface are all associated with the Bernoulli equation, which is coupled through flow curvature and the aerofoil surface curvature itself [147, 148].

Typically, the aerofoil section of a wing may be determined by the following two methods [33]:

1. Aerofoil design methods
2. Aerofoil selection methods

Aerofoil design is a fairly complex process, and developers need to be sufficiently expert in the field of aerodynamics. Aerofoil performance also needs to be verified by wind tunnel testing data. This can be prohibitively expensive. In general, larger aircraft companies such as Airbus and Boeing have many experts in aerodynamics and large budgets for testing in the course of commercial research and development. However, as for academic research, some sponsored researchers may be funded to design their own aerofoils. Conversely, for most small companies – and typically in low budget research – it may be pragmatic to select an existing aerofoil design from reliable sources rather than opt for custom design [33].

Aerofoil design is not as challenging as it was 30 years ago, thanks to technological advances in high speed, powerful instruments, for example, computational fluid dynamics software (CFD) [149, 150]. It is not just aircraft designers who design aerofoil; many other

areas of engineering have to need aerofoil design for certain products: the jet engine compressor blade, jet turbine blade, power plant turbine blade, turboprop engine blade, steam engine power turbine blade, and windmill. Mechanical and aircraft industries are heavily reliant on the aerofoil section for devices. Thus, designing an aerofoil is a big project and needs to be cohesive accurately into an aircraft design system.

For the above reasons, in this *EWBA* design project, it was decided to proceed by methodically selecting the aerofoil from existing designs in order to meet the requirement of a high lift-to-drag ratio. *NACA* and Eppler are two currently available and reliable aerofoil resources. Eppler details have been accessible for a long time [151]. According to Abbott [67], the *NACA* aerofoil specification was first published in 1959, and it is still available in aerospace-related libraries.

Generally, Eppler aerofoils have used very low Reynold numbers, while *NACA* used moderate Reynolds numbers for low-speed and mid-speed aerofoils [32, 106, 123]. The primary selection criteria for aerofoil are focused on cruise flight; the lift is equal to total weight; drag is the same as engine thrust. Therefore, the wing must produce a sufficient lift coefficient once the drag coefficient is minimum. Those coefficients derive from the aerofoil section.

Indeed, the aerofoil is the heart of the aircraft; an aircraft designer must be paid additional heed to various aspects of the aerofoil. The aerodynamic efficiency of aircraft in all phases of flight depends on aerofoil behaviour, namely take-off, landing, cruise, stall speed, and handling qualities, particularly near the stall [33, 70, 152-155]. Later, the design chapter 3 will present a brief overview of aerofoil computational selection methods and that illuminated by numerical data.

2.6 Brief overview of the non-planar wing

Planar and non-planar wing designs are historically well-known. Firstly, this research will perform the only configuration of non-planar wings with respect to analysing the aerodynamic performance. Secondly, the study will recognise previous researchers' findings on the non-planar wing base with regard to the aerodynamic efficiency of traditional aircraft, which tends to find the link of the buoyant hybrid aircraft (HBA) and comparison with planer wind.

2.6.1 Wing configuration for reducing induced drag

The principal cause of induced drag is aircraft lift which is created at the tips of the wing by the vortices. This drag resulting from the causes of lift, vortices on the wingtips, pressure differences forming between the upper and lower surface. A downwash velocity of the vortices induce are leading to a reduced effective angle of attack $(\propto_{eff})$. These reduction magnitudes are definite by the induced angle of attack $(\propto_i)$. Figure 2.14: shows a free steam

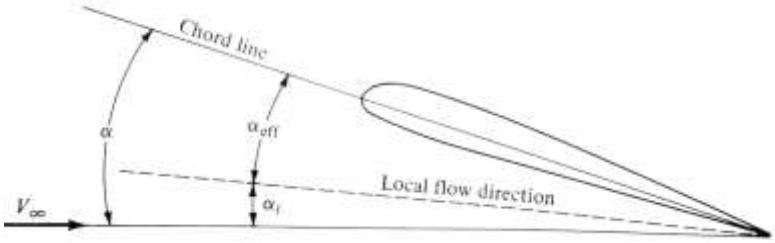

Figure 2.14: Downwash effect on local aerofoil for local flow [62]

lift vector rotated through a $(\propto_i)$. This formed a dimensionless formula as equation 2.7. In the box wing, one portion of the wing can be created a positive lift. However, another portion of the wing can be cancelled by producing downwash force due to wing-tips vortices leading to induced drag[65]. The resulting cause there is no lift.

However, induced drag magnitude varies according to the generated aircraft wing lift, which is also related to the shape and size of the wingspan [57, 150, 156]. The common expression is that the wing efficiency is referred to as the span efficiency in terms of induced drag. Once again, the variation of the drag with lift is indicated by the span efficiency [65, 134, 140, 157-159]. In 1924, Munk [103] tested his lifting hull during aircraft design and found that the plane could attain maximum induced drag once the downwash constant flow motion constant at far Wakefield. Therefore, the planar wing could be achieved with an elliptical lift distribution along the wingspan; the efficiency factor was maximum once the total lift value became maximum.

Kroo [65] claimed that 17% of induced drag could be reduced by increasing 10% of the wingspan. So, this induced drag (C_{Di}) accomplishes a fundamental aerodynamic drag in accordance with Equation 2.6. This equation shows that induced drag could be reduced with an increased span efficiency or wing aspect ratio. However, the span is often constrained because of structural factors. Cavallaro, Gerami, Housner, and Fazelza [160-162] presented a series of studies indicating that wingspan increases mean the aerodynamic centre of the force

pushes to move away from the root, which causes increased wing weight, bending moment, and vibration frequency. It also accelerates the factors in the aeroelasticity effect, i.e. divergence and flutter speed. Consequently, seeking to increase span efficiency by increasing the wingspan is not always a viable strategy.

Thus, the non-planar wing configuration can be eliminated on the basis of the above description and in light of the extensive literature base evidencing that the box wing can significantly reduce the induced drag compared to the planar wing [71, 140, 159, 162]. Very fast, the non-planar wings such as the box wings concept have been rapid development and are derived from Prandtl works [157, 163], which have also been explored by Garcia-Benitez et al. [159] of his prior research. Their design concepts were based on two wings tips joint with offset horizontal wings, and the height-to-span ratio was varied to determine the relative vortex drag.

Wingtip vortices are circular patterns that rotate the air left behind the wing, which configuration generates the extra lift. These vortices are occasionally referred to as tailing or lift induced vortices [162, 164]. Meanwhile, some scholars bring some corroborating evidence as suggested by many researchers [65, 140] that a span efficiency could be improved via mutual interference drag reductions such as increasing the lifting surface gap. Indeed, the span efficiency is similar to the correction factor that represents the changing drag with the lift of the *3D* wing [50, 65, 150, 162]. Kroo [65] has developed different possibilities for non-planar wing configurations with regard to their consistent optimal span efficiency at an advance over span ratio (h/b) of 0.2, as illustrated in Figure 2.15. Some of the other concepts can be used, for example, high lift devices as winglets. In contrast, few of them have a developed aspect ratio by associating multiple wings with the same span and equal wing area for each wing [71, 165].

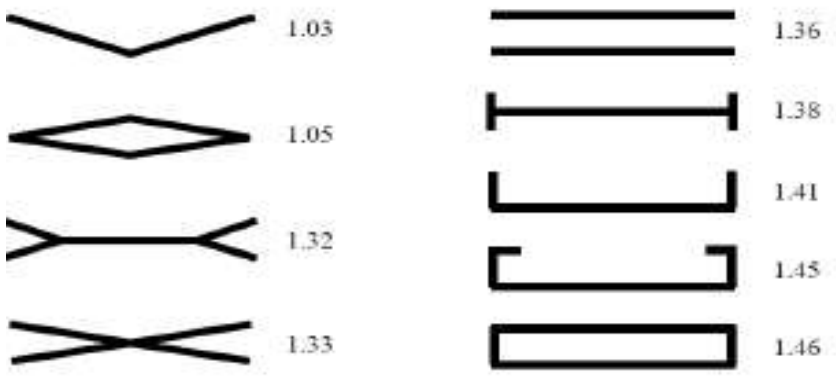

Figure 2.15: Span efficiency for nonplanar wing efficiency configuration [65]

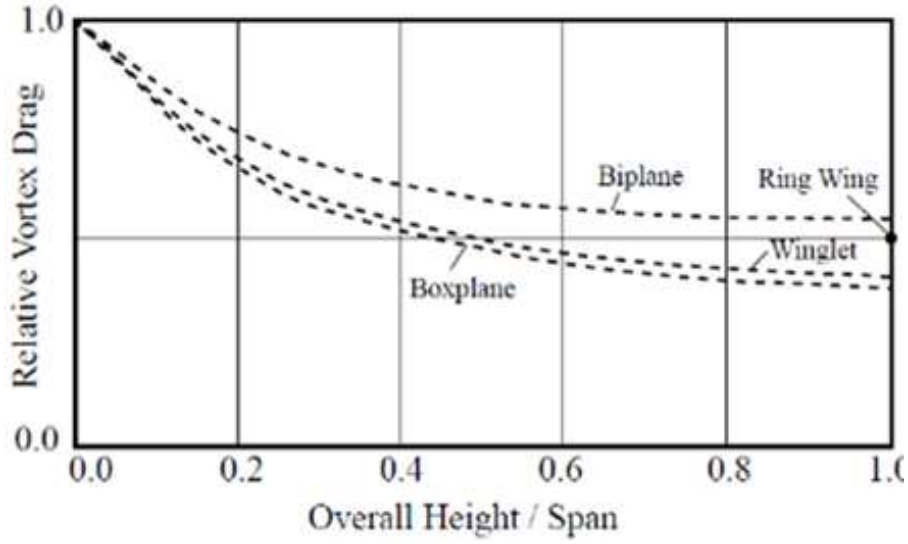

Figure 2.16: Vortex or induced drag vs span ratio for non-planar wing [65]

Zhu [153] has also proposed a configuration of biplanes as a closed box wing with the highest hypothetical span efficiency factor. This was a highly successful study, although it should be noted that these configurations drew concepts from the original version of Prandtl's best wing system. Kroo [65] (see Figure 2.16) has also shown in his experimental studies that interference drag decreased with a reduced wing gap between the top wing and the fuselage surface. Nonetheless, he achieved a higher efficiency factor with a height over span ratio (h/b).

Another brief explanation can be cited from the research conducted by Prandtl [163] in 1924. He explored the effect of induced drag on biplanes and triplanes. First, induced drag was decreased to a minimum when he used two wings with the same span. He also examined the effect of the addition of endplates; these enabled a further reduction of induced drag. Figure 2.17 shows Prandtl's box wing configuration of the proposed model where tips of the biplane are connected on the top wing; this is called the closed box wing.

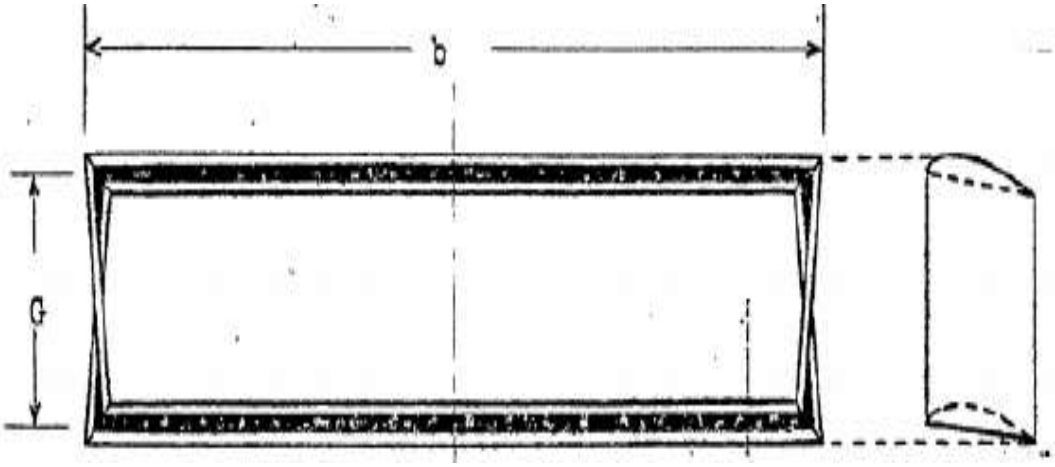

Figure 2.17: Best wing system by Prandtl [103, 163]

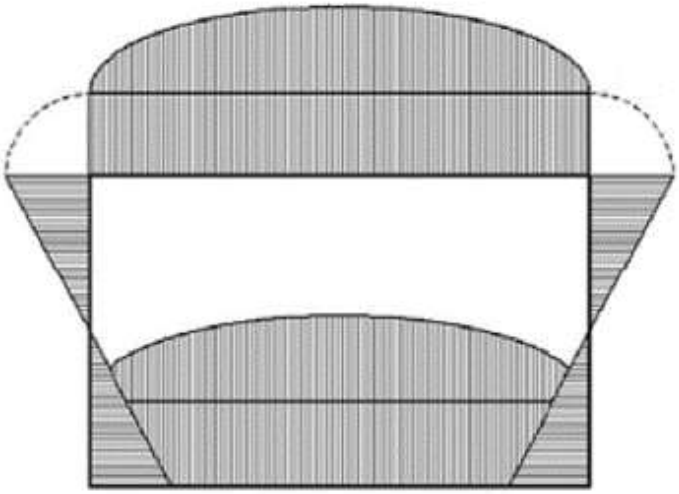

Figure 2.18: Optimal lift distribution for box wing [163, 164]

The closed box wing is identical to the best wing method, while lift distribution along each horizontal wing was elliptical and butterfly-shaped on the vertical wingtips where lift goes to zero in the middle of the wingtips, as depicted in Figure 2.18. This configuration and fact are also confirmed later by Demasi et al. [157].

Furthermore, Munk [103] showed that interference drag varied on each lifting surface as changes occur for longitudinal distances between the upper and lower surface. He found that the total induced drag of the wing remains constant if lifting circulation on each surface remains unchanged. Munk [103] concluded that the longitudinal distance of the lifting surface remains constant as long as the total circulation in the methods is unchanged. Therefore, induced drag is independent. This system is called Munk's stagger theorem [166]. In his further investigations, he showed that induced drag is not affected by the stagger and sweep of the lifting surface while the distribution of the lift remains constant on the wing. Hence, the box

wing has advantages in efficiency for the full range of aircraft. Thus, the joint wing concept would be the best option for efficient wing buoyant aircraft ($EWBA$).

2.7 Wing area and design configuration

Wings are an important component of aircraft design. The proper design of an aircraft wing can also be reduced a significant amount of drag and $C0_2$ emission [152, 167]. The basic requirements of wing design are flexibility, economy, satisfactory structural integrity, operational safety, sufficient space for the fuel tank, and undercarriage arrangement. Moreover, the flight characteristics must be capable of fulfilling various configurations of speed and altitude (high to low) [146, 168].

Indeed, the box wing configuration is an innovative procedure with each wing trip cord constantly joint each other, where the top wing and bottom wing height in respectively the same. Different researchers have carried out several pieces of research and predicted several advantages of box wings [65, 157, 159]. The lower aerodynamic drag and higher efficiency is the probable interest of this research; signify the potential proficiencies of precedent non-planar configurations and comparative performance of planar wing in aerodynamic points of view [65].

The assessment of the induced drag coefficient, drag coefficient, and lift coefficient variation relies on gematrical layouts of the non-planar wing. Thus, all configurations of non-planer studied were attained by altering the lifting surfaces of a traditional aircraft [169]. The Vortex Lattice methods (VLM) have been used to accomplish the study of the non-planar wing, developed by T.J. Mueller [170]. The ‘’Tornado’’ vortex lattice code is also included. The present version of Tornado can be handled multi cranked wings such as tapered, swept, heigh, dihedral and twisted box wing configurations with the trailing edge control surface. The governing equations came from the vortex lattice concept to solve the physical problem. The Biot- Savart law followed around the finite straight vortex line for the flow field vortex section needed for lattice. These vortices strength and induced flow field can be determined by no air flow through boundary conditions.

There are 4-DOF that tolerate the different geometrical configurations of box wing such as:

- The ratio between the upper and lower wing area: $W_R = \frac{S_2}{S_2 + S_1}$, S_2 is an upper wing, S_1 is the lower wing;
- Vertical separation in the upper and lower wing.
- The root chords distance from the Datum line (nose) and
- Dihedral angle of lower wings.

Therefore, certain modification were made during configuration, such as box wing considered zero sweeps and twist angle zero. A *NACA* 23024 aerofoil is adopted from the *NACA* chart as a base on an ideal lift (C_{li}) and maximum lift coefficient (C_{lmax}) as the requirement to model the desired box wing *(BW).* The aerodynamic parameter of aerofoil data was obtained from *XFLR-5,* which was designed based on the modern *XFOIL* theorem (more details in chapter 3). The reference wing area kept persistent for equal as planer wing 13.14 m^2 in all cases, which is attained by the designed point. Hence, it was influences in an aerodynamic parameter such C_L, C_D and $\frac{L}{D}$. Then, the *VLM* results of the non-planar wing compared with the conventional straight wing results that find from lifting line theory (LLT).

In considering wing design characteristics, a joint wing would be the best design strategy to reduce the drag coefficient (C_D). It can also minimise harmful environmental emissions by approximately 75% [71, 171]. On the other hand, the box wing yields a lower induced drag and higher wing stiffness when compared to a conventional cantilever wing [103, 155, 157, 162, 163, 172, 173]. In this research, a closed box wing for *EWBA* will be considered.

The selection of the wing area should be based on the required performance. The *EWBA* under consideration requires a maximum lift and low drag wing design [44]. The box wing can have an equal wingspan for both wings. In 1924, Prandtl [163] presented his best wing system design based on the biplane concept. In this case, the total wing aspect ratio is the squared span of the wings divided by the sum of individual wing areas. The equation is expressed as follows [71, 140, 174]:

$$AR = \frac{b^2}{S_{1+}S_2} = \frac{b^2}{S} \qquad 2.4$$

This expression may use individually for different wingspans in each wing. Where *AR* is the aspect ratio, S_1, S_2 are lower wing area and upper wing area consistently. In this design, the arbitrary aspect ratio (AR) was chosen to be equal to 15. Thus, the box wing assumes, the total wingspan and area remain the same. However, it can be adapted to different wingspans for both

wings. The former researcher Schiktanz and Scholz has also followed the same philosophy [175].

2.8 Analytical configuration of *EWBA* drag

The aerodynamic force is known as the drag force that resistance an aircraft's motion through the fluid. It is caused by the difference in the function of velocity between aircraft and the air. The drag force is dependent on the shape of the object's reference area and the coefficient of drag (C_D) [33, 120]. These areas could account for the wing area, fuselage cross-sectional area, tail area, and fuselage surface area[176, 177]. The general drag (D) equation [28] is presented in Equation 2.5.

$$D = \frac{1}{2}\rho V^2 S C_D \tag{2.5}$$

Where the non-dimensional drag coefficient (C_D) captures every aerodynamic configuration aspect such as the wing, tail, fuselage, landing gear, and even small elements like rivets. The drag has two parts: one is the induced drag coefficient (C_{Di}), and the other is the zero-lift drag coefficient (C_{Do}).

As stated by Sadraey [33], the sum of all resistive forces against aircraft motion is called drag. Drag increases as the airspeed increases; conversely, drag decreases if airspeed decreases. Indeed, the component build-up method has widely been used for the analytical calculation of total aircraft drag, which enables a reasonable estimate of drag at the preliminary stage [65]. However, to achieve greater accuracy in analysing aerodynamic performance, it is imperative that the Oswald factor is calculated correctly. Basically, this correction factor represents the change in drag in a *3D* aeroplane, ideally having the same *AR* and elliptical distribution [31, 178]. In the preliminary design, the Oswald factor (e) is estimated based on the following equation [33, 65, 98, 171]:

$$C_D = C_{Do} + C_{Di} = C_{Do} + \frac{C_L^2}{\pi ARe} = C_{Do} + \frac{C_L^2}{\pi ARe}(1+\sigma) \tag{2.6}$$

Where, C_D is the drag coefficient, C_{Do} is the zero-lift drag, and C_{Di} is the induced drag. The lift depends on drag with a parabolic variation and is expressed as follows [20, 21, 28, 33]:

$$C_{Di} = \frac{kC_L^2}{\pi AR} = \frac{1}{\pi eAR} C_L^2 \tag{2.7}$$

Where $k = \frac{1}{\pi eAR}$ is the induced drag (due to lift) factor [1, 33, 171, 179]. In order to define the C_{Di} of the box wing aircraft, it is obligatory to know its AR and the Oswald efficiency $(e)$for an airship is much less than one [1, 162]. In the case of traditional aircraft, the factor is called span efficiency [33]. The maximum Oswald efficiency is assumed to be one; it is normally between 0.7-0.9 in general aircraft. Historically, the well-known mathematical expression of Oswald efficiency is (e) =1.78× $(1 - 0.045AR^{0.68})$ – 0.64. However, during an experimental study by Wolkovitch [173] for box wing and traditional aircraft with the same fuselage, where he consists of some assumptions; so an amendment had to make regarding the span efficiency (Oswald efficiency) of box wing; then he used the following equation:

$$\frac{e_{actual}}{e_{theoretical}} = 1 + \frac{0.04\,(tan\,\Lambda_{Fr} + tan\,\Lambda_R)}{(tan29^0 + tan20^0)} \qquad 2.8$$

Throughout the research Wolkovitch [173] also found 4 % higher efficiency in the box aircraft than conventional aircraft for the theoretical calculation, which was used Letcher's recommended method [180]. Nonetheless, the experimental efficiency of the box wing was 9% higher than the traditional wing aircraft [173]. Finally, Wolkovitch [173] created these above correction equations 2.8 between analytical and actual Oswald factors (span efficiency) concerning these obtained results. The values 29^0 and 20^0 are represent front (Λ_{Fr}) and rear (Λ_R) sweep angles respectively in the denominator of equation 2.8. In fact, this becomes proved that it works only the front and rear wing $(\Lambda_{Fr}$ and $\Lambda_R)$ once both have high sweep angles, it does not integrate to configure a rectangular wing planform. Therefore, this research is summarised three different methods in the following Table 2.2 to calculate the Oswald efficiency factor (e) for box wing aircraft.

Table 2.2: Oswald efficiency factor with different methods for box wing aircraft.

Method	References	Oswald factor (e)
Kroo	[65]	1.46
Nita and Scholz	[181]	1.44
Wolkovitch	[173]	1.43

Hence, this design selected an average value from the three calculations of Oswald efficiency factors to deal with a conservative approach regarding the aerodynamic configuration of box wing aircraft $(EWBA)$, where the differences of span efficiency factor negligible.

However, for *HBA* or traditional airships, there is an alternative equation that estimates the '*K'* and AR for the hull (width) ^{2}/span as follows [1, 182]:

$$K = -0.0145\left(\frac{1}{AR}\right)^4 + 0.182\left(\frac{1}{AR}\right)^3 - 0.514\left(\frac{1}{AR}\right)^2 + 0.838\left(\frac{1}{AR}\right) - 0.053 \quad 2.9$$

Indeed, equation 2.9 is still an open research area, given that for conventional aircraft, the major lift is produced by the wing, but for the hybrid aircraft, some extra lift is produced by the fuselage. There is no aerodynamic lift at the angle of attack of zero [4, 18, 60] because of the symmetrical shape of the hull body. Though, Nicolai et al. [1] suggested that any standard shape of the hull body could produce lift while it uses an angle of attack. As a result, induced drag (drag due to lift) might exist since the lifting hull body is generated lift by $AOA > 0$. Nevertheless, in traditional aircraft design, induced drag is calculated from the empirical relationships pertaining to the aspect ratio of the aircraft wing as a lifting surface, as well as lift and drag [168, 183]. In most designs, the induced drag formula is available, based on Prandtl's lifting line theory (LLT). The mathematical model of *LLT* is predicted lift distribution over a *3D* wing based on its geometry [23, 60, 61]. This is only applicable in high aspect ratio areas of the wing, and it is the same for the fuselage as well. For the low aspect ratio wings as like as hull wide of the mark [31, 33, 65, 178, 183, 184]. At this stage, only pragmatic solutions are achieved via simulation and numerical calculation for the lift as well as the total drag [3, 10]. In fact, *K* values for the airship and hybrid aircraft design are set out in **Appendix B.2**, which are multiplied by N_L (this is determined by the number of lobes as seen in **Appendix B.3 (Table B.3.1)**, where $Re \geq 10^7$ and $M < 0.2$ and $AR = \frac{4}{\pi FR}$ for body revolution) [1]. In addition, the zero-lift drag or parasitic drag of the lifting hull is mostly comprised of skin friction drag, which is very similar to the case of the fuselage in a traditional aircraft where it is considered as a flat-plate skin friction coefficient [4, 120]. This skin friction drag is estimated to be the pressure drag due to viscous separation [181]. The *EWBA* drag may be computed using the equation $C_{D0f} = C_f f_m f_{LD} \frac{Swet_f}{S_{ref}}$ which was taken into account at the beginning of the aircraft design for major aerodynamic components [33, 171], and where C_{D0f} is the zero-lift drag for a fuselage or parasitic drag, C_f is the skin friction coefficient, f_m is a function of Mach number, f_{LD} is a function of the fuselage diameter ratio, $Swet_f$ is the aircraft fuselage wetted area and S_{ref} is the wing surface area. For aircraft design, very little attention is paid to the above equation, because in these vehicles parasitic drag does not result from the initiation of lift on the body. However, in *HBA*, airship, and *EWBA*, the equation must be considered very carefully because

most of the lift is generated by the hull of the airship or *EWBA*. Alternatively, there are other equations that have been developed for estimating the hull drag, as follows [4]:

$$C_{DoH} = C_{fH} FF_H \frac{S_{wet.H}}{S_{Aero}} \quad 2.10$$

Where, (C_f) is the skin friction drag, (FF_H) is the form factor, $(S_{Wet\,H})$ is the hull wetted area, and (S_{Aero}) is the *EWBA* wing area.

The total drag can thus be calculated in a step-by-step manner using the component build-up method. According to Nita [181], Roskam [183], and Haque [4], the wetted hull area for the aircraft could be calculated in many different ways, but the case of airship and *HBA* is entirely different. Nicolai and Carichner [1] used the lifting body surface reference for the skin friction drag coefficient which is expressed by Equation 2.11.

$$C_{DF} = \frac{\sum C_{f.comp}(FF)\times(S_{wet})comp}{V^{\frac{2}{3}}} \quad 2.11$$

Where (S_{wet}) is the wetted area of the component, FF are the form factors, and (C_{fcomp}) is the flat plate skin friction coefficient for each element. Hence, the few suggested formulas which would be appropriate for determining a form factor are shown in **Appendix B.4**.

According to certain authors, in the case of a whole aircraft in low subsonic flight, once a flow is turbulent, it would be appropriate to use the Schoenherr-von Karman equation, which is expressed below as Equation 2.12 [1, 171, 179] :

$$C_f = \frac{0.455}{[log10Re]^{2.58}} \quad 2.12$$

Where C_f depends on the Re, Mach number, and skin roughness. The most common useful subsonic parasitic-drag analytical method is the combination of component build-up procedure and the total drag, as presented in Equation 2.13. Additionally, more equations for component drag could be inserted into Equation 2.13 in order to get a sum of total zero-lift drag with the correction factor [1, 24, 178]; the analytical details with regard to the conceptual design are presented in Chapter 3.

$$C_{D0} = K_c(C_{D0H} + C_{D0W} + C_{D0T} + C_{D0G} + Others) \quad 2.13$$

In Equation 2.13, K_c is the correction factor. This mathematical method has been used for the *EWBA* model proposed in this thesis. The correction factor will be discussed in more detail later, in the design section in Chapter 3.

According to Zyskowski [185],'' The total induced drag for any multiplane lifting system is unaltered if any of the lifting elements are moved in the direction of the motion provided that the attitude of the elements is adjusted to maintain the same distribution of lift among them''. This quotation referred to Munk's method. Hence, the ratio of the gap of span ratio $\left(\frac{h}{b}\right)$ is a significant parameter for the box wing aerodynamic characteristic[155, 174, 186]. This parameter is adopted on the base of the mid-range of typical aircraft.

The validation of the *VLM* is carried out using two different approaches, for example, compared with *LLT* results and experimental results of traditional wings composed by *NACA* 23024 aerofoil[187], for evaluating the box wing results with the Prandtl presented data [163]. However, in this case, induced drag can only be compared. This research followed an approximation scheme of Prandtl, which referred to an induced drag of a convention wing and a box wing relationship with the same wing area, aspect ratio, and function of gap ratio as bellow;

$$\frac{D_{i\,BW}}{D_{iCW}} \cong \frac{1+0.45\left(\frac{h}{b}\right)}{1.04+2.81\left(\frac{h}{b}\right)} \qquad 2.14$$

The wing loading distribution is elliptical as a purpose of Prandtl. Hence, the sum of box wing areas such as the top and bottom wing is equal to the traditional wing area. Then, the ratio of induced drag calculated from isolating the same span efficiency factor calculated by *VLM* for the traditional wing (S), that can be used for box wing configuration. The plotting results of Figure 2.19 by equation 2.14 still well-suited for the span ratio of wing height up to 0.3.

Hence, the comparison of the entire non-planar wing and planer wing with the same wingspan and efficiency factor can be used following for total induced drag(D_i) [157, 163]:

$$D_i = \frac{(L)^2}{q\pi.b^2 e} \qquad 2.15$$

By equation 2.15 can be assumed the box wing induced is related to isolated reference wing aircraft. The equation (2.15) subsequently an individual section of the box wing that means the lift is half of the isolated wing, but all of the rest of the parameters being constant. Therefore, induced drag is 25% of that planer isolated wing as compared to equation 2.7, due to span efficiency is different.

The lift coefficient in each wing and the total coefficient for the box wing

In general, the box wing lift coefficient depends on the sum of an individual lift coefficient of each wing. Thad can calculate as follows:

$$C_{L\,bw} = C_{L1} \times S_1 + C_{L2} \times S_2 \qquad 2.16$$

can define by the lift curve slope, $C_L = \frac{\partial C_L}{\partial_\propto} \times \alpha$ for the individual wing, where α is *AOA*. So, by substituting these lift curve slopes in equation 2.16 can compute the total lift coefficient with the downwash results as follows [188]:

$$C_{L\,bw} = \left[\frac{\partial C_{L1}}{\partial_\propto} \times \propto\right] \times S_1 + \left[\frac{\partial C_{L2}}{\partial_\propto} \times \propto \left(1 - \frac{\partial_\varepsilon}{\partial_\propto}\right)\right] \times S_2 \qquad 2.17$$

Thus, the above equation is helpful to recognise a probable lift polar for configuration of the box wing, where have no wings decalage. The differences in incident angles between the top and bottom wings are called decalage. Indeed, the lift curve slope is assumed the same for isolated wings such as $\left(\frac{\partial C_{L1}}{\partial_x} = \frac{\partial C_{L2}}{\partial_x}\right)$. Though the reality is different, such as the aft wing lift curve slope is lower due to the downwash of the forward wing.

2.9 Combined aerostatic and aerodynamic lift and drag for the *EWBA* model

In some research studies [25, 28, 36, 121], it has been shown that an *HBA's* aerodynamic lift is created by a lifting surface similar to an aircraft's, and it is characteristic of low subsonic speed flight as similar as *HTA* vehicles. Zhang et al. [36] developed a mathematical *HBV* model of an airship where they used Equation 2.18 with the volume of the airship instead of the wing area. In the case of *HTA* like *HBA*, the calculation for wing lift is as follows:

$$C_{Lwing} = \frac{L_{wing}}{\frac{1}{2}\rho_a v^2 S} \qquad 2.18$$

Where L is the aircraft aerodynamic lift, ρ is the air density, V is the velocity, S is the wing area, and C_{Lwing} is the coefficient of the wing lift. In the same manner, the drag coefficient for the wing is expressed as follows [36]:

$$C_{Dwing} = \frac{D_{wing}}{\frac{1}{2}\rho_a v^2 S} \qquad 2.19$$

The expression for the total combined aerostatic and aerodynamic lift coefficient is expressed as follows [36]:

$$C_L = \frac{L}{\frac{1}{2}\rho V^2 S_{aero}} = C_{L.buoy} \times \frac{gV}{\frac{1}{2}\rho v^2 S_{aero}} + C_{L.aero} = C_{L.buoy} \times R_F + C_{L.aero} \quad 2.20$$

Where, R_F is a function of variable velocity, $C_{L.buoy}$ is the buoyancy lift coefficient, and $C_{L.aero}$ is the aerodynamic lift coefficient. Equation 2.20 works with a hybrid aircraft though its shape is invariant, but internal air molecule changes with altitude. However, the $C_{L.buoy}$ should remain constant until pressure height, even if gases are free to expand. Indeed, the aerostatic lift at some point, which is no longer towards the aerodynamic lift because of the altitude of aircraft described as the dead weight lift. In contrast, the aerostatic lift could be balanced by some percentage (%) of total take-off weight [26, 168, 189].

So, the above S_{aero} in *HBA* can be obtained by determining the sum of the fuselage planform projected area and wing area. These are the areas of wing outer surfaces of the fuselages. This can be defined by $S_{aero} = S_W + S_F$.

2.10 Actual drag polar for *EWBA*

Aerodynamic lift is produced by a lifting surface. Equation 2.21 can be defined as the total drag coefficient [3, 86].

$$C_D = C_{D0} + K\left(C_{Laero} - C_{(L_{md\_aero})}\right)^2 \quad 2.21$$

Where $C_{Lmd\ aero}$ is C_L for a minimum C_D. In conventional aircraft, airship, and even *HBA* designs, the $C_{Lmd\ aero}$ is close to zero, so this term can still be considered for Equation 2.21 to compute analytical drag for an *EWBA* because the *EWBA* is attached with a very low camber wing. Indeed, this analytical co-relation of airship and aircraft in all the above equations would be an essential starting point for a novel *EWBA* design.

2.11 Aerodynamic efficiency of *EWBA*

The *EWBA* behaves like a traditional aeroplane due to being heavier than air. In the case of the steady level flight, thrust is equal to drag and lift is equivalent to the weight. An assumption of flight at constant lift would be used in a unique equation that precisely computes the value of C_L and speeds [1]. For *EWBA* flight, maximum aerodynamic efficiency $\left(\frac{L}{D}\right)$ occurs once C_D minimum at steady level flight. However, $\left(\frac{L}{D}\right)$ is not constant since drag varies with velocity for a given constant buoyancy lift. Recently, Zhang et al. [36] used the following

Equations 2.22 and 2.23 for their mathematical model, which does not rely on speed if Equation 2.20 can be rearranged, as shown in Equation 2.23.

$$\frac{L}{D} = \frac{C_L}{C_D} = \frac{C_L}{C_{Do} + KC_{L\,wing}^2} \quad 2.22$$

$$C_{Lwing} = C_L - R_F C_{L.buoyancy} \quad 2.23$$

Furthermore, for *EWBA*, the formula to find velocity for maximum efficiency can be presented as follows [1]:

$$V_{\left(\frac{L}{D}\right)_{max}} = \sqrt{\frac{2L_{wing}}{\rho Vol^{\frac{2}{3}}}\sqrt{\frac{K}{C_{D0}}}} \quad 2.24$$

Where wing area (S_w) was replaced by $Vol^{\frac{2}{3}}$ as heaviness and $W_H = L_{aero}$ at steady level flight. This portion heaviness component is usually supported by buoyancy, and it is $W_H = W_T - L_{buoy}$ where the aerodynamic force will be needed for carrying these weights, it is a key influential for Hybrid buoyant aircraft's balance wight offers a typical downward force during the manoeuvre and landing, which has never been proposed for an innovative soft landing with aircraft balanced weight in existing design. Hence, the total ratio of the weight difference is one (1) for traditional aircraft and zero (0) for lighter than air vehicles $(LTAV)$. Thus, there is very little attention has been paid weight ratio between zero (o) to one (1), and even none of their weight balance studied between 0.40 to 1 for a long time in this intermediate range. Therefore, this research would be reviewed maximum aerodynamic efficiency $\left(\frac{L}{D}\right)$ for weight balance above 0.4.

Besides, at steady level flight, an airship/aircraft proceeding in a non-accelerated flight mode has a climb angle of zero. In fact, at level flight velocity, this is the function of wing loading. So, in a winged airship that is heavier than air, such as *EWBA*, it is necessary to bridge the gap between the airship and traditional aircraft with a low-emission alternative. Such an aircraft has real promise, investigation, and development in the near future. For *EWBA*, $\left(\frac{L}{D}\right)_{total}$ is expressed in Equation 2.25.

$$\frac{L}{D} = \left(\frac{L_{aero} + L_{buoy}}{Drag}\right), \text{ and } \frac{L}{D} = \left(\frac{C_{L\,aero}\, qV^{\frac{2}{3}} + (BR)W}{\left(C_{D0} + KC_{L\,aero}^2\right) qV^{\frac{2}{3}}}\right) \quad 2.25$$

Equation 2.25 illustrates the relationship between aerodynamic and aerostatic performance related to the above parameters. With this equation, the where planar wing hybrid

aircraft produced an efficiency of aerodynamic 24.36, non-planer wing 43.43 with the combination of aerostatic values for ratio weight balance 0.51 while prolate spheroid airship produced only 2.08 for aerodynamic efficiency. These results are adequately impressive compared to the Zhang [36] model, personal airship research by Liu et al.[190] and a hybrid air vehicle design by Meng et al.[189], though the weight balance was investigated below 0.4. However, equation 2.25 also indicates that the buoyancy lift is increased and decreased with respect to volume. If the buoyancy lift decreases, the aerodynamic lift must increase, but the weight ratio does not merely affect aerodynamic efficiency. Nevertheless, aerodynamic efficiency is significantly increased with improved aerodynamic lift, but C_{D0} increases more with increased hull volume than increased wing area.

2.12 Summary

This chapter is to examine the aerodynamic features with a focus on the conceptual design of different types of wing hull airship—a current analysis of airship, a hybrid airship to identify the most important design parameters. Since there has been much speculation, an advantage of an airship with adding a pair of wings to the main hull can produce a substantial aerodynamic lift, stability, and aerodynamic efficiency for a variety of civil and defence flight missions. There have been extensive studies and investigations on the *HBV* over the past few eras, Nicolai [1] was one among them, discusses in detail for performance analysis and design of hybrid airship with time constrain, while the design of the *HTA* vehicle is not addressed over *BR* ratio 0.40, since the hybrid airship needs aerodynamic support for the extended weight.

Although the numerous developments on the airship and *HBV* in the literature have been noticed, maintaining the aerodynamic shape of an airship is still challenging to consistently reduce the hull drag. But, maintain aerodynamic hull shape, not substance, since hybrid airships performed very similarly to traditional aircraft. In comparison, the maximum aerodynamic lift comes from an aircraft's advanced wing. There is still uncertainty in the case of *EWBA* and developed a combination of a conventional airship and with *HTA* concepts. Thus, researchers need to draw more attention to the aerodynamic performance of *EWBA.*

To the best of the author's knowledge, the advance (box) wing airship has not yet been investigated. There are only rare published existing experimental data available for hybrid airship [4, 27], but it is limited to the application only in convention aircraft design [65, 153, 163]; though, box wing is capable of improving aerodynamic efficiency for the full assortment of a hybrid airship. Hence, the traditional aircraft and airship experimental data can be used as

an advantage for an alternative comparison of *EWBA*. The researcher concluded, as mentioned earlier, the airship model with a novel concept of box wing adding to the main hull would be a great enhance to form the sustainable aerodynamic efficiency of a buoyant hybrid airship.

Chapter 3. Conceptual design and methodology

This chapter presents the methodology for this study. A clear exposition and understanding of methodology are required before outlining the basis of the models used in this research. The chapter also describes the research design and the analytical tools used in the study.

3.1 Introduction

In aircraft design, it must be decided at the outset whether the model is to be based on mega-lifter concepts with 50 per cent (approximately) of lift provided by aircraft wings[95]. At the beginning of the conceptual design process, it is important to develop a design specification according to the potential customer's requirements, to consider aircraft payload, range, take-off, landing, and manoeuvring parameters. In the case of innovative design, the process can begin with ideas at the cutting edge of science rather than a customer's demands. This research started 'from scratch' with a novel concept of a wing hull that is grounded in state-of-the-art know-how for the development of a hybrid aircraft that is slightly more substantial than heavier-than-air (HTA) and closer to lighter-than-air (LTA) aircraft.

Another key decision to be made in the design process relates to technological design tools, such as *CAD* tools, simulation tools like *CFD*, flight simulation, and so on, for modelling and analysis. The design of an aircraft involves not only the actual layout of the vehicle but also the determination of the analytical process. The review of the aircraft design has the aim of creating new concepts and technologies that can be used to formulate a new model. The typical design plan consists of the aircraft fuselage, wing, tail, crew location, and payload [171].

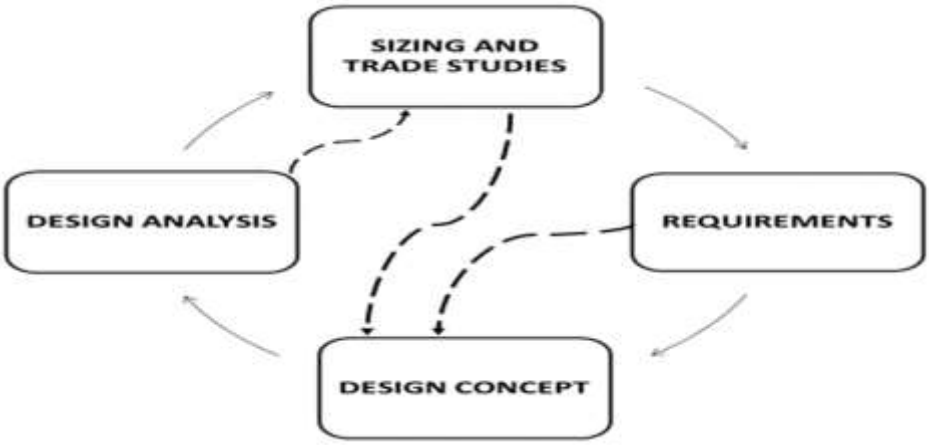

Figure 3.1: The design wheel

As shown in Figure 3.1, the design process is like a 'wheel' of interaction between the design concept and stages of study and analysis. The conceptual design method begins with sizing according to the unique requirements of the aircraft's performance objectives. The constraints of design are summarised in **Appendix C.1**.

The method of sizing in this research involved a quick and accurate process enabling computation of essential take-off weight from a conceptual phase and mission profile.

3.2 Design methodology, systematic approach, and preliminary performance

The complexity of an aircraft design calls for various methods to determine the aircraft's sizing appropriately. According to Mihm et al.[191] and Braha and Bar-Yam [192] iteration is a more novel and more consistent scheme among them. Particularly it is prominent in the improvement of intricate methods: in this context aircraft, even global leading concerns projects are assumed for inevitable in their development. In fact, for the field of research, an iteration method has been played huge impacts especially for aircraft design, as well as in other engineering disciplines during design or in development of a new product and including exploration of concepts, discovery and revising errors, and enabling development under complexity, uncertainty, and change as Li et al.[193] and Wang et al.[194]. Generally, the accepted opinion, as articulated by Smith and Tjandra [195] that the concern of iteration is essential to refining and accelerating product design. Several scholars have been considered this accepted reflection of the matters of iteration. Santos et al.[196], models of design perception define an essentially iterative method of study and convergence, in which changes are repetitively generated, studied, and appraised. Clark et al. [197], these series of problematic solving, which arise once a clear solution is not apparent for a specific issue, can contain a solely distinct and can also be happening on a larger scale. Eppinger [198] offers a considerable form of study due to complex inter necessities by iteration scheme. It is commonly denoted using different terms, such as rework, loop-backs, feedback loops, and churn, that have been described as re-entering either problem or tasks or a design. Indeed, the scholars also consider processes from a different point of view and base on their objectives.

Some of the empirical studies suggest that spending more effort to explore the space of design concepts iteratively yields better designs; overall iteration over perceptions might lead to better designs. For instance, Chusilp and Jin [199] start an experiment and found that more iterations and extra time spent on each iteration naturally lead to enhanced quality and more

novel perceptions. It also claims that quick feedback of design activities with resulting changes inspires an ‘‘iteration-rich’’ method, which is proposed as an optimistic behaviour. Since iteration does not only comprise the enhancement of the design but also nursing as self-replication and regulator of the design scheme.

Overall, iteration is influenced not only by administration tactics but also by the design's appearances under progress. For example, in any design scheme, the redesign is also feasible to be iterative irrespective of whether it ensues before or after design publication. One study that Eckert et al. [205] highlight the impact of design connectivity and limits on revision from an engineering perspective of evaluation is reported, who conducted 22 consultations from helicopter manufacturers. Inclusive, suitable modularity may decline the iterations in the platform; it might also decrease the life cycle rate with the variation of the original system as in accordance Engel and Reich [200]. Suss and Thomson[201], an iteration scheme has also been treated in numerical simulation and mathematical models based on a design's crucial properties. That is influenced by harmonisation between flow simulation and model directly. Therefore, the design would be used newton’s iteration method for approximating the gross take-off weight and throughout the design phase.

The design will specify the typical size of an aircraft model, concentrating on aircraft weight, geometry, and its mission parameters, in order to manifest the novel, state-of-the-art concept [171]. Thus, this chapter reports how the weights of the aircraft’s components were separately estimated and calculate aircraft performance related to these factors. An aircraft take-off weight (W_{To}) is an important parameter for modelling or computing its flight paths and fuel consumption as well as the vehicle’s characteristics and performance, for example, take-off rate, climb, cruise, endurance, ceiling, and descent [34, 202]. In fact, traditionally, W_{To} is estimated by the components’ weights, namely the payload weight (W_P), fuel weight (W_f) and operating empty weight (W_f). This method is very useful for aircraft design where W_P is an input. It is also suitable for estimating the average aircraft take-off weight if details are available for the average passenger load factor [171, 183, 203, 204].

However, these load factors are stringently controlled by the relevant authorising bodies. Therefore, this approach is not ideal for calculating the W_{To} for a particular flight of the model *EWBA* since the individual load is unknown. However, following previous researchers [205, 206], the W_{To} can be estimated from the original flight path data during the climb for a particular flight by simulation. Indeed, the estimate is characteristically equal to W_{To} such that the power check with climb model whether or not matched in equivalent to

W_{To} on historical trajectory points. Alternatively, approximations of aircraft W_{To} can be revised by using either a device such as a design tool or unconstrained least-squares algorithms. Alligier et al. [206] also argued that sometimes an instrument has also been used pragmatically to estimate W_{To} from radar data, to predict aircraft trajectory for future use. For aircraft, existing methods of estimating data are instrumental once the aircraft design parameters are available. However, due to the unavailability of valid radar data for the *EWBA* trajectory, this method is not helpful in the present study.

Raymer [171] has formulated a breakdown of the steps involved in the conceptual development of aircraft design. His method requires consideration of the initial requirements for aircraft sizing parameters. The author [171] proposed two different types of sizing processes: class-I and class-II. However, his first method (class I) is quite complicated because it is calculated on the basis of the empirical ratio of take-off weight to the empty weight of aircraft. In the class-II approach, he used the statistical weight equation during the sizing for the aircraft design. The class-II method also follows a sequence of phases for the estimation of fuel fractions throughout the aircraft mission profile and precedes an empty weight calculation. Finally, he used an iterative system to calculate an estimated take-off weight. Indeed, this approach is iterated until results are converged. Therefore, this iterative method is beneficial in the *EWBA* design.

For preliminary design, two convenient design methods have been developed by an earlier researcher [30]. Using these methods, the three key parameters W_{To}, S_w and P_E can be obtained with precision. The first technique accords with Raymer's statistical method but uses different aspects: wing area (S) and engine power (P). In addition, the second method was subsequently established based on aircraft performance as required to determine the same aspect $(S\ and\ P)$ as the first method. So, his second method is still widely used in state-of-the-art aircraft design. It is often referred to as a graphical representation matching plot in which the designer can easily identify wing loading and power loading parameters. Thus, for this research, a *MATLAB* code was modified to govern all the above fundamental features of the *EWBA*. This computational matching plot technique $(MATLAB)$ would be utilised in the further development of the *EWBA*

First, the design process used a popular components build-up method for estimating the W_{to} since this is the crucial parameter in design optimisation, as can be seen in the following equations [33, 154, 171, 179]: $W_{To} = W_e + W_P + W_f + W_g$, where W_{To} is take-off weight which consists of W_e operating empty weight, which consists of equipment weight (engine, wheels,

avionics' and seats) and aircraft structure. It can be obtained by a fraction of W_{To}. W_P payload weight, W_f fuel weight W_g gas weight; and $W_e = W_{fix} + W_{var}$, where W_{fix} is the fixed weight (like the engine), W_{var}, the variable weight (fuel), this weight could be considered as a fraction of the take-off weight [33, 154, 171, 179].

$$\text{So, } W_{to\_Calculated} = \frac{W_p + W_{Crew}}{1 - \frac{W_e}{W_{to\_guess}} - \frac{W_f}{W_{to\_guess}}} \quad 3.1$$

According to Torenbeek [179], equation 3.1 may be used for several types of aircraft, such as (a) lightweight aircraft and (b) turbojet and turbo propeller aircraft. Indeed, in these cases, cruise fuel is determined by the Breguet range equation. On the other hand, Mohammad [33], Wang et al. [194], and Smith and Tjandra[195] has shown an iterative method. Precisely Newton's iterative process. It can be adopted for solving equation 3.1, making an initial estimation for take-off weight that will then converge to the original value in the preliminary stage through *MATLAB* in step.

Now, assume cruise altitude is 4000 m as a design requirement, with a crew and pilot weight (W_C): (1) x (180+10+16) = 206 lbs or 93.4 kg. According to the *FAA* (2005) regulations [33, 171, 179], one crew member weighs 180 lbs with a maximum clothing allowance of 10 lbs and 16 lbs for personal items. So, payload weight (W_P) is equal to 3pax × (180+50) which is 690 lbs or 312.978kg (domestic flights allow 50 lbs for bags).

3.2.1 Mission segment

There is one other critical aspect of an aircraft's weight, the W_{MTOW}, which is the maximum take-off weight. Its value must be known so that the vehicle can fulfil the customer's mission specification. Since the specific fuel consumption (SFC) of an aerodynamic model is estimated from its configuration by recalling the fuel fraction $\left(\frac{W_f}{W_{To}}\right)$, the total fuel weight is different from the flight mission segment weights, as shown in Figure 3.2 (*EWBA* mission profile). This mission consists of six segments, the cruise $\left(\frac{W4}{W3}\right)$ being one of the most extended segments. In each stage of the flight path, an aircraft loses weight due to fuel burn, so it is necessary to estimate the fuel weight fraction throughout an aircraft's flight operation. Hence, the weight difference between take-off and landing is equal to fuel weight [33, 207]. In **Appendix C.2,** more details are provided for each segment of the mission profile's analytical analysis.

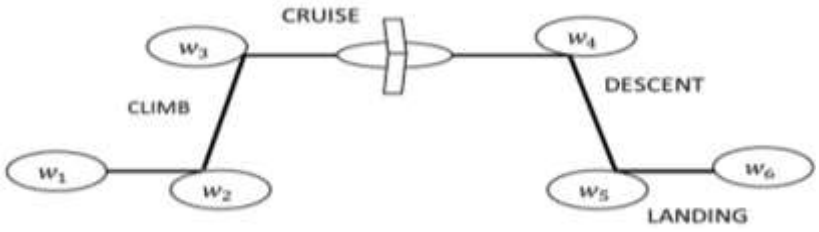

Figure 3.2: *EWBA* mission profile.

Finally, $\left(\frac{w_6}{w_1}\right)$ can be expressed as [33, 171], $\frac{W6}{W1} = \frac{W2}{W1} \times \frac{W3}{W2} \times \frac{W5}{W4} \times \frac{W6}{W5} \times \frac{W4}{W3}$

Where we could use the weight fractions for take-off segment, climb, descent, and landing segments, set out in Table C.3.1 in **Appendix C.3.**

EWBA cruise fuel fraction

In buoyant aircraft, the cruise fuel fraction is determined by calculating the total distance that the *EWBA* can be flown with a full fuel tank without refilling. This is also called the Breguet range equation. However, this approximation of the fuel weight fraction does not consider wind effects. The cruise fuel fraction can be obtained by the following equation [33, 178, 208]:

$$\frac{W4}{W3} = e^{\left[\frac{-RC}{0.866V\left[\frac{L}{D}\right]max}\right]} = e^{\left[\frac{-4500km\times\frac{10^3}{1km}\times\frac{.4}{3600}}{0.866\times46\times[17]}\right]} \qquad 3.2$$

Where *R* is the range, *C* is the engine specification; *v* is cruise velocity, and *L/D* is the lift to drag ratio. So, $\frac{W4}{W3}$ = 0.4779, and $\frac{W6}{W1}$ = 0.4497. For safety purposes, 5% extra fuel (relating to total weight) is required. Therefore, $\frac{W_f}{W_{To}} = 1.05\left[1 - \frac{W_6}{W_1}\right] = 0.5778$. Thus, the take-off weight (W_{To}) is = $\frac{405.98}{0.4222 - \frac{W_E}{W_{To}}}$, where $W_P, W_c, \frac{Wf}{W_{To}}$ and $\frac{W_E}{W_{To}}$ are payload, crew weight, fuel fraction, and empty weight fraction respectively [33, 171]. The empty weight ratio can be determined by the following statistical equation [33]:

$$\frac{W_E}{W_{TO}} = aW_{To} + b \qquad 3.3$$

Where regression coefficients '*a*' and '*b*' have been defined from Table 3.1[33], $a = 2.73 \times 10^{-4}$, $b = -9.08$ as GA-twin engine aircraft, which is reflected in aviation during aircraft design.

Table 3.1: Coefficient a and b valid for empirical equation

No	Aircraft	*a*	*b*
1.	Hang glider	6.53×10^{-3}	-1.663
2.	Man-powered	-1.05×10^{-5}	0.31
3.	Glider/Sailplane	-2.3×10^{-4}	0.59
4.	GA- single-engine	1.543×10^{-5}	0.57
5.	GA- twin engine	2.73×10^{-4}	-9.08
6.	Jet transport	-7.754×10^{-8}	0.576

Substituting the 'a' and 'b' values in the above formula yields:

$W_{T0}\left(0.4222-\frac{W_e}{W_{TO}}\right)$ = 405.98, since, $\frac{W_e}{W_{TO}}$ = 0.5759. Therefore, W_e = 691.15 kg, and W_f = 595.65 kg. Now equation 3.1, iterate in *MATLAB* as suggested Newton's method for defining the aircraft take-off weight (see *MATLAB CODE* and output results in **Appendix C.4**); start with the initial estimation of W_{To} is equal to 560.002 kg and stopping at a 1202 kg criterion with the rate of error $7.\times 10^{-5}$ % after 24 iterations, it can be seen in Figure 3.3, that is quite acceptable results with a comparison of the similar characteristic of small aircraft.

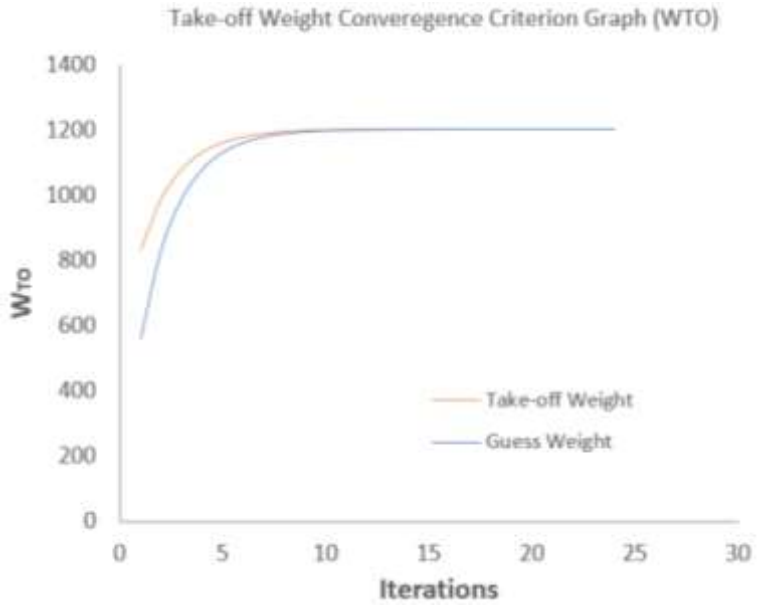

Figure 3.3: A realistic convergence criterion of *EWBA*

The W_e could be appraised as a fraction of W_{To}, as a conventional lightweight aircraft are corresponded for following Figure 3.4[209]. Yet, the ratio of W_e to W_{To} has apparently be contingent on the type of aircraft and its size, however, this parameter is not wide in the base

of range. Thus, a likely to conclude final aircraft's empty weight fraction, which provides consistency of future projection.

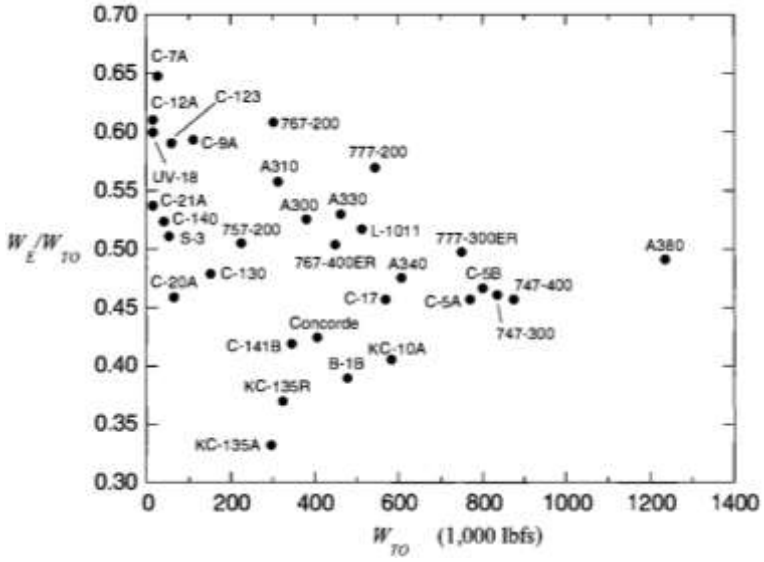

Figure 3.4: Weight fractions of cargo and passenger aircraft [209]

These empty weight fractions are also deemed adequate, with reference to the four aircraft values listed in Table 3.2 below [33].

Table 3.2: Empty weight fraction for several aircraft [33]

No	*Aircraft*	*Engine*	$S(m^2)$	$\boldsymbol{M_{To}}(kg)$	$Me(kg)$	$\frac{W_e}{W_{To}}$
1.	Quester Spirit	Piston	6.74	771	465	0.6
2.	Sky star kit fox V	Piston	12.16	544	216	0.397
3.	Beech Bonanza A36	Piston	16.8	1655	1047	0.63
4.	Cessna 750	Turbofan	48.96	16011	8341	0.52
5.	EWBA	Piston	13.14	1202	691.15	0.5759

The above empty weight fraction was computed for an aluminium structure, and an *EWBA* would be made up of aluminium as implicitly presumed. If it would change the mind in composite material to consist of an *EWBA*, it must be multiplied by a factor of 0.9 [210], which is standard load and resistance factor design $(LRFD)$ for composite materials. It is a benchmark that establishes parameters for additions to the composite structure of nominal strengths. Hence, this validation has become much accurate and remarkably acceptable.

However, buoyant lift (L_{buoy}) is defined = 1.03× hull× 9.81(equation 1.1), where 1.03 Kg/m^3 is the buoyancy lift by 1 m^3 of helium at sea level, the hull volume is 577.05 m^3.

Therefore, 5830.69 N of mass is enabled to be lifted by helium in *EWBA*. The maximum heaviness (ΔW) is often called aerodynamic maximum weight or load = (W_{to}- L_{buoy}) = 607.63 kg or 5960.85 N that is 50.64% of total lift by aircraft wing, which is called the aerodynamic lift, and the buoyancy ratio at take-off (BR_{To}): $\frac{L_b}{\mathrm{W_{to}}}$ = 49.36 % of the total lift, where the L_b is buoyancy lift that divided by the total weight (W_{To}) of the aircraft. This weight fraction is influenced by Liu et al. [119] during research on a hybrid airship platform, and they proposed that winged hybrid airship achieved the maximum lift to drag ratio $\left(\frac{L}{D_{max}}\right)$ at optimol *BR* 0.6. The buoyancy ratio of the conventional airship (CA) is usually (BR_{To}) > 0.8 and hybrid airship (BA) is > 0.60 with depends upon the *CA*'s lift generation aptitude of aerodynamic or engine thrust during take-off. But buoyant wing hybrid airship ($BWHA$) or box wing hybrid buoyant aircraft can carry much more payload, fuel, and range than the *CA* and *HA*.

The aerodynamic lift created by buoyant wing hybrid aircraft is a crucial advantage for supporting its weight. It is more likely can be performed as a conventional aircraft with minimum fuel consumption. Thus, 50.64% of aerodynamic lift is the value that will be studied in *CFD* for further investigation of the aerodynamic efficiency of *EWBA*.

3.3 Wing and engine sizing for *EWBA*

In the preliminary stage of the design phase of a propeller-driven aircraft, the maximum take-off weight ($MTOW$) is 1202 kg, C_{Do} is 0.0157, the stall speed is less than 58.73 knots equivalent airspeed ($KEAS$), cruise speed is 46 m/s, the maximum speed is 98 m/s, the rate of climb is more than 2700 fpm at sea level, the take-off run is less than 1000 ft, and the ceiling is 35000 ft. As before, all analytical details and calculations are provided in **Appendix C.5**. The matching plot is created by *MATLAB* using the following five equations.

3.3.1 Stall speed

One of the most important performance parameters of air transport is the aircraft's stall speed (V_S), which must not be exceeded, and which is also restricted by the *EASA* certification specification (CS). The stall speed can be obtained through the following equation:

$$\left[\frac{W}{S}\right]V_S = \frac{1}{2}\rho V_s^2 S C_{Lmax} \qquad 3.4$$

It is provided in the first matching plot graph in Figure 3.5. Low stall speeds are desirable for safety reasons during take-off and landing; in the event of an accident, a lower stall speed would result in less damage and fewer casualties.

3.3.2 Maximum speed

The second most important parameter is maximum aircraft speed (V_{max}). This speed influences take-off weight, wing area, and engine power. The aircraft V_{max} can be computed with the following equation:

$$\left[\frac{W}{P}\,SL\right]_{Vmax} = \left[\frac{\eta p}{\frac{\frac{1}{2}\rho_0 V^3 max\, C_{D0}1}{\frac{W}{S}} + \frac{2K}{\rho\sigma V_{max}}\left(\frac{W}{S}\right)}\right] \qquad 3.5$$

where η = propeller efficiency, assumed to be 0.8, while the Mach number (M) = 0.15, and relative density at 4000m. So, the velocity maximum contribution graph can be seen in Figure C.6.1, **Appendix C.6.1.**

$$\left[\frac{W}{P}\right] S_{TO} = \frac{1 - e^{\left(0.6\rho g C_{DG} S_{TO} \frac{1}{\frac{W}{S}}\right)}}{\mu - \left(\mu + \frac{C_{DG}}{C_{LR}}\right)\left[e^{\left(0.6\rho g C_{DG} S_{TO} \frac{1}{\frac{W}{S}}\right)}\right]} \times \frac{\eta p}{V_{To}} \qquad 3.6$$

The take-off run contribution for matching plot in Figure C.6.2 **Appendix C.6.2**. That has been shown in an acceptable region on the graph.

3.3.3 Rate of climb (ROC)

The *EWBA* configuration has been specified in the investigation of *ROC*. In fact, *ROC* is a function of propeller efficiency and engine power for a certain altitude. The *ROC* is required to be more than 41.748 m/s or 4228.24 fpm at sea level. Based on the wing and engine sizing, the *ROC* is expected to be as follows for propeller-driven aircraft:

$$\left[\frac{W}{P}\right]_{Roc} = \left[\frac{1}{\frac{ROC}{\eta p} + \sqrt{\frac{2}{\rho\sqrt{\frac{3C_{D0}}{K}}} \times \frac{W}{S}} \times \frac{1.155}{\left(\frac{L}{D}\right) max \times \eta p}}\right]$$

$$= \left[\frac{1 \times 550}{270.05 + \left(\sqrt{3298.45 \times \frac{W}{S}} \right) \times (0.168)} \right] lb/ph \qquad 3.7$$

The results values fall in the acceptable region, according to Figure C.6.3 in **Appendix C.6.3.**

3.3.4 *EWBA* ceiling

The ceiling refers to the upper limit in terms of flight altitude. There are four different types of the ceiling: absolute ceiling, service ceiling, cruise ceiling, and combat ceiling, where the *ROC* is 0, 0.5 m/s, 1.5 m/s, and 5 m/s respectively. (Note that the combat ceiling altitude is applicable only to combat aircraft.) For simplicity, the innovative matching plot technique will consider only the cruise ceiling.

The service ceiling must be greater than 35000ft, and the *ROC* at that ceiling must be 100 ft/m, 1.6 ft/s, or 0.487 m/s; the density, at 35000ft, is about 0.380 kg/m^3.

$$\left[\frac{W}{P_{SL}} \right]_C = \left[\frac{\sigma C}{\frac{(ROC)c}{\eta p} + \sqrt{\frac{2}{\rho \sqrt{\frac{3C_{D0}}{K}}} \times \frac{W}{S}} \times \frac{1.155}{\left(\frac{L}{D}\right) max \times \eta p}} \right]$$

$$= \left[\frac{0.31 \times 550}{2.083 + \left(\sqrt{5001.06 \times \frac{W}{S}} \right) \times (0.168)} \right] lb/ph \qquad 3.8$$

The above ceiling contribution plot in Figure C.6.4, **Appendix C.6.4**. Then, by developing a *MATLAB* code, all of the above equations can be plotted in the same graph as depicted in Figure 3.5 below; the *MATLAB* code is also provided **in Appendix C.6**, where power is a function of wing loading.

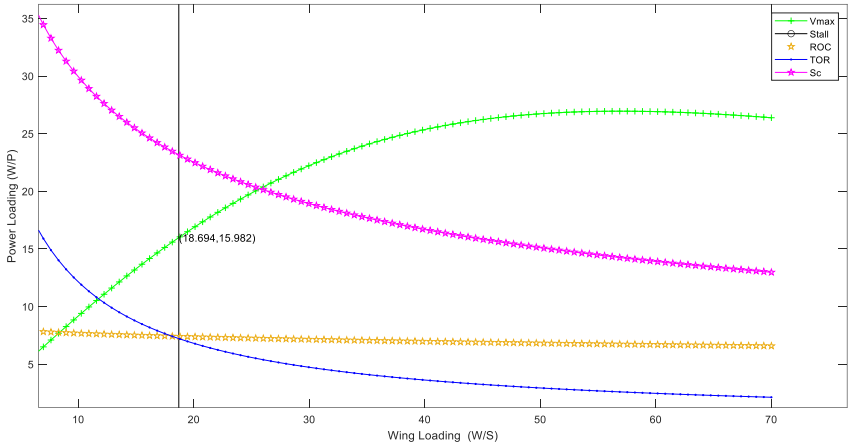

Figure 3.5: An *EWBA*'s matching plot diagram to identify the design point

Indeed, this chart of the maximum speed, take-off run, and stall is the target point. The design point method strives for the least power that would have the least operational cost [33, 211]. The method is called the matching plot technique, used to determine satisfactory performance with the required design specifications. The highest point in this region is called the design point. The design point is the intersection of the V_{max} and V_S graph lines. The graph marks a region where has been confirmed to all *EWBA* flight performance obligations on that same point. The acceptable region is located below each graph line, and the stall speed is on the left of the graph. As a result, we can compute the power loading and wing loading as 15.98 lbf/hp, 18.694 lbf/ft^2 respectively. Then, the wing area(S) 13.14 m^2; power (P) 123.36 kW or 165.46 hp as required by the design point.

Hence, the graphical output of the matching plot technique applied to *EWBA* that the performance requirement values are within the acceptable regions and in one single point. The outcome of attained results is feasible; this classical scheme has been proved for conventional aircraft [212]. Though, yet to approach hybrid airship (HA) or *EWBA* design. Therefore, this technique has been demonstrated that the achievements of *MATLAB* results are accurate, reliable, and robust. It could be achieved more stable results with regular exercise of this design method.

3.4 Wing design

During preliminary design, three main parameters were determined, namely, wing area (s), maximum take-off weight, and engine power. The primary purpose of the wing is to generate sufficient lift and existing accessible aerodynamic data. This chapter will focus on aerofoil selection according to Sadraey methodologies [33] since the lifting line theory will be

used to determine the spanwise lift distribution along the wingspan. The design of the wing area must take into account: wing area (*S*) 13.14 m^2, cruise velocity (V_c) 46 m/s at 4000m, stall speed (Vs) = 37.08 m/s, maximum velocity 98 m/s and maximum take-off weight 1202 kg.

3.4.1 Aerofoil selection for *EWBA*

The aerofoil selection scheme is the best compliment for wing planform; a popular and well-accepted method was followed to determine the most appropriate aerofoil for lift coefficient (C_l) , low drag aimed at operational cost and pitching moment in minimum to keep trim drag in minimum as required characteristic of an aerofoil, more detailed in **Appendix C.7**. In particular, Figure 3.6 in **Appendix C.7** shows C_{li} and $C_{l.max}$ in the same graph for several *NACA* aerofoils for different characteristics. The horizontal and vertical axes represent the ideal lift coefficient (C_{li}) and the maximum lift coefficient $(C_{l.max})$ respectively. So, as per *EWBA* requirements, C_{li} = 0.289 and $C_{l.max}$= 1.21, taken from the analytical calculations. Then, it has been chosen a few *NACA* aerofoils from *NACA* Figure 3.6 in **Appendix C.7,** where were found that the following *NACA* aerofoils are the closest matches: *NACA* 23024, *NACA* 2412, *NACA* 2421, *NACA*63012, and *NACA* 65-210 could be used. It is also suggested by the literature base on accessible data [67]. Finally, we select the best model by comparing the aerofoils in terms of minimum C_{mo}, C_{do} and $\left(\frac{C_l}{C_d}\right)$ by assessing the graphical representations of their performance data. These comparisons were carried out using *XFLR5* aerofoil tools, which is an improved version of *XFOIL* software, to compare their aerodynamic characteristics. It was written with C^{++} and C programming languages and is capable of analysing lifting line theory (LLT), vortex Latics method (VLM), and *3D* panel [213]. This potential flow analysis code of *XFLR5* used an internal boundary layer model to calculate the lift and drag of a *2D* aerofoil. The *XFLAR* 5 data are available in **Appendix C.8.**

Moreover, Figure 3.6 shows that for C_l Vs AOA, the *NACA* 23024 maximum lift coefficient is 1.21, which is in range, but *NACA* 23012 has been shown to be the highest lift coefficient, but which is out of range as required. Again, Figure 3.7 represents the *NACA* 23012 also has the highest lift to drag ratio compared to others, and it is dropped since the $\left(\frac{C_l}{C_d}\right)$ beyond the range, however, *NACA* 23024 revealed good agreed with theoretical aerodynamic results. Furthermore, in Figures 3.8 and 3.9, results show that the *NACA* 65-210 aerofoil's low drag and low c_{lmax} (Figure 3.6), which is not a good match for the *EWBA* requirement and released from contention. But, the drag coefficient is also higher as the requirement for *NACA* 2412

aerofoil (Figure 3.8 and Figure 3.9), then it is dropped from the further argument. Indeed *NACA* 2421 among the rest of the two aerofoils are adequate in the lift to drag ratio for maximum regions as an expected (Figure 3.7), and the lift coefficient (c_l) in range for the cruise (Figure 3.6). However, the *NACA* 2421 aerofoil shows a higher c_{d0} than projected (Figure 3.8 and 3.9), so it is also dropped for further investigation. Since the model with the lowest moment coefficient is *NACA* 23-012 (-0.0067) but this is expensive in terms of design and unavailable aerodynamic relatable data. However, in terms of safety issues, *NACA* 23024 is acceptable as *XFLAR5* data, as shown in **Appendix C.8.**

Finally, the *NACA* 23024 aerofoils, the $c_{l\,max}$, drag (c_{d0}) and c_{lc} at the cruise region in the desired range (Figure 3.6, Figure 3.8, and Figure 3.9). However, the aerofoils performance's decisive aspect is changed, since low speed and high load at the wingtips during certain manoeuvres, for example, in turning flight. Furthermore, *NACA* 23024 aerofoils have accessible wind tunnel data, it is enabled to assist in the determination of aerodynamic effects, and the *NACA* 23024 aerofoil is less expensive, the aerofoil responded fairly well with respect to the $c_{l\,max}$ and c_{d0} [67] as requirements and long endurance than others. In fact, the experimental comparison in Table 3.3 below shows that *NACA* 23024's *XFLAR5* results are adequately accepted as experimental data as the base on aerodynamic performances: lift coefficient, drag coefficient, and moments coefficient.

Table 3.3: Comparison of Aerofoil

Methods Aerofoil	C_{lmax}	C_{d0}	C_m
XFLAR5_NACA23024	1.21	0.0088	0.0188
Experiment_NACA23024	1.23	0.0085	0.0184

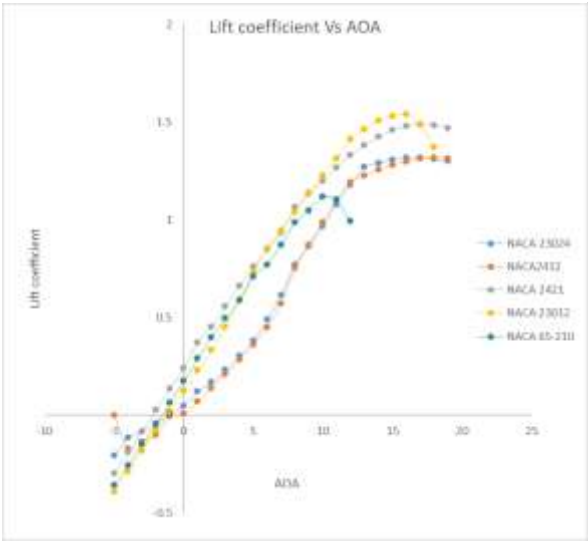

Figure 3.6: Lift coefficient vs AOA

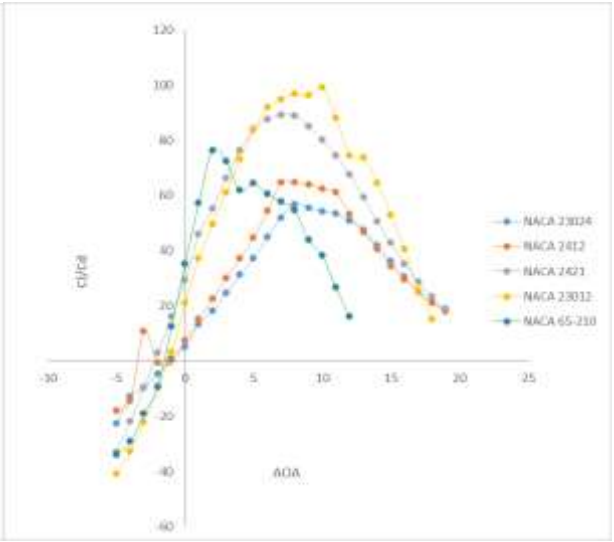

Figure 3.7: Lift to drag ratio vs AOA

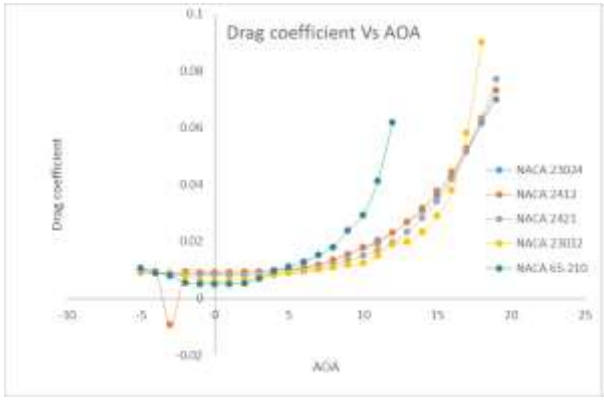

Figure 3.8: Drag coefficient vs AOA

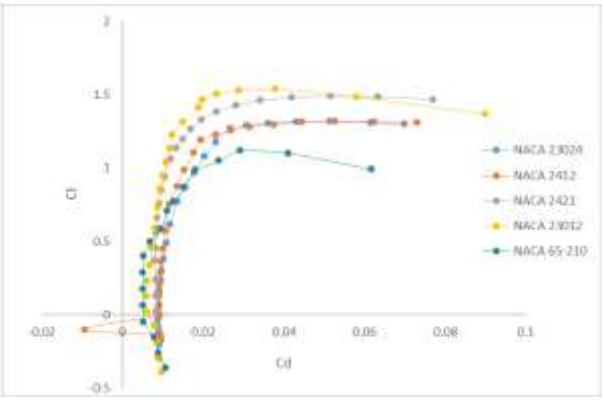

Figure 3.9: Lift coefficient vs drag coefficient

Figure 3.10 shows experimental lift coefficient trends line an impartially rapid stall at *AOA* 12^0, due to technical error. However, *XFLAR5* is showing a smooth stall at the same point. The author Abbott [67] suggests using trip strips that can be improved aerofoil performance. Figure 3.11 and 3.12, drag coefficient versus *AOA* and lift coefficient versus drag coefficient respectively. Yet, it is realised in the data, and the *XFLAR5* data are followed the resulting experimental data nonlinearly, the drag coefficient of *NACA* 23024 of *XFLAR5* data well responded with experimental data. Hence, aerofoil's characteristic data are verified.

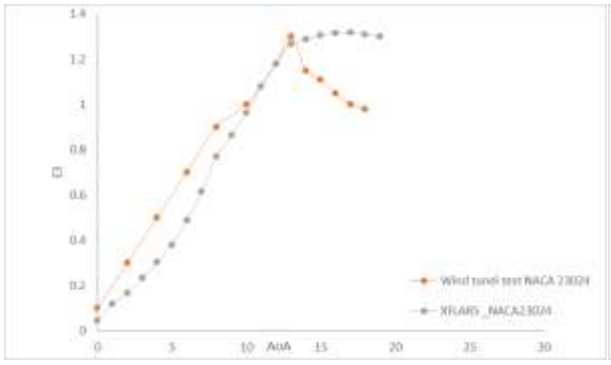

Figure 3.10: Lift coefficient *Vs AOA*

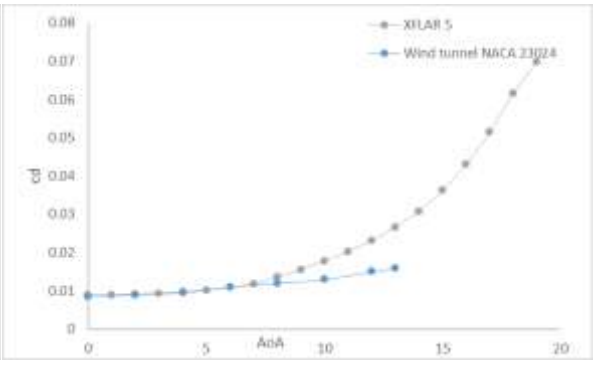

Figure 3. 11: Drag coefficient *Vs AOA*

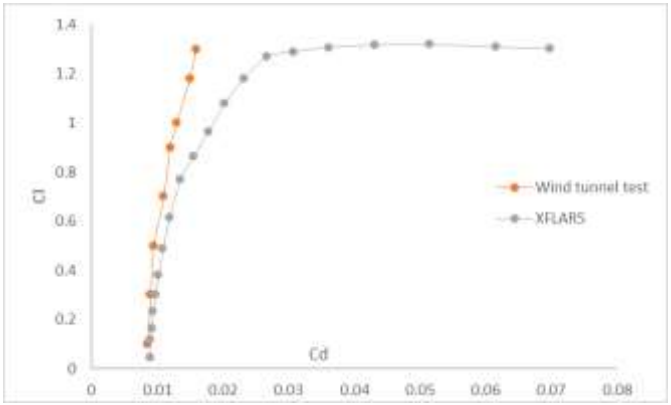

Figure 3. 12: Lift coefficient Vs drag coefficient

So, in sum, *NACA* 23024 is the aerofoil best matched to the *EWBA* requirements for planer and non-planer hybrid wing aircraft.

3.4.2 Lift distribution

The proper aerodynamic systems and selection in the conceptual design phase are constrained by considerations of time and accuracy. In other words, aerodynamic prediction techniques and a model must be accurate enough to ensure a feasible aircraft design. Currently, at the conceptual phase, the *CFD* solution would be a too time-consuming method, but the simple lifting line theory (LLT) can be led to an aircraft design during lift distribution that would be enabled to amendment once the design is needed. According to Anderson and Corda [138], several types of research are conducted with the extension of non-linear effects in *LLT* methods, which begins in the late 1930s. Anderson et al. [214] demonstrated that the leading-edge droop for spin/stall resistance during the non-linear lifting line theory's analytical study. On the other hand, the Vortex lattice method (VLM) is the modernised version of Prandtl's *LLT*[138], which was developed by Falkner[215]. It is refined further using a *MATLAB* code developed by Thomas. The *VLM* used a lattice of horseshoe vortices instead of one horseshoe for each wing; this is the main difference between *LLT* and *VLM* methods. In fact, the *VLM* designs the base on ideal flow theory as known as potential flow. However, the viscous effect is neglected in this method.

The non-dimensional lift coefficient along the spanwise wing is called the lift distribution. This research would be used the *LLT* method planer wing and *VLM* for box wing to predict the aerodynamics parameter and lift distribution along the wing with the spanwise location under the time constraints of conceptual design. The *LLT* and *VLM* are both remarkably accurate technique which has been used for a long time for the lift force calculation. These systems are very simple and only need to consider half of the wingspan and could be extended later to both sides since the wing has symmetrical geometry [33, 163, 216].

Now we need to apply the following technique, step by step: Divide half the span into 18 segments; they should be an equal distance in each segment. The number of span segments can be called N. Compute each angle of span segment. This is a function of lift distribution along the semi-span. Calculate the zero-lift angle of attack and mean segment geometry, wing twist, and twist angle. Then consider the segment lift coefficient by using the corresponding equation. Finally, determine the total lift coefficient by $C_{Lw} = \pi.AR.\ A_1$. In Figure 3.13, the distribution of lift is elliptical, which was desired for the wing design; the lift goes to zero at

the wingtips. Indeed, the lift coefficient (C_L) is 0.2073 (for a half wing), which can generate 10592 N of lift and 16039.58 N for the full planer wing. This application of lifting line theory was conducted using *MATLAB*, and the *MATLAB* code is provided in **Appendix C.9**. On the other hand, in Figure 3.14, lift distribution can be seen for the non-planer wing, which can carry 15072.03 N of lift, it is less than the planer wing lift, though it is produced enough lift to carrying the *EWBA*. All *VLM* code and Tornado menu script with outport results are in **Appendix C.10:**

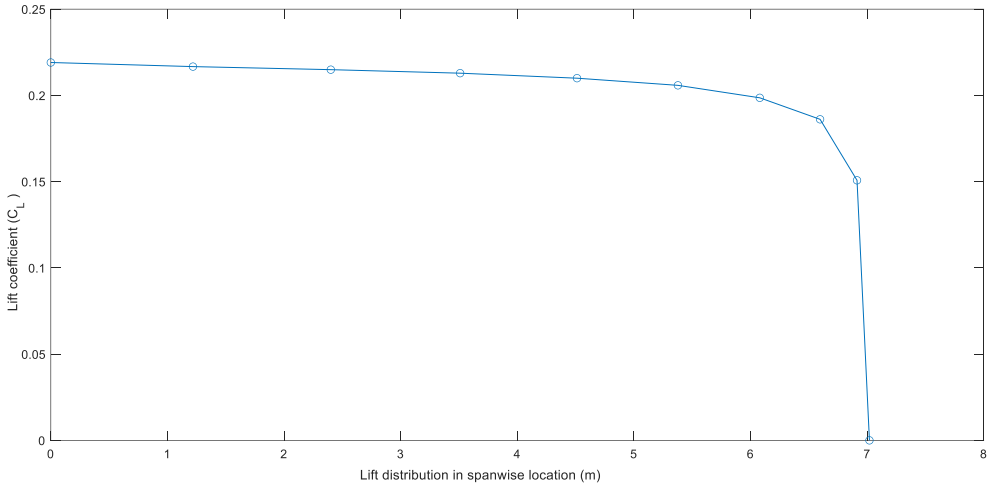

Figure 3.13: Elliptical lift distribution along the half of the planer wing

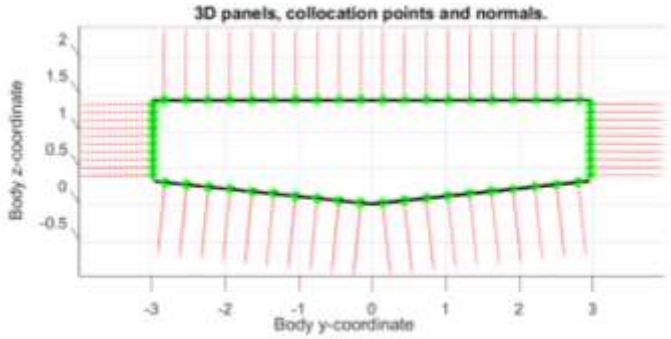

Figure 3.14: Lift distribution along the wingspan for box wing (VLM)

3.5 Tail design parameters

The wing details: *NACA* 23024, wing area, 13.14 m^2; aspect ratio (AR), 7; root chord (c_r), 1.37 m; tip chord (C_t), 1.37 m; mean aerodynamic chord $(\bar{C})$, 1.37 m. For the tail configuration and design, the aerofoil selection method was the same as for the wing design. The function of the vertical tails and horizontal tails along with the wing are together referred to as the lifting surface. The wing generates most of the lift, but the tail fraction also generates the lift. The V-tail volume coefficient was determined as 0.047 [1]. In this research, we are not

interested in a detailed analysis of the tail at this stage. However, in the future, it will be necessary to analyse the *EWBA'*s aerodynamic performance with tails in various manoeuvring conditions. Accordingly, Table 3.4 sets out the relevant tail parameters, while more detailed calculations (with *MATLAB* code for tail design) can be found in **Appendix C.11.**

Table 3.4: Tail parameters

Tail Arm (m)	*V*_tail area (m^2)	*AR*	$MAC_V\ m$	$\overline{V_V}$
4.9	2.20	3	0.8981	0.047

When the tail volume $(\bar{V}_v)$ is increased, the aircraft tends to be more longitudinally stable, and if decreased longitudinally, it becomes less stable [21].

3.6 Flight speed, drag, and cruise performance

This subchapter will deal with a few of the most crucial parameters among the characteristics of aircraft performance. The main focus relates to the flight features of traditional aircraft through the air and response to the four forces of flight, which are governed by a set of equations of motion. This chapter also addresses trim at level flight, the aircraft's climb, and cruise performance.

3.6.1 Trim at level flight

The lift (L), drag (D), weight (W), and thrust (T) or power (P) are the four forces of flight. Figure 3.15 is a schematic depiction of how these forces operate for a level flight in an equilibrium condition[217]. If the aircraft moves from left to right, the velocity (V) of airflow is parallel to the aircraft. Thus, aircraft '*L'* and *'D*' are perpendicular and parallel to *'V'* respectively [36]. Weight (W) always acts down through the centre in level flight.

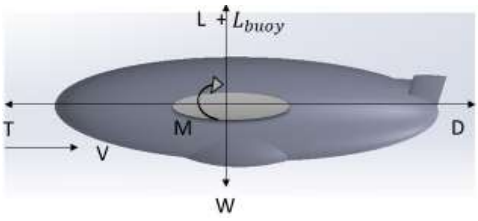

Figure 3.15: Steady level flight in an equilibrium condition

In ideal flight, most of the lift is produced by wings, usually fuselage and tail contribution very small. However, in the case of a hybrid airship, the hull volume generated a

significant amount of lift by lifting gas. Since longitudinal static stability of hybrid aircraft must consider wing lift, buoyancy lift, tail force, and total weight for considering the equilibrium flight[218, 219]. The moment of longitudinal stability of aircraft in equilibrium condition is called trim. Thus, the equation of forces (vertical direction) $W_{To} = L_{Aero} + L_{buoy} + L_{tail}$, where W_{To} is total take-off weight, L_{Aero} aerodynamic lift, L_{buoy}, buoyancy lift and L_{tail}, tail lift. Indeed, the lift is the related angle of attack (α).Therefore, $L_{total} = \left(\frac{1}{2}\rho v^2 S_w + Vol(\rho_a - \rho_{helium})g\right) + \frac{\delta C_L}{\delta\alpha}(\alpha - \alpha_0)$, where, ρ, ρ_a are the density of air, *v*, velocity, *Vol*, hull volume, S_w, wing area, and α_0 camber angle[220]. In the case of the tailplane, the force is responded to as updated and downward as flight condition[89]. The aft surface is playing key responsibility or leverage for static stability to restoring disturbance. It generates a moment arm between the centre of mass and in surface area and preserves the aircraft balance incorrectly. The change of angle of attack will be negative for pitching moment as respect to partial derivative; in the large angle of attack the pitching moment of aircraft lean-to back down. Hence, the tail lift is: $L_{tail} = \left(\frac{1}{2}\rho v^2 S_t\right)\ \left(\frac{\delta C_l}{\delta\alpha}\left(\alpha - \frac{\delta_\epsilon}{\delta\alpha}\propto\right) + \frac{\delta C_l}{\delta\eta}\eta\right)$, where, S_t, tail area, C_l, tail lift coefficient, η, ϵ is elevator deflection and down wash angle for consistently. In fact, the nose-up moment from centre of gravity (cg) is $M = \left(L_{Total\ (Aero+buoy)}\right) x_{cg} - \left(l_t - x_{cg}\right)L_t$, where, x_{cg} is cg distance from datom line, which is after ward the aerodynamic centre (more detail weight balance in **Appendix C.12**) and tail moment arm (l_t). The trim is must be zero for buoyancy lift control flight at cruise flight.

In the trim condition, the pitching moment increased with the increase of α as designed static stability of wing-body buoyancy aircraft. It is longitudinal unstable during nose-up; on the other hand, it is stable if the flight is nose down. Now after differentiating the equation of moment is become $\frac{\delta M}{\delta\alpha} = \left(x_{cg}\left(\frac{\delta L_{total}}{\delta\alpha}\right) - \left(l_t - x_{cg}\right)\frac{\delta L_t}{\delta\alpha}\right)$, where stability derivative is $\frac{\delta M}{\delta\alpha}$ [221]. Moreover, this equation can be a rewrite $\frac{\delta M}{\delta\alpha} = \left(h\left(\frac{\delta L_{total}}{\delta\alpha}\right) + \frac{\delta L_t}{\delta\alpha}\right)$, since static mergin *(h)* ahead of cg position. Further increment of moment, the equation reformatted as h = $\left(x_{cg} - (l_t)\frac{\frac{\delta L_t}{\delta\alpha}}{\frac{\delta L_{total}}{\delta\alpha} + \frac{\delta L_t}{\delta\alpha}}\right)$, now replacing the tail moment arm by the $V_t = \frac{l_t S_t}{cSw}$, wherever the mean aerodynamic chord c and tail volume,V_t. So, the compact static mergin expression can be derived as : $h = \left(x_{cg} - 0.5cV_t\right)$, *h* is must be negative for case of stability of aircraft, sometimes static margin is written $-h$; as a result, positive stability is linked with positive *h* [28, 217, 222].

The longitudinal static stability is mathematically yielded the *CG* for a whole aircraft where the stability is neutral, which is called the neutral point (NP)[220, 223]. Indeed, the distance between *CG* and *NP* is called static margin (h). This static margin is most essential for the longitudinal stability of an aircraft. It is mostly expressed as a per cent of the Mean aerodynamic chord (MAC). For the positive stability or positive margin, *CG* must remain ahead of *NP*; aircraft would be unstable when *CG* is behind the *NP*, and '*h*' is negative. In the following Figure 3.16. illustrated the natural behaviours of an aircraft since *'h*' is different with different pitch disturbances. The stability margin can be made strongly positive $(+ve)$ by moving the cg position forward, which would be given adequate pitch stability and strong resistance to pitch upsets. However, it has some undesirable demerits: extensive annoying pitch trim at different speeds.

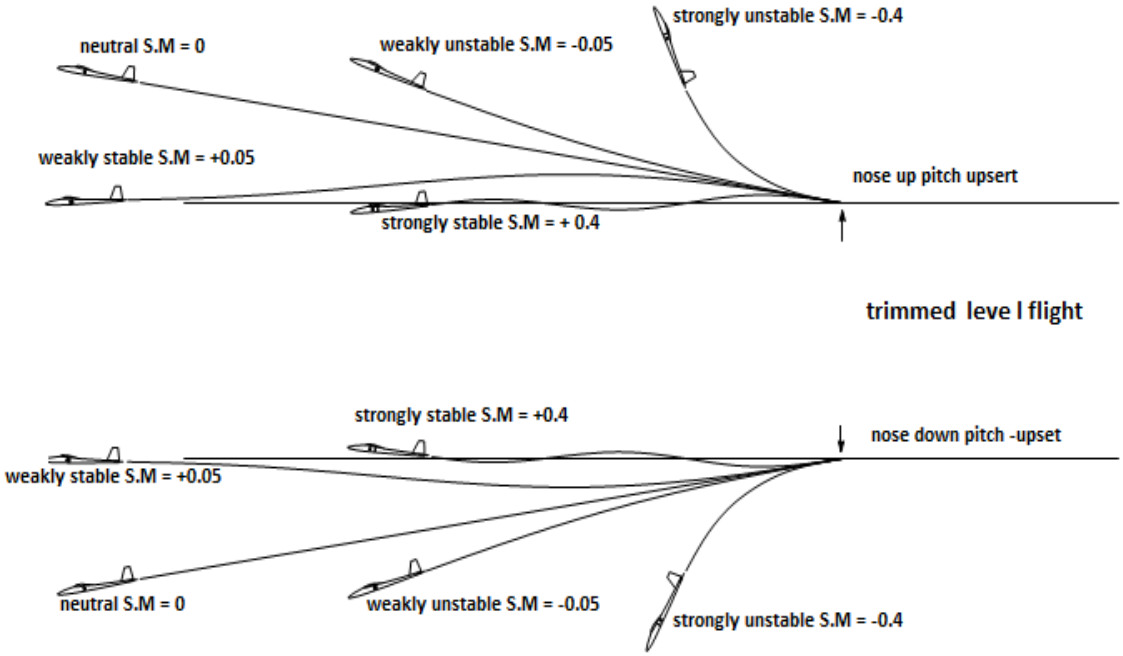

Figure 3.16: Different pitch stability for natural response in pitch disturbances[221]

The handling characteristic of static stability is key for a buoyant aircraft, and the dynamic stability is must essential to fly by a human pilot with ease and cosiness. A statically stable, longitudinal dynamic aircraft can be defined as whether buoyant aircraft enable them to return in a unique position or not. It is true that buoyant aircraft could be statically stable but dynamically unstable. Hence, static stability does not guarantee the dynamically stable for an aircraft. However, dynamically stable an aircraft must be statically stable. Consequently,

longitudinal dynamic stability is important to determine the ability to manoeuvre for a short period and long period longitudinal mode, which is more detailed in **Appendix C.13**.

3.6.2 Cruise model and performance

In steady level flight, there is no acceleration once the climb angle and roll angle are zero. Hence, the governing equation of motion for steady level flight is also consistent with the path being straight. The relationships $T = D$, $L = W$, therefore, illustrate an aircraft at a steady level flight. This chapter will calculate the speed, drag, and flight performance of an *EWBA* at a steady level flight.

Firstly, as discussed earlier, Newton's second law for the equation of motion is simply derived: the force is equal to mass times acceleration ($F = ma$). The speed of sound is $a^2 = \gamma RT$, where $\gamma = 1.4$, the ratio of specific heat of air, gas constant $R = 287.053$ *j/kgK*, T is the temperature at cruise altitude and cruise velocity; $V = Ma$, where *EWBA* was used, $V = 46$ m/s, where M is the Mach number. Thus, the lift coefficient at cruise is (C_{Lc}) 0.31 [33, 171].

More technical details of flight performance are provided in **Appendix C.14**. According to equation 2.7, the drag due to the lift factor $(K)/N_L$ is 0.0523, where $N_L = 2$ is the number of lobes (which was determined empirically from real airship/hybrid airships as shown in **Appendix B.3**). So, $S_{plan} = N_L \times Vol^{\frac{2}{3}} = 47.409\ \text{m}^2$. S_{plan} is called the planform area [224]. Although the exact planform of an envelope is difficult to determine, it could be approximated as above due to its usefulness in progressing the *SWBA* design.

3.7 Frictional coefficient for *EWBA* hull

The characteristic boundary layer is dependent on a non-dimensional parameter called the Reynold number (Re). Hence, the Reynold number of the hull, $(Re) = \frac{\rho VL}{u} = 4.2 \times 10^6$[ρ, air density; V, true airspeed; L, length of aircraft and u, air viscosity]. It is an inertial force in the boundary layer and a frictional force ratio [96, 121]. The flat plate boundary layer (laminar and turbulent) and the transition point were explained earlier in chapter 2.

Using the Von-Karman equation (2.12), the frictional coefficient (c_f) is 0.00338. Therefore, a turbulence model equation was used in this design due to the high Re (4.2×10^6). In fact, the drag coefficient in streamline body 70%−80% of skin-friction drag[60]. So, this expression can be written as $C_{D0} = 1.2 \times C_{Df}$ (C_{Df} is skin friction drag), the C_{Df} can be

considered by equation 2.11 for the airship, for wing body $\left[C_{f\_hull}\frac{S_{Hull}}{S_{ref}} + C_{f\_hull}\frac{G_{gondola}}{S_{ref}} + C_{f\_wing}\frac{S_{wing}}{S_{ref}} + C_{f\_tail}\frac{S_{tail}}{S_{ref}} + \cdots \text{so on}\right]$ with multiplied by form factor (FF). Thefore, according to Thibert and Arnal [225], the drag assessment is an essential part of the design schemes and consist of the wave drag projection, viscous drag, and vortex-induced drag, which influencing approximately 50% of the total drag at cruise flight. However, the viscous drag is often achieved by form factor (FF) and flat plate theory once the transition location is known. Indeed, C_f is dependent on the wetted area of each component and this wetted area of each component is reflected as a flat plate as mentioned in earlier chapter 2. Hence, this approximation technique is relied upon a precise experiment result of the C_f. Figure 3.17 shows that skin friction decreases with an increase of *Re*. Figure 3.17 also shows the function of Re where typical length is taken into account from the nose as the leading edge to the end of the fuselage as the trailing edge of the *EWBA*. Thus, C_f is moderately acceptable, with reference to Table 3.5, which lists the values for relevant aircraft. It is clearly shown that the *EWBA*'s C_f (0.005077) is comparable to the skin friction coefficients for civil transport aircraft [33, 171, 181], as follows:

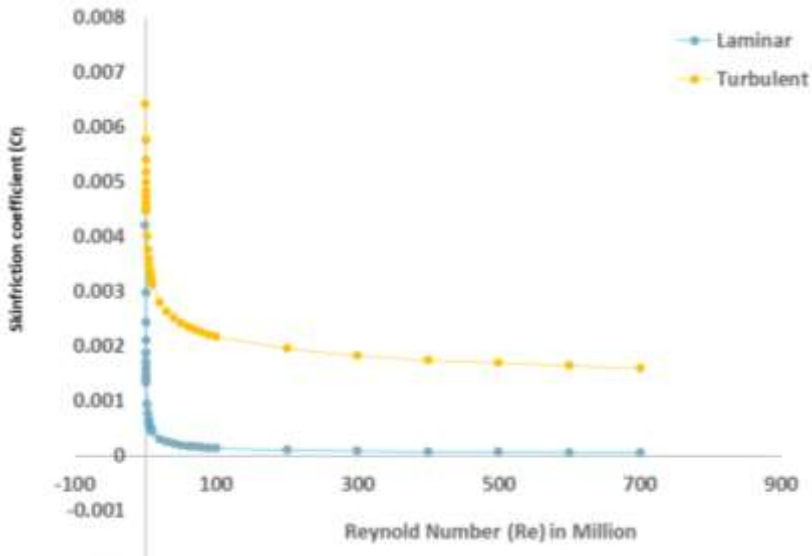

Figure 3.17: Skin friction coefficient vs Reynold number

Table 3.5: Equivalent skin friction for different aircraft [171]

Aircraft	C_f
Bomber and civil transport	0.0030
Military cargo (high upsweep fuselage)	0.0035
Air force fighter	0.0035
Navy fighter	0.0040
Light aircraft single-engine	0.0055
Prop seaplane	0.0065
Jet seaplane	0.0040
Prolate spheroid 6:1	0.00199
Airship (tail model)	0.00434
Planner wing airship	0. 00555
SWBA (Smart wing buoyant airship)	0.00496

Thus, it is concluded that the measurements of C_f with a different large range of *Re* match the prospects of Van- Karman well enough for extrapolation purpose of skin friction (C_f).

Now, the form factor *(FF)* of body drag can be calculated using the equation *(FF = 1+1.5/*$(FR)^{\frac{3}{2}}$ *+ 7/*$(FR)^3$*,* where *FR* is the fineness ratio[1]. This method is also used for obtaining the *FR* for other major parts (wing, tail, and gondola). Prior researchers Takahashi et al. [226] argued that an infinitely thin symmetric wing's the *FF →1* as a function of limit at zero *AOA*. Sergey et al.[227] also said, it is a useful mechanism to keeping data (drag) record and correction in the design schemes cause of large separations of Reynold number (Re) on impacts of skin friction drag. Additionally, the theoretical calculation of *FF* is usually used as the basis of the empirical zero-lift drag method, which apparently establishes their ancestry as mentioned by Hoeroner [60], it typically functions of aerofoil thickness. This model includes two conditions such as a proportional to aerofoil thickness ratio $\left(\frac{t}{c}\right)$, secondly, proportional to fourth power of $\left(\frac{t}{c}\right)$, and the matmatical form as *FF= 1+ 2* $\left(\frac{t}{c}\right)$ *+ 60* $\left(\frac{t}{c}\right)^4$. Mostly, the traditional *FF* model are fuction of aerofoil $\left(\frac{t}{c}\right)$, wing, fuselarge or hull similar to Nicolai model [1, 60, 65, 171, 179, 183].

The hull wetted area is 167.12 m^2 and the volume $(Vol)^{(2/3)}$ is 23.70 m^3 (all geometrical parameters and details are given in **Appendix C.15**). Now, for the computation of the total zero-lift drag coefficient (C_{Do}), we consider only the aircraft's major parts (hull, wings, tail,

and gondola). In addition, the C_{Do} for an analytical model of *EWBAs* is determined to step by step using the components build-up method, which is set out in **Table 3.6**; the estimation of total C_{Do} is also provided in **Appendix B.4**, as component drag coefficient.

Table 3.6: Drag coefficients for different components

No	Component	C_{D0}
1	Wing	0.0021
2	Hull	0.00238
3	Nacelle	0.0091
4	Tail	0.00088
5	Gondola	0.00072
	Total (C_{D0})	0.01518

So, by the build-up technique, the overall C_{D0} is the sum of the C_{D0} of the individual aircraft components and factors. Infect, it is a traditional preliminary design method based on wetted areas. However, the zero-lift drag (C_{D0}) drives from skin friction drag coefficient (C_f), form factor (FF), and interference factor. There is no lift produced at a subsonic flight. The C_{D0} is considered constant value at sea level and during the aerodynamic investigation of this research. Therefore, C_{D0} is 0.01518 as per equation 2.13, where *Kc* = the correction factor 1.05, taken from the case of a glider [1, 171] (see **Appendix C.16** for a useful schedule of correction factors for different aircraft). Basically, C_D is increased with increases of altitude due to kinematic viscosity; it is a ratio of dynamic viscosity and air density. On the other hand, the rate of density decreased significantly greater than dynamic viscosity while the dynamic viscosity increased at altitude. So, kinematic viscosity increased exponentially with altitude, which may consequence of overall C_{D0} increment, regardless of individual Mach number (MAC). Though, real possessions are to be reflected for an actual force that acted upon the object of aircraft. For the buoyancy of the plane, we need to calculate the lift coefficient for the *EWBA*: $(C_{L.buoy})=\frac{L_{buoyancy}}{\rho_a g V_{ship}}$ ∴ C_L buoyancy = 0.84 and aerodynamic lift ($C_L$aero): $\frac{L_{Aero}}{\frac{1}{2}\rho_a V^2(S_{aero})}$, (at altitude 4000 m for a density of 0.82) $C_{L_{aero}}$ = 0.291, where, R_F is a function of the hull variable and is equal to 0.001478 by equation 2.20. It is ignored in *EWBA* design due to the hull volume being invariant, and the value of R_F being quite small.

Therefore, the total lift coefficient is $C_L = C_{Lbuoy} \times R_F + C_L aero$ = 1.15 by equation 2.20. The further aerodynamic characteristic of wing buoyant aircraft investigation will focus on the aerodynamic performance by the computational fluid dynamic (CFD) of all configurations. Indeed, the wing planform area has been considered for the configuration of wing buoyant aircraft since aerodynamic efficiency significantly relies on it. However. The total drag coefficient can be measured by looking at equation number 2.21 as $(C_D)_{total}$ = 0.02072 for planer wing, where C_L mid = 0 and *K* is 0.0523, calculated by $K = \frac{1}{\pi e(AR)}$, Oswald (e) factor 0.869, estimated from (e) =1.78× $(1 - 0.045AR^{0.68})$ – 0.64, due to straight wing buoyant aircraft. But $(C_D)_{total}$ = 0.0187 for box wing, where *K* is 0.0147 and (e) 1.443 as Prandtl Bi-plane theory [65, 171, 173, 181]. Since the drag is 236.2 N at cruise and 352.86 N at sea level for the planer wing. However, the drag 213.175 N, 318.4328 N at cruise and seal level in order to box wing buoyant aircraft, where, $q_\alpha = \frac{1}{2}\rho V^2$. Thus, the maximum efficiency is $\frac{L}{D} = \frac{C_L}{C_D}$ = 14.96 for planer wing aircraft and 16.577 for box wing or efficient wing aircraft, which is a significant improvement of *EWBA*'s efficiency by rationally. Hence, the consequences of buoyancy and aerodynamic efficiency become 24.36 and 43.43 for planar buoyant aircraft and box wing buoyant aircraft, respectively.

3.8 Range and SFC

The total flying distance between take-off and landing of a powered aircraft for the full volume of fuel is called range (R) and as equation $R = 8808 log_e\left(\frac{W_{start}}{W_{end}}\right)$, where W_{start} = maximum all-up weight = 1202 kg without considering buoyancy, W_{end} = zero fuel weight = 691.15 kg (landing heaviness) and more details are in Appendix C.18, the *R* = 2116.84 km, and Fuel Specific $(SFC) = 0.8\ \frac{lb}{h\ hp}$; *SFC* is assumed to be 0.8 for a piston engine due to its more efficient and economical than a turboprops engine for small aircraft. (see Table 3.7) [178, 179]:

Table 3.7: *SFC* for various piston engines

No	Engine Type	SFC in cruise	SFC in loiter	Units
1	Turbojet	0.9	0.8	lb/h/lb
2	Turboprop	0.5 -0.8	0.6-0.8	lb/h/lb
3	Piston (fixed pitch)	0.4- 0.8	0.5- 0.7	lb/h/lb
4	Piston (variable pitch)	0.4-0.8	0.4-0.7	lb/h/lb

$$= 0.8\,\frac{lb}{3600s\times\left(550\frac{lb\,ft}{s}\right)} \quad = 4\times 10^{-7}\ ft^{-1}$$

3.9 Take-off and landing performance

Take-off can only begin once the speed of *EWBA* is equal to or greater than the aircraft's stalling speed. An aircraft is accelerated along the runway to achieve the take-off speed (V_{T0}). Hence, before take-off, the aircraft must cover a certain distance (called the take-off run). Similarly, the lift must be close to landing weight once an aircraft comes to land. Thus, there is a touch-down velocity (V_{T0}). While the aircraft is on the ground, it must cover a certain distance (called the landing distance) before coming to a stop. The typical take-off and landing performance of the *EWBA* are fully considered when it is in the air and steadied. The analysis of take-off and landing is detailed in **Appendix C.17.**

There are three phases in the take-off: ground run, transition, and climb. In the transition phase, the *EWBA* interchanges along the tracks and seeks to achieve a steady climb. The take-off phase is completed when the *EWBA* achieves an altitude that is equal to screen height.

3.10 Flight endurance

The fuel consumption of a piston engine and turboprops engine is proportional to the power in steady level flight conditions. The endurance (E) for a propeller-driven aircraft [33, 36, 171, 178] by the Breguet equation is 74.607 hrs or 3.108 days, which is a desirable level; more detailed calculations are given in **Appendix C.18** (Range) and endurance *E* **Appendix C18.1**. However, by these equations, maximum endurance can be achieved for a high propeller efficiency (more details about propeller performance as shown in **Appendix C.19**), brake-specific-fuel-consumption $(BSFC)$, and high weight of fuel available, and maximum lift to drag ratio.

3.11 Summary

The initial novel *EWBA* design concept is developed based on distinctive tools to wing hybrid airships and approaches the desired specifications. The design offered great geometrical freedom in constraint to explore an *EWBA*, other factors, and related analysis. After several iterations of the preliminary design in *MATLAB*, the *MTOW* of 1202 kg was calculated using an iterative method. This preliminary design has an empty weight fraction of 0.5759, which is in good agreement with the values for similar kinds of conventional aircraft, as shown in Table

3.2. Thus, the empty weight value is appropriate for the propeller-driven *EWBA* since it is heavier than air (HTA) Vehicle.

During initial sizings, the requirements were: wing loading 18.694 lbf/ft^2, power loading 15.98 lbf/hp, wing area 13.14 m^{2,} and estimated power 165 hp. In addition, the net weight (Δw) is used 607.63 kg in *MATLAB* due to the *EWBA* having a 49.36% buoyancy lift and the buoyancy ratio (BR) is 0.4936. Indeed, this 49.36% buoyancy lift comes from lifting gas, typically helium (He). Since the analytical results show that 577.05 m^3(25.73 kilomoles) helium can lift approximately 5830.69 N of total weight, the lifting capabilities are linear, and that would be costs come once a life. For this design, helium is selected as the ideal lifting gas because it is safe, non-toxic, and non-flammable. Therefore, the *EWBA* requires only 50.64% aerodynamic lift, whereas traditional aircraft need a 100% aerodynamic lift. These [fossil] fuel savings contribute to making *EWBA* potentially a more economical and environmentally friendly vehicle.

Furthermore, in traditional aircraft, the primary function of a wing is to generate the lift. This lift is mainly generated by a special cross-section of a wing called an aerofoil. The aerofoil can be specified in two ways: custom design or a systematic selection from existing designs. This research opted for the selection method because computationally designed aerofoils are prohibitively expensive and time-consuming and also require verification through wind tunnel testing. Therefore, the *NACA* chart was used to identify aerofoil designs that meet current requirements in terms of the ideal lift coefficient and the maximum lift coefficient.

In the comparison process, *NACA* 23024 proved to be one of the most promising aerofoils when considering the lift and minimum drag; it also fulfils safety requirements (see Figures 3.7 and 3.8) during the stall. Moreover, Figures 3.11 show that the drag coefficient is 0.0088 at 0^0 *AOA*, which is reasonable compare to the other aerofoils. Likewise, in Table 3.3, the *XFLR5* results are agreed with experimental results: $C_{lmax,}C_{do}$ and C_{mo}; since one of the best values among the five aerofoils. Overall, *NACA* 23024 is a superior aerofoil with the base on the lift, efficiency, speed, and lowest drag. These investigations were conducted using *XFLR5*, an upgraded version of the *XFOIL* tools.

Furthermore, in the wing design process, lift and load distribution were investigated after several alterations, such as wing twists. The lifting line theory (LLT) produced a remarkably perfect output of the lift coefficient, which is 0.2073. The lift coefficient of 0.2073 can generate 10592 N of lift (planer wing), and the non-planner wing developed 0.291 vortex lattice method *(VLM)* 15072.03 N (non-planer wing) as shown in *MATLAB* application.

According to these data, the wings are capable of lifting the 1202 kg weight of the aircraft. However, it should be noted that the analytical results indicated that the lift coefficient was 0.289. Thus, there was an error rate of 0.689 %, 28.26% with *VLM* and *LLT* respectively, which is in good agreement with the theory due to the high lift device was ignored in analytical results. Also, as Figure 3.13 clearly shows that in the wing lift distribution becomes zero at the wingtips. As a result, the distribution of lift is elliptical, as required. This aircraft is statically and dynamically stable, which has been shown in **Appendix. C** 13. Indeed, throughout the investigation of wing lift distribution, we considered one half of the wing without considering other contributions since the wing has asymmetric geometry. Overall, the wing airship has been offered a performance advantage compared to the wingless airship. Hence, this chapter has been considered all intellectual major pivot points of a conceptual design of a wing airship.

To sum up, one of the effective methods is the iterative method, which widely accepted approach for traditional aircraft design in the conceptual stage. So far, yet to apply in hybrid wing airship for the conceptual design phase. It is started from mission profile, aircraft weight fraction and followed to evaluate the weight of the aircraft. The wing loading, power loading can be estimated by *MATLAB* from the design point; they can find the required wing area and power. This influential iterative method, particularly useful for the approximation of weights, sizes, and performances of aircraft. However, sometimes airship design is not considered an engineering approach due to a lack of literature and method for sizing an airship or hybrid airship. Thus, it is a very simple, time-efficient and economical scheme that allows a designer to modify or evaluate their design and resulting data in a short time.

Chapter 4. Computational Approach and methods Verification

4.1 Introduction

The Computational Fluid Dynamics (CFD) has been significantly advanced and regularly applied as a design tool for optimising aerodynamic performance over the last few decades. In fact, an understanding of flow separation over the surface of the solid objects is crucial for certifying in regard to operational safety issues of traditional aircraft. This investigation of the flow over a 6:1 prolate spheroid has been used as a validation of *CFD* methods. Hence the researchers have exposed that the interaction between vortices around the prolate spheroid, where the maximum length (L) of the body are 1.372m and diameter 0.2268m with a finite ratio (FR) 6:1. The investigation also concentrates on an appropriate application of the *CFD*, validating current schemes with respect to existing methodologies, turbulence modelling, and mesh resolution for flow simulations.

The *RANS (Reynolds-Averaged Navier-Stokes)* as a turbulence model is a still key engineering approach for numerical simulations. Though the *RANS* equation has some drawbacks to afford turbulence data in high angle of attack and for a large scale unsteady flows since affected by a large magnitude of the force as according to the prior researcher, Rhee, and Hino [228], Amiri et al. [229]. Indeed, the number of studies [85, 230-232] *LES* (large eddy simulation) was used on the flow past a prolate spheroid as alternative turbulent approaches for the aerodynamic investigation, for example, Watt et al. [233, 234], he found the most useful numerical simulation scheme is *LES*. It is solved computationally, while the existing small-scale flow may be solved by modelling. Though *LES* has certain disadvantages in large volume calculation. However, the computation of *LES* is abridged to a convinced level compared to *DNS* (direct numerical simulation). Later, Watt [233] also investigated a prolate spheroid using the *DES* (detach eddy simulation) method to study the flows around a cylinder. The point of view from this author [233] is that the *DES* method might be good enough to simulate the propagation of strong flows around a circular cylinder during the inverse pressure gradient. But, on higher *AOA* at 20^0, the separation of the flow around a prolate spheroid is very poor. So, the *DES* method is not as good as an advantage for this *CFD* simulation of 0^0 to 20^0 *AOA*. Jiang et al. [235, 236], a 6:1 prolate spheroid were used *DNAs* in his flow simulation with *Re* numbers at 1000 and 3000. He found that in the near wake section, the wake vortices are stable and allocate symmetrically at *Re* number 1000. Though, the asymmetric vortices have appeared

in the middle of the wake region. On the other hand, a strong asymmetrical wake vortex was developed in the near-wake region at *Re* number 3000, since the pair of a near reverse vortex is decomposed toward a small scale vortex, but the rest is conveyed into the spiral vortex form. The laminar flow has become the transition flow in the wake region. At a *Re* number 3000, 75% of the drag force was accounted for a strong lateral force as resulting in asymmetrical pressure distribution. Khoury et al. [237, 238], also scrutinised in *CFD*, at a *Re* number 10000 and *AOA* 100^0 for a 6:1 prolate spheroid, and the resulting flow simulation was showed that the shear layer impregnates in the form of turbulence from the beginning of separation. Wikstrom et al. [230] and Fureby et al. [85, 232] explored that the case of feasibility, the *LES* method is considerable for higher *Re* numbers, where were simulated the flow around a prolate spheroid at $Re = 4.2\times 10^6$. On the other hand, an experiment was conducted by Granlund [239] at $AOA < 6^0$, in steady-state flow, with this small *AOA*, the force and torque were linear. In the lee side region, cross flow separation appeared and shears into a vortex roll-up since an *AOA* increased. If as *AOA* increased, the centre of pressure moves invertedly, and unsteadiness increases; since the leeward region's vortex lift force of the ellipsoid is in the maximum limits. Also, many pieces of experimental research have been conducted at Virginia Polytechnic Institute to scrutinise the turbulent flow over 6:1 prolate geometry at different angle of attack[73, 84, 240]. But experimental flow visualisation at *AOA* in around axisymmetric bodies requires more details investigation to measure each local variable, which is time consuming and expensive process. However, *CFD* can be provided higher level of exact results, whereas it is tough to get in experiment.

Furthermore, the Reynolds stress turbulence models (RSM) produced significantly better results than the isotropic eddy viscosity base on the turbulence model. For instance, lift force, drag force, local skin friction, and variables as observed in the previous researcher [241, 242]. Though, the *RSM* models enhanced the performance of *RANS* simulation noticeably. However, a significant difference still could be detected between experimental and computational results. Indeed, the current developments of *CFD,* especially for steady-state flow simulation around the *EWBA*, still need to be comprehensively considered for validation of the sophisticated *CFD* method during design.

Moreover, the *CFD* is also significantly used for the enhancement of *LTA* vehicles during design. Suman et al.[125, 243] considered a bare hull of the ZHIYUAN-1 stratospheric airship [2] by the unstructured *TAU* solver of *DLR*. They also employed the *RANS* equation in their simulations and fixed the transition point via suppressing the turbulence model in the laminar

area. The grid sensitivity studies at the location of transition revealed a reduction in drag up to 75% of the length (L) once it moved downstream, because of existing laminar flow. Subsequently, the drag developed as a distance of that point and flow separated. At the *AOA* up to 5^0 , the computational results with an attached transition point at 52%L reasonably agreed upon the experimental results. A prior researcher Dumas et al.[244] offered an airship preliminary concept in the *MAAT* (Multibody Advanced airship for transport) project of *CFD* studies for an open volume scheme. Indeed, the case of validation and advancement of numerical approaches associated with *LTA* vehicles and the prolate spheroids have been widely adopted. Several pieces of literature have been published for a 6:1 prolate spheroid of experimental data [73, 84, 229, 240] with an inclusive series of flow conditions and a 3:1 prolate spheroid[245]. Therefore, this research decided to use the $(k-\varepsilon)$ and *RSM* equations during the investigation of the aerodynamic performance of *EWBA*, especially in the cruise condition at a different angle of attack and compared with experimental results of 6:1 prolate spheroid as validation of *CFD* methods.

4.2 The solver selection

An *ANSYS Fluent* solvers are applied to produce the results in this research. The *ANSYS Fluent* turbulent solver offered the outline to attain the results in the next chapter 5. The commercial *CFD Fluent ANSYS 16.1* tools are available at the University of Sheffield with the integration of properties of an intuitive *GUI*, pre-processing, and post-processing program.

4.2.1 Method validation

During the validation of the method, the 6:1 prolate spheroid was employed. First of all, a 6:1 prolate spheroid designed in CAD software *(Solidwork)* which Length (L) 1.372m, aspect ratio 6:1, maximum diameter (D) 228.6 mm, most rear (r) 38 mm, which in the following Figure 4.1:

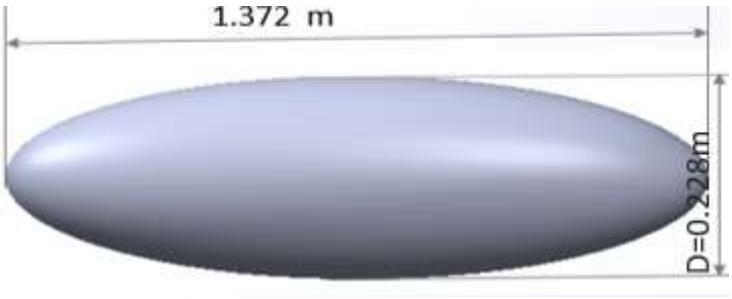

Figure 4.1: 6:1 prolate spheroid CAD model

Then a structure and unstructured *ICEM* mesh was created, where 40 million and 15 million grid cells were adopted accordingly, as can be seen in the following Figure 4.2(a) and Figure 4.2(b), however, in Figure 4.2 (a), structured grids with 40 million cells are used as a contrast. The diameter of a fluid domain is 12.96m in all directions from the centre. Indeed, the *CFD* simulation run at 4.2×10^{6} Reynolds number based on prolate length with the Mach number 0.135, pressure outlet and velocity inlet is set as a boundary condition. The *RSM* and $(k-\varepsilon)$ are employed as the turbulence models.

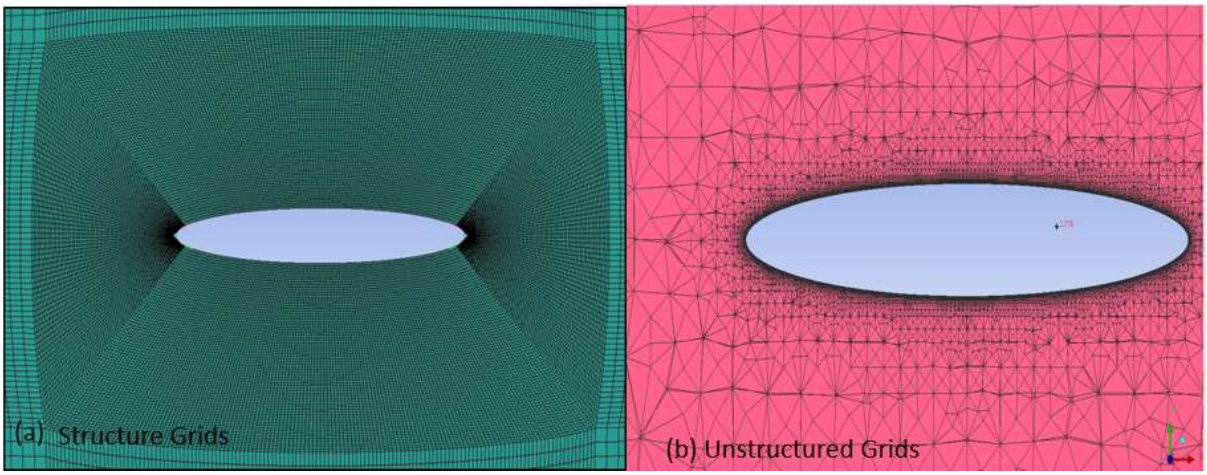

Figure 4. 2: (a) Structure grids and (b) an unstructured in *ICEM*

In Figure 4.3, At *AOA* over the 10^{0}, fluid flow is separated from the surface of the prolate spheroid in two different lines, called the primary and secondary separation lines. In fact, over 20^{0}AOA, the 6:1 prolate spheroid has been observed the local skin friction distribution in regarding to surface roughness. The prediction of skin friction coefficient is carried out using *RSM* in Figure 4.3 (a) for structure mesh with 40 million grids and $(k-\varepsilon)$ in Figure 4.3 (b), for unstructured mesh with 15 million grids, in two different turbulence models, which can be seen in skin friction contour (Figure 4.3), there are no significant differences between them. Both results also strongly agreed with the experimental results of Chesnakas et al. [73].

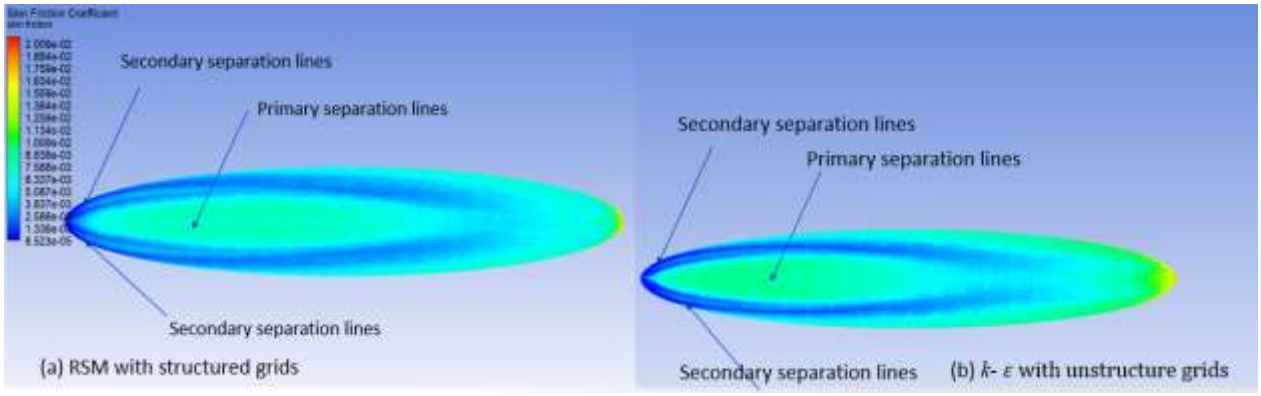

Figure 4.3: Demonstration of Skin friction coefficient distribution over the prolate at 20^0 AOA

Figure 4.4 has also shown the primary and secondary vortex, whereas the secondary vortex is closed to the surface. Mainly the secondary separation line, in terms of a detachment of a secondary vortex at 20^0 *AOA* and location of x=77%L. These simulation results have been obtained by structure grids for 40 million with *RSM* turbulence model in Figure 4.4 (a), and Figure 4.4(b) unstructured grids for 15 million with *k-ε*, in two different turbulence models. It is obvious that structure results in little fineness than unstructured grids, but vortices are more elaborated in unstructured grids. On the other hand, the structured mesh is also a time-consuming process in *ICEM.* Though, this numerical visualisation results significantly agreed with the experimental results of Chesnakas et al. [74] and Wetzel[240].

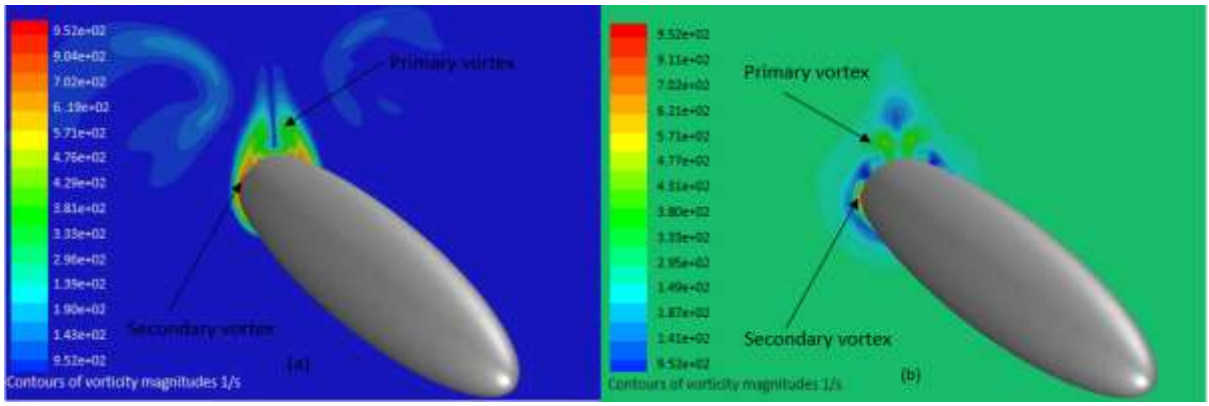

Figure 4.4: Prediction vortex over the prolate spheroid at 20^0 AOA and location x=77%L with (a) structured in *RSM* and (b) Unstructured in $(k - \varepsilon)$ models

In Figure 4.5, the precise flow estimation can also be revealed the pressure coefficient (C_p) distribution on around the surface, at 20^0*AOA* of the spheroid, the *CFD* results revealed that C_p was $-2.0, -2.8, -7.5$ and -1.6 at $45^0, 90^0, 135^0, 180^0$ of azimuthal position in accordance with $\times 77\%$ L. A second vortex also was occurrences at nearby to the spheroid surface of $\times$ 77% L at 20^0 *AOA* that leads to a drop in pressure. So, it was a perfect agreement with the experimental data offered by Wetzel et al. [240]. On the other hand, in Figure 4.6, the

skin friction coefficient (C_f) were employed for comparison of *CFD* results with the experimental results by Chesnakas and Simpson [84] and Chesnakas et al.[73]. Figure 4.6 offer helpful information about fluid flow behaviour at azimuthal distribution over the prolate spheroid for the axile location of $\times 77\%$ L at 20^0AOA. The *CFD* results of C_f, at 90^0 and 150^0 of azimuth were followed the experimental results, and it is reasonable to agree with experiment data [73, 84] since windward side flow is laminar. Evan though, the differences were spectacular from 150^0 to 180^0 on leeward side of the prolate spheroid for both numerical results compared to experimental results since flow is highly vortical and susceptible. Yet, the C_f is unfortunate to assess for each one of two numerical model, even experimental predictions were contained unchartanity[246]. Furthermore, the experimental results near the attachment line at this azimuthal location (150^0 to 180^0) are extra typically higher that can not be justified by a turbulent boundary layer since such boundary layers never tolerate the C_f based on edge velocity over 6×10^{-3} and it is near to free steam velocity, even not by a laminar boundary layer at current *Re* number. Hence, the *CFD* results of C_f data was obtained lower than experimental data. In fact, in the prior researcher [247] were attained very similar results as obtained as peak to peak difference. But they were used *RANS* and *DES* for Spalart-Allmaras as a different turbulence model.

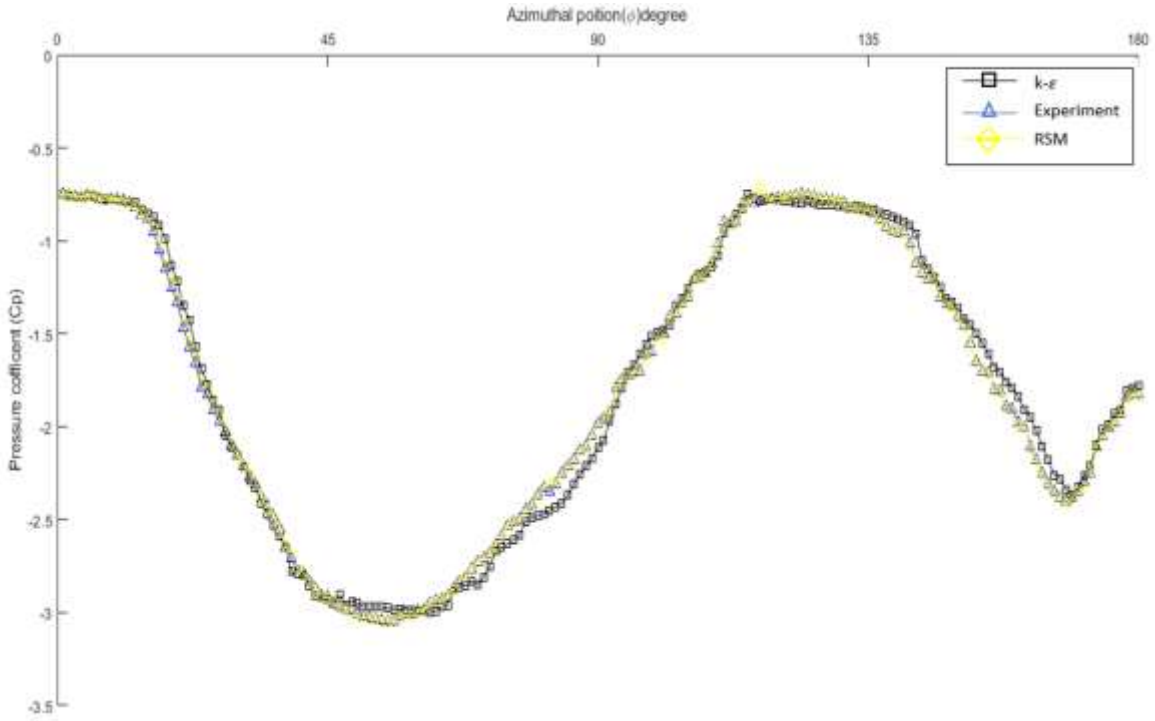

Figure 4.5: The comparison of pressure coefficient distribution in different Azimuthal locations at X=0.77% on $\propto = 20^0$ with Wetzel et al.[240].

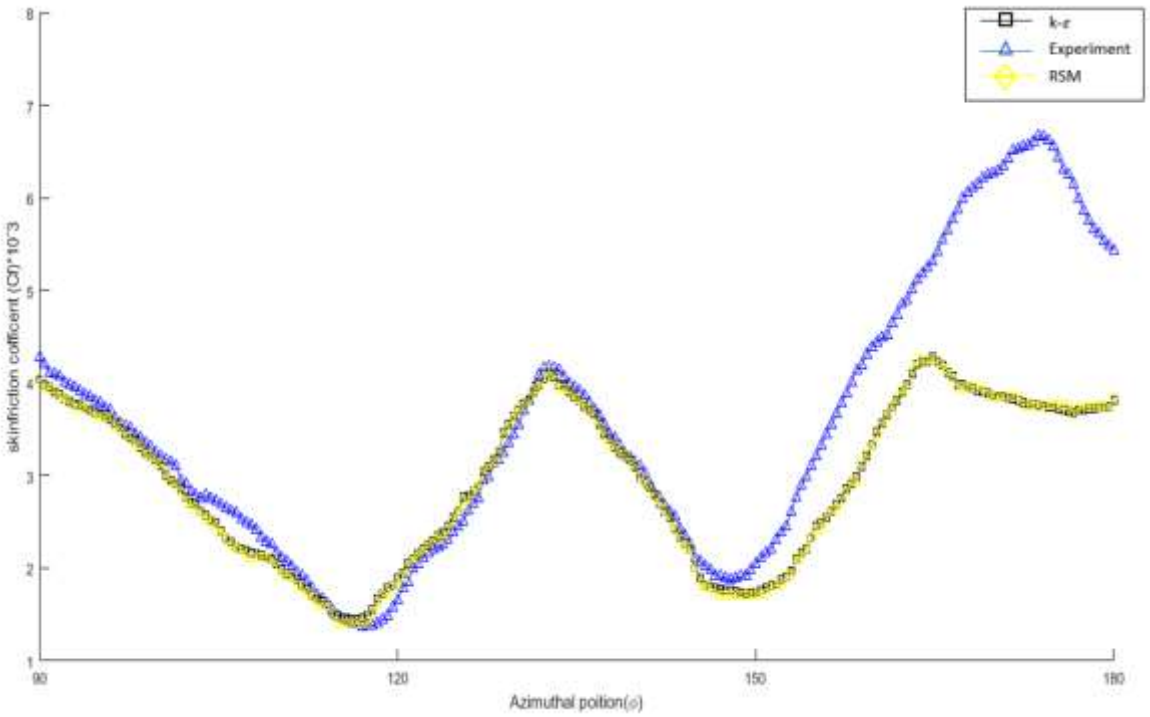

Figure 4.6: The comparison of Skin friction coefficient in different Azimuthal location at X= 0.77% on $\propto = 20^0$ with the experiment [73, 84].

Steady-state flow cases, in the following Figure 4.7, Figure 4.8, shown that the lift coefficients (C_L) and drag coefficients (C_D) at the function of different *AOA* between 0^0 to 20^0, it is represented the prolate spheroid simulations respectively. Currently, the *3D* set of replications is only conducted in this research. Noted that in Figure 4.7 has been shown as *AOA* increased, the lift coefficient increased with non-linearly, where the minimum lift coefficient of -0.0115 for $(k-\varepsilon)$, -0.0195 for *RSM* at 0^0; maximum lift coefficient of 0.128 in $(k-\varepsilon)$ and 0.138 in *RSM* at *AOA* 20^0, which is yet to separate due to airflow still attached to the surface. On the other hand, the drag coefficient increased precisely in the same manner in Figure 4.8, where 0.015 in $(k-\varepsilon)$, 0.019 in *RSM* and 0.017 in experimental data at 0^0 *AOA*, which is not a pretty big difference compared to numerical results, and it is in an acceptable region.

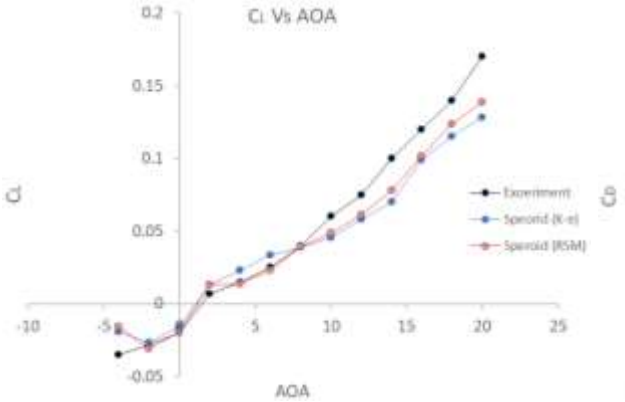

Figure 4.7: Lift coefficient Vs *AOA*

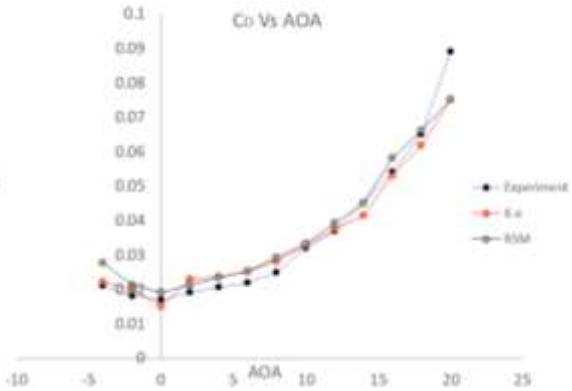

Figure 4.8: Drag coefficient Vs *AOA*

The evaluation of numerical data shows good agreement with the experimental results of Chesnakas et al.[74] and Wetzel [240], in the case of lift coefficient, drag coefficient, as well as skin friction coefficient, and pressure coefficient. Therefore, it is an encouraging result for onset location of the transition model.

4.3 Summary

In the current study, flow passed over a 6:1 prolate spheroid at different *AOA* for Reynolds number 4.2×10^{6}, which was investigated using the Raynolds stress model (RSM) and $(k-\varepsilon)$ with structured and unstructured grids. The precision of both results was observed with the experimental data of Chesnakas et al.[73] and Wetzel[240]. Hence, the present method is performed very well in the prophecy of an aerodynamic external flow phenomenon over a prolate spheroid. However, structured grids are quite an economical and time-consuming process during *ICEM* mesh. But, an unstructured mesh could be produced similar results with less afford in minimal time. That is why this research will use unstructured mesh for further investigation of the aerodynamic performance of $EWBA$. Thus, the current scheme can be used to predict the three-dimensional turbulent fluid simulation and fluid separation analyses behind various typical *3D* models.

Chapter 5. Numerical Characteristic of Computational Aerodynamics model (CAM)

5.1 Introduction

The aerodynamic performance of the *EWBA* model was analysed using the *Fluent* via *CFD.* Generally, *CFD* is a branch of computational fluid mechanics that offers a cost-efficient natural flow solution of the numerical governing equation. It is called a Newtonian fluid governing equation, specifically the Navier-Stoke *(NS)* equation. Joseph [248] observed that it is a common practice to design *CFD* aerodynamic models with the Reynolds Average Navier-Stoke ($RANS$) equation which plays an instrumental role in this computational research; more details were discuses in **Chapter 4**.

Furthermore, Tomas et al.[249] also argues that the differentiation of the primary equivalence system is converted to the arithmetical equation, and then a numerical solution is obtained digitally. *CFD* is playing an increasingly crucial role in advancing state-of-the-art aircraft designs and is one of the most advanced engineering tools for research [156, 249]. In fact, it is used for numerical analysis and algorithms to solve and analyse the flow problems, the interaction of liquids or gases through surfaces defined with boundary conditions. Hence, the most important requirement to obtain precise results in *CFD* is the meshing quality: more details about meshes follow in the section on mesh generation.

According to Singh [250], the drag is proportional to the square of velocity on moving transport, so aerodynamic drag is a highly significant factor for an aircraft during flight. Thus, *CFD* is employed in the numerical optimisation of aerodynamic parameters, for example, lift coefficient (C_L), drag coefficient (C_D), and Moment coefficient (C_M), for aerodynamic performance estimations.

In the current research, the Ansys Workbench Fluent code has been used for the investigation of numerical results, using the *RANS* equation of *k- ε* model and Reynolds stress model (*RSM*) since *EWBA* is complex geometrically and higher Reynolds number (Re). In fact, both of these equations are designed specifically for aerospace applications involving flow over the surface boundary layer. Indeed, the *k- ε* model is proposed for wall-bounded turbulent flows [144], for a free shear layer, and in limited geometries. These eddy viscosity are well-

known in aerospace industries for aerodynamic investigation as long as flow stays with surfaces [251]. However, the Reynolds stress model (RSM) is applied to compare the *k*- ε results near the wall treatment. The *RSM* transport equation is a combination equation of Reynolds stresses and Menter's *BSL*- ω equation yields as a consistent form of the Stress- ω model by Wilcox, near the wall, the ε -bassed *SSG* model; it offers advanced prophecies of flow separation in adverse pressure gradients [252]. Thus, it offers exceptionally well accurate predictions of flow separation. Therefore, the model is significantly valuable for *EWBA* and a lifting body airship in the external flow problem's aerodynamic investigation. It is particularly beneficial for these studies since the *Re* is higher in *EWBA.*

5.2 *EWBA* design and modelling

This chapter contains the following three sections:

1. Pre-processing:
    - 3-D model design in Solidworks
    - Design modeller in the *ANSYS Workbench*
    - Meshing the aircraft model in the *ICEM CFD.*
2. Solution: analysis with the *CFD* package *ANSYS Fluent.*
3. Post-processing: various visualisations analyse the results and compare the analytical results.

5.2.1 Pre-processing in *CFD*

In the design process, the missions including the design model, meshing, and philosophies, before starting the numerical solution process, called pre-processing. In fact, the final solid model was designed after several iterations in the *CAD* device. The key objectives were to improve the design object's quality with minimal surface roughness for the frontal area of the hull and enhance the lifting surfaces as the wing, using computational design tools. Generally, the proposed *EWBA* model was designed via a user-friendly *CAD* software-based computational tool called Solidworks (2016). These were then designed updated in Solidworks (2018) and saved in a step file, and then exported as an *IGES* file, as a standard and widely accessible type of baseline file. All the design aspects, requirements, and considerations have been analysed with regard to the safety regulations of the International Civil Aviation Organization $(ICAO)$ and *EASA.*

Chapter 5. Numerical Characteristic of Computational Aerodynamics model (CAM)

Firstly, during the *CAD* model design, on the *XY, YZ,* and *ZX* planes, the three extrude surfaces were created. Then sketches for the model were drawn using standard fixtures such as line, point, circle, and so on. The hull was created first with *3D* curves. Then, the wing and tail were built separately in the same manner and later assembled through an assembly feature. First of all, the airship was considered with a capsule-type geometrical fuselage with a rectangular wing, but this would not produce enough aerodynamic lift. In a second trial, the hull was kept the same. However, the tail wing was swept forward to be joined with rearward swept the main wing. So, the wing forms a triangle when viewed from the front. Still, it developed more drag than anticipated which made it untenable from an aerodynamics perspective. Afterwards, a further design was trialled for the advanced airship, where the hull was kept constant, but the frontal area of the hull is cleaned up carefully to reduce the surface roughness. However, it is even produced excitable drag. Again, the hull shape was changed with a spheroid-type, and design four individual models for aerodynamic comparisons, such as 1. Spheroid hull, 2. Tails hull model with a gondola, 3. Regular wing model and 4. Box wing model with respect to '*Prandtl'* theorems[163], where are two wingtips chord jointed with one another in the constant chord; this signifies a uniform profile irrespective of aerodynamic performance (see Figure 5.3). Thus, the geometrical and aerodynamic configuration of the novel *EWBA* is entirely different from a conventional airship and aircraft as the earliest *Prandtl* joint wing concept. Hence, this *EWBA* design can be reduced drag as well as improve aerodynamic efficiency. The development of *3-D* geometries can be seen in Figure 5.1, Figure 5.2, Figure 5.3; the geometrical parameters, *2-D* scale model are in **Appendix C.15** and **Appendix 15.1** accordingly. Where the wings planform area (S) is 13.14 m^2 for planar wing airship. In contrast, the upper wing planform area (S_1) and lower wing planform area (S_2) are identical as 6.57 m^2 for box wing airship. Consequences of this both wing planform area are the equivalent since *EWBA's* wing planform area is $S_1 + S_2 = 13.14\, m^2$. In fact, the design plane must be specified and consistently set to a *3-D* geometry in the *CAD* environment; consequently, the files need to be saved in a step file and later in an *IGES* file. In fact, it is a simple procedure, but some alterations must be made in the build. The *IGES* file does not maintain solids' forms. Thus, the geometry must be converted back to the original solid model. It can be done by using the 'Boundary represented' *(B-rep)* system in the 'solid-create' new window. *B-rep* solids are defined by surfaces that are fully enclosed to make a solid.

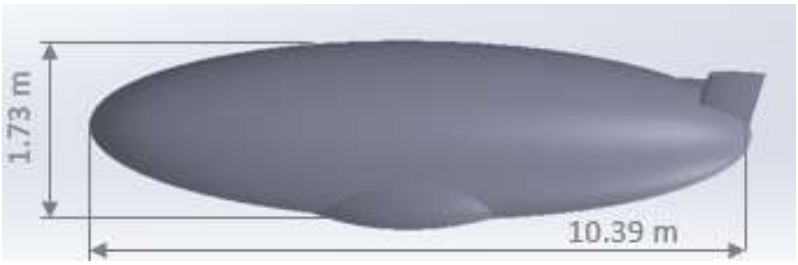

Figure 5.1: *3D* Prolate spheroid tail model (Airship)

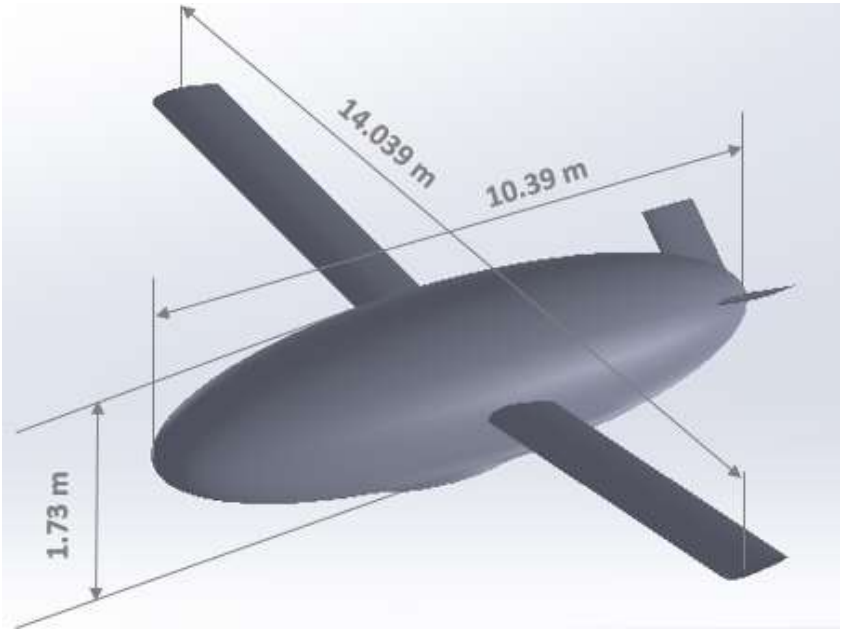

Figure 5.2: *3D* Prolate spheroid shape Hybrid aircraft with planer wing

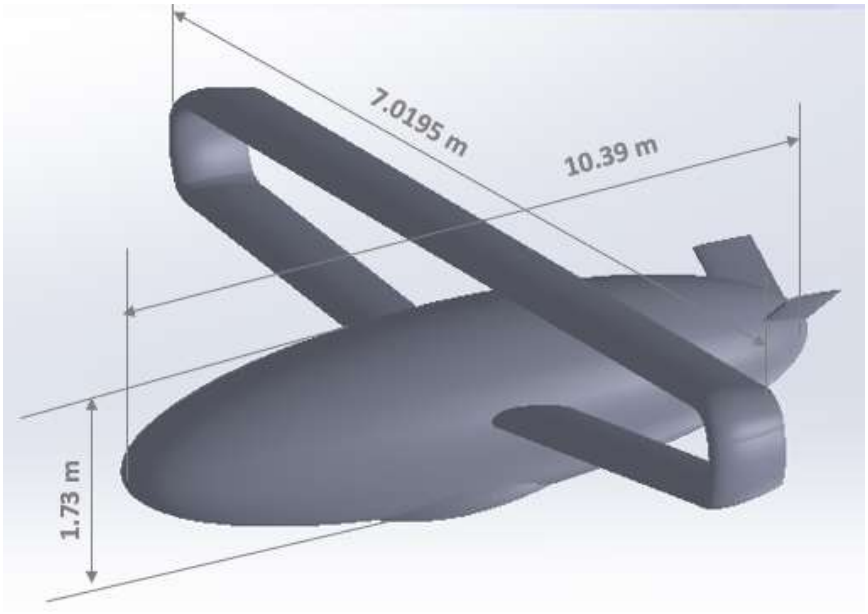

Figure 5.3: *3D* Prolate spheroid Hybrid aircraft with box wing

The completed model can then be directly transferred as a data file into the *CFD Fluent* step by step as follows:

The *CAD* model must be enclosed in a continuum for *CFD* investigation. The enclosure would be made around the import model; the inclusion has been made for half of the model since the smart wing airship is symmetrical about the *YZ* plane. Indeed, this would be saved computational time and cost-effective. It is required to set-up a working directory of *ICEM* mesh in *ANSYS* before going to the *CFD* solver. So, the first step of *CFD* investigation is to define and creation of geometries in the fluid region as a fluid domain for the numerical calculation of *CFD*. The dimensions of the fluid domain are: 12.96 m for all directions from the centre of 1:7.5 scale model. Subsequently, the model is detracted to get the complete continuum from the enclosure.

Hence, this simulation has been completed by using the incompressible Reynolds averaged Navier-Stokes *(RANS)* governing equation. Solidworks has been used in pre-possessing since the Solidworks software is much more user-friendly than *CATIA* and others, as found in the comparisons between the various *CAD*-based software packages.

5.2.2 Mesh Generation

Mesh generation in *ANSYS Fluent* is an essential process, particularly during fluid simulation in the *CFD* phase, where several parameters control the overall development of mesh generation. The *ANSYS ICEM CFD* meshing tool was used to create the grids for this aerodynamic investigation.

The unstructured mesh was approached for enabling the accurate representation of *EWBA* surfaces. A semi-sphere of the domain, the airship within the centre (see Fig. 5.4). The initial communal unstructured grids in surround complex geometries of spheroid/airship/*EWBA* contain *'O'* typical grid. Hence, element distribution can be manipulated since *ICEM CFD* assigns to the edges along with the structure. For the *O*-grid strategy, it was constructed on the outside towards the inside. The *O*-grids are best practices to achieve typical *'O'* block. So, the *'O'* block is opportune for *EWBA* due to the geometrical configuration of complex shapes.

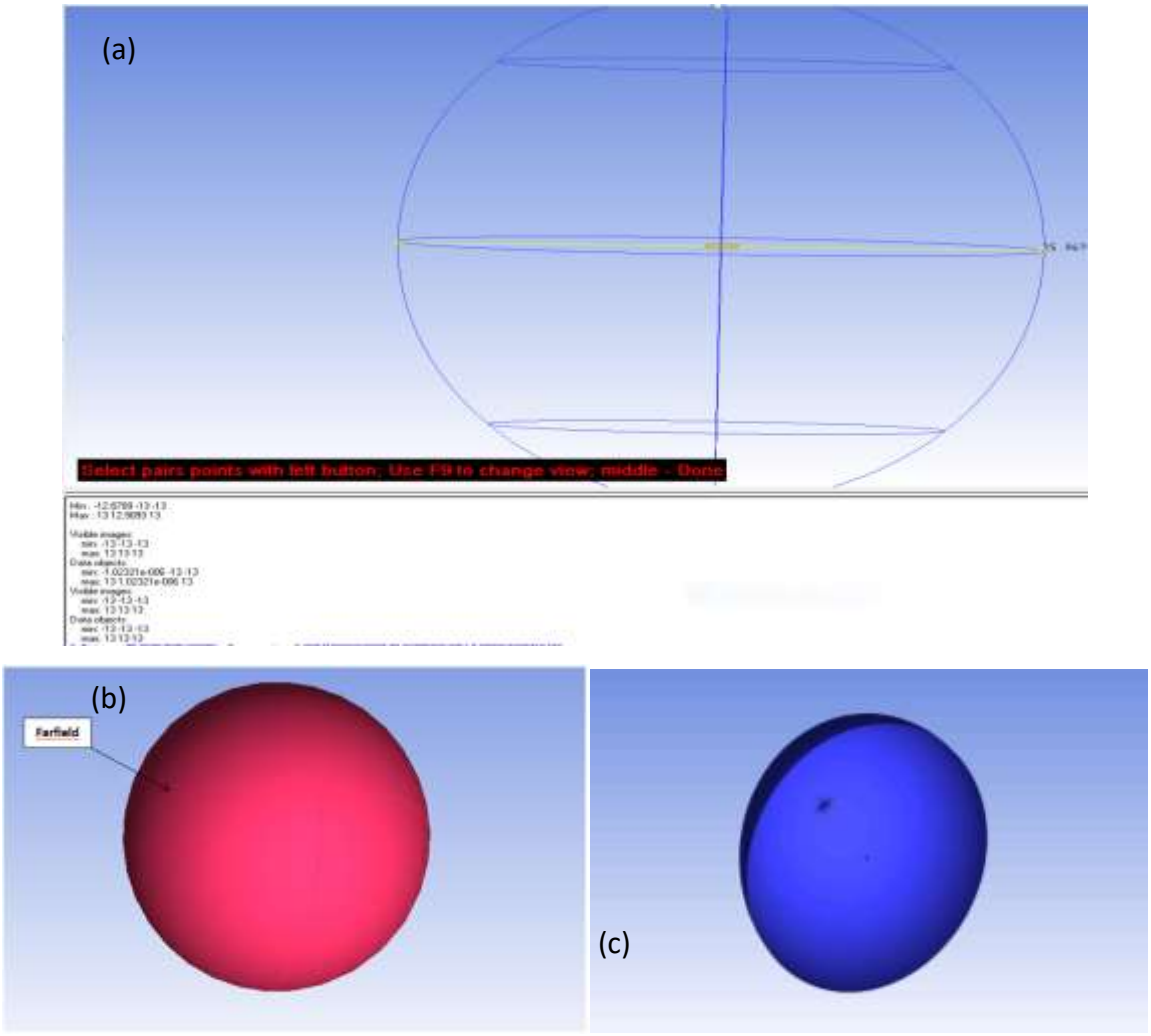

Figure 5.4: Full fluid domain (a), (b), and (c) cross-section of the domain

The approach of grids refinement from coarse to medium and fine contains in developing by the number of nodes with the arbitrary manner in each direction (*x*, *y*, and *z*). Besides, decreased the first cell height by a factor of 0.3. The characteristics of the three reference grids are provided in Table 5.1.

Table 5.1: Three different grids characteristics

Grid Characteristic	Coarse	Medium	Fine
Node (million)	8	11.92	15.12
The first cell (Hight), M	0.0001	0.00003	0.000003
Value of y^+	30	10	2

5.2.3 Fluid flow Solver and boundary conditions

The *ANSYS Fluent* 16.1 solver is used to solve the discretised *RANS* equations with the Finite Volume Method (FVM). In the current investigation, two turbulent models are considered as suitable closures, such as $k-\varepsilon$ [251, 252] and *Linear Pressure-Strain RSM [251]*. A 2nd order Boussinesq hypothesis was employed during the discretisation of *RANS*, turbulent kinetic energy (k), and dissipation (ε) equations. At far-field freestream conditions were set as follows:

Table 5.2: Far-field freestream conditions

Freestream Condition	Parameter
Mach (M_∞)	0.135
Temperature (T_∞)	300 K
Density (ρ_∞)	1.225 kg/m^3
Reynolds Number ($R_{e\ mac}$)	4.2× 10^6

The Viscosity was considered as the Sutherland law. In fact, the variation of incident depends on the appropriate velocity components. The turbulent intensity and turbulent length scale were set at 0.5% and 0.49 respectively as a base on *ANSYS* guidelines with the chord length. The no-slip condition was picked at the wall. The incompressible and pressure base solver is used.

Moreover, the mesh treatment is needed for the higher-density area close to the surface of the model and the less dense area in the far-field for reducing analysing time. Indeed, in the numerical simulation of *CFD*, we simply consider half of the *EWBA* since it is an asymmetrical model that would cut down computational simulation time, memory, and improved accuracy of computational results as well as cost. The next step is editing surface mesh if required, such as moving nodes, merge nodes, create elements, and delete or mesh split by editing tools. The angular resolution system has been applied to them for this *CFD* analysis. The angle was 7^0, edge length 0.003 metres, and 0.2 for the minimum length, a maximum length, and a growth rate 1.2 was used accordingly. Additionally, a smooth transition was allowed between the inflation layer prisms and the regular tetrahedral mesh since a maximum number of layers (10) have been used for this sophisticated model.

The steady-state simulation was set. This can be used to solve conventional problems with the time constant, and it would be saved *CPU* time, computation space and faster than transient simulation. Mesh adaption is another optional menu that needs extra care. So, this is a creative

option where the simulation can also be resolved or alter if needed. All parameters are set in *MKS* units such as metre, kilogram, and second.

Furthermore, the *k-ε* turbulence model was considered due to *EWBA* being geometrically complex with high *Re*. Then, the *RSM* model was adopted to compare the aerodynamic parameters in each model (see Appendix D.1.2 for more detail). This turbulence model also generally produces good results, and it is widely used in aerospace industries for aircraft external flow in *CFD* calculation. To obtain accurate results, the y^+ value is 30,10 and 2 used for both turbulence models: the *k* -ε model and the *RSM*.

Firstly, in the mesh generation process, the geometry was imported in *ANSYS ICEM* from Solidworks, which was cleaned up in *CAD* tools before being imported. The number of total degrees of freedom was kept under control in order to produce a computational simulation that could be reduced in a reasonable computational time, and it is relatively easier to afford complex features of surface mesh. Inclusive overviews of the domain and surface mesh can be seen in Figures 5.5 and 5.6. The *ICEM CFD* tools were created an unstructured grid where the inflation layer enclosed to the surface of the model, and the far-field tetrahedral mesh was generated since it has better accuracy in multipart geometry-based modelling and cases of higher Reynolds numbers. Air was used as a material, the velocity inlet was 46 m/s, and the pressure outlet boundary conditions were imposed on the flow and outflow zones, respectively.

5.2.4 Fluid domain and elements surface mesh

The following Figure 5.5 is a visual representation of closer mesh. It shows only a portion of the control volumes since the grid is unstructured. In the domain near the wall, it can be seen that mesh density is increased; however, in the outer domain, it is less dense and coarser.

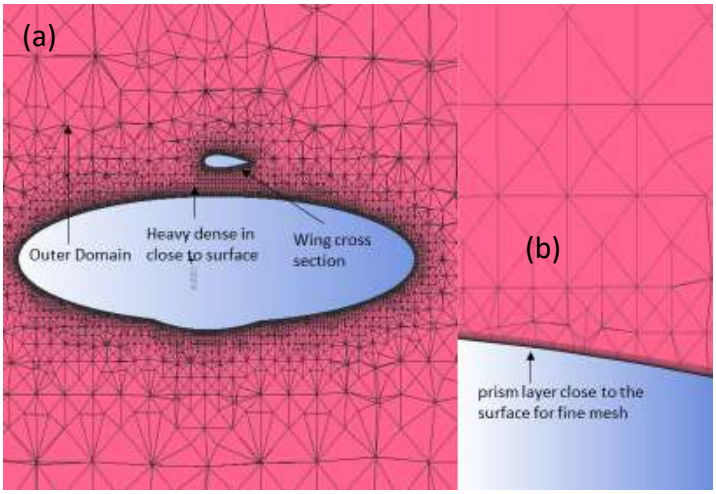

Figure 5.5: The Cross-section (a) and Closer view (b) of the domain for fine mesh

Figure 5.5 (b) also depicts the close-up appearance of the mesh near the *EWBA* surface. Here, the inflated boundary can be observed. The mesh near the region of the hull is prism-shaped, and there are tetrahedral meshes in the far-field (outside this region). The first layer distance from the surface airship was kept in 1×10^{-5}c (approximately) chord length to confirm that turbulent flow is approximated correctly.

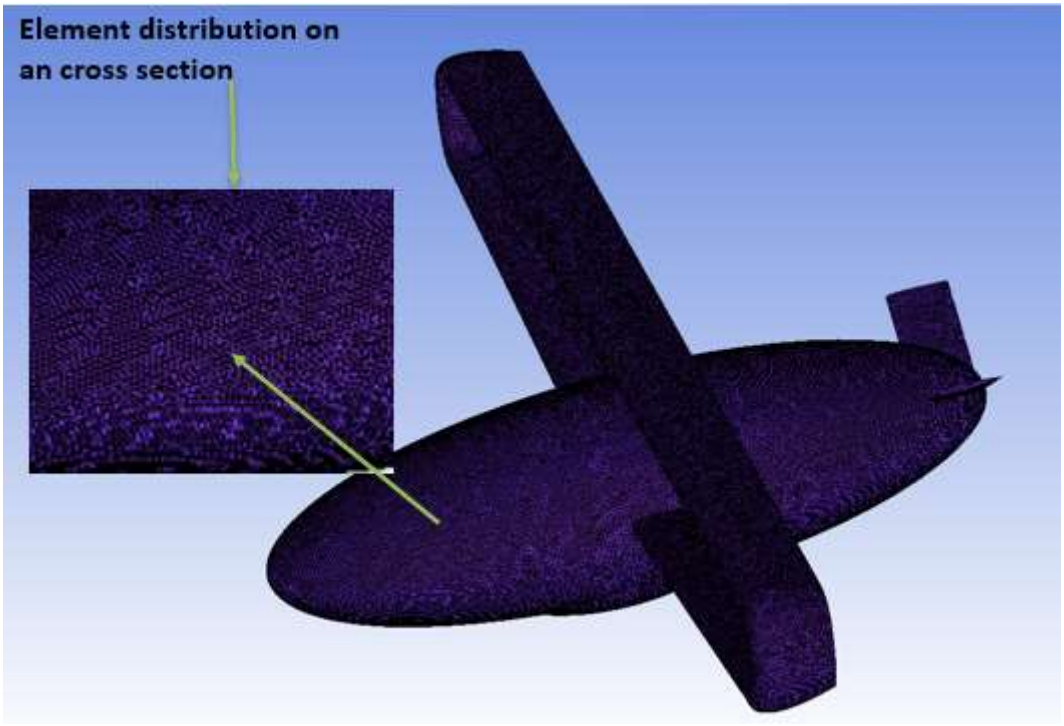

Figure 5.6: Element distribution on the surface for fine mesh

In Figure 5.6, the surface mesh is refined on geometry by the mesh parameters, such as angular meshing, maximum or minimum edge length, and expansion factor. Also, the mesh propagates from the surfaces after increasing the control volume size by the expansion factor. As shown in Figures 5.5 and 5.6, the overall outer surface was discretised in triangular elements and clustered in closes to flow separation in the wall region. The mesh engine increment near the edge of the model: here the high-density mesh enables refinement of the stagnation points. However, it should also be noted that the mesh around the symmetric body is not symmetric. Thus, the inflated boundary generation is concluded upon formation and progress for adaptation from one mesh to additional meshes. The total elements distribution was obtained 2.7×10^{7} during surface mesh. The result was set to converge at a maximum residual of 1. So, this enables to performance of accurate numerical simulation for the *EWBA.*

5.2.5 Grid Independence study

The accuracy of *CFD* investigations for a precise algorithm on an *FVM* is used, which is a simplified problem. But, usually an accuracy of the problem-dependent; a system that is correct for one model, however, may not be certain as appropriate for another problem. On the other hand, getting accuracy is to attain solutions on consecutively refined grids and continue monitoring and succeeding refinements, satisfying some prearranged accuracy since the solution is not changing. These approximation methods will converge to the exact solution. These grids approximated solutions refine enough to enable the progress of further assessment for the particular numerical solution. The key awareness of the *CFD* results is that a converged solution always does not certainly mean a precise solution. However, a mesh independence study should be accomplished to analyse the aptness of the mesh; thus, yield an estimation of the computational errors in the solution. Usually, it is involved in monitoring the fluid flow parameter as an interest of study and changing behaviour under succeeding grid refinements. Indeed, the convergence of a *CFD* simulation is a simple scheme for defining the methodical discretization error. It is a regular exercise to defined the values of the parameter; before starting the simulation, it should be scrutinised to ensure that the desired point reaches a steady-state in solution; *RMS* Residual error values are at least 10^{-4}; in the domain, for all variables, the overall imbalance is less than 1%. In this research, the grid convergence study was performed by evolving three different meshes (coarse, medium, and fine mesh) to obtain the drag coefficient, lift coefficient, and moment coefficient. First, a coarse grid was produced, which estimated the coefficient of drag; it monitors until the solution converged and mesh refined globally with the rate of 1.2. The current grids are 1.5 times more cells than the first mesh. Efforts were made to avoid grid cell skewness or discontinuous changes, particularly in close-to-the-wall regimes and compared with previous mesh solutions. The grid was studied for skewness and negative volume once the numerical simulation was initiated on a medium-sized grid. Further refinement of the grid did not show a significant change in coefficients of drag. The number of nodes, elements and the simulation times for the different three cases is set out in Table 5.3. It is apparent that the *CFD* simulation time is heavily dependent on the

Table 5.3: Grid independent study

Mesh type	Elements	Nodes	C_D	Time (hrs)
Coarse	12239644	8162210	0.022534	75.43
Medium	18359466	11921437	0.021014	140.50
Fine	27539199	15127508	0.021010	320.51

number of nodes. In consideration of the above results (Table 5.3), the grids refinement has appeared since the drag coefficient (C_D) does not change significantly where were error 2.75×10^{-5} in an acceptable range. Thus, the 15127508 nodes' results for this domain would be reliable for further aerodynamic investigation.

5.2.6 Enhanced wall treatment (EWT) and y^+ Sensitivities

The appropriate consideration range of y^+ is very important for CFD simulation. The value of y^+ vary according to *Re* numbers. The higher *Re* numbers over $1e\times 10^{7+}$accommodate maximum y^+ value, the results might be degraded beyond that. Thus, the near-wall region can be summarised as bellows for a turbulent boundary layer:

$y^+ < 5$: Viscous sublayer

$5 < y^+ > 30$: buffer region

$30 < y^+ < 300$: fully turbulent region

The mesh sensitivity investigation was carried out to get the y^+values in a precise range. Indeed, the first prism height of the inflated boundary was y^+ values as an effect of the relationship between them. Indeed, the y^+ is a non-dimensional distance, typically used in computational fluid dynamics to define a mesh how coarse or fine is for a specific flow. It is also shown that the ratio between the laminar and turbulent effects in a cell.

The correct demonstration of the flow in the near-wall region can be decided by successfully predicting the wall-bounded turbulent flows. The values of $y^+ \approx 1$ are most desirable for near the wall modelling to resolve the viscous sublayer [253, 254]. In fact, turbulent flows are significantly concerned by the presence of the walls. So, the strategy of y^+ values with the corresponding turbulence model are assisted in selecting a most suitable near-wall treatment. This research used enhanced wall treatment (EWT), a near-wall modelling

method due to near-wall flow characteristics that need to be resolved, *EWT* a two layer model, the *EWT* in *k-ε* model are the combination process of different wall functions. Consequences of, it is called two layer scheme. Two layer technique is an crucial element of the enhanced wall treatment and is used to define both ε and the turbulent viscosity in the near-wall cells. The *EWT* is a technique to implement hybrid wall function for varying y^+values in *CFD* model [255]. Rahman et al. [256] was used the blending function for velocity and wall shear stress, but with a highly modified *k-ε* are also relaxes in y^+requirement. In fact, the *k-ε* and *RSM* turbulent models are initially functioning for turbulent core flow, but paired with *EWT* can bring them with the solution variables in the viscosity effected region. The key constrain is that near wall mesh must be desirably fine enough deliver precise results.

` In the following Figure 5.7, the classical behaviour of lift coefficient has been shown at different angles of attacks with different y^+values. Here, δ is the boundary layer thickness. Case of y^+ values 2,10 and 30, the lift coefficient is increased linearly along with an increase of AOA up to 8^0 in different δ values. The AOA 10^0observed first abrupt the loss of lift that is characteristic of a stall while y^+=30 and boundary layer thickness (δ)=0.02m, due to fluid flow unstable over the surface, and it also noticed the phenomena of lift decreased with increased boundary layer thickness. In fact, the lift coefficient is increased once the y^+=10 and the boundary layer thickness (δ) reduced to 0.002m, even increased of AOA. Indeed, the stall behaviour is delayed to 12^0 at AOA. However, the stall is smoother than y^+=30 with (δ)=0.02m. Again, the lift coefficient is improved by reducing of y^+values in 10 by keeping δ values as the same as 0.02m. In Figure 5.7, the lift coefficient is non-linearly increased once y^+=2 and δ = 0.001m, whereas the exhibition of stall behaviour is smooth. Moreover, the magnitude of the flow detachment point attenuated, leading to a smaller. Since, the C_L tends to increase with the decrease in each combination of y^+ and delta (δ) values. Therefore, the boundary layer thickness is playing a significant role with y^+values, during the CFD for the aerodynamic performance. The y^+= 2 and y^+ = 10 shows desirable, consistent results for the case of lift coefficient. This research is accomplished using y^+= 2 for further aerodynamic investigation; however, any one of them y^+ values could be convenient.

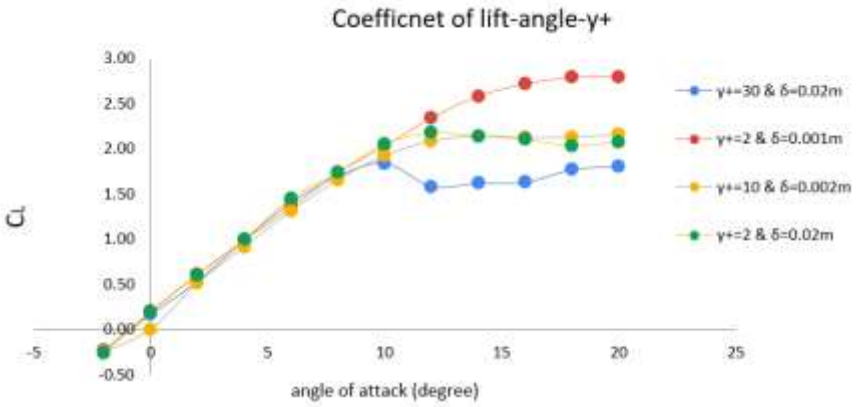

Figure 5.7: C_L for different y^+ values for different AOA with boundary layer thickness

Again, the following Figure 5.8: shows y^+ values in a variable colour plot along the entire *EWBA.* Most of the y^+values are in the range of 2 to 10. The y^+ values in higher at the front section of the airship wing (leading edge). However, in the tail, the values of y^+ is lower

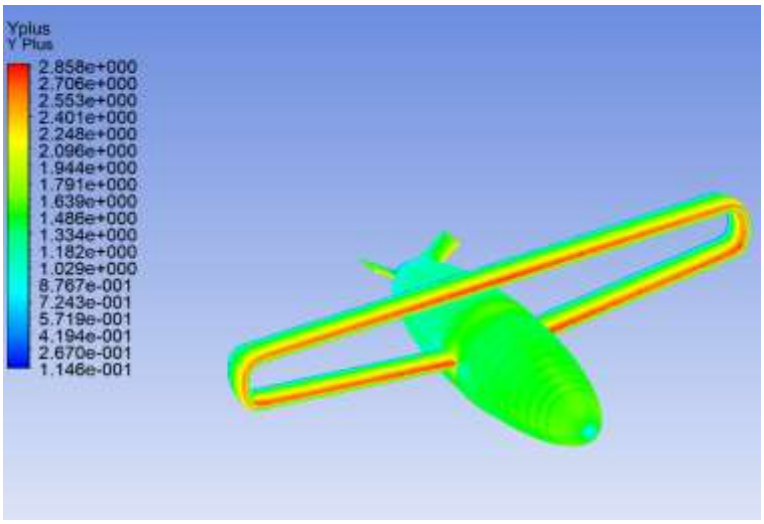

Figure 5.8: y^+ Values in a variable contour

(approximately 2) since y^+ values rely on the nearest node to the surface and thickness of the actual boundary layer. The boundary layer is thin at the front section of the hull due to a favourable pressure gradient. On the other hand, the y^+ are lower at the tails since the advanced pressure gradient is thicker. However, the across flat surface of the hull y^+ values approximately constant, which are foremost compared to the flat plate boundary theory. In fact, the boundary layer thickness 0.0183 meters and 0.0729 meters for 1 meter and 5 meters marks, respectively, as flat plate theory for a turbulent model. In the case of the *EWBA,* the nearest node was set in order to 0.00003 meters since the boundary layer is outside of this node as an approximation of a small portion of the boundary layer. It is (y^+) also relay with the wall shear.

Hence, the *k-ε* and *RSM* models have been used to evaluate the turbulent model for various aspects of fluid flow in previous Chapter 4 with a moderate Reynolds number of 4.2×10^6, including skin friction coefficient (C_f), pressure coefficient (C_P), and an aerodynamic parameter such as C_L and C_D. Indeed, the numerical predictions of both $(k-\varepsilon$ and $RSM)$ models were compared with accessible experimental data of Chesnakas et al.[73] and Wetzel [240] for y^+equal 2. This study has also been shown that the *CFD* model is in good agreement with experimental results. So, the enhanced wall treatment (EWT) an appropriate resolution of near-wall flow phenomena, based on a consideration of near-wall behaviour of the *k-ε* and *RSM* models. Thus, the present models can be delivered suitable results for near-wall turbulence with moderate Reynold numbers.

5.2.7 Solution

In the next step, the different parameters of the flow were assigned to the turbulence model. The flow velocity was used 46 m/s, Mach number 0.135, and Reynold number (Re) 4.2×10^6 at sea level. The details of flow during the simulation are as follows:

- Viscous flow model
- Pressure based, with selected skewness alteration, usually bigger than 0 (zero) selected for high skewness
- The discretisation systems offered a standard equation, selected from the drop-down as a second-order solver
- Finite volume
- *SIMLEC* scheme as pressure-velocity coupling
- Standard wall function as near-the-wall treatment.

All the above aspects were selected to avoid the undesirable results of both the *k- ε* and *RSM* turbulence models. Once all boundary conditions were set, the controls and solutions were ready to be simulated using the computational model. In the coupled solver, a 0.25 solution control was set as the Courant number; under the relaxation factor, the pressure was set to 0.75; the turbulent kinetic energy and the turbulent dissipation rate were computed as 0.99. In convergence, the iteration was requested at 1600 and initialised, and the solution processes were stopped by *ANSYS Fluent* after 1500 iterations, as shown in **Appendix D.2,** which was converged successfully. This method accomplished highly superior mesh in output throughout the vast range of inputs.

5.2.8 Post-processing

After the solution process, defined the numerical results that have been generated for lift coefficient, drag coefficient, moment coefficient, and pressure coefficient; these data were analysed using various contour plots in graphical representations as shown in Figures 5.14, 5.15, 5.16, and 5.17.

5.3 Results, Validation, and Discussion

In this section, the numerical results are introduced. During the validation of the *CFD* method, the prolate spheroid 6:1 was employed [74, 240]. Since the lack of experimental data for *EWBA*, and the wing airship hull has kept as same as a spheroid for analysis of the aerodynamic performance of *EWBA*. The steady-state, second-order, *SIMPLEC* pressure-based scheme was used. The numerical solution of the convergence criterion was controlled by monitoring the computational error of the results.

Indeed, two different *RANS* governing equations: $(k\text{-}\varepsilon)$ and (RSM) *the* model was performed. Both of the turbulence models have been demonstrated in different validation studies to yield better performances [257]. In particular, a mesh independent study was implemented. The meshing strategy and technical detail are set out in Table 5.3. Firstly, in the coarse grid, the drag coefficient was 0.022534, with elements 12239644, nodes 8162210, while the convergent time taken was 75 hours 43 minutes. Then, the y^+ was increased to generate another mesh for further refinement where the coefficient of drag was 0.021014, elements 18359466, nodes 11921437, and time taken to convergence was 140 hours 50 minutes. Although the grid has not shown big changes in terms of drag coefficient (just 7.23%), but time was increased by 47.02%. Moreover, an additional refinement was implemented for fine mesh, where the drag coefficient was 0.021010, the number of elements 27539199 and nodes 15127508, and the time was taken 320 hours 51 minutes for converging the meshes. The accentuating parameter of drag coefficient was very similar to coarse and medium meshes, and the error taken into account was 6.74% and 0.019% respectively. However, the mesh convergent time was increased more than 76.46% compared to coarse meshes and 56 % for medium meshes. Additionally, Figure 5.9 below shows that the C_D values are reduced with increased nodes; after a certain stage, the value of C_D continues to decrease, but the rate of change is 0.019 %. That is within an acceptable range toward the continuous analysis. For these reasons, the fine meshes would be adopted in order to further investigation of *CFD*.

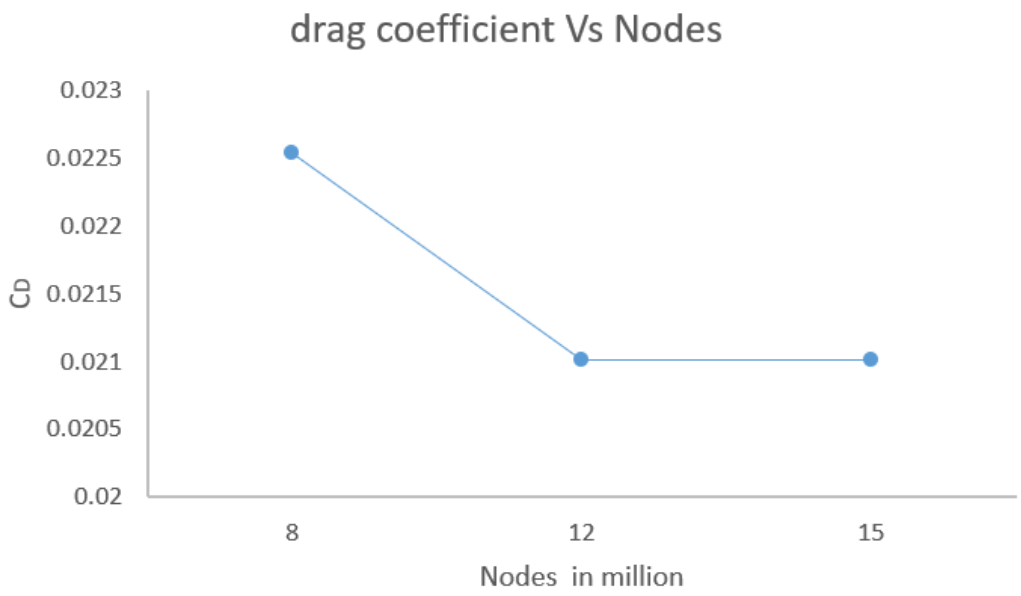

Figure 5.9: Mesh independence solution

During convergence, residuals in the *Workbench* iteration for 1500 were converged successfully, as shown in **Appendix D.2 for** *k-ε* model **Appendix D.2.1** for *RSM* model. This graph was plotted to view the distribution of continuum velocity throughout the simulation. It is a most fundamental residual converging the evaluation of a particular solution of an error; Considering the drag coefficient in the residuals graph at the point of 1500th iteration, the error was 1e-5% related to the immediate at 1499th iteration in the same graph for the elegant *EWBA.* It was decreased by three orders of magnitude before C_D steady-state and in converged. In **Figure** D.1.1, D.1.2 (**Appendix** D.2 for *k-ε* model) and Figure D.1.3, D.1.4 (**Appendix** D.2.1 for *RSM* model) are the illustrations of evaluation of continuity residuals and C_D as output by the flow simulation by *RANS* closed of *k-ε* and *RSM*. Thus, it is considered as robustly converged since the *ANSYS Fluent* residual level varies between 1e^{+01} to 1e^{-9}. However, the convergence history showed that the graphs became more precise as the number of iterations increased, but it is not easy to achieve a residual level as low as 1e^{-6}. This process was refitted 13 times for different *AOAs*, such as $-4°$ to $20°$ for 2^0 intervals, in each *AOA* during the simulation of both turbulence models. The solution was dynamically checked, including lift coefficient (C_L), drag coefficient (C_D) and lift to drag ratio by mean of aerodynamic efficiency $\left(\frac{C_L}{C_D}\right)$ and later plotted in graphical form in *Microsoft Office* $(Excel)$ software to investigate the solution in more detail and to compare with the analytical results; those parameters $(C_L, C_D$ and

$\frac{C_L}{C_D}$) are also compared between the wing hull and wingless hull as well. The replication was run in a constant inlet velocity of 46 m/s with constant coincided to 4.2 $\times 10^6$ Reynold number, which was kept the same for all remaining simulations, including the wingless model.

The lift coefficient at the cruise design point is determined by relative dynamic pressure at 4000m altitude. In the design point at cruise, the weight equals the lift, which is 1202kg. These can be achieved by 0.30 as cruise lift coefficient (C_{Lc}). Referring to Figure 5.10, the finite box wing hull at 0^0 *AOA*, the C_L are 0.330, 0.243 and planner wing 0.283, 0.314 for $(k-\varepsilon), (RSM)$ respectively. The cruise lift coefficient (C_{Lc}) is obtained at AOA 0^0 (approximately) in the case of planar and non-planer (box wing) aircraft. However, for the spheroid hull and spheroid with the tails hull at 0^0 AOA, the lift coefficient (C_L) are -0.0155 for $(k-\varepsilon)$, $-$ 0.0195 for *(RSM)* and – 0.0179 $(k-\varepsilon)$, $-$ 0.0138 (RSM) accordingly. This graph (Figure 5.10) also shows box wing produced a slightly higher (14.24%) lift than the planer wing hull in the case of $(k-\varepsilon)$, while the wingless hull is still in the negative lift. The compare to the analytical (0.289) results, the numerical results are also 12.42% higher in the $(k-\varepsilon)$ for box wing, but the lift coefficient by the *RMS* model produced 15.91% less at the angle of attack *(AOA)* 0^0 in cruise. In fact, the magnitude of the C_L is increased with an increase in aircraft *AOA*. The angle of attack *(AOA)* keeps increased further until the aircraft reached maximum *AOA*. At this point, flow over the surface of the aircraft is fully separated. The consequences of flow simulation remained entirely attached for all wingless models at *AOA* 14^0, but the flow is separated for both wing hull models; due to the increased boundary layer separation at a particular stage, a sufficient lift will not be generated to carry the airship weight; the flow is fully separated from the upper surface, and aircraft stalled; this is the 'stall angle' for *EWBA*. Thus, the maximum C_L 1.48 for box airship 1.395 for planner wing in $(k-\varepsilon)$ model, but 1.349 in *RSM* at 14^0 *AOA*, whereas the flow is still attached with the surface in the box wing airship as a case of *RSM*. A further increase in *AOA* at 16^0, the tail model and box wing airship are reached at a peak point in the lift coefficient, and it stalled, which is (1.4246) for box wing, tail model 0.181, 0.188 for the case of $(k-\varepsilon)$And *RSM* consistently. There is no notable difference between the *CFD* model and the analytical model for *EWBA*. Nevertheless, in the *EWBA*, the lift coefficient is significantly improved compared to the experimental results of the wingless hull in the case of the computational results. Figure 5.10 also shows that the wing's body contributes to the largest amount of lift.

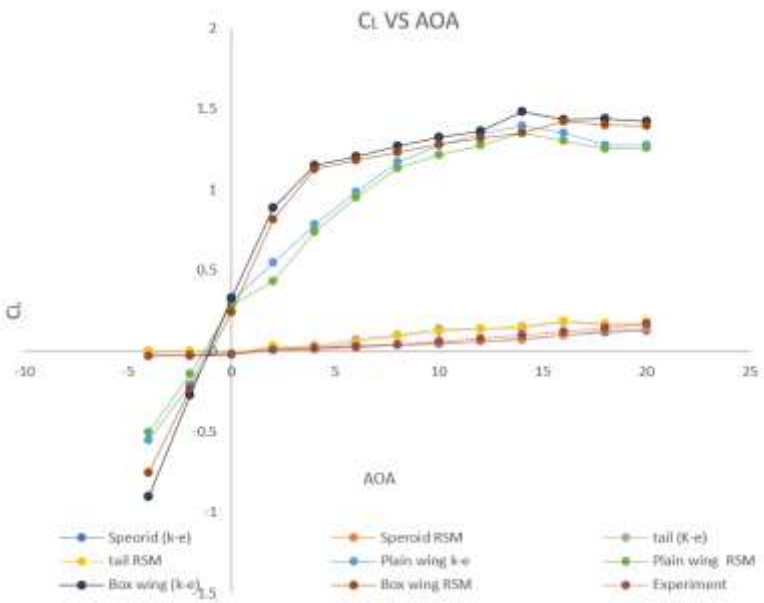

Figure 5.10: The comparison of C_L *vs AOA* in *CFD* and experimental results

Turning to Figure 5.11, the finite box wing hull at 0^0 AOA for cruise condition: the C_D is 0.0314, 0.0331 for $(k-\varepsilon), (RSM)$ and planner wing 0.0211, 0.0225 respectively, but for the wingless tail hull and plain spheroid, the C_D is 0.0205$(k-\varepsilon)$, 0.0204(RSM), and 0.0157$(k-\varepsilon)$, 0.0191(RSM) accordingly. Although, in the analytical consequences of *EWBA*, the C_D was 0.0187 for box wing airship and 0.02072 for planner wing at 0^0 AOA, which is significantly lower than numerical results as both turbulence models, but 50 % higher than for the wingless hull. That means the finite wing generated 50 % of drag itself. In addition, the magnitude of the C_D is varied on the gematrical shape, *AOA*, and velocity of the airship.

In Figure 5.11, C_D *vs AOA* tread has been revealed that the C_D is raised with *AOA* increased, and after 4^0 *AOA*, the C_D rises rapidly due to the increase of the frontal area of the airship and increases the boundary layer in flow separation and thickness on the upper surface of the model. So, at a 14-degree angle of attack, the $C_{D\,max}$ is 0.0857, 0.0862 for planar wing airship, 0.089, and 0.098 for box wing airship in both numerical models. The drag coefficient is much higher in the box wing model than in the planner wing model; also, the RSM model produces higher drag than $(k{-}\varepsilon)$ due to the RSM free steam flow in the inlet boundary very sensitive for complex model and flow in far-field. It can be enhanced by resolved boundary layer distance. Certainly, the comparison of drag polar was at Mach number (M) = 0.135; however, it needs more variation for different Mach numbers, where more identical differences

could be recognised. These polar drag curves can be used for analysing the aerodynamic configurations by changing wingspan efficiency by altering wing height.

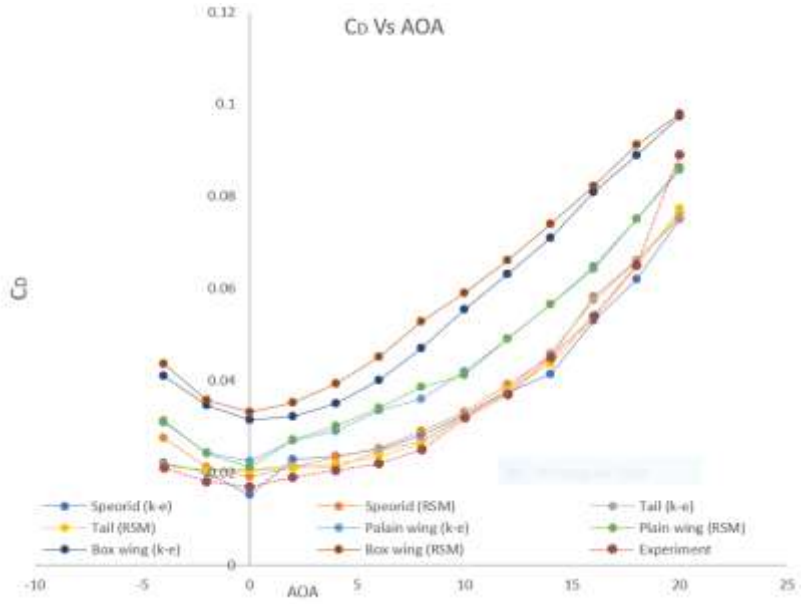

Figure 5.11: C_D comparison in different *AOA* for *CFD* and experimental results

Furthermore, in Figure 5.12, the lift to drag ratio $\left(\frac{L}{D}\right)$ is a function of AOA. It provides important knowledge of the aerodynamic efficiency *(E)* of the key goal being studied. Thus, the ratio of $\left(\frac{L}{D}\right)$ obtained for buoyant aircraft as was expressed as (C_L) divided by the (C_D). In Figure 5.12, the *(E)* or $\left(\frac{L}{D}\right)$ vs *AOA* shows that the maximum aerodynamic efficiency (E) is $32.77(k-\varepsilon)$, 28.119 (RSM) in the box wing airship at 4^0 AOA, whereas it is $32.51(k-\varepsilon)$, 29.50 (RSM) at 8^0 AOA for planar wing airship in honour of the numerical results; thus, the E is 87.03% higher than the wingless tail model, 94.32% higher than spheroid as a case of $(k-\varepsilon)$. However, as a case of *RSM*, the E is 86.9%, 93.719% higher than the tail and spheroid model as respectively. In fact, the comparison of box wind airship, the E is 0.61% higher on account of $(k-\varepsilon)$ than planner wing model, but 2.71% less than planner wing airship for a case of *RSM*. Indeed, this simulation was run in steady because all investigation has been done in steady level flight. Hence, the aerodynamic efficiency (E) is significantly enhanced regarding the wing airship and the box wing airship compared to the wingless hull.

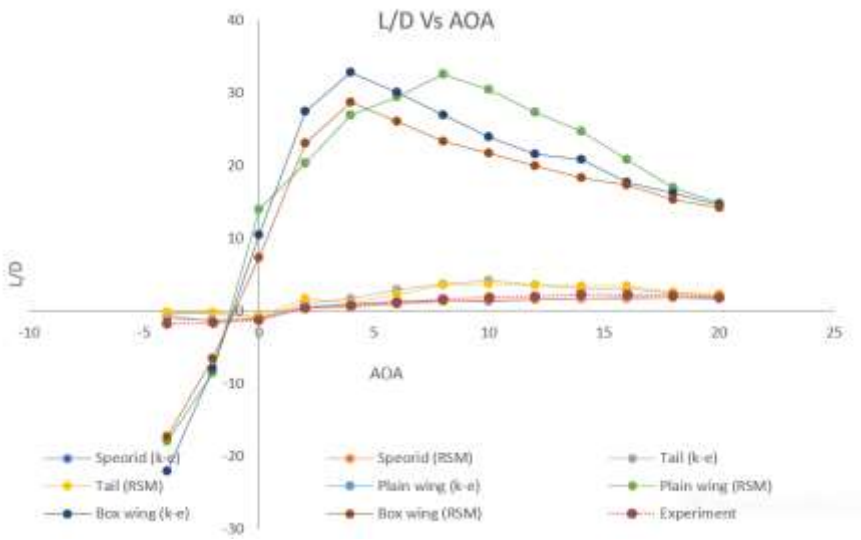

Figure 5.12: Aerodynamic efficiency (E) vs AOA

Moreover, these plots (Figure 5.12) also show that the aerodynamic efficiency is decreased after 4^0 and 8^0 *AOA* if increased *AOA* further as according to box wing airship and planar wing airship. Indeed, the considerable reduction of *'E'* happened at level flight due to a higher drag being produced at high speed. However, it is obvious that the aerodynamic efficiency would be improved significantly with changes in the *EWBA* wing configuration.

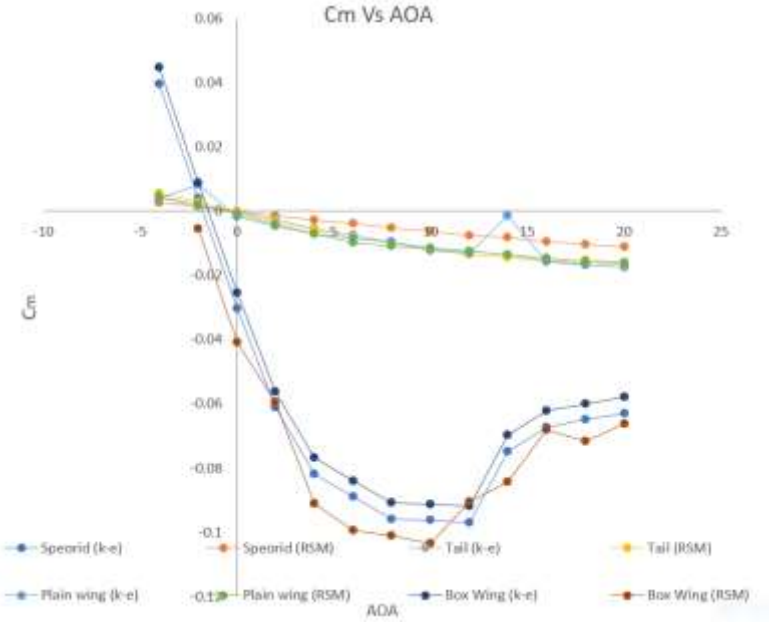

Figure 5.13: Pitching moment coefficient

During the investigation of the stability of *EWBA*, the coefficient of pitching moment (C_m) are varying with *AOA*, as presented in Figure 5.13, it is noted that the negative pitch angle

($C_{m\alpha}$) means airship nose down and model statically stable. In above Figure 5.13 reveals, spheroid, tail model, planar wing model, and box wing airship all configurations seem to be negatively stable. In contrast, the airship is the tendency to pitch down with positive changes of pitch. In the wingless model, the hull is observed to be a key sponsor in terms of pitching stability. Likewise, the static pitching stability is also found in both wing models, which is even produced a larger pitching moment coefficient to ensure that longitudinal static stability. Indeed, the pitching moment coefficient (C_M) at 0^0 for box wing -0.02539 ($k-\varepsilon$), -0.04086 (RSM) and planar wing -0.00165 ($k-\varepsilon$), -0.00102 (RSM). Hence, the box wing model has generated higher static stability than planar wing airship since in box wing airship the C_M is greater than planar wing airship. Though, this computational simulation was not considered a buoyancy force as other work in the literature, where it ignored buoyancy effects. Table 5.4 summarised the aerodynamic parameters of planar and efficient wing hybrid airship for comparison in below at cruise conditions:

Table 5.4: Comparison of box wing's aerodynamic parameters at cruise

Models	Aerodynamic parameters	*k-ε*				*RSM*		
		C_L	C_D	C_M		C_L	C_D	C_M
Box wing airship		0.330065	0.031473	-0.02539		0.243	0.0331	-0.04086
Planar wing airship		0.314388	0.022543	-0.00166		0.283	0.0211	-0.00102

The aerodynamic features of *EWBA* can be seen in Figure 5.14, which shows pressure co-efficient (C_p) magnitude over the wing trip and rood chord at different *AOA* in the chordwise location. The vortex at wing trip is observed to steadily increase as *AOA* increase. It is reduced the effectiveness of wing lift by modifying the airflow around the wings and formed extra drag proportional to wing lift. This clearly can be seen in the box wing airship (Figure 5.11). With the distractions of an *EWBA* complete form, it would be enabled to recognise flow properties over the wings; the magnitude of airflow velocity is reduced with a pressure rises; on the other hand, the pressure is reduced or suppressed as the *AOA* rises on the *EWBA* over the surface. Eventually, the amalgamation of total pressure, for instance, the pressure distribution can be shown in Figure 5.18 along the span-wise.

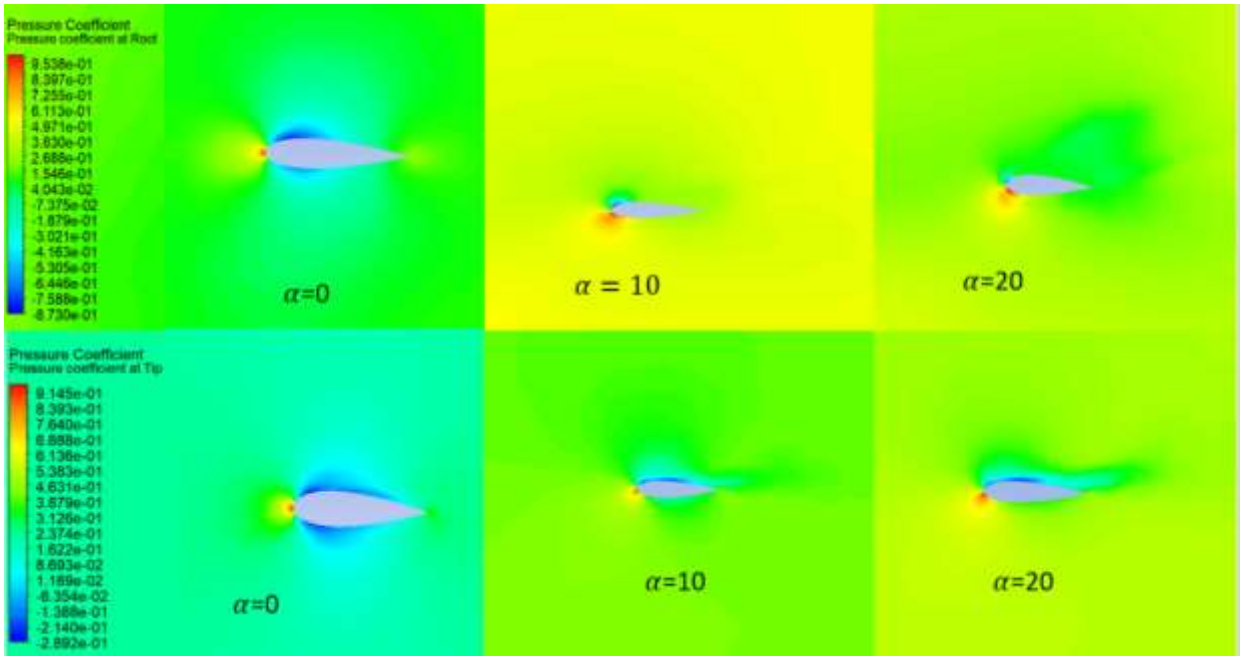

Figure 5.14: C_p magnitude on a trip chord and rood chord in different *AOA*

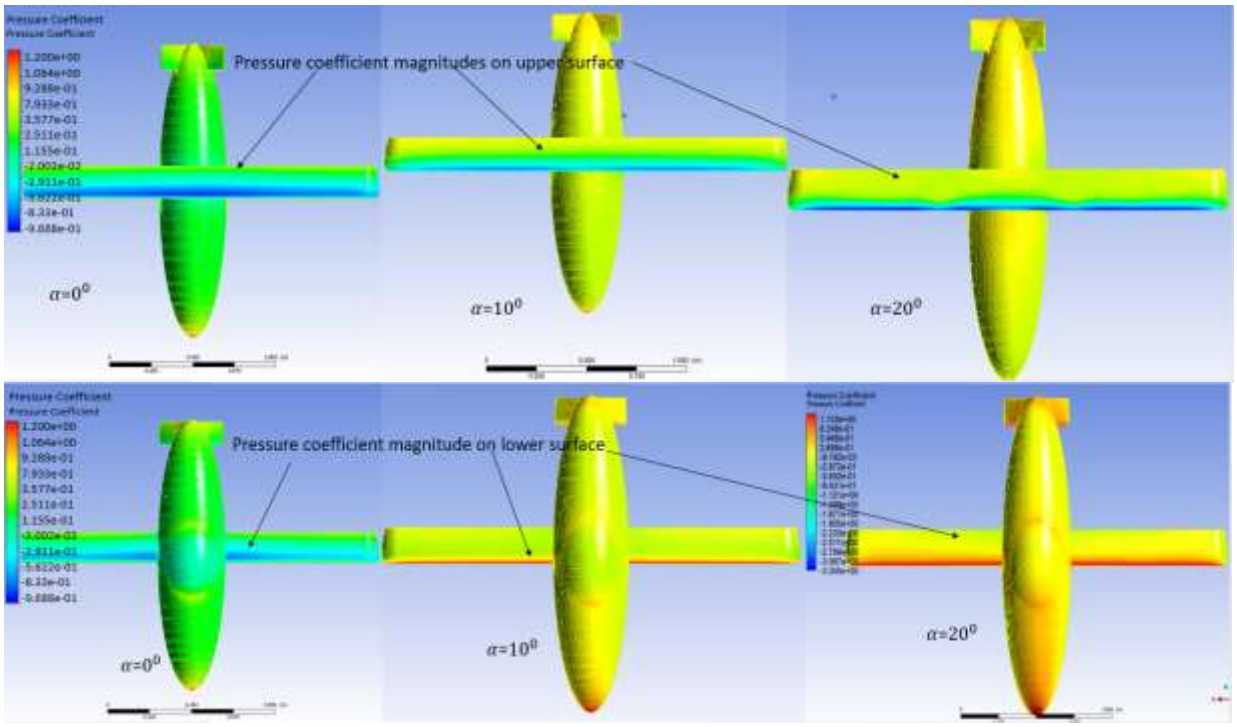

Figure 5.15: C_p magnitude over top and bottom the surface in different *AOA*

Furthermore, in Figure 5.15, can be seen, C_p magnitude over the upper and lower surface of the *EWBA*, where the C_p is $1.556e^{-01}$ at the top surface and on the bottom surface $2.511e^{-01}$ at 0^0 *AOA*, that is 38% higher compared to the top surface. A further increased of *AOA*, the C_p is increased rapidly on the lower surface corresponds to the top surface, which is 47.8% (lower

surface) higher than the top surface, as can be seen in Figure 5.15 at 10^0 AOA. It also can be seen, the C_p on the bottom surface is $9.288e^{-01}$ and on top surface $5.22e^{-01}$ at $20^0 AOA$. Consequently, the bottom surface of the *EWBA* displayed is 43.79% higher pressure than the top surface. This would enable the generation of a positive lift to carry the 1202 kg weight of the *EWBA.* Since, the lower fragments experience more pressure and the lowest velocity, while the upper fragments experience lower pressure and higher velocity due to the aerodynamic shape of the *EWBA*, according to the Bernoulli equation. These pressure differences result in a cost for an upward lift.

However, Figure 5.14 shows that a stagnation point is precisely at the leading edge of the wing and precisely in the middle of the nose of the aircraft in **Figure 5.15** at $0^0 AOA$ would move with changes in *AOA*, as shown above in both figures. In **Figure 5.14**, **Figure 5.15** has also been addressed a typical point of the vicinity of the stagnation point on the *EWBA* for the $(k-\varepsilon)$ and (RSM) turbulence model. Indeed, the phenomenon of the stagnation point is due to the surface roughness of *EWBA*, which is mainly responsible for opening flow conception over the aircraft, as a consequence of the higher pressure on the leading edge of the bottom region and lower pressure on the upper surface region on the model. As referred to earlier, Bernoulli's principle as addresses a velocity contour in below (Figure 5.16). The velocity is higher on the upper surface, i.e. at the low-pressure region, and lower on the bottom surface of the aircraft in the higher-pressure region, again in line with Bernoulli's equation as can be revealed.

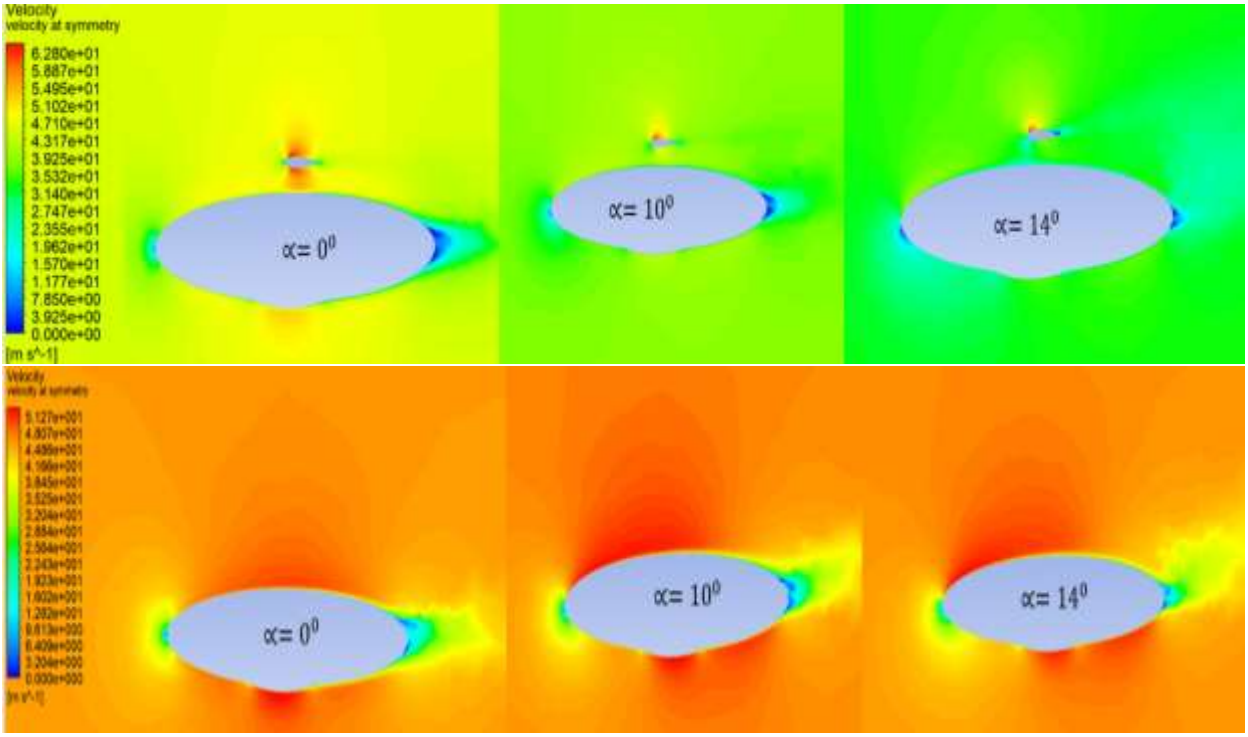

Figure 5.16: Velocity magnitude at a different angle of attack for box wing (on top) and planner wing (on bottom) airship

However, Figures 5.14 and 5.15 show that the pressure coefficient is higher in some places on the *EWBA* due to rough-edged surfaces and corners, especially on wing chords. Moreover, Figures 5.15 also show that the pressure coefficient at the nose of the *EWBA*; and the frontal area of the passenger unit was higher than the flat surface of the hull, which was unexpected. This kind of error could be reduced by refining the design.

The visual representation of velocity magnitude can be seen in Figure 5.16 for three different *AOA*. At 0^0 *AOA*, the velocity on the upper surface is a little higher than the bottom surface for both models; as increased *AOA*, the velocity is increased promptly and becomes stronger on the top surface of the airship. Besides, velocity is decreased and wicker on the bottom surface. Figure 5.16 also notice that the flow is fully separated from the top surface of the airship in the case of both model at 14^0 and 16^0 which gradually causes to stall. **Figure 5.17** and **Appendix D.4** showed the skin friction coefficient (C_f) 27% higher in planner wing, 14.28 % higher in box wing configuration than the conventional configuration of the tail model due to increase of wetted area in wing configuration airship. However, the skin friction coefficient (C_f) The box wing produced 10% less compared to the planner wing configuration under the constraint of fixed volume and length of the airship hull. Consequently, the proposed

efficient wing configuration not reduced only friction drag but also reduced the ratio of component drags to the total drag.

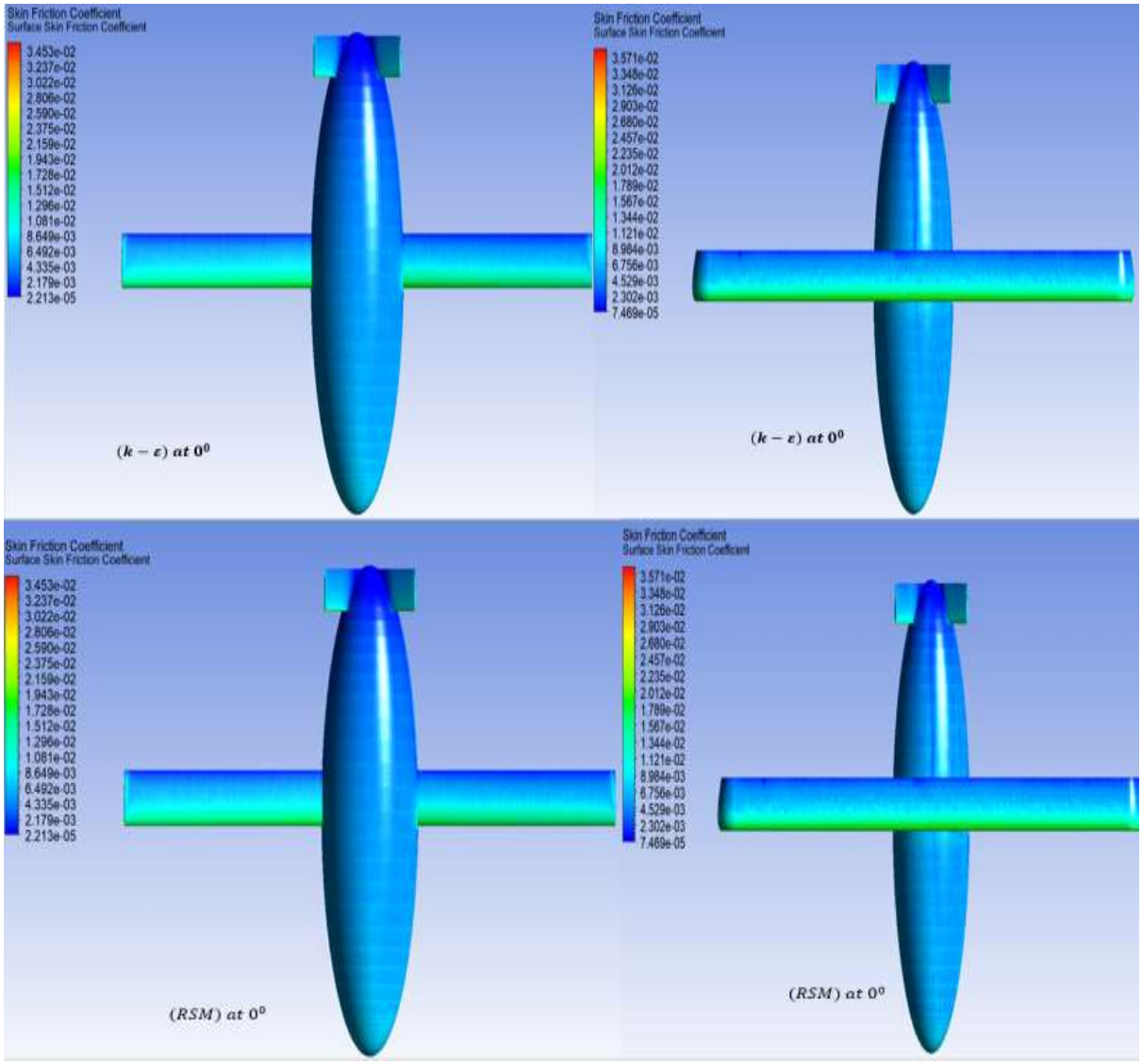

Figure 5.17: Contour of skin friction coefficient in two different turbulence models at *AOA* 0^0, *Re* = 4.2× 10^6, *M*=0.135 on planar and non-planer

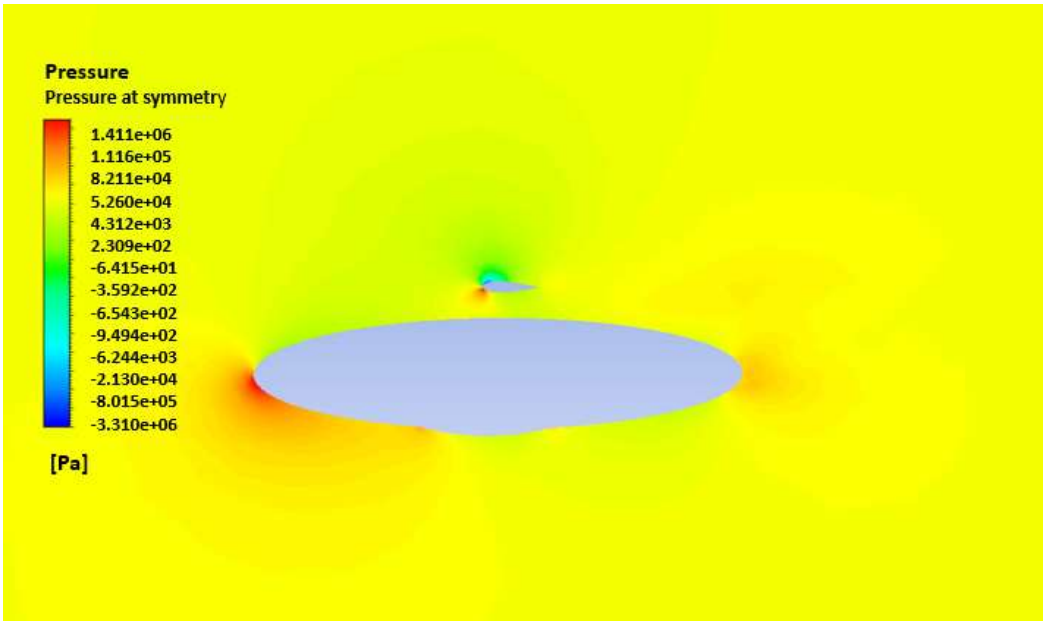

Figure 5.18: Contour total pressure of *SWBA* surface *(Pa)*

Therefore, the *EWBA* will generate a significant lift force allowing the aircraft to fly in the air. Thus, the combination of a qualitative and quantitative investigation of a novel *EWBA*, it has demonstrated comprehensive results in terms of aerodynamic behaviour in a cruise condition. The statistics aerodynamic qualitative results have been demonstrated through the visualization characteristics of *EWBA*. Indeed, including buoyancy lift, it represents a significant improvement of lift and aerodynamic efficiency, details of which are referred to further research.

5.4 Summary

Computational data must be verified before acceptance. The 6:1 prolate spheroid experimental data were used to validate the advances in *CFD*-based aerodynamic performance. Numerical computation and simulation with those configurations were carried out to investigate the aerodynamic behaviour of *EWBA* in the *CFD ANSYS Fluent* 16.1. The *CFD* numerical analysis is employed to get the lift force, drag force, and aerodynamic efficiency produced for four different airships by two turbulence models at cruise condition; compared them. Hence, the wing airship produced higher aerodynamic performance than the wingless airship. The analytical results and consequences of the computational error of the drag coefficient were reasonably acceptable. However, the $(k-\varepsilon)$ and *RSM* resulting data was fluctuating in some cases, as can be seen in Figures 5.10, 5.11, and 5.13. It would be improved by mesh retreatment if the intake boundary condition and layer separation could be resolved.

Moreover, the aerodynamic efficiency values in the numerical results were in respectable agreement with the theoretical results as well as prolate experimental results. The static stability is longitudinally stable for the box wing, as well as the planner wing airship. However, a significant error margin was found (7.53%) for the *RSM* model and (19.11%) for the $(k-\varepsilon)$ model, and although this is slightly higher than was anticipated, there is certainly room for improvement. In contrast, in Figures 5.14, and 5.15 the C_P contour revealed that the aerodynamic shape of the *EWBA* produces positive upward pressure. Hence, as can be seen in Figure 5.18, the total pressure would generate a positive lift to carry the *EWBA.*

Finally, the numerical data from two typical turbulent models and existing experimental results of aerodynamic efficiency parameters have shown that outstanding; especially in cruise flight, compared to the 6:1 prolate spheroid experimental results, which have been considered at (-4, -2, 0^0, 2, 4, 6, 8, 10, 12, 14,16,18 and 20) degree *AOA* in **Appendix D.3**. Thus, the concepts of a box wing configuration airship achieved the best aerodynamic performance amongst the convention airship and planer wing airship.

Chapter 6. Conclusion and Recommendations

This chapter concludes the efficient wing buoyant aircraft $(EWBA)$ design and verified with four different models via Computational fluid dynamics (CFD). The resulting data were considered with specific objectives and compared with the theoretical predictions. Secondly, the outcomes of computational fluid dynamics (CFD) analysis and data for the aerodynamic parameters were critically analysed and compared with wingless 6:1 prolate spheroid existing data as well as the analytical results obtained earlier in the research process to gain further understanding of the *EWBA's* aerodynamic properties. Indeed, the novel aircraft design derives from lighter-than-air (LTA) to heavier-than-air (HTA) aircraft; combines these technologies, it is a geometrically and aerodynamically unique design. Finally, this research summarised the depth analyses of the novel *EWBA* design, with the aerodynamics characteristic of four different configurations of an airship, including two wings buoyant hybrid airship, and recommendations as to future research.

6.1 An *EWBA* design and its improvement

The aircraft take-off weight (w_{To}) was computed using the traditional iterative technique, involving several cycles of iteration to converge on a suitable take-off weight for *EWBA*. This methodology is one of the most potent techniques for novel aircraft design. The cyclic method has been applied throughout the *EWBA* design in relation to payload weight, weight fraction, power loading, wing loading, *CAD, CFD.* (See Figure 1.6 in Chapter 1 for a schematic diagram of the enhancement process). This system sought to improve functionality and quality at every step of the design process in line with the design objectives, enabling each iteration's design values, fluctuations, and enhancements to be modified rapidly. Thus, the design enrichment process was time-efficient and less expensive to implement in the earliest phase of novel *EWBA* development.

6.2 Combined lift in a novel *EWBA*

In the investigation of the aerodynamic performance of the *EWBA*, the coefficient of lift $\left(C_{L_{aero}}\right)$ was determined to be 0.2913, 0.2073 non-planer and planer wing respectively, the $C_{L_{buoyant}}$ is 0.8408. Thus, in combination, the total lift coefficient $(C_{L_{total}})$ are 1.138 (non-planner), 1.0481(planer).

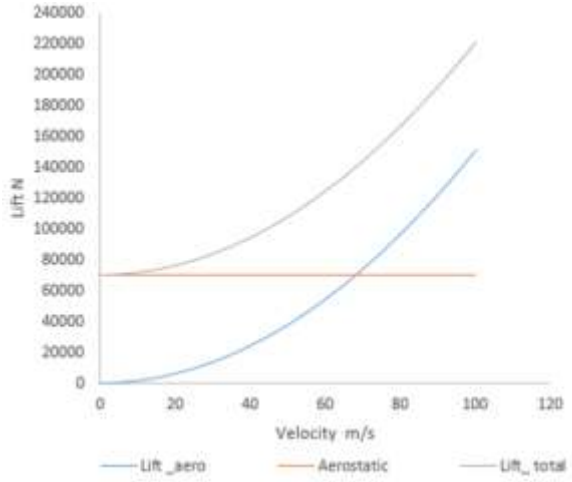

Figure 6.1: Aerostatic lift, aerodynamic lift, and combined lift

Figure 6.1 compares the aerostatic lift and aerodynamic lift at different velocities at sea level. Aerostatic lift remains constant because of the density of helium constant at the same pressure height. These forces are also subject to the volume of the hull, altitude, density, and temperature, even if velocity increases.

Figure 6.1 also evidences the exciting phenomenon that the *EWBA's* combined aerodynamic and aerostatic lift rapidly increases with increased velocity. This means that the *EWBA* becomes additionally fuel-efficient and even faster than a traditional airship. The *EWBA's* lift is generated primarily from the wing but also the lifting hull. The aerodynamic configuration of the box wing provides additional stability and aerodynamic efficiency for the *EWBA* at each stage of the flight path. Thus, the implications are that the *EWBA* with the concern of amalgamation method and balance of buoyancy ratio (BR) of 50.64:49.36. The analytical calculations only took into account for gas lift, not the surface lift. The *BR* is shown to be a stable parameter in the initial stage of development as an objective.

6.3 Conclusion and evaluation of the novel *EWBA*

Chapter 6 proves the research outline inferences from the objectives set out at the beginning of the thesis, contributions to knowledge, principal findings, limitations of the study, and recommendations for future research work. The research objective was to develop and optimise a conceptual design step by step for the novel configuration of *EWBA.* For this purpose, it was essential to design the aerostatic model and the aerodynamic model separately and then examined the aerodynamic behaviour associated with them both. The study also considered issues relating to the *EWBA's* aerodynamic efficiencies and stability. The proposed

model was efficiently investigated by *CFD* in $(k-\varepsilon)$ that belongs to Reynolds-average Navier-Stokes $(RANS)$ based turbulence model since this simulation is commonly used in the aerodynamic analysis. Then these results are evaluated with the full Reynolds Stress Models (RSM) which are second-moment closures for the aerodynamic fluid flow scenario.

The mathematical model of the *EWBA* optimised the maximum take-off weight via the traditional iterative method and rearranged them based on the weight fraction after several iterations. The empty weight fraction of the proposed new design is 0.5759; it is observed, almost similar to Quester Spirit aircraft; the comparative study of weight fraction can be seen in Table 3.2. This is an important coefficient since the *EWBA* is *HTA*, with a buoyancy ratio of 50.64:49.36. Thus, *CFD* is only employed for 5960.85 N lift force that balances by 607.63 kg of mass. Indeed, 49.36% of the total lift comes from helium, which has already been noted, that is not associated with further refill costs. This buoyancy ratio is one of the most encouraging findings in the *EWBA* design.

In this novel design, a *MATLAB* simulation script was used to determine the wing area and the power, along with the optimal design features. This computational method can greatly reduce the time costs during the preliminary design process. The power value obtained for the *EWBA* was in an acceptable region and comparable to similar types of conventional aircraft. Indeed, this method is convenient for scientific engineering design but had not been used before for buoyant airship design.

The comparison of aerofoils demonstrated that the *NACA* 23024 was the most appropriate aerofoil to achieve optimal aerodynamic performance with minimum drag and maximum efficiency. This investigation was conducted using *XFLR5*, which is a modern form of the *XFOIL* tool. Moreover, during wing design, an elliptical lift distribution along the wing was demonstrated. These investigations were computed by an advanced aerodynamics tool called lifting line theory (*LLT* for the straight wing, *VLM* for box wing) without considering the fuselage, flap, and other components' contributions to the *EWBA* and the adequate lift coefficient was obtained. This value represents the *EWBA*'s potential to lift the aircraft maximum take-off weight W_{To} (Chapter 3).

Secondly, the numerical analysis employed the Reynolds Average Navier-Stock $(RANS)$ equation and applied it to the *k-ε* and *RSM* models. Both of them Turbulence model was efficient in representing the aerodynamic performance of planar wing buoyant airship $(PWBA)$ and efficient wing buoyant airship $(EWBA)$ with a high level of accuracy. The lift coefficient (C_L) in wing airship are 90% to 97% and 80% to 95% higher compared to the

prolate spheroid and tail model as respectively at positive *AOA*. On the other hand, the observation of the drag coefficient (C_D) is increased as parabolic as an increase of *AOA*. In comparison, the wing hull generated a higher drag with a contrast of the wingless hull body, it in a range between 15% to 45% because of induced drag produced by the wing in the wing hull. Since the wingless hull is originating to be donated most of the drag, due to the larger volume and surface of the hull.

In addition, the maximum lift-to-drag ratio $\left(\frac{C_L}{C_D}\right)_{max}$ was significantly improved at 8^0 *AOA* in the case of numerical simulation during *CFD* in both turbulence models (*k-ε* and *RSM*) regarding planar wing. However, the $\left(\frac{C_L}{C_D}\right)_{max}$ the ratio in the non-planner (box) wing was generated at 4^0 as concerns of $(k-\varepsilon)$ and (RSM), and results indicated that the efficient wing buoyant airship $(EWBA)$ produced higher efficiency than 6:1 prolate spheroid as well as the conventional configuration of the airship model in case of $(k-\varepsilon)$, in *RSM*. The $\left(\frac{C_L}{C_D}\right)_{max}$ ratio formed at low AOA (4^0) in honour of *EWBA*, since less induced drag compares to planar wing airship and tail configuration, it can be seen in Chapter 5. It is another optimistic achievement of this research. Although, the planner wing airship has merited with respect to aerodynamic efficiency among the 6:1 prolate spheroid and tail model.

Hence, it is a significant enhancement of aerodynamic efficiency and positive feasibility of the wing airship real test. Thus, the numerical results concerning the aerodynamic characteristics behaviour of a 6:1 spheroid prolate values were verified by the experimental results[73, 240]. The pitching moment curve slop showed the wing airship satisfied the condition of longitudinal static stability (Figure 5.13). Though, both wing airship has been shown larger pitching moment coefficient (C_M) than the wingless hull, it is also negative, which confirms that longitudinal static stability. Therefore, the aerodynamic performance of computational data was nearly identical to the experimental results in the case of a 6:1 prolate spheroid and the analytical results for both the turbulence model.

However, the numerical values slightly fluctuated in some cases, and there is certainly room for improvement. As for the pressure coefficient contour, the visual representations in Figures 5.14, and 5.15 (Chapter 5) demonstrated that the positive vertical upward pressure is sufficient to support the aerodynamic shape of the *EWBA*. A primary results base on *CFD* (Figure 5.16), velocity is increased as an increase of *AOA*, in certain *AOA*, the airflow is

separated and airship stall which was at (14^0) for wing airship, however, there is no sign of strolling in the wingless configuration for the selected *AOA.*

To summarise, this thesis has proposed a novel *EWBA* with outstanding *CFD* results, especially regarding aerodynamic performance in cruise flight. Nevertheless, there are still some issues that need to be addressed in the *EWBA* design. One issue concerns the aerodynamic performance during take-off, landing, and several altitudes due to the maximum weight and buoyancy difference at altitude. Another issue that remains to be considered is that the aerodynamic efficiency increases with the increased height from the bottom wing to the top wing. For conventional aircraft, such as the box wing and unconventionally linked wing aircraft configuration, most investigations in this regard have been conducted over several decades. A computational code has been developed in the present work to identify the lift distribution along the wing, which will help the researcher scrutinise and improve the joint wing for the *EWBA.* All in all, the novel *EWBA* represents a promising design concept with the potential for further assessment and refinement to produce an economical, lean, and green form of air transport.

6.3.1 Research contributions to knowledge in this field

The specific contributions of this research project to knowledge in the field of aerospace engineering are summarised below:

1. Establishing empty weight computing methods for a novel *EWBA.*
2. The evaluation and optimisation of an original wing configuration for the *EWBA.*
3. The box wing configuration achieved higher aerodynamic efficiency and longitudinal stability among the convention model.
4. Box wing airships have an advantage in terms of aerodynamic efficiency at low *AOA,* and it is produced less induced drag than panner wing hybrid airship
5. Full integration analyses of the *EWBA* as well as by parts evaluation. This comprehensive integration evaluation proved the advantageous features of *EWBA* concerning traditional concepts.

6.4 Further research

This thesis has advanced the understanding of the *EWBA's* aerodynamic properties, but there is room for more research and development of the novel aircraft to extend this

understanding and refine the model. The following section outlines the suggested research directions.

Future studies should focus on aerodynamic efficiency and seek to optimise the efficient wing height, and wingtip joined with different aerofoils. The aerodynamic properties could be improved by the span efficiency (e), which is proportional to the induced drag coefficient. Studies could investigate the efficient wing bridge height between upper and lower wings in order to assess aerodynamic efficiencies and span efficiencies. It could be kept continuous changed these heights to gain maximum aerodynamic efficiency, using the Lifting line theory (LLT) method, and an assigned wing sweep angle between 0^0 and 30^0 to check C_L and C_D from different angles of attack (AOA). The computational code developed during the investigation of the *EWBA's* lift can be modified for the vortex lattices method (VLM). The *VLM* method can determine optimal aerodynamic efficiency by investigating whether the induced drag coefficient increases or decreases as the distance of the top wing is increased by changes to the height of the wing.

These aerodynamic efficiency test results would then be compared with *CFD* results for each sweep angle. The *CFD* study itself should assess the freestream disturbance and effects of unsteady flow to probe the response of the *EWBA* to authentic ecological situations.

In addition, wind tunnel experiments are recommended to test the prototype to validate the numerical results and contribute to the critical analysis of the optimal aerodynamic parameters for the *EWBA*. The suggested approach to the traditional wind tunnel experiments is as follows:

1. Manufacture of a *3-D* prototype solid model was developed in S*olidworks* at scale ratios 1:7 to 1:20 using a *3-D* printer.
2. Test section set-up: 1.2 × 1.2 × 3m; velocity between 22 to 46 m/s (with different velocity); Reynolds number 4.2×10^6.

To conclude, the *EWBA* would potentially be a valuable asset to the aviation industry, particularly in light of the climate crisis. It brings technological innovation that dramatically reduces fuel costs and the ecological impact of air transport. Therefore, for pressing economic and environmental reasons, this novel aircraft design merits further exploration soon.

Chapter 7. References

[1] L. M. Nicolai, *Fundamentals of aircraft and airship design*. Reston, VA: Reston, VA : American Institute of Aeronautics and Astronautics, 2010-, 2010.

[2] T. Metlen, A. N. Palazotto, and B. Cranston, "Economic optimization of cargo airships," *CEAS Aeronautical Journal,* vol. 7, no. 2, pp. 287-298, 2016, doi: 10.1007/s13272-016-0188-1.

[3] A. Collozza and J. L. Dolce, "High- Altitude, Long- Endurance Airships for Coastal Surveillance - NASA/ TM- 2005- 213427," ed: Sponsoring Organization: NASA Glenn Research Center, 2005.

[4] H. Anwar Ul, A. Waqar, A. O. Ashraf, S. Erwin, and J. S. A. Mohamed, "Aerostatic and aerodynamic modules of a hybrid buoyant aircraft: an analytical approach," *International Islamic University Malaysia Engineering Journal,* vol. 16, no. 1, 2015.

[5] O. Seungyong, K. Sungchul, L. Kyungjoon, A. Sangchul, and K. Euntai, "Flying Display: Autonomous Blimp with Real-Time Visual Tracking and Image Projection," ed, 2006, pp. 131-136.

[6] S. C, C. A. and, and M. P, "Airship research and Development in the areas of Design, Structures, Dynamics and energy systems.," *international Journal of Aeronautical and space (IJASS),* vol. 13, no. 2, pp. 170-187, 2012.

[7] P. Tatham, C. Neal, and Y. Wu, "Hybrid cargo airships: a humanitarian logistic game changer?," *Journal of Humanitarian Logistics and Supply Chain Management,* vol. 7, no. 2, pp. 102-125, 2017, doi: 10.1108/JHLSCM-09-2016-0036.

[8] B. Stevenson, "Airlander testing falls behind after delay to funding," vol. 186, ed. London, 2014, p. 13.

[9] M. Morrison, "Airlander floats out and nears lift-off," *Flight International,* vol. 190, no. 5551, p. 9, 2016.

[10] M. Morrison, "After the fall, the only way is up for Airlander," *Flight International,* vol. 190, no. 5555, pp. 37-39, 2016.

[11] J. T. Pringle, "Unmanned aerial systems (UAS's) and aerial surveillance platforms, how to select the right tools during an oil spill response for tactical support and to provide better situational awareness," *41st AMOP Technical Seminar on Environmental Contamination and Response, AMOP 2018,* pp. 71-89, 2018.

[12] Z. Gao, D. Mu, Y. Zhong, and C. Gu, "Constrained Unscented Particle Filter for SINS/GNSS/ADS Integrated Airship Navigation in the Presence of Wind Field Disturbance," *Sensors.*, vol. 19, no. 3, p. 471, 2019, doi: 10.3390/s19030471.

[13] C. Pope, "The big lift," *Professional Engineering*, vol. 17, no. 8, pp. 24-25, 2004.

[14] A. Elfes, S. Bueno, M. Bergerman, E. de Paiva, J. Ramos, and J. Azinheira, "Robotic Airships for Exploration of Planetary Bodies with an Atmosphere: Autonomy Challenges," *Autonomous Robots*, vol. 14, no. 2, pp. 147-164, 2003, doi: 10.1023/A:1022227602153.

[15] T. Kusagaya, H. Kojima, and H. A. Fujii, "Estimation of Flyable Regions for Planetary Airships," *Journal of Aircraft*, vol. 43, no. 4, pp. 1177-1181, 2006, doi: 10.2514/1.18570.

[16] J. J. Santapietro, "Persistent wide area surveillance from an airship," *Aerospace and Electronic Systems Magazine, IEEE*, vol. 27, no. 6, pp. 11-16, 2012, doi: 10.1109/MAES.2012.6328548.

[17] G. Dorrington, "Development of an airship for tropical rain forest canopy exploration," *Aeronautical Journal*, vol. 109, no. 1098, pp. 361-372, 2005.

[18] E. Hygounenc, P. Soueres, and S. Lacroix, "The autonomous blimp project of LAAS-CNRS: Achievements in flight control and terrain mapping," *International Journal of Robotics Research*, vol. 23, no. 4-5, pp. 473-511, 2004, doi: 10.1177/0278364904042200.

[19] D. K. Schmidt, J. Stevens, and J. Roney, "Near- Space Station- Keeping Performance of a Large High- Altitude Notional Airship," *Journal of Aircraft*, vol. 44, no. 2, pp. 611-615, 2007, doi: 10.2514/1.24863.

[20] Y.-G. Lee, D.-M. Kim, and C.-H. Yeom, "Development of Korean High Altitude Platform Systems," *Int J Wireless Inf Networks*, vol. 13, no. 1, pp. 31-42, 2006, doi: 10.1007/s10776-005-0018-6.

[21] Y. Yang and Y. Yan, "Neural network gain-scheduling sliding mode control for three-dimensional trajectory tracking of robotic airships," *Proceedings of the Institution of Mechanical Engineers, Part I: Journal of Systems and Control Engineering*, vol. 229, no. 6, pp. 529-540, 2015, doi: 10.1177/0959651815570353.

[22] J. Gonzalo, D. López, D. Domínguez, A. García, and A. Escapa, "On the capabilities and limitations of high altitude pseudo-satellites," *Progress in aerospace sciences*, vol. 98, pp. 37-56, 2018, doi: 10.1016/j.paerosci.2018.03.006.

[23] H. AU, Asrarw, O. A.A, S. E, and A. J. M.(2014), "Conceptual Design of a Winged Hybrid Airship",," *American Institute of Aeronautics and Astronautics, AIAA-2014-2710.*

[24] G. A. Khoury and J. D. Gillett, *Airship technology*. Cambridge: Cambridge : Cambridge University Press, 1999.

[25] G. T. Agte J, Kunzi F, Match A, sato S, Suarez B and Yutko B, "Conceptual design of a hybrid lift Airship for intera - regional flexible Access transport," no. American Institute of Aeronautiecs and Astronautics (AIAA 2010-1391). 2010.

[26] F. Jelenciak, M. Gerke, and I. Masar, "Airship aerodynamics - Modeling principle of the aerodynamic forces by PEM method," ed, 2013, pp. 25-30.

[27] H. A. U, O. A. A, S. E, and A. J. M, "A Novel Design of a hybrid buoyant aircraft - A potential greener Solution for Inter connectivity of Malasian Island.," *International Islamic University Malaysia (IIUM).50728 Kuala Lumpur, Malaysia.*

[28] A. U. Haque, W. Asrar, A. A. Omar, E. Sulaeman, and M. J. S. Ali, "Preliminary aerodynamic and static stability analysis for hybrid buoyant aerial vehicles at low speeds using digital DATCOM," *Canadian Aeronautics and Space Journal,* vol. 61, no. 3, pp. 51-60, 2015, doi: 10.5589/q16-001.

[29] K. Spela, B. Tanja, C. Maja, F. Gregor, S. Gregor, and C. Uros, "Safety aspects of atmospheric pressure helium plasma jet operation on skin: In vivo study on mouse skin," *PLoS ONE,* vol. 12, no. 4, p. e0174966, 2017, doi: 10.1371/journal.pone.0174966.

[30] H. Tomáš, Č. Jiří, Š. Karel, and O. Jana, "Advantages and Disadvantages of Substitution of Helium as Carrier Gas in Gas Chromatography by Hydrogen. Part I. - Technical and Safety Aspects," *Kvasný průmysl,* vol. 59, no. 6, pp. 162-166, 2013, doi: 10.18832/kp2013015.

[31] Obert and E., *Aerodynamic Design of Transport aircraft.* Delft: IOS Press, 2009.

[32] A. Abbas, J. de Vicente, and E. Valero, "Aerodynamic technologies to improve aircraft performance," *Aerospace Science and Technology,* vol. 28, no. 1, pp. 100-132, 2012, doi: 10.1016/j.ast.2012.10.008.

[33] M. H. Sadraey, *Aircraft design : a systems engineering approach*. Chichester, West Sussex, U.K.: Chichester, West Sussex, U.K. : Wiley, 2013.

[34] M. H. Sadraey, *Aircraft Design a Systems Engineering Approach.* New Hampshire, USA.: Daniel Webster college, 2013.

[35] R. R. Boyd, "Performance of Hybrid Air Vehicles," 2002.

[36] K.S. Zhang, Z.H. Han, and B.F. Song, "Flight Performance Analysis of Hybrid Airship: Revised Analytical Formulation," *Journal of Aircraft,* vol. 47, no. 4, pp. 1318-1330, 2010, doi: 10.2514/1.47294.

[37] Kreider, J, and F, "Mathematical Modeling of High Altitude Balloon Performance," presented at the AIAA-75-1385, Albuquerque NM, 1975.

[38] C. Harrington, "Near-space airships - Plugging the gap," *Jane's Defence Weekly,* no. OCT., 2006.

[39] A. United States Committee on Extension to the Standard, *U.S. standard atmosphere: 1962; ICAO standard atmosphere to 20 kilometers; proposed ICAO extension to 32 kilometers; tables and data to 700 kilometers*. Washington: U.S. Govt. Print. Off., 1962.

[40] S. United and A. United States Committee on Extension to the Standard, "U.S. standard atmosphere," *U.S. standard atmosphere,* 1976.

[41] C. M. Snell and A. M. Heiser, "Air mass determinations from the u.s. standard atmosphere," *Publications of the Astronomical Society of the Pacific,* vol. 80, no. 474, pp. 336-338, 1968.

[42] G. Keating, L. Chiou, and N. Hsu, "Improved ozone reference models for the COSPAR International Reference Atmosphere," *Advances in Space Research, Oxford, England,* vol. 18, no. 9/10, pp. 11-58, 1996, doi: 10.1016/0273-1177(96)00050-6.

[43] J. M. Forbes, M. E. Hagan, and K. S. W. Champion, "Neutral temperatures from Thomson scatter measurements: Comparisons with the CIRA(1972)," *Advances in Space Research,* vol. 3, no. 1, pp. 125-128, 1983, doi: 10.1016/0273-1177(83)90216-8.

[44] E. Shettle *et al.*, "POAM II: Early results and comparisons with the COSPAR international reference atmosphere ozone models," *Cospar International Reference Atmosphere (Cira), Pt Iii,* vol. 18, no. 9/10, pp. 311-314, 1996, doi: 10.1016/0273-1177(96)00063-4.

[45] A. H. Oort, *Global atmospheric circulation statistics, 1958-1973*. Rockville, Md: U.S. Dept. of Commerce, National Oceanic and Atmospheric Administration ; Washington, D.C.: U.S. Dept. of Commerce, National Oceanic and Atmospheric Administration, 1983.

[46] N. M. Gavrilov, A. V. Koval, A. I. Pogoreltsev, and E. N. Savenkova, "Numerical modeling of inhomogeneous orographic wave influence on planetary waves in the middle atmosphere," *Advances in Space Research,* vol. 51, no. 11, pp. 2145-2154, 2013, doi: 10.1016/j.asr.2012.12.024.

[47] A. Dumas, M. Trancossi, and M. Madonia, "Effect of altitude and temperature on volume control of an hydrogen airship," vol. 7, ed, 2012, pp. 499-512.

[48] H. K. Kallmann-Bijl and W. L. Sibley, "Diurnal variation of temperature and particle density between ~100 km and ~500 km," *Planetary and Space Science,* vol. 11, no. 12, pp. 1379-1394, 1963, doi: 10.1016/0032-0633(63)90105-3.

[49] M. C. LoPresto and D. A. Jacobs, "An exercise in modelling using the us standard atmosphere," *Physics Education,* vol. 42, no. 1, pp. 76-80, 2007, doi: 10.1088/0031-9120/42/1/010.

[50] "Announcement of Committee on Extension to the Standard Atmosphere," *Journal of Geophysical Research,* vol. 62, no. 1, pp. 172-172, 1957, doi: 10.1029/JZ062i001p00172-03.

[51] N. Conklin, "Air Mobility Liaison Officer Promotions: Perception and Reality," *Air & Space Power Journal,* vol. 32, no. 1, pp. 34-51, 2018.

[52] "Royal Navy launches centenary of Naval Aviation," *Aircraft Engineering and Aerospace Technology,* vol. 81, no. 4, 2009, doi: 10.1108/aeat.2009.12781daf.006.

[53] K. Chiba, "Feasibility studies on a high-altitude captive lighter-than-air platform system," 2015.

[54] J. Wilson, "A new era for airships," *Aerospace America,* vol. 42, no. 5, pp. 27-31, 2004.

[55] J. Winslow, H. Otsuka, B. Govindarajan, and I. Chopra, "Basic Understanding of Airfoil Characteristics at Low Reynolds Numbers (104–105)," *Journal of Aircraft,* vol. 55, no. 3, pp. 1050-1061, 2018, doi: 10.2514/1.C034415.

[56] A. S. M. Al-Obaidi, "Effect of atmospheric altitude on the drag of wing at subsonic and supersonic speeds," *Journal of engineering science & technology.,* vol. 12, no. Special Issue 2, pp. 71-83, 2017.

[57] Schmitz, F., and W., "Aerodynamics of the Model Airfoil Part1," *Airfoil Measurements, Translated from German, Redstone Scientific information Center RSIC-721,,* pp. 42-44, Nov.1967.

[58] J. Mueller, "Design and Analysis of Optimal Ascent Trajectories for Stratospheric Airships," Y. J. Zhao, W. Garrard, D. Gebre, and M. Jovanovic, Eds., ed: ProQuest Dissertations Publishing, 2013.

[59] Seling, M, and S, "The design of Airfoil at low Reynold Number," *AIAAA, Published by H.A Stokely, 1504 North Horsehoe Circle, Virginia Beach, VA23451, U.S.A,* vol. 85-4416, July 1984.

[60] S. F. Hoerner, *Fluid- dynamic drag: practical information on aerodynamic drag and hydrodynamic resistance* (Aerodynamic drag). Midland Park, N. J., 1958.

[61] Hoerner, S, and F, "Fluid Dynamic Lift," *L.A. Hoerner, 2nd ed,,* pp. 42-44, 1985.

[62] Mueller *et al.*, "An overview of micro aitvehicles aerodynamics," *Prog. Asronaut. Aeronaut,* vol. 195,1, 2001.

[63] Mueller, T, and J, "Aerodynamic measurements at low Reynolds Numbers for fixed wing Micro -Air Vehicles, "RTO AVT/VKI special course on Development and operation of UAVs for Military and civil Application, Von Karman Ins, Brussels," *Prog. Asronaut. Aeronaut,* vol. 6, no. 1-21, sep 1999.

[64] Mueller *et al.*, "Experimental studies of Separation on a Two -Dimensional Airfoil at Low Reynolds Number," *AIAA,* vol. 20, no. 4, pp. 457-463, sep 1999, doi: 10.2514/3.51095.

[65] I. Kroo, "DRAG DUE TO LIFT: Concepts for Prediction and Reduction," in *Annu. Rev. Fluid Mech.* vol. 33, ed, 2001, pp. 587-617.

[66] G. Andreas and F. F. Hermann, "Active Control of Laminar Separation: Simulations, Wind Tunnel, and Free-Flight Experiments," *Aerospace,* vol. 5, no. 4, p. 114, 2018, doi: 10.3390/aerospace5040114.

[67] I. H. A. Abbott, *Theory of wing sections : including a summary of airfoil data*, [New ed.], Dover ed. ed. New York: New York : Dover Publications, 1959, 1959.

[68] R. T. Gonçalves, G. R. Franzini, G. F. Rosetti, J. R. Meneghini, and A. L. C. Fujarra, "Flow around circular cylinders with very low aspect ratio," *Journal of Fluids and Structures*, vol. 54, pp. 122-141, 2015, doi: 10.1016/j.jfluidstructs.2014.11.003.

[69] X. L. Wang, "Research on shape of airship hull," *Yuhang Xuebao/Journal of Astronautics,* vol. 32, no. 3, pp. 457-461, 2011, doi: 10.3873/j.issn.1000-1328.2011.03.001.

[70] D. Küchemann, *The aerodynamic design of aircraft*. Reston, Virginia : Published by the American Institute of Aeronautics and Astronautics, Inc., 2012, 2012.

[71] H. Gagnon and D. Zingg, "Aerodynamic Optimization Trade Study of a Box- Wing Aircraft Configuration," *Journal Of Aircraft,* vol. 53, no. 4, pp. 971-981, 2016, doi: 10.2514/1.C033592.

[72] Y. Xiong, H. Guan, and C. Wu, "Unsteady analysis of six-DOF motion of a 6:1 prolate spheroid in viscous fluid," *Science China Physics, Mechanics & Astronomy,* vol. 60, no. 11, pp. 1-17, 2017, doi: 10.1007/s11433-017-9071-y.

[73] C. J. Chesnakas, D. Taylor, and R. L. Simpson, "Detailed Investigation of the Three-Dimensional Separation About a 6:1 Prolate Spheroid," *AIAA Journal,* vol. 35, no. 6, pp. 990-999, 1997, doi: 10.2514/2.208.

[74] C. Chesnakas and R. Simpson, "Detailed investigation of the three-dimensional separation about a 6:1 prolate spheroid," *AIAA Journal,* vol. 35, no. 6, pp. 990-999, 1997.

[75] T. Han and V. C. Patel, "Flow separation on a spheroid at incidence," *J. Fluid Mech.,* vol. 92, no. 4, pp. 643-657, 1979, doi: 10.1017/S002211207900080X.

[76] M. Tobak and D. J. Peake, "Topology of Three-Dimensional Separated Flows," *Annu. Rev. Fluid. Mech.,* vol. 14, no. 1, pp. 61-85, 1982, doi: 10.1146/annurev.fl.14.010182.000425.

[77] K. C. Wang, "Boundary layer over a blunt body at low incidence with circumferential reversed flow," *J. Fluid Mech.,* vol. 72, no. 1, pp. 49-65, 1975, doi: 10.1017/S0022112075002935.

[78] T. Cebeci and W. Su, "Separation of three-dimensional laminar boundary layers on a prolate spheroid," *J. Fluid. Mech.,* vol. 191, no. -1, pp. 47-77, 1988, doi: 10.1017/S002211208800151X.

[79] L. A. Yates and G. T. Chapman, "Streamlines, vorticity lines, and vortices around three-dimensional bodies," *AIAA Journal,* vol. 30, no. 7, pp. 1819-1826, 1992, doi: 10.2514/3.11142.

[80] X. Zhang, C. Pan, J. Shen, and J. Wang, "Effect of surface roughness element on near wall turbulence with zero-pressure gradient," *Science China Physics, Mechanics & Astronomy,* vol. 58, no. 6, pp. 1-8, 2015, doi: 10.1007/s11433-015-5677-4.

[81] K. C. Wang, "Separation Patterns of Boundary Layer over an Inclined Body of Revolution," *AIAA Journal,* vol. 10, no. 8, pp. 1044-1050, 1972, doi: 10.2514/3.50292.

[82] K. C. Wang, H. C. Zhou, C. H. Hu, and S. Harrington, "Three-Dimensional Separated Flow Structure over Prolate Spheroids," *Proceedings of the Royal Society of London. Series A, Mathematical and Physical Sciences (1934-1990),* vol. 429, no. 1876, pp. 73-90, 1990, doi: 10.1098/rspa.1990.0052.

[83] A. W. Cary, M. Yousuf, P. Li, and M. Mani, "Current practice unstructured grid CFD results for 3rd AIAA High Lift Prediction Workshop," no. 210059, p. 252, 2018, doi: 10.2514/6.2018-1037.

[84] C. Chesnakas and R. Simpson, "Full three-dimensional measurements of the cross-flow separation region of a 6:1 prolate spheroid," *Experimental Methods and their*

Applications to Fluid Flow, vol. 17, no. 1-2, pp. 68-74, 1994, doi: 10.1007/BF02412805.

[85] C. Fureby and D. Norrison, "RANS, DES and LES of the Flow Past the 6:1 Prolate Spheroid at 10° and 20° Angle of Incidence," p. 625, 2019, doi: 10.2514/6.2019-0085.

[86] S. Vogel, *Life in moving fluids : the physical biology of flow*. Princeton, N. J.: Princeton, N. J. : Princeton U. P., 1983, 1983.

[87] R. Huyssen, E. Mathews, L. Liebenberg, and G. Spedding, "On the wing density and the inflation factor of aircraft," *The Aeronautical Journal*, vol. 120, no. 1224, pp. 291-312, 2016, doi: 10.1017/aer.2015.12.

[88] "Santos-Dumont's Airships," ed. New York, N.Y., 1904, p. BR139.

[89] F. Nicolosi, P. Della Vecchia, and S. Corcione, "Design and aerodynamic analysis of a twin-engine commuter aircraft," *Aerospace Science and Technology*, vol. 40, pp. 1-16, 2015, doi: 10.1016/j.ast.2014.07.018.

[90] S. Dodbele, C. P. Van Dam, P. M. H. W. Vijgen, and B. J. Holmes, "Shaping of airplane fuselages for minimum drag," *Journal of Aircraft*, vol. 24, no. 5, pp. 298-304, 1987, doi: 10.2514/3.45444.

[91] T. Lutz and S. Wagner, "Drag Reduction and Shape Optimization of Airship Bodies," *Journal of Aircraft*, vol. 35, no. 3, pp. 345-351, 1998, doi: 10.2514/2.2313.

[92] M. I. Alam, "Surrogate based shape optimization of airship envelopes," *24th AIAA Aerodynamic Decelerator Systems Technology Conference, 2017*, p. 12, 2017.

[93] L. Y, N. M, and S. I, "Airship dynamic modelling: A literature review," *Progess in aerospace Science*, pp. 217-239, 2011.

[94] A. R. Verma, K. K. Sagar, and P. Priyadarshi, "Optimum Buoyant and Aerodynamic Lift for a Lifting-Body Hybrid Airship," *Journal of aircraft*, vol. 51, no. 5, pp. 1345-1350, 2014, doi: 10.2514/1.C032038.

[95] D. Fink, "Hybrid heavy-lift vehicle under study (airship-lifting body-conventional wing combination)," *Aviation Week and Space Technology*, vol. 101, pp. 49-51, 1974.

[96] G. Warwick, "Managed Buoyancy Gives Airship Lift," *Aerospace Daily & Defense Report*, vol. 252, no. 34, pp. 6-6, 2015.

[97] M. Tischler, R. Ringland, and H. Jex, "Heavy- lift airship dynamics," *Journal of Aircraft*, vol. 20, pp. 425-433, 1983.

[98] A. Cimarelli, M. Madonia, D. Angeli, and A. Dumas, "Aerodynamic Study of Advanced Airship Shapes," *Journal of aerospace engineering*, vol. 30, no. 3, p. 04016087, 2017, doi: 10.1061/(ASCE)AS.1943-5525.0000687.

[99] A. Dumas, M. Trancossi, M. Madonia, and I. Giuliani, "Multibody Advanced Airship for Transport," ed. Warrendale: Warrendale, PA: SAE International, 2011.

[100] M. Carrión, R. Steijl, G. N. Barakos, and D. Stewart, "Analysis of Hybrid Air Vehicles Using Computational Fluid Dynamics," *Journal of aircraft,* vol. 53, no. 4, pp. 1001-1012, 2016, doi: 10.2514/1.C033402.

[101] M. Tezzele, F. Salmoiraghi, A. Mola, and G. Rozza, "Dimension reduction in heterogeneous parametric spaces with application to naval engineering shape design problems," *Advanced modeling and simulation in engineering sciences.,* vol. 5, no. 1, 2018, doi: 10.1186/s40323-018-0118-3.

[102] G. E. Dorrington, "Drag of Spheroid-Cone Shaped Airship," *Journal of Aircraft,* vol. 43, no. 2, pp. 363-371, 2006, doi: 10.2514/1.14796.

[103] Munk, M, and M, "The aerodynamic force on airship hull," *NACA, TR-184,* 1924.

[104] S. P. Jones and J. D. Delaurier, "Aerodynamic estimation techniques for aerostats and airships," *Journal of aircraft,* vol. 20, no. 2, pp. 120-126, 1983, doi: 10.2514/3.44840.

[105] M. Judd, M. Vlajinac, and E. E. Covert, "Sting- free drag measurements on ellipsoidal cylinders at transition Reynolds numbers," *J. Fluid Mech.,* vol. 48, no. 2, pp. 353-364, 1971, doi: 10.1017/S0022112071001617.

[106] W. J. Duncan, *Mechanics of fluids,* 2nd ed. ed. London: London : Edward Arnold, 1970, 1970.

[107] E. Achenbach, "Experiments on the flow past spheres at very high Reynolds numbers," *J. Fluid Mech.,* vol. 54, no. 3, pp. 565-575, 1972, doi: 10.1017/S0022112072000874.

[108] J. R. Pannell and R. and Jones, "Experiments on a Model of an Airship of the 23 Class," *Aeronautical ResearchCommittee, His Majesty's Stationary Office, London,* vol. R&M, No. 456, April 1918.

[109] R. Jones and D. H. and Williams, "Experiments on a Model of Rigid Airship R.32 Together with a Comparison with the Results of Full Scale Turning Trials and Consideration of the Stability of the Ship," *Aeronautical ResearchCommittee, His Majesty's Stationary Office, London,* vol. R&M,No.779, April 1921.

[110] F. L. Thompson and H. W. and Kirschbaum, "The Drag Characteristics of Several Airships Determined By Deceleration Tests," *NACA TR 397,* March 1931.

[111] F. R. Goldschmied, "Aerodynamic Hull Design for HASPA LTA Optimization," *Journal of aircraft,* vol. 15, no. 9, pp. 634-638, 1978, doi: 10.2514/3.58418.

[112] A. F. Zahm, R. H. Smith, and F. A. and Louden, "Air Forces, Moments and Damping on Model of Fleet Airship Shenandoah," *NACA TR 215,* Nov. 1925.

[113] R. A. 5Frazer and A. G. and Gadd, "Tests on Two Streamline Bodies in a Compressed Air Tunnel," *Aeronautical Research Committee, His Majesty's Stationary Office, London,* no. R&M, No. 827, July 1922.

[114] R. Jones, D. H. Williams, and A. F. and Brown, "Tests on Two Streamline Bodies in a Compressed Air Tunnel," *Aeronautical Research Committee,His Majesty's Stationary Office, London,* no. R&M, No. 1710, April 1936.

[115] R. A. Frazer and L. F. G. Simmons, "Investigation of the Forces and Moments Upon a Complete Model Airship of Type S.S.Z. with an Analysis of the Effects of Full and Partial Rigging," *Aeronautical Research Committee,* no. R&M, No. 457, July 1918.

[116] E. Ower, "Some Aspects of the Mutual Interference Between Parts of Aircraft," *Aeronautical Research Committee, His Majesty's Stationary Office, London,* no. R&M, No. 1480, June 1932.

[117] P. Mi, "Aerodynamic and overall parameters analysis of buoyancy-lifting hybrid airship," *Beijing Hangkong Hangtian Daxue Xuebao/Journal of Beijing University of Aeronautics and Astronautics,* vol. 41, no. 6, pp. 1108-1116, 2015, doi: 10.13700/j.bh.1001-5965.2014.0404.

[118] K. Risse and E. Stumpf, "Conceptual aircraft design with hybrid laminar flow control," *CEAS Aeronaut J,* vol. 5, no. 3, pp. 333-343, 2014, doi: 10.1007/s13272-014-0111-6.

[119] T. Liu, W. W. Liou, and M. Schulte, "Aeroship: A Hybrid Flight Platform," *Journal of Aircraft,* vol. 46, no. 2, pp. 667-674, 2009, doi: 10.2514/1.39950.

[120] M. A. A. F. R. A. S. M.H. Lyon, "The Drag of Streamline Bodies The Relative Importance of Skin Friction and Pressure in Relation to Full‐Scale Design," *Aircraft Engineering,* vol. 6, no. 9, pp. 233-239, 1934, doi: 10.1108/eb029841.

[121] P. Liu, G.-Y. Fu, L.-J. Zhu, and X.-L. Wang, "Aerodynamic characteristics of airship Zhiyuan-1," *Journal of Shanghai Jiaotong University (Science),* vol. 18, no. 6, pp. 679-687, 2013, doi: 10.1007/s12204-013-1443-9.

[122] A. Ul Haque, W. A. Asrar, A. A. Omar, and E. Suleiman, "Wind Tunnel Testing on a Generic Model of a Hybrid Lifting Hull," *Journal of aerospace technology and management,* vol. 8, no. 4, pp. 467-474, 2016, doi: 10.5028/jatm.v8i4.645.

[123] A. Haque, W. Asrar, A. Omar, E. Sulaeman, and J. Ali, "Estimation of pitching moment of a hybrid lifting fuselage - disguised as hull of an airship," *Journal of Engineering and Applied Sciences,* vol. 11, no. 4, 2016.

[124] J. C. Holt, K. P. Garry, and T. Smith, "Investigation of the Aerodynamic Characteristics of a Lifting Body in Ground Proximity," p. 304, 2016, doi: 10.2514/6.2016-3881.

[125] X.-L. Wang, G.-Y. Fu, D.-P. Duan, and X.-X. Shan, "Experimental Investigations on Aerodynamic Characteristics of the ZHIYUAN-1 Airship," *Journal of Aircraft*, vol. 47, no. 4, pp. 1463-1468, 2010, doi: 10.2514/1.C000243.

[126] Von, Karman, Th, TrefFtz, and E, "Potentialstr omung um gegebene Tragflachenquerschnitte, Zeitschrift fur Flugtechnik und Motorluftschiffahrt," vol. 9, pp. 111-116, 1918.

[127] T. von Karman and J. M. Burgers, "General Aerodynamic Theory—Perfect Fluids," *Aerodynamic Theory, (W. F. Durand, Ed.) Berlin*, vol. 2, 1935.

[128] M. Munk, "General Theory of Thin Wing Sections, NACA Report 142, 1922. Elements of the Wing Section Theory and of the Wing Theory," *the Franklin Institute*, vol. Vol.193(6), pp. 855-855, 1924.

[129] L. Prandtl, "Berichtigung zur Tragflügeltheorie," *ZAMM Journal of applied mathematics and mechanics : Zeitschrift für angewandte Mathematik und Mechanik.*, vol. 10, no. 4, pp. 418-418, 1930, doi: 10.1002/zamm.19300100414.

[130] T. Von Kármán and H.-S. Tsien, "Lifting-line theory for a wing in non-uniform flow," *Quarterly of Applied Mathematics*, vol. 3, no. 1, pp. 1-11, 1945, doi: 10.1090/qam/12010.

[131] C. B. Millikan, "An Extended Theory of Thin Airfoils and Its Application to the Biplane Problem," *the Franklin Institute*, vol. Vol.211(3), pp. 394-395, 1931.

[132] J. Luckring, "The discovery and prediction of vortex flow aerodynamics," *The Aeronautical Journal*, vol. 123, no. 1264, pp. 729-804, 2019, doi: 10.1017/aer.2019.43.

[133] A. L. Canamar and L. Smrcek, "Seaplane Conceptual Design," ed, 2011.

[134] E. a. Levis, "Design synthesis of advanced technology, flying wing seaplanes," [Great Britain] : Imperial College London (University of London), 2012., 2012.

[135] T. I. Saeed, W. R. Graham, and C. A. Hall, "Boundary-Layer Suction System Design for Laminar-Flying-Wing Aircraft," *Journal of aircraft*, vol. 48, no. 4, pp. 1368-1379, 2011, doi: 10.2514/1.C031283.

[136] M. T. Montgomery and R. K. Smith, "Recent Developments in the Fluid Dynamics of Tropical Cyclones," *Annu. Rev. Fluid Mech.*, vol. 49, no. 1, pp. 541-574, 2017, doi: 10.1146/annurev-fluid-010816-060022.

[137] J. D. Anderson and S. Corda, "Numerical lifting line theory applied to drooped leading-edge wings below and above stall," *Journal of Aircraft*, vol. 17, no. 12, pp. 898-904, 1980, doi: 10.2514/3.44690.

[138] W. F. Phillips and D. O. Snyder, "Modern Adaptation of Prandtl's Classic Lifting-Line Theory," *Journal of Aircraft,* vol. 37, no. 4, pp. 662-670, 2000, doi: 10.2514/2.2649.

[139] A. Somerville, M. Marino, G. Baxter, and G. Wild, "Understanding box wing aircraft: Essential technology to improve sustainability in the aviation industry," *Aviation.,* vol. 20, no. 3, pp. 129-136, 2016, doi: 10.3846/16487788.2016.1195076.

[140] F. A. Khan and H. Åkerstedt, "Preliminary aerodynamic investigation of box- wing configurations using low fidelity codes," ed, 2010.

[141] J. Garcia-Benitez, C. Cuerno-Rejado, and R. Gomez-Blanco, "Conceptual design of a nonplanar wing airliner," *Aircraft Engineering and Aerospace Technology: An International Journal,* vol. 88, no. 4, pp. 561-571, 2016, doi: 10.1108/AEAT-11-2014-0204.

[142] P. K. Chang, *Separation of flow*. Oxford: Oxford : Pergamon, 1970, 1970.

[143] A. Cavalieri and P. Soviero, "Analysis of compressible potential flow over aerofoils using the dual reciprocity method," *Aeronautical Journal,* vol. 116, no. 1178, pp. 391-406, 2012.

[144] C.-C. Yang, "Low Speed Virtual Wind Tunnel simulation for educational studies in introducing Computational Fluid Dynamics and flow visualization," R. Taghavi, D. Downing, and S. Farokhi, Eds., ed: ProQuest Dissertations Publishing, 2008.

[145] T. Lee and Y. Y. Su, "Low Reynolds number airfoil aerodynamic loads determination via line integral of velocity obtained with particle image velocimetry," *Experiments in fluids,* vol. 53, no. 5, pp. 1177-1190, 2012, doi: 10.1007/s00348-012-1353-x.

[146] A. Elfes *et al.*, "An Autonomy Architecture for Aerobot Exploration of the Saturnian Moon Titan," ed, 2008, pp. 1-9.

[147] W. King, "Air flow and particle trajectories around aircraft fuselages. I - Theory," *Journal of Atmospheric and Oceanic Technology (0739-0572),* vol. 1, pp. 5-13, 1984.

[148] W. Chin, "Thin airfoil theory for planar inviscid shear flow," *ASME, Transactions, Journal of Applied Mechanics,* vol. 51, pp. 19-26, 1984.

[149] Z.-y. Liang, P. Cui, and G.-b. Zhang, "An inverse design method for 2D airfoil," *Thermophysics and Aeromechanics,* vol. 17, no. 1, pp. 51-56, 2010, doi: 10.1134/S0869864310010051.

[150] Q. Wang, J. Chen, X. Pang, S. Li, and X. Guo, "A new direct design method for the medium thickness wind turbine airfoil," *Journal of Fluids and Structures,* vol. 43, pp. 287-301, 2013, doi: 10.1016/j.jfluidstructs.2013.08.003.

[151] H. K. Cheng, "Airfoil Design and Data (Richard Eppler)," *SIAM Review,* vol. 34, no. 2, pp. 331-333, 1992, doi: 10.1137/1034070.

[152] O. Gur, J. A. Schetz, and W. H. Mason, "Aerodynamic Considerations in the Design of Truss-Braced- Wing Aircraft," *Journal of Aircraft,* vol. 48, no. 3, pp. 919-939, 2011, doi: 10.2514/1.C031171.

[153] F. Zhu, "Geometric Parameterisation and Aerodynamic Shape Optimisation," ed: University of Sheffield;Mechanical Engineering (Sheffield); 2014, 2014.

[154] E. Torenbeek, *Synthesis of subsonic airplane design : an introduction to the preliminary design of subsonic general aviation and transport aircraft, with emphasis on layout, aerodynamic design, propulsion and performance*, Student ed. ed. Delft : Dordrecht ; London: Delft : Delft University Press ; Dordrecht ; London : Kluwer, 1982, 1982.

[155] J. Pérez-Álvarez, C. Cuerno-Rejado, and J. Meseguer, "Aerodynamic parametric analysis of an unconventional joined- wing aircraft configuration," *Proceedings of the Institution of Mechanical Engineers, Part G: Journal of Aerospace Engineering,* vol. 230, no. 10, pp. 1917-1933, 2016, doi: 10.1177/0954410015620444.

[156] G. McKechnie and A. Rizzi, "Wing Design for the ECO1 Aircraft," ed, 2015.

[157] L. Demasi, G. Monegato, E. Rizzo, R. Cavallaro, and A. Dipace, "Minimum Induced Drag Theorems for Joined Wings, Closed Systems, and Generic Biwings: Applications," *J Optim Theory Appl,* vol. 169, no. 1, pp. 236-261, 2016, doi: 10.1007/s10957-015-0850-5.

[158] G. Chen, B. Chen, P. Li, P. Bai, and C. Ji, "Study of Aerodynamic Configuration Design and Wind Tunnel Test for Solar Powered Buoyancy-lifting Vehicle in the Near-space," *Procedia Engineering,* vol. 99, pp. 67-72, 2015, doi: 10.1016/j.proeng.2014.12.509.

[159] J. Garcia-Benitez, C. Cuerno-Rejado, and R. Gomez-Blanco, "Conceptual design of a nonplanar wing airliner," *Aircraft Engineering and Aerospace Technology,* vol. 88, no. 4, pp. 561-571, 2016, doi: 10.1108/AEAT-11-2014-0204.

[160] J. M. Housner and M. Stein, "Flutter analysis of swept-wing subsonic aircraft with parameter studies of composite wings - NASA-TN-D-7539," ed: Sponsoring Organization: NASA Langley Research Center, 1974.

[161] J. S. Bae, D. J. Inman, and I. Lee, "Effects of structural nonlinearity on subsonic aeroelastic characteristics of an aircraft wing with control surface," *Journal of Fluids and Structures,* vol. 19, no. 6, pp. 747-763, 2004, doi: 10.1016/j.jfluidstructs.2004.04.005.

[162] R. Cavallaro, R. Bombardieri, L. Demasi, and A. Iannelli, "PrandtlPlane Joined Wing: Body freedom flutter, limit cycle oscillation and freeplay studies," *Journal Of Fluids And Structures*, vol. 59, pp. 57-84, 2015, doi: 10.1016/j.jfluidstructs.2015.08.016.

[163] L. Prandtl, "Induced drag of multiplanes," ed, 1924.

[164] P. O. Jemitola, J. Fielding, and P. Stocking, "Joint fixity effect on structural design of a box wing aircraft," *Aeronautical Journal*, vol. 116, no. 1178, pp. 363-372, 2012.

[165] L. W. Traub and A. Nurick, "Effects of wing-tip vortex flaps," *Journal of Aircraft*, vol. 30, no. 4, pp. 557-560, 1993, doi: 10.2514/3.46382.

[166] J. L. Speyer, "High-altitude, solar-powered, formation-enhanced UAV development program," *Collection of Technical Papers - InfoTech at Aerospace: Advancing Contemporary Aerospace Technologies and Their Integration*, vol. 4, pp. 2335-2347, 2005.

[167] A. Ul Haque, W. Asrar, A. A. Omar, E. Sulaeman, and J. S. Mohamed Ali, "Stability and Takeoff Ground Roll Issues of Hybrid Buoyant Aircraft," *Applied Mechanics and Materials*, vol. 660, pp. 503-507, 2014, doi: 10.4028/www.scientific.net/AMM.660.503.

[168] J. Roskam, "Airplane flight dynamics and automatic flight controls. Part 1, Rigid airplane flight dynamics (open loop)," ed. Ottawa, Ka: Ottawa, Ka : Roskam Aviation and Engineering Corporation, 1979.

[169] C. Cuerno-Rejado, L. Alonso-Albir, and P. Gehse, "Conceptual design of a medium-sized joined-wing aircraft," *Proceedings of the Institution of Mechanical Engineers, Part G: Journal of Aerospace Engineering*, vol. 224, no. 6, pp. 681-696, 2010, doi: 10.1243/09544100JAERO648.

[170] T. J. Mueller, *Fixed and Flapping Wing Aerodynamics for Micro Air Vehicle Applications [electronic resource]* (Progress in Astronautics and Aeronautics). Reston: Reston : American Institute of Aeronautics and Astronautics, 2000, 2000.

[171] D. P. Raymer, *Aircraft design : a conceptual approach*, 5th ed. ed. Reston, VA: Reston, VA : American Institute of Aeronautics and Astronautics, c2012, 2012.

[172] L. Demasi, R. Cavallaro, and A. Razon, "Postcritical Analysis of Prandtl Plane Joined-Wing Configurations," *AIAA Journal*, vol. 51, no. 1, pp. 161-177, 2013, doi: 10.2514/1.J051700.

[173] J. Wolkovitch, "The joined wing - An overview ((aircraft tandem wings in diamond configurations))," vol. 23, J. Wolkovitch, Ed., ed, 1986, pp. 161-178.

[174] M. Kalinowski, "Structural Optimization of Box Wing Aircraft," *Archive of Mechanical Engineering,* vol. 62, no. 1, pp. 45-60, 2015, doi: 10.1515/meceng-2015-0003.

[175] Schiktanz, D, and, Schold, and D, "Box wing fundamentals- An aircraft design perspective.," *In: DGLR Dtsch Luft_und Raumfahrtkongress, Bonn, Germany,* pp. pp.601-615, 2011.

[176] K. Shields, "CFD applications in airship design," W. Huebsch, Ed., ed: ProQuest Dissertations Publishing, 2010.

[177] Z. Liu, H. Qu, H. Shi, G. Hu, and B.-S. Hyun, "Application of 2D numerical model to unsteady performance evaluation of vertical- axis tidal current turbine," *Journal of Ocean University of China. JOUC,* vol. 15, no. 6, pp. 977-986, 2016, doi: 10.1007/s11802-016-2995-8.

[178] R. D. P., *Aircraft Design: A conceptual approach* . Fourth ed. Virginia: AIAA, American Institute of Aeronautics and Astronautics,Inc, 2006, pp. pp777-779.

[179] E. Torenbeek, *Advanced aircraft design [electronic resource] : conceptual design, technology and optimization of subsonic civil airplanes*. Chichester : John Wiley & Sons, 2013, 2013.

[180] J. S. Letcher, "V-Wings and Diamond Ring-Wings of Minimum Induced Drag," *Journal of Aircraft,* vol. 9, no. 8, pp. 605-607, 1972, doi: 10.2514/3.59045.

[181] M. Nita and D. Scholz, "Preliminary aircraft cabin design to cabin design to cabin optimisation-part 1," *U.P.B. Sci. Bull,* vol. series D, 75(3). no. htt://www.fzt.hawhamburg.de/pers/scholz/operA/OPerA_PUB_-sci_Bull-D-75-3_13-07-01pdf,, 2013.

[182] C. P. Burgess, "Airship design," ed: New York: The Ronald Press Company, 1927.

[183] J. Roskam, "Airplane design," ed. Ottawa, Ka: Ottawa, Ka : Roskam Aviation and Engineering Corporation, 1990.

[184] T. Anderson and J. Shattuck, "Design-Based Research," *Educational Researcher,* vol. 41, no. 1, pp. 16-25, 2012, doi: 10.3102/0013189X11428813.

[185] (1993). *Incorporating biplane theory into a large, subsonic, all-cargo transport*.

[186] L. Demasi, G. Monegato, E. Rizzo, R. Cavallaro, and A. Dipace, "Minimum Induced Drag Theorems for Joined Wings, Closed Systems, and Generic Biwings: Applications," *Journal of Optimization Theory and Applications,* vol. 169, no. 1, pp. 236-261, 2016, doi: 10.1007/s10957-015-0850-5.

[187] B. S. Anil Kumar, Ramalingaiah, S. Manjunath, and R. Ganganna, "Computational Investigation of Flow Separation over NACA 23024 Airfoil at 6 Million Free Stream Reynolds Number Using k-Epsilon Turbulence Model," *Materials Today: Proceedings*, vol. 5, no. 5, pp. 12632-12640, 2018, doi: 10.1016/j.matpr.2018.02.246.

[188] C. Douglas Aircraft, *USAF stability and control datcom*. Springfield, Va.: National Technical Information Service, 1975.

[189] J. Meng, M. Li, L. Zhang, M. Lv, and L. Liu, "Aerodynamic performance analysis of hybrid air vehicles with large Reynolds number," ed, 2019, pp. 403-409.

[190] T. Liu, W. Liou, and M. Schulte, "Aeroship: A Hybrid Flight Platform," *Journal of Aircraft*, vol. 46, no. 2, pp. 667-674, 2009, doi: 10.2514/1.39950.

[191] J. Mihm, C. Loch, and A. Huchzermeier, "Problem-solving oscillations in complex engineering projects," *Management Science*, vol. 49, no. 6, pp. 733-750, 2003, doi: 10.1287/mnsc.49.6.733.16021.

[192] D. Braha and Y. Bar-Yam, "The Statistical Mechanics of Complex Product Development: Empirical and Analytical Results," *Management Science*, vol. 53, no. 7, pp. 1127-1145, 2007, doi: 10.1287/mnsc.1060.0617.

[193] Q. Li, H. Wei, C. Yu, and S. Wang, "Model and Data Driven Complex Product Development: from V, Double Vs to Triple Vs," *2019 International Conference on Intelligent Computing, Automation and Systems (ICICAS)*, pp. 860-864, 2019, doi: 10.1109/ICICAS48597.2019.00185.

[194] L. Wang, C. Xiong, R. Wang, X. Wang, and D. Wu, "A novel method of Newton iteration-based interval analysis for multidisciplinary systems," *Science China Physics, Mechanics & Astronomy*, vol. 60, no. 9, pp. 1-16, 2017, doi: 10.1007/s11433-017-9068-5.

[195] R. Smith and P. Tjandra, "Experimental observation of iteration in engineering design," *Theory, Applications and Concurrent Engineering*, vol. 10, no. 2, pp. 107-117, 1998, doi: 10.1007/BF01616691.

[196] N. Pessanha Santos, V. Lobo, and A. Bernardino, "Two-stage 3D model-based UAV pose estimation: A comparison of methods for optimization," *Journal of field robotics.*, vol. 37, no. 4, pp. 580-605, 2020, doi: 10.1002/rob.21933.

[197] K. Clark, W. Chew, and T. Fujimoto, "Product development in the world auto industry," *Brookings papers on economic activity*, vol. 3, pp. 729-781, 1987.

[198] S. D. Eppinger, "Model-based Approaches to Managing Concurrent Engineering," *Journal of engineering design,* vol. 2, no. 4, pp. 283-290, 1991, doi: 10.1080/09544829108901686.

[199] P. Chusilp and Y. Jin, "Impact of Mental Iteration on Concept Generation," *Journal of Mechanical Design (Transactions of the ASME),* vol. 128, no. 1, pp. 14-25, 2006, doi: 10.1115/1.2118707.

[200] A. Engel and Y. Reich, "Advancing Architecture Options Theory: Six Industrial Case Studies," *Systems Engineering,* vol. 18, no. 4, pp. 396-414, 2015, doi: 10.1002/sys.21312.

[201] S. Suss and V. Thomson, "Optimal design processes under uncertainty and reciprocal dependency," *Journal of Engineering Design: Dependency modelling in complex system design,* vol. 23, no. 10-11, pp. 829-851, 2012, doi: 10.1080/09544828.2012.704546.

[202] R. McDonald, "Mission Performance Considered as Point Performance in Aircraft Design," *Journal of Aircraft,* vol. 48, no. 5, pp. 1576-1587, 2011, doi: 10.2514/1.C031290.

[203] R. Iovinelli, "Aviation environmental design tool," ed, 2011, pp. 1-18.

[204] J. A. Leger Monteiro, J. C. Páscoa, and C. M. Xisto, "Aerodynamic optimization of cyclorotors," *Aircraft engineering.,* vol. 88, no. 2, pp. 232-245, 2016, doi: 10.1108/AEAT-02-2015-0051.

[205] O. Dababneh and T. Kipouros, "A review of aircraft wing mass estimation methods," *Aerospace Science and Technology,* vol. 72, no. C, pp. 256-266, 2018, doi: 10.1016/j.ast.2017.11.006.

[206] R. Alligier, D. Gianazza, and N. Durand, "Machine Learning and Mass Estimation Methods for Ground-Based Aircraft Climb Prediction," *IEEE Transactions on Intelligent Transportation Systems,* vol. 16, no. 6, pp. 3138-3149, 2015, doi: 10.1109/TITS.2015.2437452.

[207] A. U. Haque, W. Asrar, A. A. Omar, E. Sulaeman, and J. S. M. Ali, "Assessment of engine′s power budget for hydrogen powered hybrid buoyant aircraft," *Propulsion and Power Research,* vol. 5, no. 1, pp. 34-44, 2016, doi: 10.1016/j.jppr.2016.01.008.

[208] A. Iwaniuk and W. Wiśniowski, "Optimization of small aircraft parameters in the initial phase of the project," *Proceedings of the Institution of Mechanical Engineers.,* vol. 231, no. 12, pp. 2248-2258, 2017, doi: 10.1177/0954410017716481.

[209] *Jane's all the world's aircraft*. Coulsdon: Coulsdon : Jane's Information Group, 2000, 2000.

[210] "Nondestructive Characterization for Composite Materials, Aerospace Engineering, Civil Infrastructure, and Homeland Security 2013," vol. 8694, ed, 2013.

[211] M. Alexei Serna, "Systems Engineering Analysis," *Revista Antioqueña de las Ciencias Computacionales y la Ingeniería de Software (RACCIS)*, vol. 3, no. 1, pp. 6-11, 2013.

[212] T. Long and L. Liu, "Comprehensive study of typical metamodel methods applied in aircraft multidisciplinary design optimization," *Applied Mechanics and Materials*, vol. 110-116, pp. 3031-3039, 2012, doi: 10.4028/www.scientific.net/AMM.110-116.3031.

[213] M. Hassanalian, H. Khaki, and M. Khosravi, "A new method for design of fixed wing micro air vehicle," *Proceedings of the Institution of Mechanical Engineers.*, vol. 229, no. 5, pp. 837-850, 2015, doi: 10.1177/0954410014540621.

[214] J. D. Anderson and T. H. Cho, "Engineering analysis of drooped leading-edge wings near stall," *Journal of Aircraft*, vol. 21, no. 6, pp. 446-448, 1984, doi: 10.2514/3.44990.

[215] V. M. Falkner, "Rotary Derivatives in Yaw," *Aircraft Engineering and Aerospace Technology*, vol. 23, no. 2, pp. 44-54, 1951, doi: 10.1108/eb031999.

[216] J. P. Giesing, T. P. Kalman, and W. P. Rodden, "Subsonic Unsteady Aerodynamics for General Configurations. Part 2. Volume 1. Application of the Doublet-Lattice Method and the Method of Images to Lifting-Surface/Body Interference," C. A. Douglas Aircraft Co Long Beach, Ed., ed, 1972.

[217] Z. Öznalbant and M. Ş. Kavsaoğlu, "Flight control and flight experiments of a tilt-propeller VTOL UAV," *Transactions of the Institute of Measurement and Control*, vol. 40, no. 8, pp. 2454-2465, 2018, doi: 10.1177/0142331218754618.

[218] A. D. Andan, W. Asrar, and A. A. Omar, "Aerodynamics of a hybrid airship," vol. 1440, ed, 2012, pp. 154-161.

[219] E. J. Rodgers, "The neutral point in stability and control analysis," *Journal of Aircraft*, vol. 2, no. 1, pp. 33-38, 1965, doi: 10.2514/3.43615.

[220] R. C. Nelson, *Flight stability and automatic control*, 2nd ed., International ed. ed. Boston, Mass.: Boston, Mass. : WCB/McGraw-Hill, c1998, 1998.

[221] M. Milenković-Babić, M. Samardžić, V. Antonić, M. Marjanović, and V. Stefanović-Gobeljić, "Longitudinal stability characteristics of the LASTA airplane," *Aircraft Engineering and Aerospace Technology*, vol. 89, no. 6, pp. 911-919, 2017, doi: 10.1108/AEAT-02-2016-0026.

[222] F. Nicolosi and S. Corcione, "Commuter aircraft aerodynamic characteristics through wind tunnel tests," *Aircraft Engineering and Aerospace Technology*, vol. 88, no. 4, pp. 523-534, 2016, doi: 10.1108/AEAT-01-2015-0008.

[223] A. U. Haque, W. Asrar, A. A. Omar, E. Sulaeman, and M. J. S. Ali, "Effect of side wind on the directional stability and aerodynamics of a hybrid buoyant aircraft," vol. 40, ed, 2016, p. <xocs:firstpage xmlns:xocs=""/>.

[224] A. Ceruti, D. Gambacorta, and P. Marzocca, "Unconventional hybrid airships design optimization accounting for added masses," *Aerospace Science and Technology*, vol. 72, pp. 164-173, 2018, doi: 10.1016/j.ast.2017.10.042.

[225] J. Thibert and D. Arnal, "A review of ONERA aerodynamic research in support of a future supersonic transport aircraft," *Progress in Aerospace Sciences*, vol. 36, no. 8, pp. 581-627, 2000, doi: 10.1016/S0376-0421(00)00010-5.

[226] T. J. Takahashi, B. J. German, A. Shajanian, M. J. Daskilewicz, and S. Donovan, "Form Factor and Critical Mach Number Estimation for Finite Wings," *Journal of Aircraft*, vol. 49, no. 1, pp. 173-182, 2012, doi: 10.2514/1.C031466.

[227] Y. e. Savin Sergey and A. Ivlev Ivan, "Stability analysis of orthotropic rectangular plates using the form factor," *Vestnik MGSU*, no. 12, pp. 1333-1341, 2018, doi: 10.22227/1997-0935.2017.12.1333-1341.

[228] S. H. Rhee and T. Hino, "Numerical Simulation of Unsteady Turbulent Flow Around Maneuvering Prolate Spheroid," *AIAA Journal*, vol. 40, no. 10, pp. 2017-2026, 2002, doi: 10.2514/2.1534.

[229] M. M. Amiri, M. A. Vitola, S. H. Sphaier, and P. T. Esperança, "RANS feasibility study of using roughness to mimic transition strip effect on the crossflowseparation over a 6:1 prolate-spheroid," *Journal of hydrodynamics. = 水动力学研究与进展B辑(英文版)*, vol. 31, no. 3, pp. 570-581, 2019, doi: 10.1007/s42241-019-0005-5.

[230] N. Wikström, U. Svennberg, N. Alin, and C. Fureby, "Large eddy simulation of the flow around an inclined prolate spheroid," *Journal of Turbulence*, vol. 5, no. 5, 2004, doi: 10.1088/1468-5248/5/1/029.

[231] C. Fureby, N. Alin, N. Wikström, S. Menon, N. Svanstedt, and L. Persson, "Large Eddy Simulation of High-Reynolds-Number Wall Bounded Flows," *AIAA Journal*, vol. 42, no. 3, pp. 457-468, 2004, doi: 10.2514/1.3982.

[232] C. Fureby, N. Alin, N. Wikstrom, and S. Menon, "Large-eddy simulation of high-Reynolds-number wall-bounded flows," *American Institute of Aeronautics and Astronautics. AIAA Journal,* vol. 42, no. 3, pp. 457-468, 2004, doi: 10.2514/1.3982.

[233] G. D. Watt, "Scripted hybrid mesh adaption for high incidence RANS flows about axisymmetric shapes," *Collection of Technical Papers - 44th AIAA Aerospace Sciences Meeting,* vol. 14, pp. 10560-10576, 2006.

[234] D. W. George, "Wind tunnel investigations of submarine hydrodynamics," *Canadian Aeronautics and Space Journal,* vol. 39, no. 3, pp. 119-126, 1993.

[235] F., Jiang, J. P., Gallardo, H. I., and Andersson, "Phys fluid," no. 26, 113602, 2014.

[236] F. Jiang, J. P. Gallardo, H. I. Andersson, and Z. Zhang, "The transitional wake behind an inclined prolate spheroid," *Physics of Fluids,* vol. 27, no. 9, 2015, doi: 10.1063/1.4929764.

[237] G. K. El Khoury, H. I. Andersson, and B. Pettersen, "Wakes behind a prolate spheroid in crossflow," *J. Fluid Mech.,* vol. 701, pp. 98-136, 2012, doi: 10.1017/jfm.2012.135.

[238] G. K. El Khoury, H. I. Andersson, and B. Pettersen, "Crossflow past a prolate spheroid at Reynolds number of 10000," *J. Fluid Mech.,* vol. 659, pp. 365-374, 2010, doi: 10.1017/S0022112010003216.

[239] K. Granlund, "Experimentally obtained forces and moments on slender bodies during steady and unsteady maneuvers," 2009.

[240] Wetzel and Todd, "Unsteady Flow Over a 6:1 Prolate Spheroid," Ph.D, Aerospace and Ocean Engineering Department, Virginia Polytechnic Institude and State University, Blacksburg, VA,, 1996.

[241] A. B. Phillips, S. R. Turnock, and M. Furlong, "Influence of turbulence closure models on the vortical flow field around a submarine body undergoing steady drift," *Journal of marine science and technology,* vol. 15, no. 3, pp. 201-217, 2010, doi: 10.1007/s00773-010-0090-1.

[242] A. G. L. Holloway, T. L. Jeans, and G. D. Watt, "Flow separation from submarine shaped bodies of revolution in steady turning," *Ocean engineering,* vol. 108, pp. 426-438, 2015, doi: 10.1016/j.oceaneng.2015.07.052.

[243] S. Suman, S. Lakshmipathy, and R. S. Pant, "Evaluation of Assumed-Transition-Point Criterion in Context of Reynolds-Averaged Simulations Around Lighter-Than-Air Vehicles," *Journal of Aircraft,* vol. 50, no. 2, pp. 450-456, 2013, doi: 10.2514/1.C031880.

[244] A. Dumas, M. Trancossi, M. Madonia, J. Pascoa, G. Ilieva, and A. Coppola, "CFD analysis and optimization of a variable shape airship," vol. 7, ed, 2012, pp. 161-166.

[245] D. B. Clarke, "Computational and experimental investigation of flow around a 3-1 prolate spheroid," *Proceedings of the 16th Australasian Fluid Mechanics Conference, 16AFMC*, pp. 1381-1387, 2007.

[246] E. Alpman and L. N. Long, "An unstructured grid Reynolds stress model for separated turbulent flow simulations," *International journal of computational fluid dynamics,* vol. 23, no. 5, pp. 377-389, 2009, doi: 10.1080/10618560902865423.

[247] G. Constantinescu, H. Pasinato, Y. Q. Wang, J. Forsythe, and K. Squires, "Numerical investigation of flow past a prolate spheroid," *Journal of Fluids Engineering (Transactions of the ASME),* vol. 124, no. 4, pp. 904-910, 2002, doi: 10.1115/1.1517571.

[248] D. D. Joseph, "Potential flow of viscous fluids: Historical notes," *International Journal of Multiphase Flow,* vol. 32, no. 3, pp. 285-310, 2006, doi: 10.1016/j.ijmultiphaseflow.2005.09.004.

[249] M. Tomac, A. Rizzi, and C. Jouannet, "Adaptive-fidelity CFD for predicting flying qualities in preliminary aircraft design," ed. Stockholm: Stockholm: KTH Royal Institute of Technology, 2011.

[250] S. N. Singh, L. Rai, P. Puri, and A. Bhatnagar, "Effect of moving surface on the aerodynamic drag of road vehicles," *Proceedings of the Institution of Mechanical Engineers, Part D: Journal of Automobile Engineering,* vol. 219, no. 2, pp. 127-134, 2005, doi: 10.1243/095440705X5886.

[251] B. E. Launder, G. J. Reece, and W. Rodi, "Progress in the development of a Reynolds-stress turbulence closure," *Journal of fluid mechanics,* vol. 68, no. 3, pp. 537-566, 1975, doi: 10.1017/S0022112075001814.

[252] F. R. Menter, "Two- equation eddy- viscosity turbulence models for engineering applications," *AIAA Journal,* vol. 32, no. 8, pp. 1598-1605, 1994, doi: 10.2514/3.12149.

[253] A and Gerasimov, *Modeling Turbulent Flows with FLUENT*. Europe,

ANSYS,lnc. 2006.

[254] C. Ariza, C. Casado, R.-Q. Wang, E. Adams, and J. Marugán, "Comparative Evaluation of OpenFOAM® and ANSYS® Fluent for the Modeling of Annular Reactors," *Chemical engineering & technology,* vol. 41, no. 7, pp. 1473-1483, 2018, doi: 10.1002/ceat.201700455.

[255] T. Knopp, T. Alrutz, and D. Schwamborn, "A grid and flow adaptive wall-function method for RANS turbulence modelling," *Journal of computational physics*, vol. 220, no. 1, pp. 19-40, 2006, doi: 10.1016/j.jcp.2006.05.003.

[256] M. Karim, M. Rahman, and M. A. Alim, "Performance of sst k- omega) turbulence model for computation of viscous drag of axisymmetric underwater bodies," *International Journal of Engineering*, vol. 24, no. 2, pp. 139-146, 2011.

[257] J. Khawar, A. Ghafoor, and Y. Chao, "Validation of CFD-CSD coupling interface methodology using commercial codes," *International Journal for Numerical Methods in Fluids*, vol. 65, no. 5, pp. 475-495, 2011, doi: 10.1002/fld.2192.

[258] K. L. Lawrence, *ANSYS workbench tutorial : structural and thermal analysis using the ANSYS workbench release 13 environment*. Schroff Development Corporation, 2011.

[259] S. Jafaria, A. Basolb, N. Chokanic, and R. Abharic, "A preconditioned multigrid for simulation of atmospheric flow and wind turbine wakes," *Computers & Fluids*, vol. 122, pp. 111-122, 2015, doi: 10.1016/j.compfluid.2015.08.022.

[260] *Technical Documentation of the DLR TAU-Code 2013.2.0, tech.rep.'*. (2013). DLR, Braunschweig.

[261] J. and Boussinesq, ""Theotie de l' ecoulement tourbillant,"," *Mem. Presentes par Divers Savants Acad. Sci Inst. Fr,*, vol. 23, 1877.

Chapter 8. Appendix

Appendix A.1: Atmospheric behaviour in different altitude

Theoretical result and calculation:

$P = \rho xRxT$

$T = 288.15 - 0.00065 \times h$

$$P = 101{,}325 \times \frac{(1 - 0.00065 \times h)^{\frac{g}{0.00065xR}}}{T}$$

Where,

$P =$ pressure height

$\rho =$ Air density

$T =$ temperature

$R =$ gas constant

$h =$ Altitude

So, the following result has been shown by using the above equation for 1 kg mass of helium [59]:

Table no1.1: Atmospheric behaviour at different altitudes.

Alt(ft)	Alt (m)	Amb P (Pa)	Amb T (K)	Rho_air	Rho_He	Vol_He (m^3)	Disp mass (kg)	Upthrust (N)	Net L(N)
0	0	101,325	288.15	1.225226	0.186232	5.369648072	6.579030725	64.51825166	54.71160166
10000	3048	69,676.8	268.338	0.904741	0.137519	7.271727059	6.579030725	64.51825166	54.71160166
20000	6096	43,746.9	248.526	0.613329	0.093225	10.72676368	6.579030725	64.51825166	54.71160166
30000	9144	24,083.1	228.714	0.366891	0.055767	17.93184555	6.579030725	64.51825166	54.71160166
36089	11000	14,121.9	216.65	0.227119	0.034522	28.96735248	6.579030725	64.51825166	54.71160166
40000	12192	19,400.0	216.7	0.311933	0.047413	21.09118557	6.579030725	64.51825166	54.71160166
50000	15240	12,110.0	216.7	0.194717	0.029597	33.78769612	6.579030725	64.51825166	54.71160166

Appendix B.1: Lift disposal in Pressure height (ISA) [35]

The density of air and gas is in the same way affected by pressure and temperature, which as follows as an equation: $\frac{I_0}{I} = \frac{\rho_a}{\rho_{a.0}}$, pressure heigh I equal 1 (I=1), $\frac{\rho_a}{\rho_{a.0}} = I_0$, for a specific density, would be assigned a numerical profile as a reference as following hypothetical *ISA* Table B.2, which is an altitude-related parameter. The I_0 the value would be remained constant till pressure height. The hull with full gas at sea level ($I_0 = 100\%$), it means 100 per

cent of pressure height is at sea level; an airship would not be ascended without lift losses. In practically, I_0 must be less than 100% and followed ratio of disposable lift $\left(\frac{L_d}{L_{do}}\right)$:

Table B.2: Lift disposal in Pressure height (ISA)

I_0	Pressure height (m)	$\frac{L_d}{L_{do}}$
100	0	100
90	1085	80
80	2265	60
70	3615	40
60	5010	20
50	6660	0
40	8580	-

Appendix B.2: Aerodynamic data for comparison [1, 102]

Airship	V_{ol} (Ref)	*AR*	*K*	$C_{L\propto}$	C_{Do}
BoR, FR = 7.2	$Vol^{\frac{2}{3}}$	0.18	3.7	0.005	0.028
BoR, FR =6.0	$Vol^{\frac{2}{3}}$	0.21	2.9	0.006	0.030
ZP5K+ tail, FR=4.4	$Vol^{\frac{2}{3}}$	0.3	0.9	0.0115	0.026
EWBA	$Vol^{\frac{2}{3}}$	0.16	0.0147	0.045	0.0157
HL-10	S_{plan}	1.16	0.57	0.023	0.05
M2- F2	S_{plan}	0.712	0.95	0.0216	0.065
Puritan	S_{plan}	1.72	0.3	0.04	0.046

Appendix B.3: N_L empirical variables [1]

Following (Table B.5.1), empirical data would be used to transform *EWBA* aerodynamic parameters from $Vol^{\frac{2}{3}}$ to S_{plan}, that can be allowed *EWBA* aerodynamic data with traditional aircraft parameters. The equational example as: $S_{plan} = Vol^{\frac{2}{3}} \times N_L$ **($N_L$number of lobs)**

Table: B.5.1 N_L empirical variables

Number of lobes	N_L
1	2
2	2.25
3	2.4
4	2.5
5	2.54

Appendix B.4: Component drag coefficient analytical calculation

The drag approximation in conceptual design has been used as the base on drag area as follows:

The zero-lift hull drag $C_{do(hull)}$ is 0.00242 as equation (1.13)

Wing

For, the wing wetted area can be calculated by equation (1.28) as follows:

$$S_{wet(w)} = 2\left[1 + 0.3\left(\frac{t}{c}\right)_{max}\right] bC$$

Where, bC is equal to wing area 'S' and maximum thickness at 30%

$$= 2[\,1 + 0.3 \times 0.12]\ 79.6 = 164.93\ m^2$$

$$FF_{(w)} = 1 + 2.7\left(\frac{t}{c}\right)_{max} + 100\left(\frac{t}{c}\right)^4 \quad \text{[as equation (1.29)]}$$

$$= 1 + 2.7\times 0.12 + 100\times(0.12)^4 = 1.344$$

$$C_{D0w} = C_f FF_w \left(\frac{Swet_w}{V^{\frac{2}{3}}}\right) \quad \text{[as equation (1.13)]}$$

$$= \left(.0018 \times 1.344 \times \frac{164.93}{929.01}\right) = 0.000429$$

$$FF_{(tail)} = 1 + 1.2\left(\frac{t}{c}\right)_{max} + 100\left(\frac{t}{c}\right)^4 \quad \text{[as equation (1.14)]}$$

$$= 1 + 1.2\times 0.12 + 100\times(0.12) = 1.164$$

$$C_{D0tail} = \left(0.0018 \times 1.164 \times \frac{56.54}{929.01}\right)$$

[as equation (1.13) tail wetted area is approximately twice than tail area]

$$= 0.000127$$

$$C_{Do\,fin} = \left(0.0018 \times 1.164 \times \frac{54.578}{929.01}\right)[\text{as equation (1.13)}].$$

$$= 0.000123$$

[Swet_f is fin wetted area is approximately twice than fin reference area]

$$C_{do(engine)} = \frac{2 \times 4.25}{929.01} = 0.0091$$

$$C_{do(Gondola)} = \frac{\left(0.18 \times C_{do(Hull)} \times \left(\text{vol}^{\frac{2}{3}}\right) + 7.7\right)}{\left(\text{vol}^{\frac{2}{3}}\right)} = 0.0085$$

Interference drag $C_{do(in)} = \frac{\left(4.78 \times 10^{-6} \text{vol}_{\text{total}}\right)}{\text{vol}^{\frac{2}{3}}} = 0.0000099$

Appendix C.1: Design requirements and constraints

No	Group	Design requirements
1	General	*CIVIL – GA* ($EASA - 23$)
2	Standard	Standard
3	Manoeuvrability	Aerobatics and acrobatic
4	GA Mission	General-purpose
5	Density	Heavier than air
6	Pilot control	Man and unmanned aircraft
7	Weight	Less than 100000 lb
8	Take-off/landing	*STOL*
9	Landing field	Land-based
10	Stage	Prototype
11	Payload	Store
12	Performances	1.Max speed 2. Range 3. Ceiling 4.ROC 5. Take-off run, and 6. Endurance

Appendix C.2: Mission analysis in each segment

Mission analysis by each segment, In Figure 3.2, w_1 has been denoted as starting of the take-off/ taxiing, w_2 is the end of the take-off/ taxiing mission but starting climb. In the same

manner, the general flight path of *HBA* w_3 is the end of the climb but also staring cruise phase, w_4 is the end of the cruise path and starting descent phase. Consequently, the mission segment w_5 is the end of the descent path but starting once again the taxiing/landing phase. Finally, w_6 is the end off taxi/ landing profile segment. Thus, in each of the segments, an aircraft loses its weight. Such as w_1 is *MTOW* but w_2 is the end of take-off weight. So, w_3 is beginning of the cruise weight, w_4 is the end of the cruising weight, but beginning descending, w_5 is the end of the descending phase weight. Eventually, the w_6 is aircraft landing weight at the end. Thus, if *'i'* is mission segment, the weight fraction can be defined $\left(\frac{w_{i+1}}{w_i}\right)$. Therefore, weight fraction now can be expressed for all flight phases. Then it can be found the aircraft ratio of the weight by multiplying all fractions in each other at the end of the flight mission. Afterwards, divided by *MTOW*. This fraction ratio would be enabled to estimate the total fuel fraction.

Hence, the weight segment fraction is the weight of an aircraft at the end of each flight segment divided by the beginning of the weight of that segment.

Indeed, the fuel weight (w_f). is total take-off weight minus landing weight. so, the mathematical expression is:

$$\left(w_{MTOW} - w_{landing=} w_f\right)$$

And the regular flight weight fraction ratio at the end of the flight mission is:

$$\left(\frac{w_{landing}}{w_{MTOW}} = \frac{w_{MTOW-w_f}}{w_{MTOW}}\right)$$

Since, for HBA, all five flight segments as Figure 3.2, as follows:

$$\left(\frac{w_f}{w_{MTOW}} = 1 - \frac{w_6}{w_1}\right)$$

Appendix C.3: A typically applicable weight fraction on average:

No	flight path of the mission	$\frac{w_{i+1}}{w_i}$
1	Taxiing and take-off	0.98
2	Climb	0.97
3	descent	0.99
4	Approach & landing	0.997

Table C.3.1: typical weight fraction in different flight paths [33]

For safety reasons, 20% of extra fuel much carried than need on a flight, *FAA* airworthiness standards, which is approximately 5% of total weight, so it can be found as follows:

$$\frac{w_f}{w_{MTOW}} = 1.05\left(1 - \frac{w_6}{w_1}\right)$$

Appendix C.4: Weight estimations and fuel fraction in *MATLAB* for the iterative method

```
% Weight _SWBA_Computation
 clc;
clear all;
% Constant
W1_w2 = 0.98;
w2_w3 = 0.97;
w3_w4 = 0.99;
w4_W3 = 0.997;
W6_W1 = 0.9382;
payload = 104.326*3; % 3pax 22.7lkg allowable personal item for domestic
flights
crew = 93.4 * 1;    % with allowable 7.257kg personal item and 4.53kg
clothings
wf = 0.4914;
we = 0.5759
Wto = 560.002;
error = 100;
eps = 1e-4;
i = 1;
while error > eps
Wg = [0.179*577.05]; %[without Wing_Tail_ Fuselage_Land-Gear_Engine weight]
W = crew + payload + sum(Wg) + Wto*we;
error = abs((W-Wto)/W)*100;
fprintf('%d, %.2f, %.2f, error: %f\n', i, Wto, W, error);
Wto = W;
  i = i+1;
 end % fprintf('%.2f, error: %f\n', Wto, error);
 Wf = 595.65;
fprintf('Gross Weight\t%4.f\nGas Weight\t%4.f\nFuel Weight\t%4.f\nPayload
Weight\t%4.f\nCrew Weight\t%4.f\nEmty Weight\t%4.f\n', Wto, sum(Wg), Wf,
payload, crew,we);
```

Results

we = 0.5759

Iteration	Guess weight	Take-off weight	% Error
1,	560.00,	832.18,	32.706230
2,	832.18,	988.92,	15.850074
3,	988.92,	1079.19,	8.364538
4,	1079.19,	1131.17,	4.595754

5,	1131.17,	1161.11,	2.578451
6,	1161.11,	1178.36,	1.463202
7,	1178.36,	1188.28,	0.835617
8,	1188.28,	1194.00,	0.478927
9,	1194.00,	1197.30,	0.275055
10,	1197.30,	1199.19,	0.158154
11,	1199.19,	1200.29,	0.090998
12,	1200.29,	1200.91,	0.052378
13,	1200.91,	1201.28,	0.030156
14,	1201.28,	1201.49,	0.017364
15,	1201.49,	1201.61,	0.009999
16,	1201.61,	1201.67,	0.005758
17,	1201.67,	1201.71,	0.003316
18,	1201.71,	1201.74,	0.001910
19,	1201.74,	1201.75,	0.001100
20,	1201.75,	1201.76,	0.000633
21,	1201.76,	1201.76,	0.000365
22,	1201.76,	1201.76,	0.000210
23,	1201.76,	1201.77,	0.000121
24,	1201.77,	1201.77,	0.000070

Therefore, it is convergence with a rate of change 7×10^{-6}. Where, Gross Weight 1202, Gas Weight 103, Fuel Weight 596, Payload Weight 313, Crew Weight 93, Empty Weight 692.23.

Appendix C.5: Analytical details of *EWBA's* sizing

At minimum drag speed AV^2 md = $\frac{B}{V_{md}^2}$

So, after rearranging: $V_{md} = \left(\frac{B}{A}\right)^{\frac{1}{4}}$ [minimum velocity at]

$$= \left(\frac{kW^2}{\frac{1}{2}(\rho S)^2 \pi A R C_D}\right)^{\frac{1}{4}} = \left(\frac{.0523\times(1202)^2}{0.5(1.225226*13.14)^2*\pi*7*0.02072}\right)^{\frac{1}{4}}$$

$= 5.98$ m/s [The margin usually $V > 1.1\ V_{md}$]

Stall speed

$\left[\frac{W}{S}\right]_{VS} = \frac{1}{2}\rho V_s^2 S C_{Lmax}$, however, $V_s^2 = \frac{2W}{\rho S C_{Lmax}} = 37.08$ m/s. When the lift coefficient corresponds to maximum values $(C_L = C_{Lmax})$; the stalling velocity depends on wing loading, air density (flight altitude) and maximum lift coefficient. Therefore, $\left[\frac{W}{S}\right]_{VS} = \frac{1}{2} \times 0.001496 \times (76.58 \times 1.688)^2 \times 1.41 = 17.62$ lb/ ft²

Maximum speed

$$\left[\frac{W}{P}_{SL}\right]_{Vmx} = \left[\frac{\eta p}{\frac{\frac{1}{2}\rho_0 V^3 max\, C_{D0}}{\frac{W}{S}} + \frac{2K}{\rho\sigma V_{max}}\left(\frac{W}{S}\right)}\right]$$

$$= \left[\frac{0.8\times550}{\frac{1}{2}\times0.002378(321.52)^3\times0.02078\times\frac{1}{\left(\frac{W}{S}\right)} + \frac{2\times.0523}{0.0089\times.374\times(321.52)}\times\left(\frac{W}{S}\right)}\right]$$

[$\eta =$ propeller efficiency, assumed 0.8, while Mach *(M)* = 0.15and relative density at 4000m]

$$\left[\frac{W}{P}\right]S_{TO} = \frac{1-e^{\left(0.6\rho g C_{DG} S_{TO}\frac{1}{\frac{W}{S}}\right)}}{\mu-\left(\mu+\frac{C_{DG}}{C_{LR}}\right)\left[e^{\left(0.6\rho g C_{DG} S_{TO}\frac{1}{\frac{W}{S}}\right)}\right]} \times \frac{\eta p}{V_{To}}$$

$\mu =$ Friction coefficient let 0.02 (icy concrete/asphalt/surface), and of speed assumed as[33]:

$V_{To} = 1.2V_s = 47.27$ m/s [for variable take-off]

In take-off, lift and drag co-efficient:

$C_{L_{TO}} = C_{L_c} + \Delta C_{L_{flap-TO}}$ [where lift coefficient assumed $(C_{L_c}) = 0.3$ and let as $\Delta C_{L_{flap-TO}}$ =0.8, this normally typical aircraft 0.3 to 0.8][33].

$C_{L_{TO}} = 0.3 + .74 = 1.04$

same as total drag coefficient, $C_{DTO} = 0.02072$.

Rotation lift coefficient at take-off: $C_{L_R} = \frac{C_{Lmax}}{(1.04)^2} = 1.303$

$C_{D_G} = (C_{D_{To}} - \mu\, C_{L_{TO}}) = 0.0072$

Thus, $\left[\frac{W}{P}\right]S_{TO} = \frac{1-e^{\left(0.6\times0.00089\times32.2\times0.0072\times1000\frac{1}{\frac{W}{S}}\right)}}{0.02-\left(0.02+\frac{0.0072}{1.04}\right)\left[e^{\left(0.6\times0.00089\times32.2\times0.0072\times1000\times\frac{1}{\frac{W}{S}}\right)}\right]} \times \left(\frac{.8}{128.017}\right)(550)$

Rate of Climb (ROC), $\left[\frac{W}{P}\right]_{Roc} = \left[\frac{1}{\frac{ROC}{\eta p} + \sqrt{\frac{2}{\rho\sqrt{\frac{3C_{D0}}{K}}}\times\frac{W}{S}} \times \frac{1.35}{\left(\frac{L}{D}\right)max\times\eta p}}\right]$

$$= \left[\frac{1\times550}{270.05+\left(\sqrt{3298.45\times\frac{W}{S}}\right)\times(0.168)}\right] lb/ph$$

$$\textit{Service ceiling, } \left[\frac{W}{P_{SL}}\right]_C = \left[\frac{\sigma C}{\frac{(ROC)c}{\eta p}+\sqrt{\frac{2}{\rho\sqrt{\frac{3C_{D0}}{K}}}\times\frac{W}{S}}\times\frac{1.35}{\left(\frac{L}{D}\right)max\times\eta p}}\right]$$

$$=\left[\frac{0.31\times550}{2.083+\left(\sqrt{5001.06\times\frac{W}{S}}\right)\times(0.168)}\right]lb/ph$$

All equation can put in following *MATLAB* as input data

Appendix C.6: *MATLAB CODE* for design point

```
clc
clf
clear all
%Design point and assume values
x=linspace(5,70);
g=32;   % gravity ft/s2
Wto=1202*2.2;  % maximum take off weight lb
CD0=0.0157;  % drag coefficient
Vmax=98*1.688;     % KATS (knots)
Vs=39.399*1.688;    % Stall speed
Vcruise=46*1.688; % ft/s
VEmax=1.3*Vs*1.688;    % velocity at max endurance
Rho1=0.001897; % density at 7000 ft slug/ft3
nup=0.7;  % propeler efficiency
e=0.8;  % Oswald span efficency factor
AR=15;       % Aspect Ratio
Rho=0.002378;  % sea level density  slug/ft3
s1=Rho1/Rho;   % air relative density
k=1/(pi*e*AR);
R=2700;    % rate of climb fpm
LD_max=18; % (L/D)max
CLc=0.3;
CLf=0.2; % CLflap_TO
Cl=1.41;  % CLmax
mu=0.04;
Vto=1.2*Vs;
St=1000.4;      % take off run ft
CLto=CLc+CLf;  % lift coefficient for take off
CDol=0.01;     %
CDoHL=0.005;
CDoto=CD0+CDol+CDoHL;
```

```
CDto=CDoto+k*CLto^2; % drag coefficients in take off
CLr=Cl/(1.04^2);    % lift coefficient in rotation during take-off
CDg=CDto-mu*CLto;
Rho2=0.001496;     % density at 15000 ft
s2=Rho2/Rho;    % relative air density at 26250
nu=0.6; E=1800;       % endurance in seconds
Ran=2117*3280.84;  % range in feet
c1=0.6/3600;  % SFC in seconds  for cruise
c2=0.7/3600;   % SFC in secnds for loiter
z=exp(0.6.*Rho.*g.*CDg.*St.*x.^-1);
% Design Mission
 Tof=0.98;             % Fuel wait ratio for take-off
 Cli=0.97;              % Fuel wait ratio for  climb
 crun=-Ran*c1;          % Fuel wait ratio for Cruise
 crud=nup*LD_max*550;
 Cru=exp(crun/crud);     % Fuel wait ratio for Cruise
 Des=0.99;               % Fuel wait ratio for Descent
 loin=-E*c2*VEmax;
 loid=0.866*nup*LD_max*550;
 Loi=exp(loin/loid);     % Fuel wait ratio for Loiter
 Lan=0.997;               % Fuel wait ratio for Landing
 Ov=Tof*Cli^2*Cru^2*Des^2*Loi^2*Lan;  % overall Fuel wait ratio
 FuelR=1.05*(1-Ov);
 denom=1-FuelR;     % value at the denominator for Wto calculation
 WempR=-7.62*10^-6*Wto+0.6;
  EmptyWeight=WempR*Wto;
  Wfuel=FuelR*Wto
  Wfuelspent=Wfuel*Ov
  Wlanding=Wto-Wfuelspent
  % % for Plotting design point equation
Vmax=nup.*550./(0.5.*Rho.*(Vmax.*1.688).^3.*(CD0.*1./x)+(2.*k./(Rho1.*s1.*V
max.*1.688)).*x);
  Stall=0.5*Rho*(Vs*1.688)^2*Cl;
den=(R/(60*nup))+(1.155./(LD_max.*nup)).*((2.*x./(Rho.*sqrt(3.*CD0./k)))).^
0.5; ROC=550./den;
  TOR=(550.*nu./(Vto.*1.688)).*(1-z)./(mu-(mu+CDg./CLr).*z);
den1=(100/(60*nup))+(1.155./(LD_max.*nup)).*((2.*x./(Rho2.*sqrt(3.*CD0./k))
)).^0.5; SC=s2.*550./den1;
  Y=interp1(x,Vmax,Stall);
  plot(x,Vmax,'g+-')
  hold on
```

```
plot([Stall],[0 70],'ko-')
hold on
plot(x,ROC,'p')
hold on
%  plot (Wto,Vcruise)
% % hold on
plot(x,TOR,'b.-')
hold on
plot(x,SC,'mp-')
hold on
plot(Stall,Y,'r')
text(Stall,Y,['(' num2str(Stall),',' num2str(Y) ')']);
S=Wto/Stall      % ft^2 for the wing area
  P=Wto/Y           % hp Engine power
      Sm=S/10.764    % convert in m^2 for Wing area
      Pkw=P*0.74555 % At the title ('Matching Plot') Kw for Engine power
      xlabel('Wing Loading  (W/S)')
      ylabel('Power Loading (W/P)');
      legend('Vmax','Stall','ROC','TOR','Sc')
      axis ([0 70 0 35]) %
```

Results :

Wfuel = 313.8985

Wfuelspent =278.4121

Wlanding = 2.000e+03

S =141.4574

P = 165.4608hp

Sm = 13.1417

Pkw = 123.3593

Appendix C.6.1: Maximum speed requirement *MATLAB* Graph

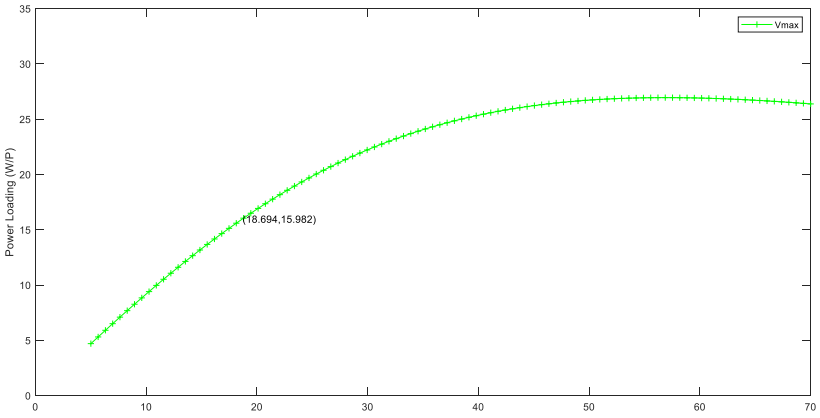

Figure C.6.1: Velocity contribution

In above Figure C.6.1. that came from equation no 3.5, the $\frac{W}{P}$ nonlinear function of $\frac{S}{P}$, as was shown once aircraft at maximum speed.

Appendix C.6.2: Take-off run contribution in a matching plot

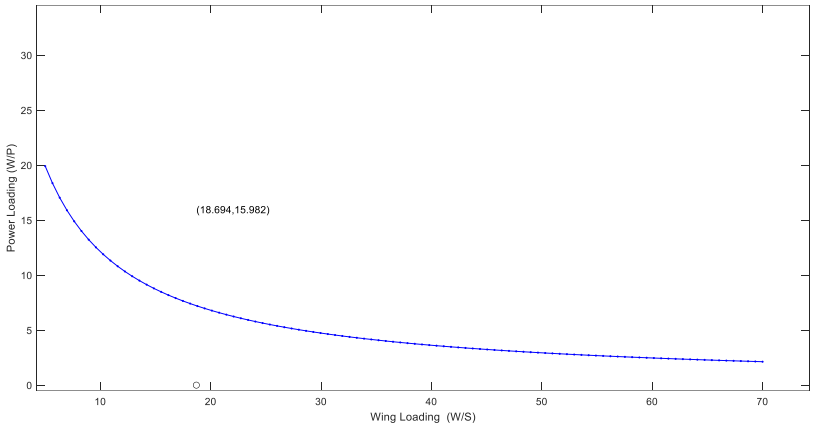

Figure C.6.2: Take-off velocity contribution

In above Figure C.6.2, as can be seen, the take-off speed is less than the required specific S_{TO} and below the graph inside the region. So, it is in an acceptable domain. It was also seen in equation 3.6, and the take-off speed increased once the exponential term increased.

Appendix C.6.3: *ROC* in the matching plot

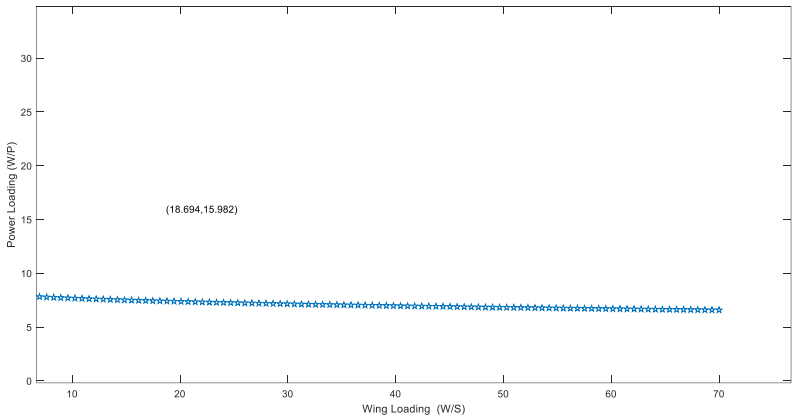

Figure C.6.3: *ROC* contribution in a matching plot

Figure C.6.3, which was constructed by equation 3.7, showed that power loading dropped with the increase of *ROC*; it is below the specific required, thus was in an acceptable section.

Appendix C.6.4: The Ceiling requires bellow the Graph

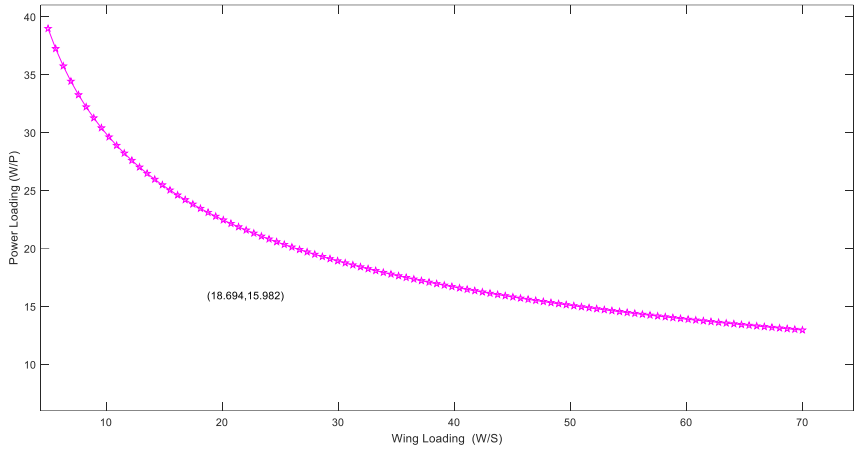

Figure C.6.4: Ceiling contribution

In above Figure C.6.4, that was constructed by equation 3.8. This graph was satisfied with climbing requirements below the region of the curve line.

Appendix C.7: Aerofoil selection

The mathematical selection process of an aerofoil is below:

Ideal lift coefficient for *EWBA* (C_{lc}) is $= \frac{2w_{ave}}{\rho S(V_c)^2} = \frac{2\times1202\times9.8}{0.82\times13.14\times(98)^2} = 0.246$

Wing lift coefficient at cruise$\left(C_{lc_w}\right) = \frac{C_{lc}}{0.95} = \frac{0.246}{0.95} = 0.259$

Wing ideal lift coefficient $\left(C_{li_w}\right) = \frac{C_{lc_w}}{0.9} = \frac{0.28}{0.9} = 0.289$

The maximum lift coefficient is $(C_{lmax}) = \frac{2w_o}{\rho_0 S(V_s)^2} = \frac{2\times1202\times9.81}{1.225\times13.14\times(34.79)^2} = 1.21$

Lift coefficient for wing $\left(C_{lmax_w}\right) = \frac{C_{lmax}}{0.95} = \frac{1.21}{0.95} = 1.27$

Wing gross lift coefficient $\left(C_{lmax_{gross}}\right) = \frac{C_{lmax_W}}{0.9} = \frac{1.27}{0.9} = 1.41$

So, it is an allowable net maximum lift coefficient for *EWBA*. Now can be select aerofoil from Figure 3.5 as required C_{li_w} and C_{lmax}.

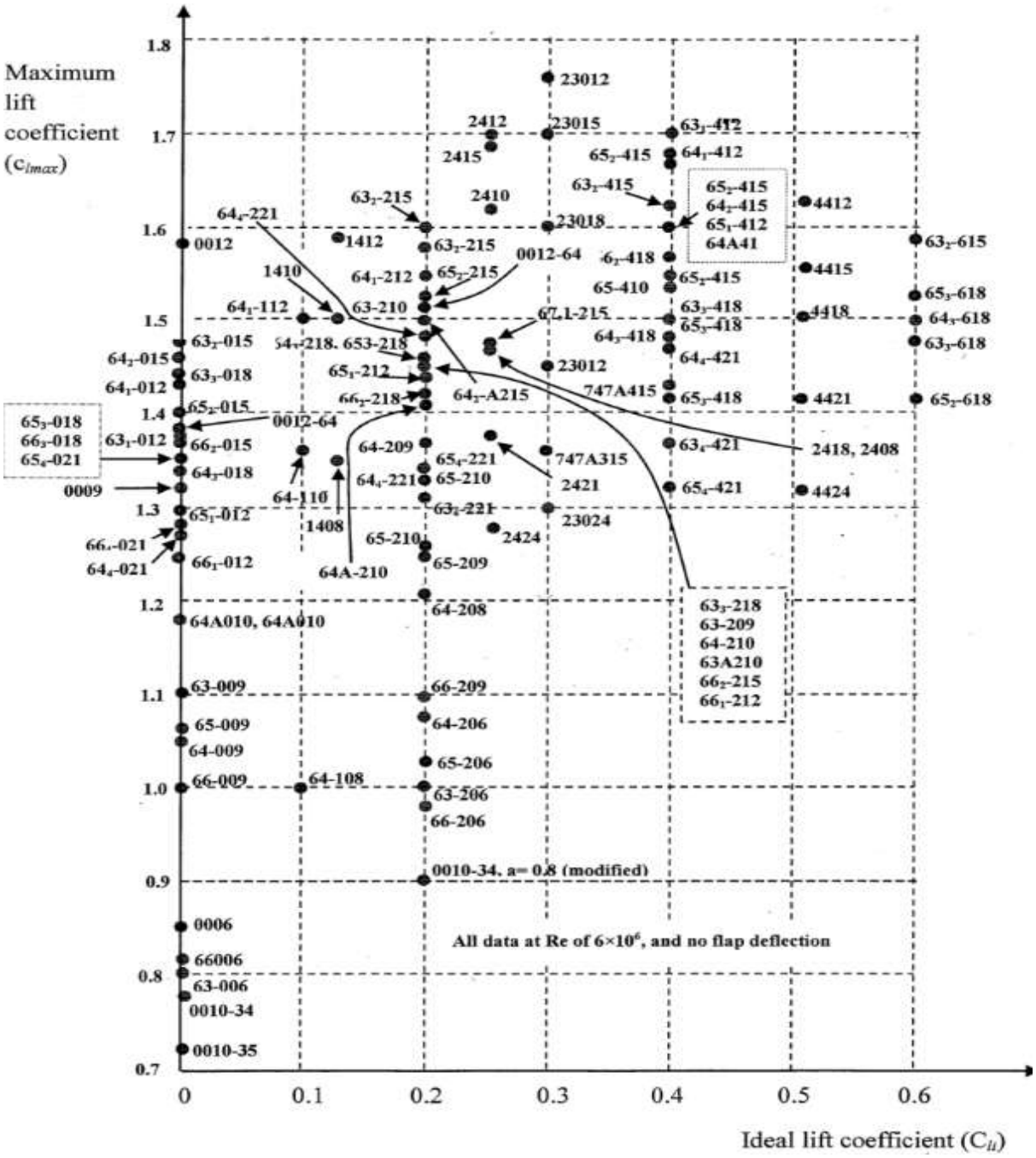

Figure 3.5: Maximum lift coefficient vs Ideal lift coefficient for *NACA* aerofoil [33]

Appendix C.8: *XFLR5* data

NACA 23024				NACA	2412				2421			
AOA	Cl	Cd	Cm	cl/cd	Cl	Cd	Cm	cl/cd	Cl	Cd	Cm	cl/cd
-5	-0.207	0.00917	-0.048	-22.57361	-0.1733	0.00962	-0.0771	-18.0146	-0.2989	0.00908	-0.00324	-32.9185
-4	-0.1146	0.00898	-0.0374	-12.761693	-0.1365	0.0094	-0.0612	-14.5213	-0.1914	0.00878	-0.0507	-21.7995
-3	-0.0844	0.00892	-0.261	-9.4618834	-0.1014	-0.00932	-0.0448	10.87983	-0.0831	0.00858	-0.0507	-9.68531
-2	-0.0416	0.00883	-0.11	-4.7112118	-0.00515	0.00924	-0.313	-0.55736	0.025	0.00845	-0.0496	2.95858
-1	0.006	0.00882	0.003	0.6802721	0.0042	0.00918	-0.0193	0.457516	0.1326	0.00827	-0.0485	16.03386
0	0.0464	0.00888	0.0186	5.2252252	0.0683	0.00916	-0.009	7.456332	0.2388	0.00815	-0.0471	29.30061
1	0.1197	0.009	0.033	13.3	0.1387	0.00915	-0.0002	15.15847	0.3722	0.00812	-0.0455	45.83744
2	0.1668	0.00916	0.0407	18.209607	0.2091	0.00921	0.0084	22.70358	0.4528	0.0082	-0.0446	55.21951
3	0.2322	0.0094	0.0503	24.702128	0.2825	0.00939	0.0162	30.0852	0.5574	0.00841	-0.429	66.27824
4	0.30324	0.00972	0.0586	31.197531	0.3599	0.00968	0.0228	37.17975	0.6608	0.00865	-0.041	76.39306
5	0.3801	0.01019	0.0648	37.301276	0.4499	0.01005	0.0265	44.76617	0.7592	0.00905	-0.0382	83.8895
6	0.4883	0.01087	0.0641	44.921803	0.5713	0.0105	0.0233	54.40952	0.8463	0.00965	-0.33	87.69948
7	0.615	0.01184	0.0591	51.942568	0.7513	0.01163	0.0076	64.60017	0.9357	0.01049	-0.0283	89.19924
8	0.7701	0.01354	0.0478	56.875923	0.8723	0.01348	0.0036	64.71068	1.0624	0.01195	-0.0329	88.90377
9	0.8627	0.01554	0.0486	55.514801	0.9872	0.01542	0.0002	64.02075	1.1372	0.01339	-0.0278	84.92905
10	0.9649	0.01779	0.0466	54.238336	1.1033	0.01767	-0.0045	62.43916	1.1978	0.01495	-0.202	80.1204
11	1.0787	0.02023	0.0411	53.321799	1.1904	0.01945	-0.0088	61.20308	1.2662	0.017	-0.0151	74.48235
12	1.1795	0.02316	0.0368	50.928325	1.2252	0.02307	0.0038	53.10793	1.3299	0.01965	-0.0104	67.67939
13	1.2682	0.02668	0.0329	47.533733	1.2545	0.02681	0.0119	46.79224	1.3824	0.02331	-0.0057	59.30502
14	1.2888	0.03079	0.0404	41.857746	1.2798	0.03154	0.0186	40.57705	1.425	0.0281	-0.0015	50.71174
15	1.3062	0.03619	0.0459	36.092843	1.2966	0.03762	0.0242	34.46571	1.4596	0.03413	0.0017	42.7659
16	1.3165	0.04307	0.0497	30.56652	1.3127	0.04441	0.0282	29.55866	1.4805	0.04197	0.004	35.2752
17	1.3182	0.05142	0.052	25.635939	1.3184	0.05269	0.0311	25.02183	1.489	0.05166	0.0052	28.82307
18	1.309	0.06156	0.0528	21.263808	1.3146	0.06242	0.0328	21.06056	1.4834	0.06334	0.005	23.41964
19	1.3002	0.06985	5.0523	18.614173	1.3073	0.07304	0.0333	17.89841	1.4676	0.077	0.0035	19.05974

23012				65-210			
Cl	Cd	Cm	cl/cd	Cl	Cd	Cm	cl/cd
-0.3925	0.0096	-0.0175	-40.8854	-0.3603	0.01064	-0.0428	-33.8628
-0.2892	0.00883	-0.0147	-32.752	-0.2583	0.00886	-0.416	-29.1535
-0.1831	0.00832	-0.0127	-22.0072	-0.1504	0.00791	-0.0413	-19.0139
-0.0761	0.00792	-0.0113	-9.60859	-0.0485	0.00529	-0.0413	-9.16824
0.0194	0.00603	-0.0086	3.217247	0.0622	0.00495	-0.0414	12.56566
0.1241	0.00587	-0.0067	21.1414	0.175	0.00496	-0.0418	35.28226
0.228	0.00612	-0.0042	37.2549	0.2881	0.00502	-0.0423	57.39044
0.3348	0.00674	-0.0026	49.67359	0.3981	0.00521	-0.0421	76.41075
0.4531	0.00742	-0.0037	61.06469	0.4956	0.00684	-0.0401	72.45614
0.5913	0.00808	-0.0095	73.18069	0.5863	0.00946	-0.0374	61.97674
0.7306	0.00873	-0.0158	83.68843	0.7091	0.01101	-0.0346	64.40509
0.8545	0.0093	-0.019	91.88172	0.7696	0.01269	-0.0305	60.64618
0.9458	0.00997	-0.0152	94.86459	0.8709	0.01509	-0.0298	57.71372
1.0385	0.01073	-0.0118	96.78472	0.9851	0.01799	-0.0282	54.7582
1.1313	0.01174	-0.0087	96.36286	1.0482	0.02389	-0.025	43.8761
1.2243	0.01236	-0.0061	99.0534	1.117	0.0292	-0.0207	38.25342
1.3128	0.01489	-0.0032	88.16655	1.1008	0.04114	-0.0078	26.75741
1.4128	0.01894	0.0014	74.59345	0.994	0.06167	-0.0008	16.11805
1.4636	0.01983	0.0051	73.80736				#DIV/0!
1.5058	0.02334	0.013	64.51585				#DIV/0!
1.5304	0.02886	0.0188	53.02841				#DIV/0!
1.539	0.0379	0.0197	40.60686				#DIV/0!
1.4857	0.05803	0.0119	25.60227				#DIV/0!
1.3702	0.09002	-0.0024	15.22106				

Appendix C.9: Lift distribution *MATLAB CODE*

```
clear all
clc
S=13.14; %[m2]
N=9; AR=15; lambda=1; twist=-1; iw=2; alpha_0=-1.5; a_2d=6.3;
b=sqrt(S*AR); MAC=S/b; Croot=1.37*MAC*(1+lambda)/(1+lambda+lambda^2);

rho= 0.81; % [kg/m3]
V=46; % [m/s]

% angles (from tip to the root) [rad]
theta=pi/(2*N):pi/(2*N):pi/2

% Segment angle of attack [deg]
alpha=iw+twist:-twist/(N-1):iw;

% Segment location
z=(b/2)*cos(theta)

% Mean chord at every segment
c=Croot*(1-(1-lambda)*cos(theta))

% LHS of the monoplane equation (vector: p)
mu=c*a_2d/(4*b);
p=mu.*(alpha-alpha_0)/57.3;  % divided by 57.3 topass from [deg] to [rad]

% Solve N equations
for i=1:N
   for j=1:N
      K(i,j)=sin((2*j-1)*theta(i))*(1+mu(i)*(2*j-1))/sin(theta(i))
   end
end

A=K\p'

% Calculate lift coefficients
for i=1:N
   sum1(i)=0;
   sum2(i)=0;
   for j=1:N
      sum1(i)=sum1(i)+(2*j-1)*A(j)*sin((2*j-1)*theta(i));
      sum2(i)=sum2(i)+A(j)*sin((2*j-1)*theta(i));
   end
end

CL=4*b*sum2./c;

% Lift coeff of every segment
CL1=[0 CL]

% Locations (tip to root)
y_s=[b/2 z]

% Plot lift distribution
plot(y_s,CL1,'-o')
grid
title('Lift distribution')
xlabel('Loaction in semispan [m]')
ylabel('Lift coefficient')
```

```
CL_wing=pi*AR*A(1)

% Lift
L=(1/2)*rho*V^2*S*CL_wing % [Newtons]
```

```
theta =  0.1745   0.3491   0.5236   0.6981   0.8727   1.0472   1.2217   1.3963   1.5708
    z = 4.7225   4.5061   4.1529   3.6734   3.0824   2.3977   1.6401   0.8327   0.0000
    c = 1.2513   1.2513   1.2513   1.2513   1.2513   1.2513   1.2513   1.2513   1.2513
K =
   1.2055   4.6545   8.9443  13.1959  16.4096  17.6441  16.1967  11.7551   4.4935
   1.2055   4.0931   5.8380   4.5829   0.0000  -6.1277 -10.5717 -10.3373  -4.4935
   1.2055   3.2330   2.0275  -2.4385  -5.6990  -3.2605   3.6715   8.1650   4.4935
   1.2055   2.1779  -1.0788  -3.7360  -0.0000   4.9954   1.9536  -5.5003  -4.4935
   1.2055   1.0551  -2.4871  -0.5528   3.7198  -0.7391  -4.5038   2.6647   4.4935
   1.2055  -0.0000  -2.0275   2.4385  -0.0000  -3.2605   3.6715  -0.0000  -4.4935
   1.2055  -0.8601  -0.3747   1.9879  -3.0324   2.6580  -0.6785  -2.1723   4.4935
   1.2055  -1.4215   1.3234  -0.8469  -0.0000   1.1324  -2.3964   3.5901  -4.4935
   1.2055  -1.6165   2.0275  -2.4385   2.8495  -3.2605   3.6715  -4.0825   4.4935
A =
    0.0094
   -0.0005
    0.0000
   -0.0000
    0.0000
   -0.0000
    0.0000
   -0.0000
    0.0000
CL1 =    0   0.0425   0.0861   0.1299   0.1726   0.2126   0.2482   0.2776   0.2989   0.3088
y_s =   4.7953   4.7225   4.5061   4.1529   3.6734   3.0824   2.3977   1.6401   0.8327   0.0000
CL_wing =    0.2073
L = 1.0592e+04 (Newton)
```

Appendix C.10: *VLM* joint wing >> Tornado - program start

```
 TORNADO  Version 135  Release version
 Main Menu

Input operations.
      [1]. Aircraft geometry setup
      [2]. Flight condition setup
```

[3]. Change rudder setting

[4]. Move reference point

Lattice operations.

[5]. Generate lattice.

Computation operations.

[6]. Processor access

Post-processing and interactive operations.

[7]. Post-processing, Result/Plot functions

[8]. Keyboard access

Auxiliary operations.

[10]. About / Release Info

[100]. Help files

[0]. Exit Tornado

Please enter choice from above:1

[2]. Load geometry

[3]. Edit current geometry

[4]. Save current geometry

[5]. Define blunt body data (for friction drag est).

[0]. Back / up menu

Please enter choice from above: 1

Number of Wings: 3

" Data regarding wing number:1

Number of semi-spanwise partitions for this wing: 1

" Data regarding partition number:1

b - Back one question.

q - Abort input sequence.

Center of gravity x-coordinate: 0

Center of gravity y-coordinate: 0

Center of gravity z-coordinate: 0

Reference point x-coordinate: 0

Reference point y-coordinate: 0

Reference point z-coordinate: 0

Is the wing mirrored in the xz-plane [1 0]: 1

Root chord: 1.17

```
******************************
 AVAILABLE AIRFOILS: FX63137.DAT  MS0313.DAT  N651012.DAT NL11215F.DAT
SC20010.DAT  SC20706.DAT  WILBYR.DAT,  GAW1.DAT  MS10313.DAT
N651213.DAT  NL20415.DAT  SC20012.DAT  SC20712.DAT  circle.DAT, CAST7.DAT
GM21mod.DAT  MS10317.DAT  N652215.DAT  NL23009.DAT  SC20406.DAT
SC20714.DAT  naca0012.DAT  ,CLARKY.DAT  HSN0213.DAT  N001035.DAT
N65410.DAT  NLR1.DAT  SC20410.DAT  SC21006.DAT  naca0018.DAT ,DAE11.DAT
K720616.DAT  N23009.DAT  N658299M.DAT  ONERAM6.DAT  SC20412.DAT
SC21010.DAT  naca4412.DAT,  DAE21.DAT  K790312.DAT  N23018.DAT
N658299R.DAT  RAE100.DAT  SC20414.DAT  SUPER11.DAT  newabb.DAT
,DAE31.DAT  K820609.DAT  N63215.DAT  N65A012.DAT  RAE101.DAT
SC20518.DAT  VEZBL32.DAT  nlf416.dat, DSMA523.DAT  KORN.DAT  N64210.dat
N663018.DAT  RAE102.DAT  SC20606.DAT  VEZCAN.DAT  prf1_wt.dat ,EPP662.DAT
LISS7769.DAT  N643418.DAT  N747A415.DAT  RAE103.DAT  SC20610.DAT
VEZWLTR.DAT  prf2_wt.dat,  EPP748.DAT  LS10013.DAT  N64A010.DAT
NL10414F.DAT  RAE104.DAT  SC20612.DAT  WILBYB.DAT  prf3_wt.dat,
FOIL31.DAT  LS10417M.DAT  N64A410.DAT  NL10416.DAT  RAE2822.DAT
SC20614.DAT  WILBYC.DAT
******************************
Enter profile filename from the list above (ex CLARKY.DAT)
OR any NACA four digits series numer (ex: 2412)
0 (zero) for a flat plate.
 Base chord airfoil: 23024
Number of panels chord wise: 10
Partition dihedral [deg]: 6
Number of panels semi-span wise: 10
Span of partition: 2.9725
Taper ratio: 1
 ******************************
 AVAILABLE AIRFOILS:

******************************
```

```
Enter profile filename from the list above (ex CLARKY.DAT)
OR any NACA four digits series numer (ex: 2412)
0 (zero) for a flat plate.
 Tip chord airfoil: 23024
Quarter chord line sweep [deg]: 0
Outboard twist [deg]: 0
  ***************
 Available mesh distribution types:
   [1] Linear
   [2] Spanwise half-cosine
   [3] Spanwise half-cosine, chordwise cosine
   [5] Spanwise cosine
   [6] Chordwise cosine
   [7] 3:rd order centerpacking. (Not for wings)
 Mesh type: 1
Is partition flapped [1 0]:0
"""""""""""""""""""""""""""""""""""""""""""""
" Data regarding wing number :2
"""""""""""""""""""""""""""""""""""""""""""""
 Number of semispanwise partitions for this wing: 1
 """""""""""""""""""""""""""""""""""""""""""""
" Data regarding partition number:1
 Is the wing mirrored in the xz-plane [1 0]: 1
Apex x-coordinate: 0
Apex y-coordinate: 2.9725
Apex z-coordinate: 0.34
Root chord: 1.17
 ******************************
 AVAILABLE AIRFOILS:
******************************
 Enter profile filename from the list above (ex CLARKY.DAT)
OR any NACA four digits series numer (ex: 2412)
0 (zero) for a flat plate.
```

```
Base chord airfoil: 23024
Number of panels chord wise: 10
Base chord twist [deg]: 0
Partition dihedral [deg]: 90
Number of panels semi-span wise: 10
Span of partition: 1.0745
Taper ratio: 1
******************************
 AVAILABLE AIRFOILS:
******************************
 Enter profile filename from the list above (ex CLARKY.DAT)
OR any NACA four digits series numer (ex: 2412)
0 (zero) for a flat plate.
 Tip chord airfoil: 23024
Quarter chord line sweep [deg]: 0
Outboard twist [deg]: 0
  ***************
 Available mesh distribution types:
   [1] Linear
   [2] Spanwise half-cosine
   [3] Spanwise half-cosine, chordwise cosine
   [5] Spanwise cosine
   [6] Chordwise cosine
   [7] 3:rd order centerpacking. (Not for wings)
 Mesh type: 1
Is partition flapped [1 0]:0
""""""""""""""""""""""""""""""""""""""""""""""""""""""""""""""""""""""""""""""""""""""""""""""
" Data regarding wing number :3
""""""""""""""""""""""""""""""""""""""""""""""""""""""""""""""""""""""""""""""""""""""""""""""
 Number of semispanwise partitions for this wing: 1
 """"""""""""""""""""""""""""""""""""""""""""""""""""""""""""""""""""""""""""""""""""""""""""""
" Data regarding partition number:1
 Is the wing mirrored in the xz-plane [1 0]: 1
Apex x-coordinate: 0
```

Apex y-coordinate: 2.9725

Apex z-coordinate: 1.4145

Root chord: 1.17

****

AVAILABLE AIRFOILS:

****

Enter profile filename from the list above (ex CLARKY.DAT)

OR any NACA four digits series numer (ex: 2412)

0 (zero) for a flat plate.

Base chord airfoil: 23024

Number of panels chord wise: 10

Base chord twist [deg]: 0

Partition dihedral [deg]: -180

Number of panels semi-span wise: 10

Span of partition: 2.9725

Taper ratio: 1

****

AVAILABLE AIRFOILS:

****

Enter profile filename from the list above (ex CLARKY.DAT)

OR any NACA four digits series numer (ex: 2412)

0 (zero) for a flat plate.

Tip chord airfoil: 23024

Quarter chord line sweep [deg]: 0

Outboard twist [deg]: 0

****

Available mesh distribution types:

[1] Linear

[2] Spanwise half-cosine

[3] Spanwise half-cosine, chordwise cosine

[5] Spanwise cosine

[6] Chordwise cosine

[7] 3:rd order centerpacking. (Not for wings)

Mesh type: 1

Is partition flapped [1 0]:0

TORNADO Version 135 Release version

build 2010 03 20 14:07 UTC

Main Menu

Input operations.

[1]. Aircraft geometry setup

[2]. Flight condition setup

[3]. Change rudder setting

[4]. Move reference point

Lattice operations.

[5]. Generate lattice.

Computation operations.

[6]. Processor access

Post-processing and interactive operations.

[7]. Post-processing, Result/Plot functions

[8]. Keyboard access

Auxiliary operations.

[10]. About / Release Info

[100]. Help files

[0]. Exit Tornado

Please enter choice from above: 1

Main Menu

|---->Geometry setup menu

---

[1]. Define new geometry

[2]. Load geometry

[3]. Edit current geometry

[4]. Save current geometry

[5]. Define blunt-body data (for friction drag est).

[0]. Back / up menu

Please enter choice from above: 4

Save the file as: Hasan_EWBA

*** File Saved. ****

Main Menu

---->Geometry setup menu

---

[1]. Define new geometry

[2]. Load geometry

[3]. Edit current geometry

[4]. Save current geometry

[5]. Define blunt-body data (for friction drag est).

[0]. Back / up menu

Please enter choice from above: 3

The number of wings are :3

Number of partition per wing are:1 1 1

Main Menu

|---->Geometry setup menu

|---------->Geometry editor menu

---

[1] Add Wing

[2] Remove Wing

[3] Add partition to a wing

[4] Remove partition from a wing

[5] View wing data

[6] Edit wing/partition data

[7] Plot Geometry

[0] Back / up menu

Please enter choice from above:7

In fLattice_setup2>geosetup15 (line 171)

In fLattice_setup2 (line 60)

In tedit (line 414)

In inpt18 (line 496)

In main (line 127)

In Tornado (line 2)

Continues….

Results:

Cl: 0.291313441633586

L: 15072.03N

Visual display :

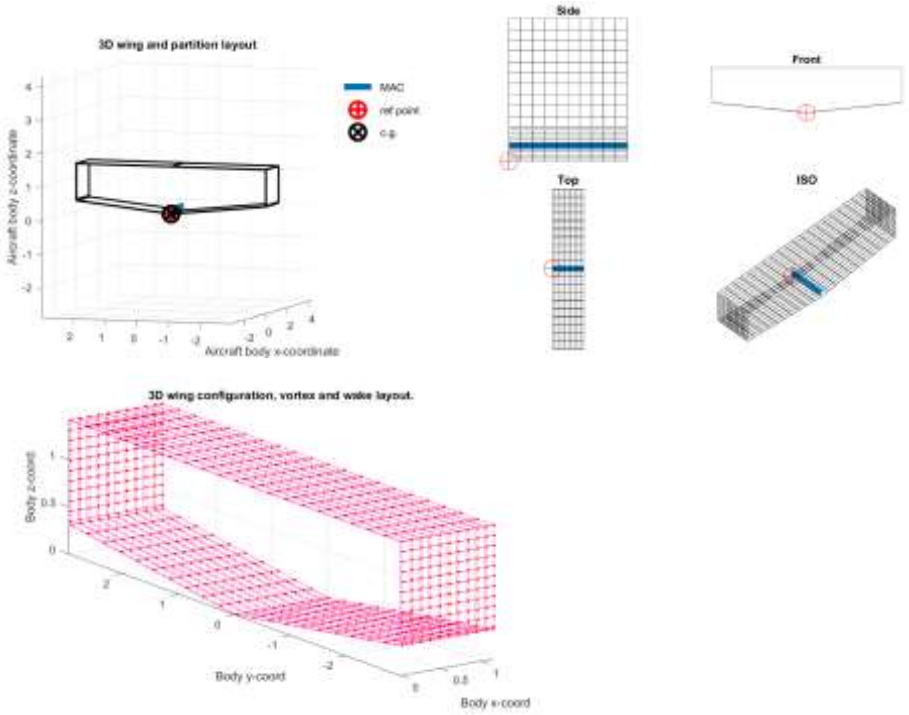

Appendix C.11: Optimum tail and *MATLAB* code with details

$$l = l_{opt} = Kc\sqrt{\frac{4\bar{C}\,S\overline{V_v}}{\pi D_f}}$$

[Where factor '*Kc*' is 1.05]

$= 4.9$ m

The V- tail area as follows:

$(S_V) = \frac{2\times b\times s\times \overline{V_v}}{I_v} = 2.4199\ \text{m}^2,$

Vertical Tail Aspect ratio $(AR) = 3$

Vertical tail volume coefficient as follows [13]: $\overline{V_V} = \frac{S_V l_V}{S_w b} = 0.064$ (3.9)

Matlab code for V-Tail design and trim

```
clc
clear all
% for stability and trim
%Convectional V-Tail is Selected
b=14.039;  % wing span
S=13.14;   % wing area
Vv=0.067; % vertical tail volume selected
lv=4.9;  % V_Tail moment arm
Sv=2*((b*S*Vv)/lv) % both V-Tail platform area % NACA 009 is selected
ARv=3; % V_tailaspect ratio
bv=sqrt(Sv*ARv);  % verical tail span
Lv=1; % V_Tail taper ratio
iv=0; % V_Tail incidence angle in degrees
Sw=0; % V_Tail sweep angle
Di=35; % V_Tail dihedral angle
MACv=bv/ARv % V_Tail mean aerodynamic chord
Cvr=(0.894*MACv)*(1+Lv)/(1+Lv+Lv^2) %V_Tail root chord
Cvt=Lv*Cvr  %V_Tail tip chord
% regaining simulation
% the V_Tail position rearrange
% changing lv to satisfy the spin recovery requirements
% Analyse directional trim
% Analyse the directional stability
%design requirements
```

Outport:

```
Sv = 2.4199, MACv = 0.8981, Cvr = 0.5353, Cvt = 0.5353
```

Appendix C.12: Weight balance

Component	Mass (kg)	Location (x)	Mass moment mx (kgm)	
Hull	55.24	5.195	286.97	
Gondola	10.1	2.5	25.25	
Engine	10.36	6.54	67.75	
Gas	103	5.195	535.085	
Fuel	596	6.19	3689.24	
Passenger	245	3.5	857.5	
Luggage	68	8.065	548.42	
Pilot	93	1.05	97.65	
Tail	5.04	9.66	48.69	
Total W_{TO} (wingless hull)	$\sum$ 1185.74		$\sum$ 6156.555	x_{cg} = 5.192 m
Wing	11.16	1.4546	16.23	
Other	5.1	5.41	27.591	
Total W_{TO} (wingless hull)	$\sum$ 1202		$\sum$ 6200.72	x_{cg} = 5.158 m

Appendix C.13: Static and dynamic stability of wing buoyant aircraft

Static margin *(h)* = $Xnp - x_{cg}$

= 5.195 −5.158

= 0.037 (stable)

$h = -\frac{C_{m\infty}}{c_{L\infty}} = -\frac{dC_m}{dc_L}$

After adding the tail on the design, the Static margin is:

$$\frac{X_{np}}{c} = \frac{1}{4} + \frac{1+\frac{2}{AR}}{1+\frac{2}{ARt}}\left(1-\frac{4}{\mathrm{AR}+2}\right)V_v$$

$$\frac{X_{np}}{c} = \frac{1}{4} + \frac{1+\frac{2}{15}}{1+\frac{2}{3}}\left(1-\frac{4}{15+2}\right)\times 0.064$$

$$\frac{X_{np}}{c} = 0.426$$

$$\frac{X_{np}}{c} = 0.283 = -\frac{dC_{m\alpha}}{dC_L}\,(\text{Stable})$$

$C_{L\alpha}$=5.54

Cm_α= $-\ C_{L\alpha}(\ Xnp - Xcg)$

$= -5.54 \times 0.007$

$= -0.205 = \frac{dc_m}{d\alpha} = \frac{dc_m}{d_{cL}} \times \frac{dC_L}{d_\alpha}$

Longitudinal Dynamic stability

At sea level, the zero-lift drag only consider major aircraft parts: v-tail, wing, and hull

For phugoid motion approximation:

$$\omega_{n_p} = \sqrt{\frac{-Z_u g}{u_o}}$$

$$\xi_p = \frac{-X_u}{2\omega_{n_p}}$$

And eigenvalues of the long period approximation are: $\lambda_{1,2} = -\zeta_p \omega_{n_p} \pm i\omega_{n_p}\sqrt{1-\zeta_p^2}$

Half cycle time ($t_{\frac{1}{2}}$): $t_{1/2} = \frac{0.69}{|\eta|}$; Number of cycles of half amplitude: $N_{1/2} = 0.110\frac{0.69}{|\eta|}$, and

$$X_u = \frac{1}{m}\frac{\partial X}{\partial u} = \frac{1}{m}\frac{\partial}{\partial u}[QSC_{x_u}] = \frac{[-(C_{D_U}+2C_{D_0})+C_{T_u}]QS}{mu_0}$$

$$Z_u = \frac{1}{m}\frac{\partial Z}{\partial u} = \frac{1}{m}\frac{\partial}{\partial u}[QSC_{Z_u}] = \frac{-(C_{L_u}+2C_{L_0})QS}{mu_0}$$

C_{D_U} And C_{L_u} are coefficients as depend on the change of the forward speed, which is neglected. And the coefficient $C_{T_U} = -C_{D_0}$

So,

$$X_u = \frac{1}{m}\frac{\partial X}{\partial u} = \frac{1}{m}\frac{\partial}{\partial u}[QSC_{x_u}] = \frac{-3C_{D_0}QS}{mu_0}$$

$$Z_u = \frac{1}{m}\frac{\partial Z}{\partial u} = \frac{1}{m}\frac{\partial}{\partial u}[QSC_{Z_u}] = \frac{-2C_{L_0}QS}{mu_0}$$

Here,

$C_{D_0} =$ Zero lift drag coefficients are included all drag coefficients of all components.

$C_{L_0} =$ Zero lift coefficient are including the lift coefficient of all components.

The wing aerofoil is *NACA* 23024. All calculation has been considered at $0^0 the$ angle of attack and velocity = 46 m/s, dynamic pressure at sea level: 1295.05 at corresponding and corresponding *Re* = 4.2×10^6

U-derivatives:

$$X_u = \frac{-3C_{D_0}QS}{mu_0} = \frac{-3 \times 0.0157 \times 1296.05 \times 13.14}{1202 \times 46} = -0.0145$$

$$Z_u = \frac{-2C_{L_0}QS}{mu_0} = \frac{-2 \times 0.3 \times 1296.05 \times 13.14}{1202 \times 46} = -0.277$$

So, Natural frequency, $\omega_{n_p} = \sqrt{\frac{-Z_u g}{u_o}}$

$= \sqrt{\frac{-(-0.277\times9.81)}{46}}$

$= 0.24$

Damping Ratio: $\xi_p = \frac{-X_u}{2\omega_{n_p}}$

$= \frac{-(-0.0145)}{2\times0.24}$

$=0.0302$

And eigenvalues of the long period approximation are:

$$\lambda_{1,2} = -\zeta_p\omega_{n_p} \pm i\omega_{n_p}\sqrt{1-\zeta_p^2}$$

$$= -0.0302\times0.24 \pm i\times0.24\sqrt{1-(0.0302)^2}$$

$$= -0.00725 \pm i0.239$$

Period = $\frac{2\pi}{\omega} = \frac{2\times3.1416}{0.24}$ = 26.18sec

Likewise, calculations have been done for another aerofoil.

Appendix C.14: Flight performance

Speed of sound is $a^2 = \gamma RT$ [Gas constant and T= Temperature at 4000m]

$T = T_o - 0.00065xh$ (h= altitude) $=288.15 - 0.00065\times4000 = 262.15$ K

Therefore, Speed of sound $(a) = \sqrt{1.4\times287.053\times262.15} = 319.45$ m/s

So, $V = Ma$ [a= speed of sound, M is Mach number for subsonic >1, when $M = 0.15$]

$= 0.15\times 319.45$ m/s $= 47.9175$ m/s

Velocity at cruise (V_c) $= \sqrt{\frac{2(W)\times9.81}{\rho S\sqrt{\frac{C_{D0}}{K}}}} = 46$ m/s

$V_{EAS} = \left(\frac{\rho_{alt}}{\rho_{SL}}\right)^{\frac{1}{2}} V_{TAS} = (0.669)^{\frac{1}{2}}\times46 = 37.62$ m/s

The cruise lift coefficient is as follows [33, 171]: $C_L = \frac{2\times W_{TOg}}{\rho V^2 S} = 0.3$

Appendix C.15: Geometrical parameter of an *EWBA*

Hull details	Wing details

FR	3.78	Wingspan (b)	14.039 m
Volume	577.05$\mathbf{m^3}$	Aspect ratio	7
$(\boldsymbol{V})^{\frac{2}{3}}$	23.70 $\mathbf{m^3}$	Root chord (C_r)	1.37 m
Length of hull and	10.39 m	Trip chord (C_t)	1.37 m
Hull scale the length (Scale ratio 1:7.5)	1.37m	Sweep Angle	0^0
Height of hull (maximum)	1.73m	Wing area	13.14m^2
Hull surface area	353.34 $\boldsymbol{m^2}$	*MAC*	1.37 m
Hull aspect ratio	0.16		
Hull wetted area	167.12 $\boldsymbol{m^2}$		
V-tails details		Aspect ratio	3
$\boldsymbol{V_V}$	0.047	*V*- tail area	2.41 m^2
Tail span	2.68 m	*MAC*	2.60 m
Root cord $(\boldsymbol{C_r})$	0.894m	Trip cord (C_t)	0.894 m

Appendix C.15.1: 2D geometry of tails, planar and box wing airship

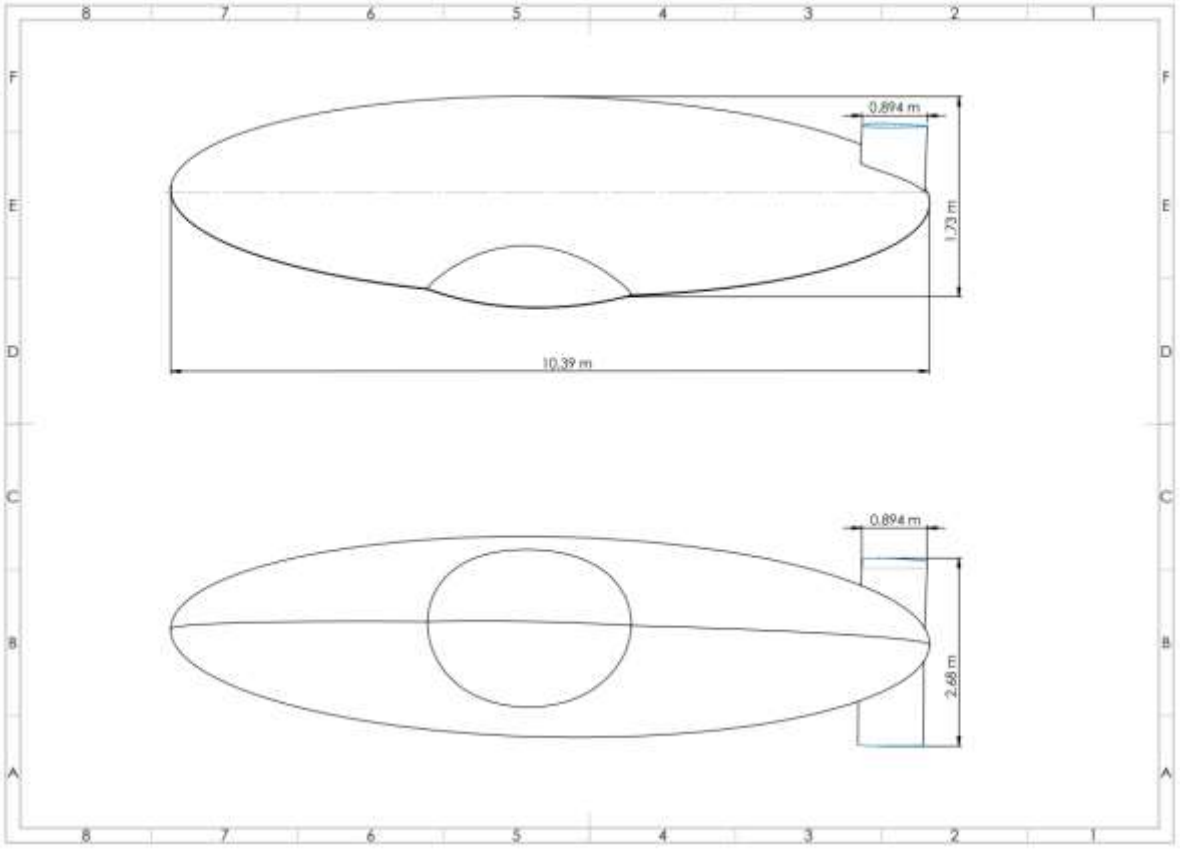

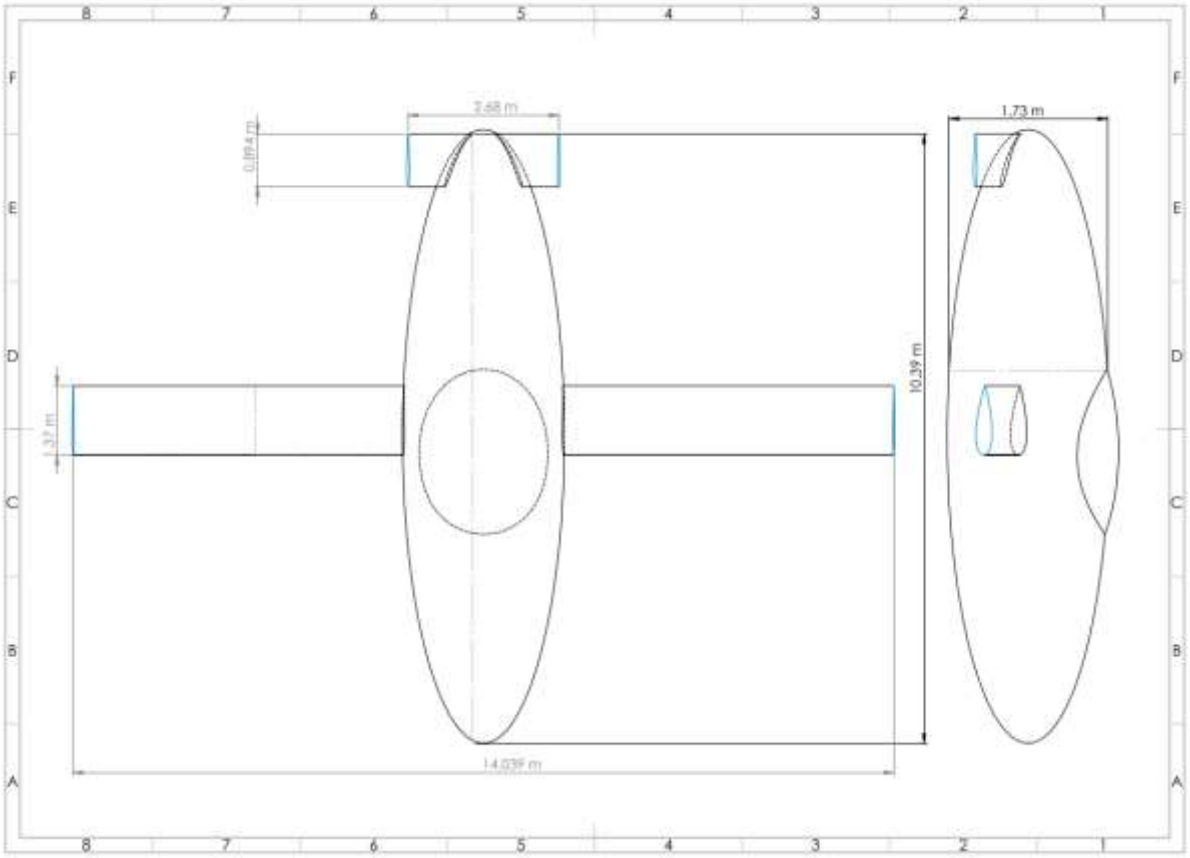

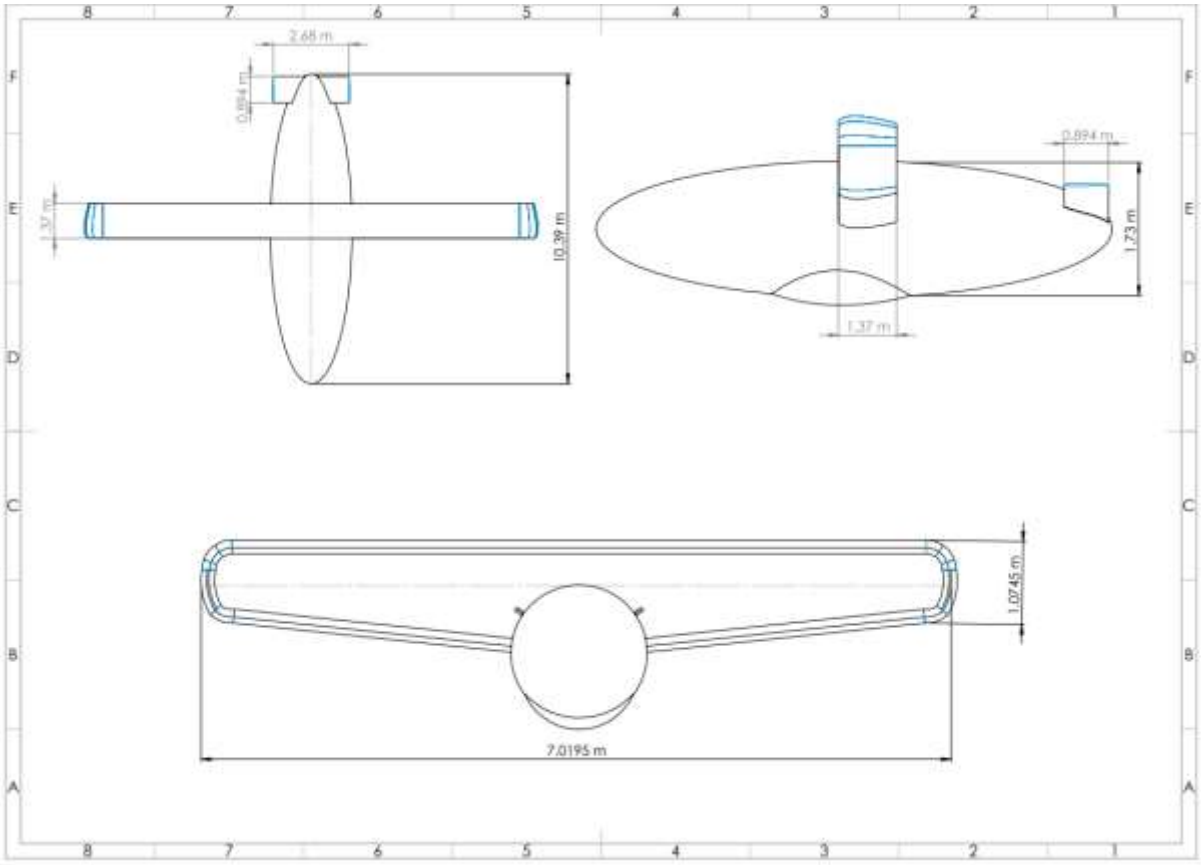

Appendix C.16: Useful various correction factor [33, 154, 171]

No	Type of aircraft	Kc
1	Jet	1.1
2	Cultivation	1.5
3	Cargo (Propeller Driven)	1.2
4	Single engine piston	1.3
5	General aviation	1.2
6	Fighter	1.1
7	Glider	1.05
8	Remote Controlled	1.2

Appendix C.17: Ground performance for *EWBA*

Climbing behaviour

Engineering operation and maintenance manual for a steady straight climbing flight become:

Climb angle $\boldsymbol{\lambda} = sin^{-1}\left(\frac{T-D}{W}\right) = 36.06^0$

$\frac{R}{C} = V\infty sin\lambda = 47\ sin\ (36.06) = 27.66$ m/s

R/C would be increased as C_{Do}or *K* decreases, *R/C* would be increased as $\frac{T}{W}$ (thrust-to-weight ratio) increased, *R/C* could decrease as well as altitude increases

Take-off performance

$$m_T \frac{\partial V}{\partial t} = T - D - u_r(\Delta W - L_{wing})$$

Where, u_r is the rolling friction coefficient. This can be rewritten as follows:

$m_T \frac{\partial V}{\partial t} = m^{-1}[T - D - u_r(\Delta W - L_{wing})]$ and

$$Ds = \frac{\partial V^2}{\frac{\partial V}{\partial t}}$$

$V_{take-off} = 1.1V_{stall}$; So, after substituting the top equation into the bottom and integrating the o in the take-off, we arrive at the following expression

$$S_g = \frac{W_T}{2g\int_0^{V_{take-off}} \frac{\partial V^2}{T-D-u_r(\Delta W - L_{wing})}}$$

where S_g is the ground distance and $T - D - u_r(\Delta W - L_{wing})$ is constant,
$T > [D - u_r(\Delta W - L_{wing})]$,

Therefore, $S_g = \frac{1}{\lambda_A} \times \frac{1.21\left(\frac{\Delta W}{S_{wing}}\right)}{g\rho_a C_{Lwing(max)} \left(\frac{T}{\Delta W}\right)_{0.7V_{take-off}}}$

Using a parametric equation

$G = \frac{\frac{W}{P} \times \frac{W}{S}}{1000}$ and $X_{TO} = 191 - 0.333\mathrm{G} + 0.0982\mathrm{G}^2$

The landing performance is

$V_{so} = \sqrt{\frac{2Wg}{\rho_a S_{wing} C_{Lmax}}}$, $S_L = 0.591\mathrm{V}_{\mathrm{So}}^2$, $S_{LG} = 0.305\mathrm{V}_{\mathrm{So}}^2$

Where, S_{LG} is called ground (run) landing dissonance, S_L total landing distance.

Take-off distance

$$X_{To} = \frac{\frac{W}{T} \times \frac{W}{S}}{\rho \times C_{Lmax}}$$

$$= \frac{6.6677\mathrm{X}\ 18.69}{1.225226 \times 1.41} = 72.13\ \mathrm{m}$$

Landing distance

Landing velocity $V_{so} = \sqrt{\frac{2Wg}{\rho S C_{Lmax}}}$

$$= \sqrt{\frac{2\times691.15\times9.81}{1.225226\times13.14\times1.41}}$$

$$= 24.44 \text{ m/s}$$

Parametric approach:

$S_{LG} = 0.305 V_{so}^2$ [S_{LG} = Ground [run)]

$= 0.305 \times (24.44)^2 = 182.18$ m

$S_L = 0.591 V_{so}^2$ [S_L = Total landing distance]

$= 0.591 \times (24.44)^2 = 358.01$ m

In above has been shown that the systematic conceptual, analytical design process of an SWBA.

Appendix C.18: The range of *EWBA*

The range of mission (R) is attained via a classic Breguet range equation for a propeller-driven air transport [1, 33, 36, 119, 154, 171].

$$R = \frac{\eta_{pr}}{c}.\frac{L}{D} In \frac{W_f}{W_{GTOW}} = 2116.84 \text{ Km}$$

Where, w_{GTOW} is the weight in the beginning and w_f is the weight at the end of a mission. SWBA might be flown with aerodynamic efficiency $\left(\frac{L}{D}\right)_{max}$ and with maximum propeller efficiency: $R \frac{1}{\lambda_A}\frac{n_{pr}}{c}\sqrt{\frac{1}{4KC_{D0}}}\frac{W_f}{W_{GTOW}}_{max}$

Appendix C.18.1: Endurance of *EWBA* and *MATLAB CODE*

Fuel consumption of piston engine and turboprops engine is proportional to power, In steady level flight condition the endurance *(E)* for propeller drive aircraft as follows [33, 36, 171, 178] by Breguet endurance equation:

$$\text{Endurance } (E) = \left(\frac{\Delta W_f}{\dot{W}_f}\right) = \left(\frac{\Delta W_f}{\frac{c}{n_{prop}} P_{R(avg)}}\right) = \left(\frac{\Delta W_f}{\frac{c}{n_{prop}} D_{ag} V_\infty}\right)$$

Where c is *SFC* and $n_{prop.}$ is the propeller efficiency factor.

$$E = \int_{W_1}^{w_0} \frac{n_{prop.} dW}{C.\ \ DV_\infty}$$

$$= \int_{W_1}^{w_0} \frac{n_{prop}.L}{C.\ \ DV_\infty}\ \frac{dW}{W} \left[if\ C_l\ constant, so\ V_\infty = \sqrt{\frac{2W}{\rho S C_l}}\right]$$

$$= \frac{\eta_{pro}}{c} \times \frac{C_L^{\frac{3}{2}}}{C_D} \times \sqrt{\frac{\rho_{\alpha S}}{2}} \times \int_{W_1}^{W_0} \frac{dw}{w^{\frac{3}{2}}} = \frac{\eta_{pro}}{c} \times \frac{C_L^{\frac{3}{2}}}{C_D} \times \sqrt{\left(\frac{\rho_{\alpha S}}{2}\right)(-2)} \times \left[W_1^{\frac{-1}{2}} - W_0^{\frac{-1}{2}}\right]$$

$$= \int_{W_1}^{W_0} \frac{\eta_{pro}}{c} \sqrt{2\rho_{\alpha S}} \times \frac{C_L^{\frac{3}{2}}}{C_D} \times \left[W_0^{\frac{-1}{2}} - W_1^{\frac{-1}{2}}\right]$$ [where η_{pro}, C, $\rho\alpha$ and $\frac{C_L^{\frac{3}{2}}}{C_D}$ is constand]

By the above Breguet endurance equation, maximum endurance can be achieved for maximum propeller efficiency and low *BSFC*, the higher weight of fuel available and maximum lift to drag ratio. Where E is maximum endurance

Fly at maximum $\left(\frac{C_L^{\frac{3}{2}}}{C_D}\right)$, Fly at sea level (maximum) $\rho\alpha$, Maximum propeller efficiency (η_{pro}), Maximum fuel capacity $\left(W_0^{\frac{-1}{2}} - W_1^{\frac{-1}{2}}\right)$, (where W_0 and W_1 are maximum take-off weight and empty respectively)

$$= \frac{0.0157}{4\times10^{-7}} \sqrt{2 \times 1.225 \times 13.14} \times \frac{1.41^{\frac{3}{2}}}{0.02072} \times \left(1202^{-\frac{1}{2}} - 692.23^{-\frac{1}{2}}\right)$$

$$= \frac{0.0157}{4\times10^{-7}} \times 558.48 \times (509.77)^{-\frac{1}{2}} = 915704.99 \text{ sec or } 10.59 \text{ days}$$

MATLAB code for Endurance

```
clc;
clear all;
close all;
% SWBA flight endurance
Wto = 1202*9.81;              %gross weight
Wf = 595.65*9.81;             %fuel weight
Wp = 313;                     %payload weight
Wtop = Wto*9.81;              %gross weight w/ paylod
W1p = (Wto - Wf)*9.81;        %gross weight w/ paylod, all fuel burned
Wtowp = (Wto - Wp)*9.81;      %gross weight w/o paylod
W1wp = (Wto - Wp - Wf)*9.81; %gross weight w/ paylod, all fuel burned
K=0.0523; c=0.8; S=13.14; CD0=0.0157;
LD=(1./(4.*K.*CD0))^0.5;
E1=(1/c)*LD*log(Wtop/W1p);
E2=(1/c)*LD*log(Wtowp/W1wp);
'Endurance with payload :'E1
'Endurance without payload :' E2
```

***MATLAB* outport**

'Endurance with payload: 'E1 = 10.59

'Endurance without payload: 'E2 = 15.8141

Appendix C.19: Propeller performance of *EWBA*

Cruise velocity *(V_c)* = *Ma* = 46 m/s,

Lift co-efficient at cruise *(C_{Lc})* = $\frac{2mg}{\rho S(V_c)^2}$ = 0.3

Drag co-efficient at cruise:(C_{Dc})=C_{D0}+ $K(C_{Lc})^2$ = 0.0157+ 0.0523×$(0.3)^2$ = 0.020407 for planer wing and 0.0185 for non-planer wing

Drag at cruise *(D)* = $\frac{1}{2}\rho v^2 s c_{Dc}$ = 0.5× 0.82 × $(46)^2$ × 13.14 × 0.020407= 236.63 N for planer wing and 210.89 for non-planer wing

T = *D* at cruise, Power required at (Cruise) 4000 m and maximum sea-level power required 165.46 hp.

Therefore, this research is referred to as engine manufacturers catalogues in Appendix C.19.1 (Table 14.1), which has been chosen as the two propeller engines. For safety reasons, this research decided to use the multi-engine configuration. Thus, two propeller engines are chosen for *EWBA* to produce about 96.6 hp (*BMW_R1150RS*) each, which is sufficient to carry *EWBA* flights.

Propeller diameter $(D_P) = K_{np}\sqrt{\frac{2Pn_P AR_P}{\rho V_{av}^2 V_c C_{Lp}}}$ (K_{np} is 0.72 for a three-blade propeller)

$$= 0.72 \times \sqrt{\left(\frac{(2\times 20327.7785\times 0.8\times 9)}{0.82\times(0.7\times 270)^2\times 0.3\times(46)}\right)} = 0.612 \text{ m}$$

(trip speed less than 270 m/s for metal prop)

Propeller Rotational Speed (*RPM*): $V_{tip\ cruise} = \sqrt{V_{tip_{static}}^2 + V_c^2}$, $= \sqrt{V_{tip_{cruise}}^2 - V_c^2}$

$= \sqrt{270^2 - 46^2}$ =266.05 m/s

$V_{tip_{static}}$ $= \frac{D_P}{2}\omega$, ω $= \frac{2V_{tip_{static}}}{D_P}$ $= \frac{2\times 266.05}{0.612}$ =869.4 Rad/s

So, $(\omega) = \frac{2\pi.n}{60}$, $n = \frac{60\omega}{2\times 3.14} = \frac{60\times 869.4}{2\times 3.14} = 8306.369$ rpm

The advance ratio or propeller efficiency by Rule of thumb $(J) = \frac{V}{nD_P}$ [*V*= velocity and n are rpm and D_p = propeller diameter 0.612 m

$$= \frac{46}{8306.369\times 0.612} = 0.009048$$

Appendix C.19.1: Several piston engines for Primary specifications

No.	Manufacturer	Designation	Arrangement	Number of cylinders	Cooling	Mass (kg)	Max power (hp)
1	Hirth	F33B	–	1	Air	13	24
2	Rotax	447 UL-1V	In-line	2	Air	26.8	39.6
3	BMW	R115ORS	Opposed	2	Air + oil	76.3	96.6
4	Subaru	EA81-140	Opposed	4	Liquid	100	140
5	Wilksch	WAM 160	In-line	4	Liquid	120	160
6	Textron-Lycoming	O-320-H	Opposed	4	Air	128	160
7	PZL	F 6A6350-C1	Opposed	6	Air	150	205
8	TCM	Tsio-360-RB	Opposed	6	Air	148.6	220
9	Textron-Lycoming	IO-540-C	Opposed	6	Air	170	250
10	TCM	IO-470-D	Opposed	6	Air	193.3	260
11	Bombardier	V300	Vee		Liquid	210	300
12	TCM	TSIOL-550-C	Opposed	6	Liquid	188.4	350
13	Textron-Lycoming	IO-270-A	Opposed	8	Air	258	400
14	VOKBM	M-9F	Radial	9	Air	214	420
15	Orenda	OE600 Turbo	Vee	8	Liquid	–	750
16	PZL	K-9	Radial	9	Air	580	1 170

Figure C.14.1: Primary specification of several engines[209]

Appendix D.1: Computational Fluid Dynamics (CFD)

CFD plays an essential role in stimulating the flows around aircraft for investigating aerodynamics behaviour [257, 258]. Concerning the current enhancement of high-performance computing, the *CFD* stipulates a powerful tool for designers, which is being applied more intensively throughout the design for aerodynamic investigation. In this research, an Ansys Workbench Fluent solver has been used to compare numerical, analytical results.

Appendix D.1.2: The Computational Fluid Dynamics Governing equations

The base on fluid dynamics, there are the following three fundamental physical principles of governing equations that must be considered during *CFD* simulation:

- Mass conservation equation
- Momentum conservation equation: $F = ma$ (Newton's second law for motion)
- Energy conservation equation

The mathematical declaration of the above law of physics equations is solved by manipulating various systems across a fluid domain defined as control volume. These computational

articulations are mostly perceived as the Navier-Stokes equations that can be seen in the following vector formula as conservative equations. It is quoted from [259, 260].

$$\frac{\partial}{\partial t}\iiint_V \vec{W}\,\mathrm{dV} = -\iint_{\partial V}\bar{\bar{F}}.\vec{n}\,\mathrm{ds} \qquad 4.1$$

$$\text{Where, } \vec{W}=\begin{bmatrix}\rho\\ \rho_u\\ \rho_v\\ \rho_w\\ \rho_E\end{bmatrix} \qquad 4.2$$

$$\text{And, } \bar{\bar{F}}=\left(\vec{F^c}+\vec{F_V^c}\right).\vec{e_x}+\left(\vec{G^c}+\vec{G_V^c}\right).\vec{e_y}+\left(\vec{H^c}+\vec{H_V^c}\right).\vec{e_z} \qquad 4.3$$

with

$$\vec{F^c}=\begin{bmatrix}\rho_u\\ \rho_{u^2+p}\\ \rho_{uv}\\ \rho_{uw}\\ \rho_{Hu}\end{bmatrix},\qquad \vec{F_V^c}=-\begin{bmatrix}0\\ \tau_{xx}\\ \tau_{xy}\\ \tau_{xz}\\ u\tau_{xx}+v\tau_{xy}+w\tau_{xz}+q_x\end{bmatrix} \qquad 3.4$$

$$\vec{G^c}=\begin{bmatrix}\rho_v\\ \rho_{uv}\\ \rho_{v^2}+p\\ \rho_{vw}\\ \rho_{Hv}\end{bmatrix},\qquad \vec{G_V^c}=-\begin{bmatrix}0\\ \tau_{xx}\\ \tau_{xy}\\ \tau_{xz}\\ u\tau_{xy}+v\tau_{yy}+w\tau_{yz}+q_y\end{bmatrix} \qquad 3.5$$

$$\vec{F^c}=\begin{bmatrix}\rho_w\\ \rho_{uw}\\ \rho_{vw}\\ \rho_{w^2}+p\\ \rho_{Hw}\end{bmatrix},\qquad \vec{H_V^c}=-\begin{bmatrix}0\\ \tau_{xx}\\ \tau_{xy}\\ \tau_{xz}\\ u\tau_{xz}+v\tau_{yz}+w\tau_{zz}+q_z\end{bmatrix} \qquad 3.6$$

Where, $\vec{W}$ are quantities of vector converse, $\bar{\bar{F}}$ is flux variable density tensor created the viscous form $\left(\vec{F_V^c},\ \vec{G_V^c}\text{ and }\vec{H_V^c}\right)$ and also inviscid flux vectors $\left(\vec{F^c}, \vec{G^c}\text{ and }\vec{H^c}\right)$ in order to three cartesian directions. Density (ρ), velocity component for cartesian $(u, v, \text{and } w)$, static pressure (p), shear stresses (τ), heat fluxes (q) and overall inner energy (E) as

denoted. Furthermore, the τ and q are accorded as the following viscous fluxes equation :

$$\tau_{xx} = 2\mu \frac{\partial u}{\partial x} + \lambda \left(\frac{\partial u}{\partial x} + \frac{\partial v}{\partial y} + \frac{\partial w}{\partial z}\right)$$

$$\tau_{yy} = 2\mu \frac{\partial v}{\partial y} + \lambda \left(\frac{\partial u}{\partial x} + \frac{\partial v}{\partial y} + \frac{\partial w}{\partial z}\right)$$

$$\tau_{zz} = 2\mu \frac{\partial w}{\partial z} + \lambda \left(\frac{\partial u}{\partial x} + \frac{\partial v}{\partial y} + \frac{\partial w}{\partial z}\right)$$

$$\tau_{xy} = \mu \left(\frac{\partial u}{\partial y} + \frac{\partial v}{\partial x}\right) = \tau_{yx}$$

$$\tau_{xz} = \mu \left(\frac{\partial u}{\partial z} + \frac{\partial w}{\partial x}\right) = \tau_{zx}$$

$$\tau_{yz} = \mu \left(\frac{\partial v}{\partial z} + \frac{\partial w}{\partial y}\right) = \tau_{zy}$$

Where the μ is dynamic viscosity as Sutherland law and where also $\lambda = -\frac{2}{3}\mu$. It is hows that viscous stresses related to the velocity profile as above Stokes equations.

$$q_x = \kappa \frac{\partial T}{\partial x},\ q_y = \kappa \frac{\partial T}{\partial y} \text{ and } q_z = \kappa \frac{\partial T}{\partial z}$$

Where $T$and K are respectively temperature and thermal conductivity. Hence, it relayed to perfect gas constant law as a state:

$$P = \rho RT = (\gamma - 1)\rho \left(E - \frac{u^2 + v^2 + w^2}{2}\right)$$

Where γ is a specific heat ratio, R is gas constant, respectively.

The RANS equation and properties

The Reynolds decomposition such as high *Re* turbulent flows are applied to full Navier–equations (*NS*) implies the separation of the flow variables: velocity u, into the mean $(\bar{u})$ in time average, fluctuating form (u') components [259]. The fluctuating mean quantities $\overline{u'}$ is zero among the set of properties as seen as follows:

$$u\,(\dot{x}, t) = \bar{u}(\dot{x}) + u'(\dot{x}, t)$$

Where position vector $(\dot{x})$ is = $\begin{bmatrix} x \\ y \\ z \end{bmatrix}$, the new quantities of properties called Reynolds stress are shown in the *RANS* equations as follows:

$$\mathcal{R}_{ij} = -\rho\,\overline{\mu_i'\,\mu_j'}$$

This scheme turns into impossible to solve as more unknown than equations which as known as the RANS closure problem.

The RANS turbulence model challenges and solution

An additional equation is generated which offer unknown Reynolds stresses $(\mathcal{R}_{ij})$ solution; since the Reynolds stresses effect is similar to shear stress, an approximation has been suggested by Boussinesq that $\mathcal{R}_{ij}$ would be modelled [261]. In fact, the concept of the Boussinesq hypothesis of the turbulent eddy viscosity μ_t are introduced and simplified the *RANS* equations as impact as follows:

$$\mu_{total} = \mu + \mu_t \;\lambda_{total} = -\frac{2}{3}\mu_{total}$$

Then the Reynolds stresses updated by Boussinesq approximation as follows:

$$\mathcal{R}_{ij} = -\rho\,\overline{\mu_i'\,\mu_j'} = \mu_t\left(\frac{\partial\overline{u_i}}{\partial x_j} + \frac{\partial\overline{u_j}}{\partial x_i} - \frac{2}{3}\delta_{ij}\,\frac{\partial\overline{u}_k}{\partial x_k}\right) - \frac{2}{3}\delta_{ij}\rho k$$

where δ_{ij} is equal to 1 since $i = j$, and 0 (zero) if $i \neq j$. The Reynolds stresses model can be used to provide a turbulent transport equation for quantities: the eddy viscosity model contains the equation of 0,1,2,3 and 4 for quantities. For example, turbulent kinetic energy (k) specific dissipation rate (ω) and turbulent viscosity (μ_t). The two main turbulent models have been approached throughout this aerodynamic investigation.

Reynolds Stress full model for second-order closures

In this project, a second-order closure method was used, which suggests a transport equation in each of the 6 $\mathcal{R}_{ij}$. It is usually referred to as the Reynolds Stress Model (*RSM*). The key merits of this scheme are the implicit computation of each specific element of the Reynolds

Stress matrix. However, a higher computational cost since more equations is being solved. It usually can be written as follows:

$$\frac{\rho(\bar{\rho}\ \mathcal{R}_{ij})}{\partial t} + \frac{\partial(\bar{\rho}\ \mathcal{R}_{ij}\bar{u}_k)}{\partial x_k} = \bar{\rho}P_{ij} + \bar{\rho}\pi_{ij} - \ \bar{\rho}\varepsilon_{ij} + \bar{\rho}D_{ij} + \bar{\rho}M_{ij}$$

Where local time derivative is $\frac{\rho(\bar{\rho}\ \mathcal{R}_{ij})}{\partial t}$; the convection of $\mathcal{R}_{ij}$ is $\frac{\partial(\bar{\rho}\ \mathcal{R}_{ij}\bar{u}_k)}{\partial x_k}$; the $\bar{\rho}P_{ij,}\ \bar{\rho}\pi_{ij}, \bar{\rho}\varepsilon_{ij},$ $\bar{\rho}D_{ij}$ and $\bar{\rho}M_{ij}$ are the term of production, pressure-strain, dissipation, diffusion, and fluctuating mass flux contribution respectively. the $\bar{u}$ refers to density-weighted velocity (Favre averaged velocity), it is classified as $\bar{u} = \frac{\overline{\rho u}}{\rho}$. This typical velocity leads to the exact phrase since large density variations during the solution. Additionally, the Reynolds stress model (*RSM*) is used for a supplementary equation for turbulent quantities: the (ε) as scalar dissipation rate or (ω) is a specific dissipation rate. That is provided with an additional function of closure during modelling.

The process of Discretization
The technique of Finite Volume Method (FVM)

The *FVM* represents the conservation of mass, momentum, energy, and also turbulent quantities, which is not possible to solve analytically in common fluid flow. The *FVM* is used to solve the equations during computational fluid dynamics (*CFD*) simulation by integrating over finite control volumes. With time the dependant *RANS* equations have been described earlier in this sections, now can be re-written as a physical domain $\Omega(t) \subset R^3$ by $\partial\Omega(t)$ as a boundary, $\vec{x}(t)$ is time-dependent coordinate and $\vec{U}[\vec{x}(t), t]$ is the velocity field. Thus, it looks as bellows:

$$\vec{U}[\vec{x}(t), t] = [u(\vec{x}\ , t), v(\vec{x}\ , t), w(\vec{x}\ , t)]^T, \text{ and } \vec{x}(t) = [x(t), y(t), z(t)]^T$$

This equation can be seen in integral form as bellows:

$$\int_{\Omega(t)} \frac{\partial \overrightarrow{W}}{\partial t}\ d|\Omega| + \int_{\partial\Omega(t)} \left(\overrightarrow{F_c}\ .\ \vec{n} - \ \overrightarrow{F_v}\ .\ \vec{n}\ \right) d|\Omega| = \int_{\Omega(t)} \vec{Q}\, d\Omega$$

Where state variables vector is $\overrightarrow{W}$ as follows:

$$\overrightarrow{W} = [\rho, \rho u,\ \rho v,\ \rho w, \rho E, \rho\mathcal{R}_{11}, \rho\mathcal{R}_{12}, \rho\mathcal{R}_{13}, \rho\mathcal{R}_{22}, \rho\mathcal{R}_{23}, \rho g]^T$$

The $\overrightarrow{F_c}$, $\overrightarrow{F_v}$ and $\vec{n}$ are vector convective fluxes, diffusion fluxes, unit normal respectively; the $d|\Omega|$ is a physical domain in the surrounding surface area, source terms are $\Omega(t)$, and $\vec{Q}$.
Now for the time-dependent terms, the above equation can be modified using Leibniz integral role as follows:

$$\frac{d}{dt}\int_{\Omega(t)}\overrightarrow{W}\,d|\Omega| + \int_{\partial\Omega(t)}\left(\overrightarrow{F_c}.\vec{n} - \overrightarrow{F_v}.\vec{n} - \overrightarrow{W}.\vec{\dot{x}}.\vec{n}\right)d|\Omega| = \int_{\Omega(t)}\vec{Q}\,d|\Omega|$$

The above equation will be solved in every control volume for the fluid domain using different three-dimensional and chronological discretization systems for typical simulation. The residual $\vec{R}$ is given the flux imbalance in the volume Ω as a function of the sum of fluxes that pass around the boundary surface of the volume as applied by the divergence theory.

Appendix D.2: Residuals Graph for k-ε model

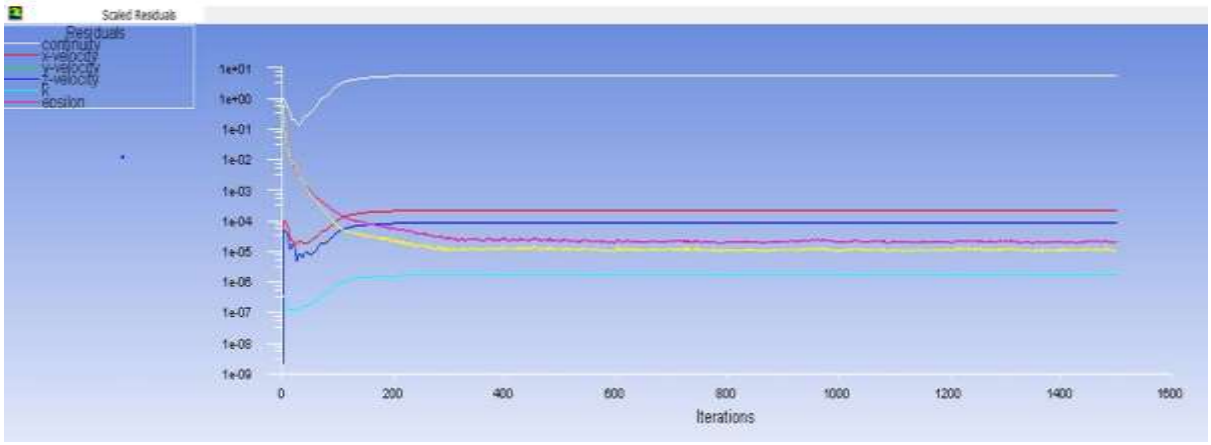

iter	continuity	x-velocity	y − velocity	z-velocity	energy	k	epsilon	Cm-1	Cl-1	Cd-1	time/iter	
1497	5.7548e+00	2.2069e-04	8.6545e-05	8.6488e-06	1.6909e-06	1.8871e-05	1.0165e-05	-2.2998e-03	3.0401e-04	2.1100e-02	0:01:02	3
1498	5.7545e+00	2.2041e-04	8.6436e-05	8.6274e-06	1.6885e-06	2.0685e-05	1.1622e-05	-2.2964e-03	3.0457e-04	2.1099e-02	0:00:41	2
1499	5.7438e+00	2.2025e-04	8.6416e-05	8.6392e-05	1.6929e-06	1.9984e-05	1.0311e-05	-2.2972e-03	3.0525e-04	2.1098e-02	0:00:21	1
1500	5.7425e+00	2.2021e-04	8.6402e-05	8.6412e-05	1.6901e-06	1.9904e-05	1.0178e-05	-2.2973e-03	3.0529e-04	2.1097e-02	0:00:00	0

Done.

Figure D.1.1: Residual and output results for k-ε model

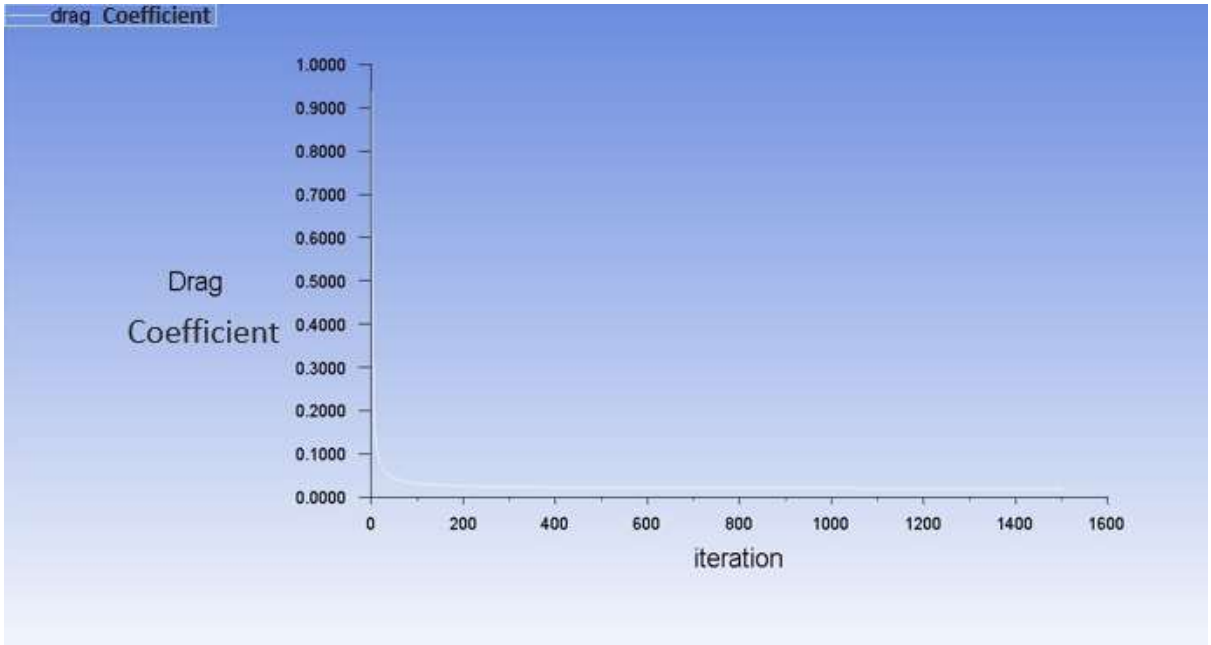

Figure D.1.1: C_D vs iteration for k-ε model

Appendix D 2.1:*RSM* model

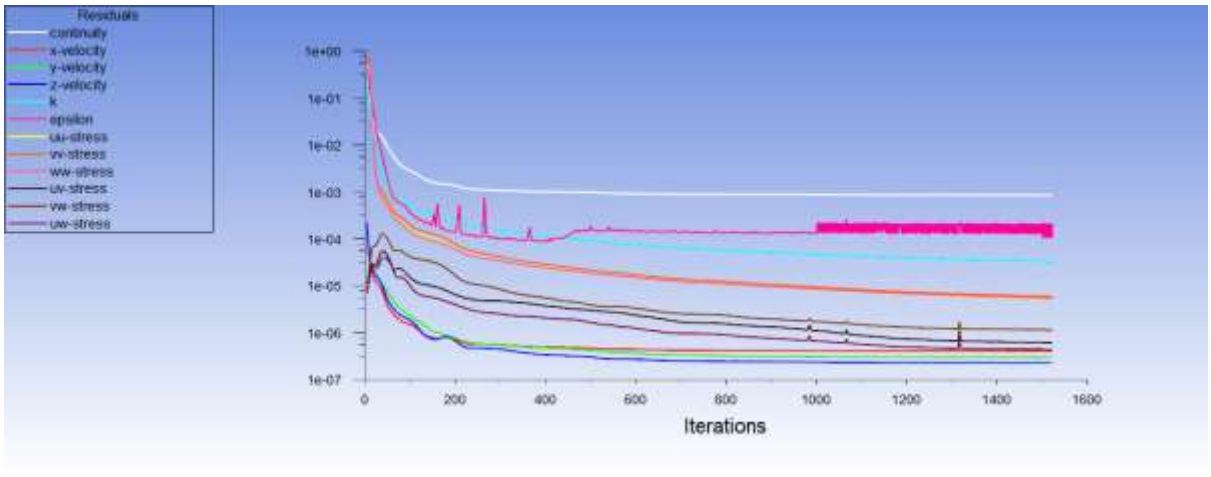

iter	continuity	x-velocity	y-velocity	z-velocity	k	epsilon	uu-stress	vv-stress	ww-stress	uv-stress	vw-stress	uw-stress	report-def	report-def	time/iter	
1513	8.5746e-04	4.1413e-07	3.0159e-07	2.3397e-07	3.2812e-05	1.0630e-04	5.3617e-06	6.0237e-06	5.9196e-06	6.1757e-07	1.1857e-06	4.4151e-07	2.3322e-01	3.1960e-02	1:01:40	9
1514	8.5451e-04	4.1456e-07	3.0171e-07	2.3305e-07	3.2788e-05	1.1249e-04	5.3611e-06	6.0120e-06	5.9156e-06	6.1708e-07	1.1859e-06	4.4089e-07	2.3322e-01	3.1961e-02	1:01:44	9
1515	8.5748e-04	4.1477e-07	3.0082e-07	2.3315e-07	3.2767e-05	1.1016e-04	5.3537e-06	6.0133e-06	5.9037e-06	6.1711e-07	1.1859e-06	4.4088e-07	2.3322e-01	3.1961e-02	1:01:34	7
1516	8.5772e-04	4.1466e-07	3.0227e-07	2.3321e-07	3.2758e-05	1.0249e-04	5.3561e-06	6.0107e-06	5.9003e-06	6.1704e-07	1.1855e-06	4.4094e-07	2.3322e-01	3.1961e-02	1:01:23	6
1517	8.5756e-04	4.1437e-07	3.0048e-07	2.3315e-07	3.2761e-05	1.0553e-04	5.3533e-06	6.0194e-06	5.9077e-06	6.1730e-07	1.1858e-06	4.4128e-07	2.3322e-01	3.1960e-02	1:01:11	9
1518	8.5707e-04	4.1422e-07	3.0090e-07	2.3304e-07	3.2759e-05	1.0868e-04	5.3509e-06	6.0041e-06	5.8921e-06	6.1706e-07	1.1862e-06	4.4138e-07	2.3322e-01	3.1959e-02	1:00:58	9
1519	8.5578e-04	4.1418e-07	3.0064e-07	2.3302e-07	3.2733e-05	1.0355e-04	5.3474e-06	6.0105e-06	5.8932e-06	6.1747e-07	1.1856e-06	4.4155e-07	2.3322e-01	3.1959e-02	1:00:45	9
1520	8.5497e-04	4.1419e-07	3.0162e-07	2.3285e-07	3.2716e-05	1.0115e-04	5.3436e-06	5.9995e-06	5.8859e-06	6.1707e-07	1.1851e-06	4.4163e-07	2.3322e-01	3.1958e-02	1:00:30	7
1521	8.4066e-04	4.1390e-07	3.0058e-07	2.3291e-07	3.2709e-05	1.0405e-04	5.3412e-06	6.0028e-06	5.8878e-06	6.1747e-07	1.1849e-06	4.4198e-07	2.3322e-01	3.1957e-02	1:00:16	1
1522	8.5670e-04	4.1430e-07	2.9933e-07	2.3281e-07	3.2691e-05	1.1470e-04	5.3385e-06	5.9824e-06	5.8828e-06	6.1802e-07	1.1849e-06	4.4247e-07	2.3322e-01	3.1957e-02	1:00:00	0

Figure D.1.3: *RSM* residual graph and output results

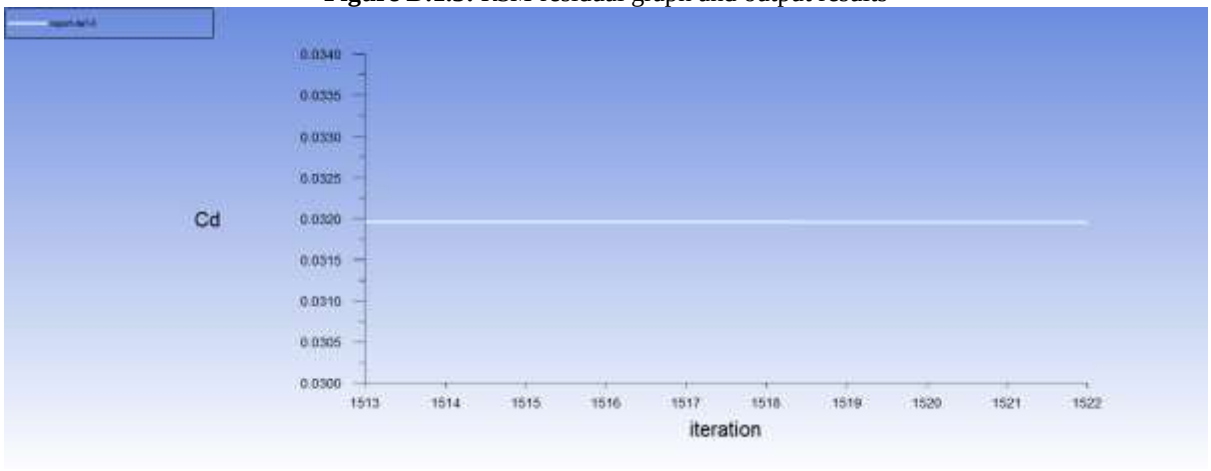

Figure 1.4: C_D vs iteration for CFD *RSM* model

Appendix D.3: Aerodynamic data and comparison

Spheroid 6:1

		K-e			*RSM*			
AoA	C_L	C_D	C_M	*L/D*	C_L	C_D	C_M	*L/D*
-4	-0.0192	0.0221	0.039617	-0.86878	-0.0158	0.0276	0.00263	-0.57234
-2	-0.0265	0.02	0.003861	-1.325	-0.03075	0.021233	0.001399	-1.44801
0	-0.0155	0.0151	-0.03039	-1.02649	-1.95E-02	0.019105	-3.94E-06	-1.01868
2	0.013229	0.0229	-0.06116	0.577686	0.01295	0.021242	-0.00139	0.609655
4	0.023259	0.02359	-0.08184	0.985969	0.013487	0.023377	-0.00275	0.57694
6	0.03357	0.02507	-0.089	1.339051	0.023215	0.025338	-0.00396	0.916237
8	0.0387	0.02806	-0.0958	1.379187	0.039266	0.0291	-0.00528	1.349334

10	0.0458	0.032534	-0.0962	1.407758	0.048707	0.033234	-0.00637	1.465591
12	0.058	0.0375	-0.09689	1.546667	0.061424	0.039179	-0.00758	1.56777
14	0.0704	0.04145	-0.07485	1.698432	0.078235	0.045095	-0.00818	1.734897
16	0.0987	0.053051	-0.0672	1.860474	0.10137	0.05818	-0.00944	1.742352
18	0.115	0.0619	-0.065	1.857835	0.123647	0.066091	-0.01035	1.870857
20	0.128	0.07504	-0.06292	1.705757	0.138706	0.075215	-0.01128	1.844125

Tail model

k-e *RSM*

AoA	C_L	C_D	C_M	*L/D*	C_L	C_D	C_M	*L/D*
-4	-0.0067	0.021645	0.004223	-0.30945	-0.00224	0.021536	0.005512	-0.10401
-2	-0.00493	0.0206	0.001383	-0.23917	-0.002	0.020513	0.002787	-0.09757
0	-0.0179	0.020559	-0.00035	-0.87066	-0.0138	0.020496	-0.00039	-0.67331
2	0.02279	0.021575	-0.00249	1.056315	0.035312	0.021051	-0.00341	1.67745
4	0.035358	0.021089	-0.0056	1.676633	0.024781	0.021926	-0.00586	1.130195
6	0.071848	0.024658	-0.00748	2.913757	0.054874	0.023588	-0.00811	2.326362
8	0.098553	0.026717	-0.0098	3.688782	0.092932	0.026261	-0.00972	3.538757
10	0.13846	0.032508	-0.01139	4.259279	0.12037	0.031995	-0.01186	3.762127
12	0.13611	0.037946	-0.01249	3.586952	0.13693	0.038046	-0.01347	3.599083
14	0.14275	0.04593	-0.01347	3.10799	0.151406	0.043634	-0.01435	3.469933
16	0.181291	0.05743	-0.0154	3.15673	0.18858	0.053776	-0.0158	3.506769
18	0.16623	0.065986	-0.01658	2.519186	0.16927	0.064715	-0.01511	2.615622
20	0.16014	0.07626	-0.01767	2.099927	0.18005	0.077274	-0.01599	2.33002

Plain Wing

k-e *RSM*

AoA	C_L	C_D	C_M	*L/D*	C_L	C_D	C_M	*L/D*
-4	-0.5514	0.030876	0.003852	-17.8583	-0.5	0.0312	0.00458	-16.0256
-2	-0.20767	0.024437	8.27E-03	-8.49809	-0.14	0.02414	0.001962	-5.7995
0	0.314388	0.022543	-0.00166	13.94646	0.283	0.0211	-0.00102	13.41232
2	0.548439	0.02693	-0.00455	20.36517	0.43	0.02713	-0.00421	15.84961
4	0.78322	0.0291	-0.0071	26.91432	0.74	0.03015	-0.00723	24.54395
6	0.986721	0.033518	-0.00836	29.43898	0.95	0.03417	-0.00983	27.80217
8	1.171962	0.036041	-0.00941	32.51778	1.1335	0.0385	-0.01091	29.44156
10	1.2771	0.041995	-0.01222	30.41044	1.2155	0.0412	-0.01171	29.50243
12	1.344279	0.049121	-0.01315	27.36658	1.2772	0.0491	-0.0125	26.01222
14	1.395909	0.056639	-0.00145	24.64562	1.349	0.0565	-0.0137	23.87611
16	1.351902	0.064806	-0.01585	20.86084	1.304	0.0642	-0.01469	20.31153
18	1.272685	0.075052	-0.0168	16.95734	1.255	0.07515	-0.01577	16.69993
20	1.274643	0.085786	-0.01663	14.85836	1.26	0.08625	-0.01598	14.6087

Box wing

k-e *RSM*

AoA	C_L	C_D	C_M	*L/D*	C_L	C_D	C_M	*L/D*
-4	-0.90292	0.041021	0.044617	-22.0113	-0.75418	0.043562		-17.3128
-2	-0.27563	0.034721	0.008861	-7.93836	-0.2327	0.03572	-5.48E03	-6.51456
0	0.330065	0.031473	-0.02539	10.48738	0.243	0.0331	-0.04086	7.34139
2	0.886127	0.032204	-0.05616	27.51581	0.81374	0.03522	-0.05957	23.10449
4	1.150546	0.035101	-0.07684	32.77787	1.12903	0.039313	-0.09114	28.719
6	1.21E+00	4.01E-02	-0.084	30.07332	1.17949	0.045123	-0.09939	26.13944

8	1.2671	0.04703	-0.0908	26.94238	1.23322	0.0529	-0.10105	23.31229
10	1.3237	0.05537	-0.0912	23.90645	1.2792	0.05905	-0.10351	21.663
12	1.362785	0.0632	-0.09189	21.56306	1.32006	0.06602	-0.0905	19.99485
14	1.48061	0.0709	-0.06985	20.88307	1.35227	0.0739	-0.08439	18.29865
16	1.431	0.0809	-0.0622	17.6885	1.4246	0.082212	-0.06816	17.32837
18	1.439503	0.08902	-0.06	16.17056	1.40014	0.091137	-0.07156	15.36302
20	1.420884	0.097444	-0.05792	14.58159	1.395	0.098	-0.06611	14.23469

Appendix D.4: Contour of skin friction coefficient in two different turbulence model such as $(k-\varepsilon)$ and *RSM* at *AOA* 0^0, *Re=4.2*$\times 10^6$, *M=0.135* for 6:1 prolate spheroid and tail model

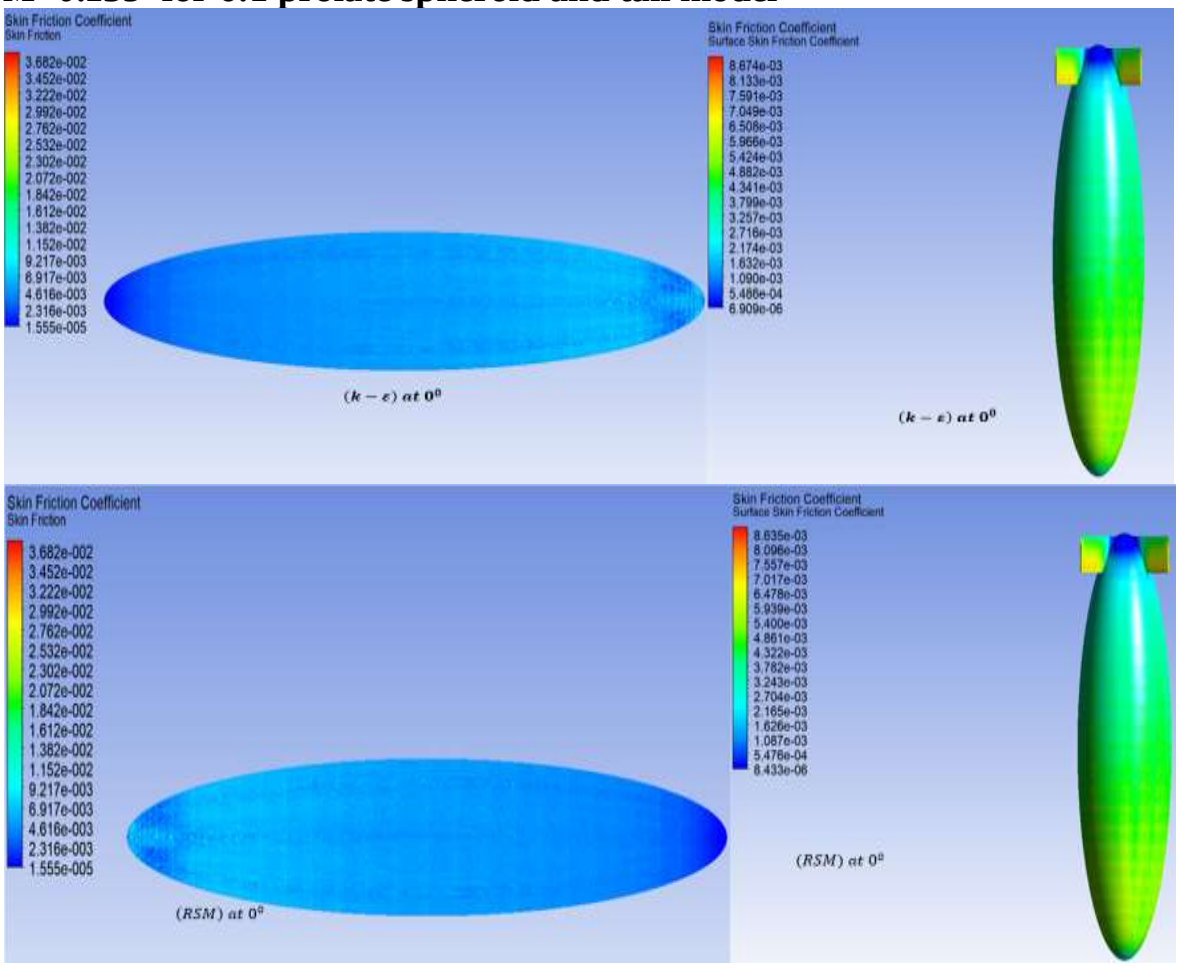

Chapter 7. References